Influence of Post Heat-Treatments on Microstructural and Mechanical Performances of LPBF-Manufactured Ti6Al4V Parts

Thesis submitted for the award of the Degree

of

Doctor of Philosophy

in the Department of Mechanical Engineering

By

Akshay Pathania

2018RME0023

Under the supervision of

Dr. S. Anand Kumar

भारतीय प्रौद्योगिकी संस्थान जम्मू
INDIAN INSTITUTE OF TECHNOLOGY JAMMU

Indian Institute of Technology

Jammu

May,2023

Dedication

Dedicated

To

My Parents,

Wife and Son

Declaration

I hereby declare that the matter embodied in this thesis entitled "**Influence of post heat-treatments on microstructural and mechanical performances of LPBF-manufactured Ti6Al4V parts**" is the result of investigations carried out by me in the Department of Mechanical Engineering, Indian Institute of Technology, Jammu, India, under the supervision of **Dr. S. Anand Kumar** and it has not been submitted elsewhere for the award of any degree or diploma, membership etc. In keeping with the general practice in reporting scientific observations, due acknowledgements have been made whenever the work described is based on the findings of other investigators. Any omission that might have occurred due to oversight or error in judgment is regretted. A complete bibliography of the books and journals referred in this thesis is given at the end of each chapter.

May,2023

Indian Institute of Technology, Jammu

Akshay Pathania

2018RME0023

Abstract

Keywords: LPBF Process, Ti6Al4V alloy, Post heat-treatment, Lamellar Microstructure, Microhardness, Tensile strength, High cycle fatigue, Fractal dimension analysis, Damping characteristics.

The present study investigated the influence of interface shear strength (ISS) on the support removal effort without deviating the dimensional accuracy of a laser powder bed fusion (LPBF) manufactured gear-type parts. The FEM simulations were carried out to evaluate the effect of different process parameters of support structures (SSs) on the distortion. Additionally, the dimensional accuracy of manufactured parts was assessed using a non-contact 3D white light scanning (WLS) technique. A simple in-house technique is adopted to evaluate the ISS of support removal using a mechanical torque wrench. The results showed that all the LPBF parts had insignificant dimensional deviation compared to the CAD (computer-aided design) model despite changing the process parameters (laser power and scanning speed). However, the results indicated that ~60% ISS could be reduced with optimized process parameters which are favourable for easy part removal after printing.

Moreover, the skin-core scanning strategy in the present study was employed to induce strength-ductility trade-off in the LPBF-manufactured Ti6Al4V. The microstructural investigation indicated that the skin region had a 34 % smaller grain size than the core region along with the presence of α' martensite needles. The microhardness values were marginally higher on the skin than in the core region due to finer grains owing to Hall-Petch relationship.

Further, the present work investigates the influence of different post-heat treatments (PHTs) (850 °C, 950 °C, and 1050 °C) on the strength-ductility trade-off aspects of the laser powder bed fusion (LPBF) manufactured Ti6Al4V alloy. The microstructural features, chemical composition and micro-hardness of as-printed and PHT Ti6Al4V samples in longitudinal and transverse directions were characterized using optical microscopy, SEM, EDS, X-ray diffraction (XRD) and Vicker's micro-hardness tester. Detailed XRD analysis was performed to quantify the phase volume fractions in the PHT executed samples. The microstructure of the Ti6Al4V samples subjected to PHT differed from the as-printed samples in grain structure and morphology. The width of α lath increased nearly twice with PHT temperature (from 850 °C to 1050 °C) in LPBF-manufactured samples. During PHT

under furnace cooling, the growth of α lath width marginally increases due to a slower cooling rate than air cooling. XRD investigation revealed that the presence of β phase content in the PHTs at 950 ºC and 1050 ºC was consistent. Further, PHT at a higher temperature (i.e. 1050 °C) favours a higher amount of β phase content than the other PHT temperatures. The presence of (002)-closed pack planes were significantly lower for LPBF-manufactured Ti6Al4V samples, PHT under 1050 °C. The Ti6Al4V samples subjected to PHT at 1050 °C exhibited a higher hardness than the other PHT samples, due to the higher β content among all the samples. The optimised PHT scheme was beneficial in generating the homogeneous and desirable microstructures.

In addition, the densification behaviour of LPBF-manufactured Ti6Al4V after employing the PHT was evaluated for horizontal and vertical build samples. Further, the porosities are classified as inter-micropores (size < 10 µm) and super-micropores (size > 10 µm). The PHT at elevated temperature (1050ºC) helps to reduce overall porosity by two times that of as-printed samples due to the sintering self-healing phenomenon. Interestingly, the super-micropores observed in as-printed samples are reduced via PHT. Moreover, refining microstructures into different phases via PHT has improved the densification behaviour.

Further, the tensile test was performed to investigate the effect of PHT and build orientation on the tensile behaviour. The FD analysis was performed on the fractured surfaces using ImageJ software integrated with an open-source MultiFrac plug-in. The PHT at a higher temperature (i.e., 1050 °C) induces a higher amount of β phase than the other PHTs. The PHT induces an isotropic tensile strength in all the orientations. However, the ductility of specimens subjected to PHT at 1050°C showed ~ 67%, 40% and 177% improvement under horizontal, inclined and vertical orientations than as-printed samples. Further FD values corroborates well with the ductility values of samples subjected to PHT.

The effect of PHT and build orientation on the high cycle fatigue resistance of LPBF-manufactured Ti6Al4V was investigated. Interestingly, the fatigue lives of samples at higher stress levels subjected to PHT at 1050°C were higher and nearly isotropic in all three build orientations compared to as-printed samples due to enhanced ductility and lesser critical pores. Due to PHT at 1050°C, the pore size modification enhanced densification in the as-printed Ti6Al4V samples. Moreover, there was a marginal improvement in fatigue limit due to PHT at 1050°C. PHT samples' ductility was ~ 67%, 40% and 177% higher than the as-

printed samples under horizontal, inclined and vertical orientations owing to the high β content and reduced porosity resulting in superior fatigue crack propagation lives. Further a strong correlation between fatigue lives and ductility of the samples was established.

The impact hammer test was performed on thin flat samples and rotor blades to characterize damping behaviour. The frequency response function (FRF) plots revealed broader peaks for thin flat samples and the rotor blade than others. The results showed that PHT performed at 1050°C enhances the overall damping of ~ 348% and 140% of rotor blade and thin flat samples, respectively. The amplitude decay for the rotor blade subjected to PHT at 1050°C was ~ 66% shorter than the as-printed one due to high β phase content relieving the energy resulting in a high damping ratio.

Overall, the studied optimised PHT (1050°C) scheme in the present work was beneficial in introducing the homogeneous microstructures, isotropic tensile properties, enhanced fatigue resistance and damping performances (rotor blades) of the LPBF manufactured Ti6Al4V parts, benefitting practical industrial applications.

Acknowledgments

I would like to sincerely thank many people without whom this thesis would not have been possible.

To a greater extent, I take this opportunity to express my sincere gratitude to my Ph.D. guide Dr. S. Anand Kumar, Assistant Professor, Department of Mechanical Engineering, for his constant motivation, consideration, total involvement, patience, and care throughout the period of my research work. It's been life-changing to work very closely with Dr. Anand who taught me so many things along with technical knowledge, which helps me to never give up and seriousness about our work. I have learned from him how to tackle a research problem with a comprehensive scientific approach. His guidance helped me throughout my research work and writing this thesis. I am really fortunate to be associated with a person like Dr. S Anand Kumar.

I would like to thank Director GTRE, DRDO Bangalore, for allowing me to use the facility available at GTRE for laser powder bed fusion for my research work.

I am deeply grateful to Mr. B.K Nagesha, Scientist 'E', GTRE, DRDO, Bangalore, for mentoring me during my duration at GTRE and giving insights to confront a research problem with an industrial application perspective in my research work.

I wish to express my special thanks to Dr. Sanjay Barad, Scientist 'G', GTRE, DRDO, Bangalore, for his meticulous suggestions, timely help, and support in my research work.

I would like to offer my thank to Mr. Soma, Scientist 'E', GTRE, DRDO, for allowing me to use the facility available in the Surface Engineering lab.

I would like to thank Dr. Shiva. S, the present Head of the MED and SRC member, Dr. Saurabh Biswas, the Chairman of Doctoral committee, MED, and Dr. Sameer K. Sarma P, SRC member, who continuously monitored and assessed my research work.

I sincerely thank the Director and Deans, IIT Jammu, and staffs for providing excellent facilities to carry out my research work.

I am deeply grateful to Mr. Damodar K Chalwadi for providing his technical insights that helped me during my research work. I am grateful to Mr. Amit Kumar Tigga for his help and support to carry out this work.

The help extended by technical staff at the Rapid Prototyping lab at GTRE is greatly acknowledged. My special thanks to Mr. Bhaskar, Mr. Gagan, Mr. Rajkiran, and Mr. Nihal for their assistance and support for my experimental work at GTRE.

I am thankful to my research mates Mr. Shreyas and Mr. Abhishek, for their valuable support during this research work. I am equally thankful to all my friends and AMRL members at IIT Jammu for their company and help.

I am deeply grateful to my grandfather for his moral support and continuous encouragement.

I wish to thank my parents and sister for their moral support and encouragement in making me what I am today. My sincere gratitude is due to my late Father-in-law, who encouraged and motivated me to carry out this work.

My heartfelt regards to my Mother-in-law, grandmother, sister-in-law, and brother-in-law for their love and moral support.

Last but not least, I wish to thank my wife, Kanika, who has stood by my family and me through all my travails and my absence. I would not have been able to complete this work without her love, support, understanding and care. I am thankful to my son Arya for coming in our life and brought happiness and joy. Their endless love, support, understanding, and everything made all this possible.

Akshay Pathania

Contents

List of Figures

List of Tables

Abbreviations

2D - 2 dimensional

3D- 3 dimensional

CAD - Computer aided design

STL - Standard tessellation file

FESEM - Field emission scanning electron microscopy

AM- Additive manufacturing

LPBF - Laser powder bed fusion

HCF - High cycle fatigue

HTs – Heat treatments

PHTs- Post heat treatments

AP-H- As-Printed Horizontal

AP-I- As-Printed Inclined

AP-V- As-Printed Vertical

SE-H- Sample E-Horizontal

SE-I- Sample E-Inclined

SE-V- Sample E-Vertical

DED - Directed energy disposition

WAAM - Wire arc additive manufacturing

BCC - Body centre cubic

HCP - Hexagonal close pack

EDM - Electric discharge machining

HIP - Hot isostatic pressing

LOF – Lack of fusion

ED - Energy density

UTS- Ultimate tensile strength

YS - Yield strength

E% - Elongation percentage

FDs – Fractal dimensions

X-CT - X-ray computed tomography

AC - Air cooling

FC - Furnace cooling

WQ - Water quenching

OM- Optical microscopy

SEM - Scanning electron microscopy

EDS - Energy dispersive spectroscopy

XRD - X-ray diffraction

SSs - Support structures

ISS – Interface shear strength

WLS - White light scanning

TD - Transverse direction

LD – Longitudinal direction

CPP - Close pack plane

CPPs - Close pack planes

FRF - Frequency response function

FRFs - Frequency response functions

FEM - Finite element method

IHT – Impact hammer test

DMA – Dynamic mechanical analysis

List of Notations

H - Horizontal

I - Inclined

V - Vertical

G - Thermal gradient

R - Solidification rate

l - length size of non-overlapping boxes/cubes

N(l) - Number of boxes/cubes

Q - Amplification factor

f_n - Natural frequency

Δf - Frequency width between half power points

A_{max} - Amplitude

ξ - Damping ratio

τ - Shear stress

T - Torque

K_P - Polar section modulus

D - Outer diameter

S - Side length of inner hexagon of a gear-type part

L1 - Location1

L2 - Location 2

L3 – Location 3

L4 - Location 4

Q_v - Heat input

f - Factor of heat dissemination

Pv - Engrossed laser power

d - Laser ray radius

r - Radial dimension from the centre of the laser source

h - Energy source depth

z - Current depth in the thickness direction

Rα – Relative integrated intensities of α peak

R_β – Relative integrated intensities of β peak

F_2 - is the structure factor

P – Multiplicity factor

V – volume of unit cell

exp^{-2m} – Temperature factor

(1+cos^2 2θ)/(sin^2 θ ×cosθ) – Lorentz polarization factor

I_α - α phase intensity

I_β – β phase intensity

$I_{\alpha c}$ - Corrected α phase intensity to estimate the phase fraction

$I_{\beta c}$ - Corrected β phase intensity to estimate the phase fraction

$V_{\alpha c}$ - Corrected phase volume fraction of α

$V_{\beta c}$ - Corrected phase volume fraction of β

ΔH – Specific enthalpy

Chapter - 1

INTRODUCTION

1.1 Background

Due to the advent of jet engines, the need for complex shape parts made with advanced materials that can endure the extreme temperatures and stresses associated with them has grown [1]. The gas flow path of a typical gas-turbine engine is divided into two sections. The first is the cold section between the intake and the injection, and the second is the hot section between the combustion chamber and the exhaust nozzle [2, 3], as shown in Figure 1.1.

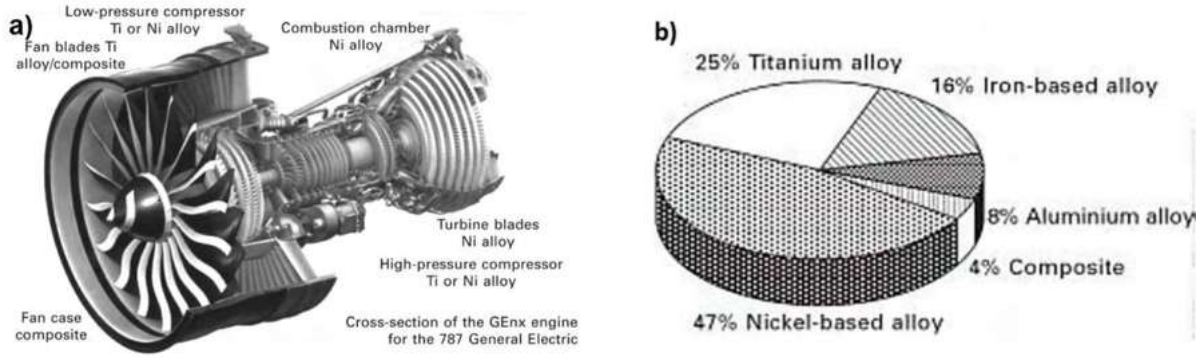

Figure 1. 1: a) Cut-section of a gas-turbine jet engine [2]; b) Engineering material distribution in aero-engine [3]

High-temperature materials are required in the hot section to fulfil the necessary working conditions [4]. However, the gas stream mainly comes into contact with the rotary and static parts made up of lightweight materials of the cold section in an aero-engine. Aero-engine rotary components are frequently replaced due to failure owing to high cycle fatigue (HCF), undesirable vibrations, and foreign object damage. Therefore, manufacturing such components' is critical to enhancing their life span.

Presently, conventional manufacturing route like bar stock machining is being used to manufacture the rotor blades of an aero-engine. However, certain limitations with traditional manufacturing routes restrict their usage. The complex shape components of an aero-engine are challenging to process through conventional manufacturing. Moreover, material wastage

and manufacturing lead time are high in traditional manufacturing. To overcome these limitations, the latest manufacturing technology, called additive manufacturing (AM), has recently gained acceptance in industries.

1.2 Role of additive manufacturing (AM)

AM's rapid emergence and evolution have raised the bar for industrial technology. It can potentially reduce waste and improve the efficiency of various processes. This process involves depositing the finished product in a layer-by-layer manner[5]. This eliminates the need for costly equipment such as moulds, dies, and punches. It allows customizing complex components without requiring traditional steps. AM is a type of manufacturing process that is commonly used to produce near-net-shaped structures[6]. It offers various advantages, such as lower material costs, faster time to market, and better efficiency. Due to its ability to make complex shapes, AM is often recognized for its role in producing aerospace components[7]. This process allows designers to create functional and intricate parts that are difficult to manufacture with conventional methods. The classification of AM processes is given in Figure. 1.2.

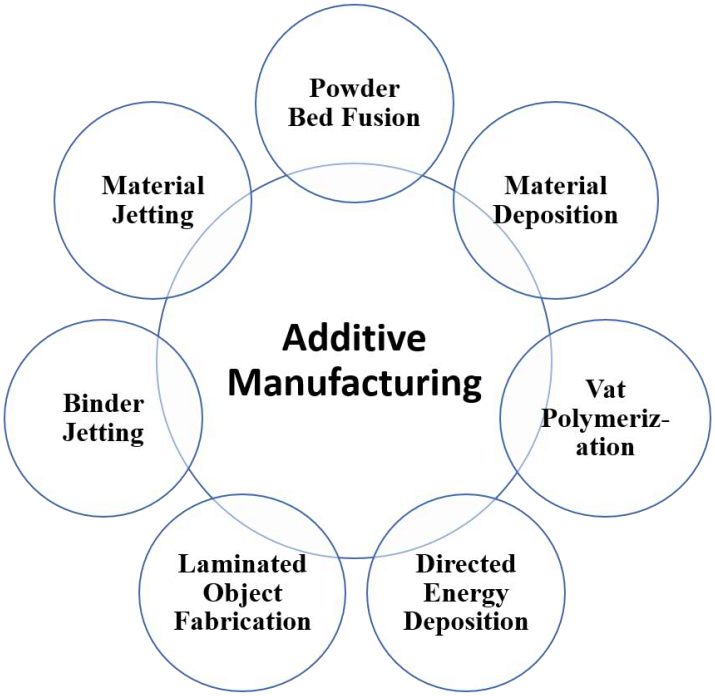

Figure 1. 2: AM classification as per ASTM ISO/ASTM52921-13 [8]

1.3 Laser powder bed fusion process

Among AM technology, laser powder bed fusion (LPBF) is popular due to its capability to fabricate the complex shape of metallic parts to produce intricate shapes with high-precision components[8]. Moreover, compared to other metallic AM processes like directed energy deposition (DED) and wire arc additive manufacturing (WAAM), LPBF has parts with high dimensional accuracy and a better surface finish[9]. In LPBF (see Figure. 1.3), a laser beam interacts with the metallic powder, and the material gets melted and subsequently solidified, and the process will continue layer by layer until its completion. The LPBF's ability to produce complex shapes is now accepted in various critical applications, such as medical implants and aerospace[10]. Although common metallurgical differences exist between AM and conventional components, such as mechanical anisotropy, defects, and residual stress, specific parts that require dynamic loading exposure, such as those exposed to high cycle fatigue (HCF) and undesirable vibrations, are required need to be addressed to avoid these issues.

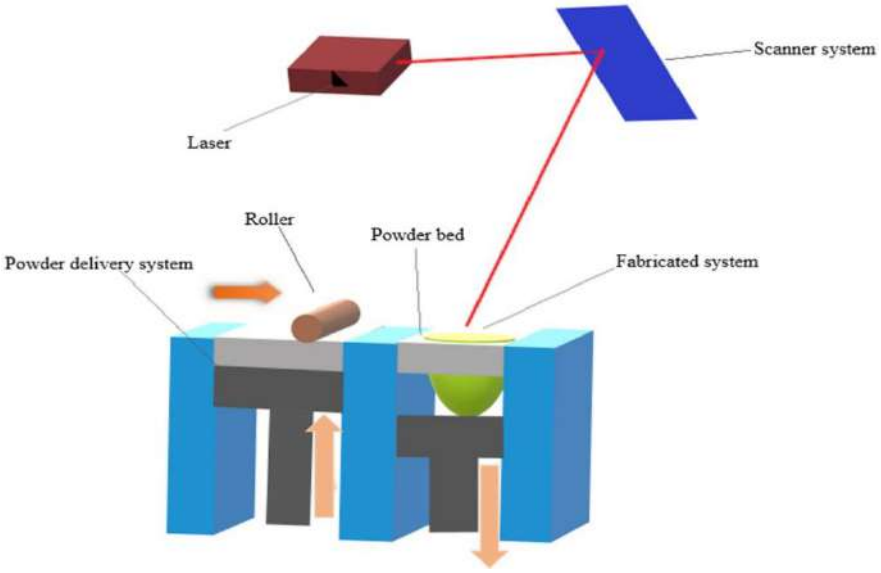

Figure 1. 3: Laser powder bed fusion (LPBF) process

1.4 Ti6Al4V Alloy

Ti6Al4V is an allotropic alpha(α) + beta(β) alloy composed of aluminium (Al) and vanadium (V) in which Al is an α stabilizer, and V is a β stabilizer[11]. The Ti6Al4V possesses the BCC (body centre cubic) crystal structure at room temperature. However, it transforms an HCP (hexagonal close pack) crystal structure above β tarsus temperature around 995ºC[12]. Ti6Al4V is a high strength, and low density, compared to other materials, as shown in Figure.

1.4. This high-strength and lightweight alloy is ideal for various aircraft components, such as jet engines and gas turbines. Despite the dominance of the aerospace industry, other industries have also started to realize the benefits of Ti6Al4V. These include marine, automobile, energy, and biomedical sectors.

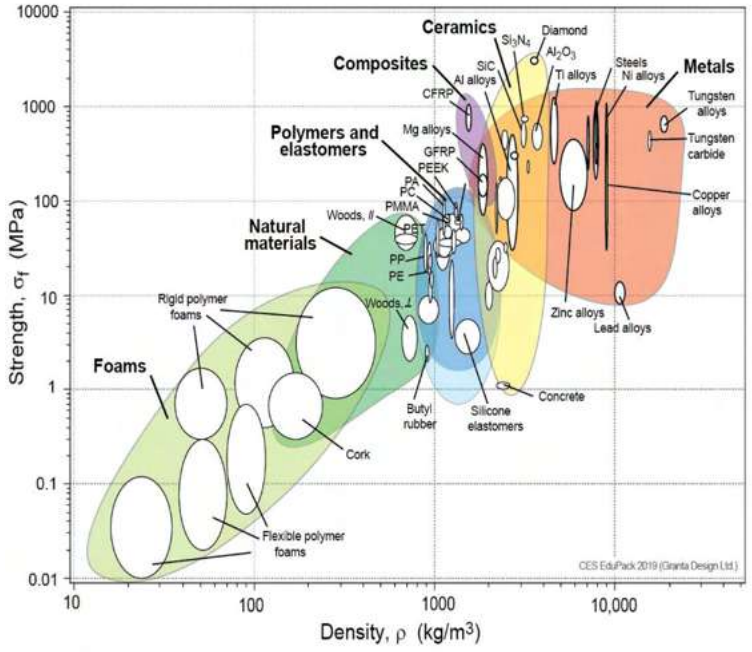

Figure 1. 4: Material selection chart of various engineering materials [13]

The machining of Ti6Al4V through a conventional manufacturing process like machining is very challenging due to its low thermal conductivity, the chemical reaction between the tool and machine workpiece, and the high heat generated at the cutting zone[14, 15]. LPBF process can overcome these challenges to process the Ti6Al4V in its net shape for its end-use applications. However, there are a few challenges, such as residual stresses, porosities and anisotropic microstructure with processing Ti6Al4V through the LPBF process, for which post-heat treatment (PHT) is inevitable.

1.5 Need for post-heat treatments (PHTs) for LPBF-manufactured Ti6Al4V

Despite having significant advantages in LPBF process compared to traditional manufacturing, some challenges still persist in it. In the LPBF process, the laser traverses very fast on the powder bed, and after melting the powder, the material gets solidified at a very high solidification rate (around 410°C/s)[16]. The high solidification rate in the LPBF process

produces non-equilibrium phases, which enhances the material's strength drastically, which is not desirable for its end-use application. Moreover, large thermal gradients developed during the LPBF process due to the low thermal conductivity (7.2W/mK) of Ti6Al4V makes an anisotropic microstructure with high thermal residual stresses[17]. The residual stresses can distort the part during the printing (see Figure. 1,5 a), and the microstructure's anisotropy features (Figure 1.5(c)) can restrict its usage in practical applications.

Furthermore, the porosities (Figure 1.5 (b)) are inevitable in the LPBF process due to the dynamic nature of processing the material. These porosities can act as stress raisers, leading to a component's HCF failure[18]. To overcome the abovementioned challenges, a PHT process is necessary to make the LPBF-manufactured part usable in its practical applications.

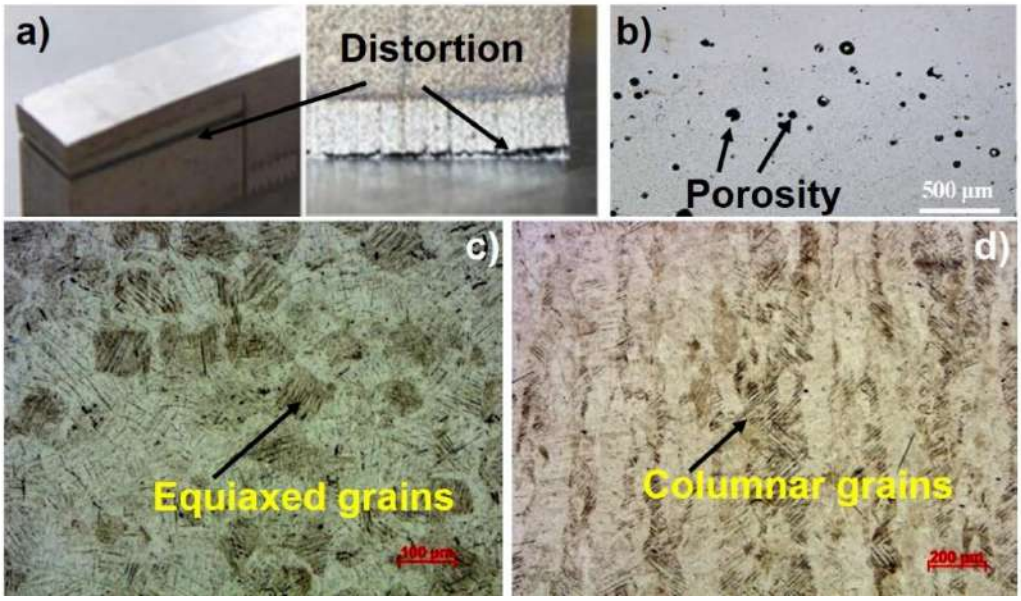

Figure 1. 5: a) Distortion of a part due to residual stresses [19]; b) porosities of LPBF-manufactured material [18]; (c) and (d) anisotropic microstructure of LPBF-manufactured Ti6Al4V[20]

In addition, to overcome the LPBF challenges using PHT, the PHT cycle should be optimized to enhance the material's mechanical performance by altering different phases and microstructural morphology.

Moreover, the rotary components in aero-engine, like compressor rotor blades, rotate at high speeds and are prone to catastrophic failure due to HCF and undesirable vibrations, as shown in Figure. 1.6. There is need for focusing on LPBF-manufactured rotary parts to resist HCF and vibration blade using PHTs.

Figure 1. 6: Damaged rotor blade of an aero-engine due to HCF and vibrations [21]

The fundamental framework adopted for the present work is shown in Figure 1.7. An AM process is employed to manufacture Ti6Al4V samples and rotor blade of an aero-engine. In addition to it, a post heat PHT process was carried out to design the material's microstructure to improve the properties which will further enhance the functional performance.

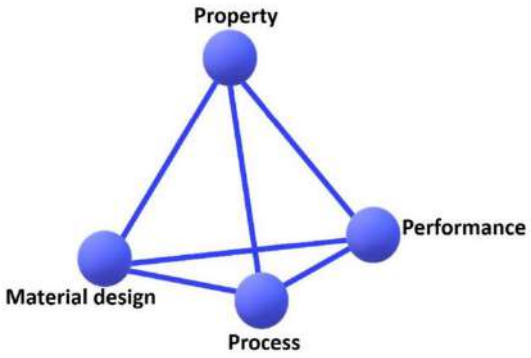

Figure 1. 7: Process-structure-property-performance relationship framework

1.6 Organization of the Thesis

Chapter 1 deals with the introduction of the general background of the area of work. Chapter 2 deals with a detailed literature survey on PHTs, the effect of PHT on porosity level, and PHT on tensile, fatigue, and damping behaviour of LPBF-processed Ti6Al4V. Chapter 3 gives the objectives and scope of the present study. Chapter 4 gives the experimental details of LPBF, PHT, tensile tests, fatigue tests, damping tests, and characterization tools used. Chapter 5 presents the results of different tests, followed by a discussion. Chapter 6 and Chapter 7 deal with the conclusions and scope for future work, respectively. Publication based on this work and references is given in the end.

Chapter - 2

LITERATURE REVIEW

2.1 Aspects of support structure in LPBF process

2.1.1 Importance of support structure in the LPBF process

A successful part-fabrication process involves the use of support structures. These are crucial components as they help hold a solidified layer and resist thermal stresses development. The presence of thermal stress can lead to various deformations and eventually lead to failure, as shown in Figure. 2.1 and Figure 2.2. The thermal stress can cause cracks in a part before it is complete, as shown in Figure 2.3. Supports are typically one of the constraint mechanism in the LPBF process when it comes to creating complex structures. Therefore, it severely limits the capabilities of the process and adds a significant amount of time and cost to production.

Figure 2. 1: Distortion and delamination in part due to thermal stresses [19]

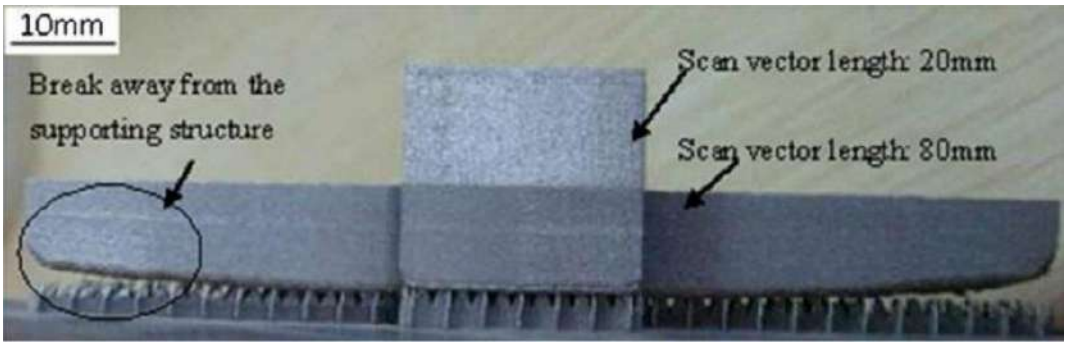

Figure 2. 2: Curling in LPBF build part **[21]**

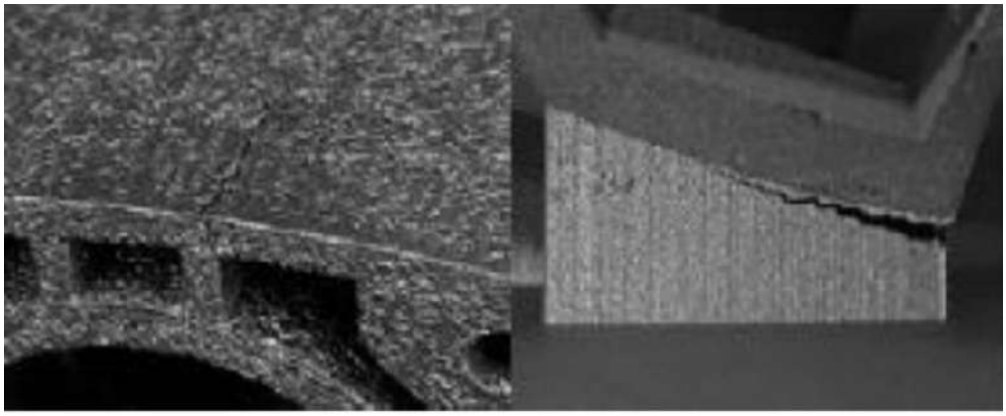

Figure 2. 3: Curling during the LPBF process **[22]**

2.1.2 Types of support structures

The support generation module of Materialise Magics pre-processing software is a widely used tool for creating and designing support structures for the LPBF platform. It can automatically generate a support structure based on a 3D model and allow users to modify it. It also allows users to select the model's orientation when attaching it to the support structure. The support generation module of Magics provides a wide range of support structures. These include the block, point, web, gusset, cone, and volume support structures [23] as shown in Figure. 2.4. In Magics, various support structures such as the cone, volume, and gusset are not commonly used. The large amount of these supports can be hard to remove, especially regarding delicate parts, and they can cause fragile members of the component to break-off.

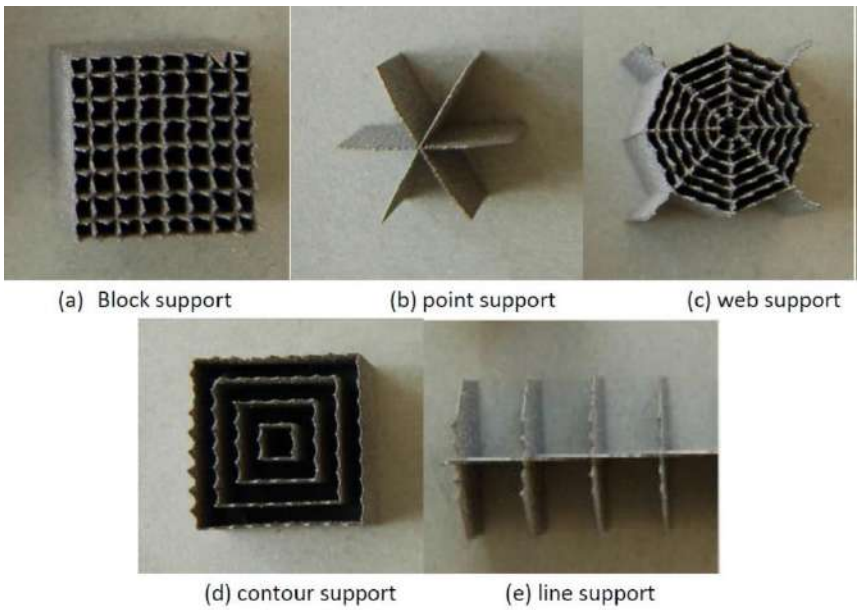

Figure 2. 4: Different types of support structures generated by Magic's tool [23]

2.1.3 Support structures type and LPBF process parameters optimization

Subedi et al.[24] optimized the support type for better part printability. Their strategy aimed to create a structurally sound support truss structure with excellent thermal performance. Compared to the standard block-type supports, their proposed supports performed well. They also had various advantages, such as reduced powder wastage and ease of removal. T. Miki and S. Nishiwaki[25] developed a numerical model to optimize a support structure's topology for easy heat dissipation during the LPBF process to avoid distortion. Dimopoulas et al.[26] have used the tooth type of support and showed that top tooth length significantly affects easy support removal. The minimum support removal effort was found at lower levels of tooth top length (0.05 mm), while the other parameters do not significantly affect the support removal. The optimized scheme of SSs showed an easy removal of support. However, the material consumption in the optimized scheme was high. In another study, JJ et al.[27] compared the web and tube types of support and found that the web type of support is easy to remove. However, studying certain types of supports is suitable for certain intricate parts.

Moreover, a study by Hussein et al.[28] used the lattice type of SSs, showing good manufacturability characteristics and easy support removal after LPBF printing. However, some thin-section lattices broke because those thin sections were fragile. Lindecke et al.[29] used block type of support by varying essential dimensions of the supports, and the SS strength was achieved ~269 MPa. The proposed methodology reduces the support strength in the order of its easy removal. However, heat conductivity decreased, which deteriorated the part quality. C. Yan et al.[30] used the 'YI' type lattice SS and found that these supports do not require an extra effort to remove. However, the large shrinkages could distort the component during LPBF printing. Bobbio et al.[31] fabricated the solid material at the bottom, followed by lattice support at the middle, and solid material at the top to evaluate the tensile strength of support. The SS was built using lower heat input than the solid part to produce stress concentration sites for easy removal. Nevertheless, the adopted process to evaluate the tensile strength of the SS increases the post-fabrication cost and time.

Further, P. Didier et al.[32] used a custom-made support structure to operate complex thin-shaped Ti6Al4V components as a machining fixture. The customized supports facilitate the printed part's machining to enhance its functional properties by reducing surface roughness. However, the chatters were still there during the milling operation, which could reduce a part's

surface and dimensional accuracy. Moreover, a study by G. Manogharan et al.[33] used base plate sacrificial supports for clamping and positioning parts during hybrid manufacturing; however, the process is not well known for complex shape parts. Another study used supports with base plates to machine the LPBF-printed Inconel 718 parts [34], where support act as a fixture to facilitate the machining of a part reducing the vibrations and chattering to enhance the functional property of a part. Calignano [35] performed physical studies while varying several geometric characteristics of block-type supports. The support structure was tuned for easy removal and warpage reduction after discovering critical parameters. Zhu et al. [36] proposed tree type supports, and several candidate topologies were identified and optimized to reduce the number of limited material parameters that ensured the self-support of structures. Wang and Qian [37] used steady heat flux on the overhang surfaces to generate the optimized support structures through topology optimization. Moreover, Paggi et al.[38] used topology optimization to save the material; however, the experimental results were not presented.

Q. Han et al.[39] designed the support structures for AlSi10Mg full and half circle overhang features. The increase in the surface area between the built components and the support structures reduced the distortion caused by the LPBF-made AlSi10Mg overhang structures. Zhang et al.[40] developed a topology optimization and inherent strain method framework for support structures to reduce deflections in LPBF-developed parts. A parallel computing framework comprises an optimization algorithm and an inherent strain method. It aims to develop stiffer support structures for easy removal. Further, the optimized results were then analyzed and compared to validate the model's effectiveness. The results show that the optimized supports can achieve a 60% reduction in part deflection and a 50% reduction in material usage. In another study, Subodi et al.[41] performed FEM simulations for truss-type support structures in LPBF process simulations. A better thermal management system for LPBF with truss-type supports is proposed due to their ease of post-process optimization and analysis. However, experimental results were not presented to validate the simulation results. C. Wei et al.[42] used SiC-316 L composite material for a support structure to build 316 L parts through the LPBF process. The study revealed that the interface between the support material and the building material could be easily broken due to the presence of cracks and pores within the structure, thus reducing less force to remove the SS.

The strength at the interface of the support and LPBF part is an essential aspect while removing support without affecting the dimensional and structural integrity of a part. Researchers have

printed tensile test-type samples to know the strength of the SS, increasing the manufacturing cost and time[29, 31]. Moreover, shear stress is more dominant at the interface of support and part while removing[43]. Therefore, evaluating the tensile strength of the SS lacks the additional insight to be understood from an interface shear strength (ISS) point of view. Hence, assessment of ISS between SS and part becomes essential. Further, in view of the above literature review, there is a scope to evolve a facile methodology to measure the ISS.

Further, torque measurements are crucial to regulate the attaching force on the assembly component and thus gauge mechanical power[44]. Torque is generally measured by mechanical-type torque wrenches/meters as per ISO 6789[45]. Recently, a mechanical torque wrench has been used to evaluate the pre-stress of an abutment screw used in dentistry to fit the tooth implant[46, 47].

2.1.4 Strength and ductility trade-off in LPBF manufactured part

The metallic materials manufactured through the LPBF process generally exhibits anisotropic microstructure due to the large thermal gradients involved particularly Ti6Al4V due to its low thermal conductivity value. Moreover, localized heating and cooling occur as the laser traverse swiftly on the powder, generating higher cooling rates, resulting in the formation of α' martensite responsible for increased strength. The high strength in LPBF-manufactured Ti6Al4V comes at the expense of loss in ductility, which is unsuitable for its practical applications.

Z.Yao et al. [48] applied machine learning models to optimize LPBF process parameters to achieve a good combination of ductility and strength. The models identified that the hatch spacing of the Ti6Al4V components under a suitable linear energy density is imperative in regulating their overall ductility. The significant synergy of strength and ductility was achieved with a yield strength of ~1044 MPa and ductility of ~10.4%. However, anisotropy was still present in the microstructure, which impedes its practical application. Further, Jeong et al. [49] used a shell and core scanning strategy to attain a good combination of strength and ductility. The shell is considered an outer part of a component, and the core is termed the inner part of the component. The process parameters were varied for shell and core regions, and gradient microstructure was achieved, which shows good ductility and strength. D. Dezfoli et al. [50] varied the LPBF process parameters, and it was found that at higher scanning speeds, the obtained microstructure contains smaller grains with high tilt angles, whereas the low speed

will give large grains with low tilt angles. The combination of different grains can be used to obtain a heterogenous microstructure which can help to produce materials with different local mechanical properties during laser processing according to their application requirements.

Moreover, the process parameter optimization can be done in the LPBF process to obtain a good combination of strength and ductility. However, it was found in the literature that anisotropy is still an issue which is not required for material's end-use applications. Therefore, the most convenient and effective way to reduce the anisotropy is to employ appropriate post-heat treatments (PHTs) to achieve a homogeneous microstructure. In addition, the PHTs can be optimized to obtain a desired amount of different volume fractions and morphology, enhancing the mechanical performance of LPBF-manufactured Ti6Al4V parts. The desired heterogeneous material with optimal strength and ductility for its end-use applications is shown in Figure. 2.5.

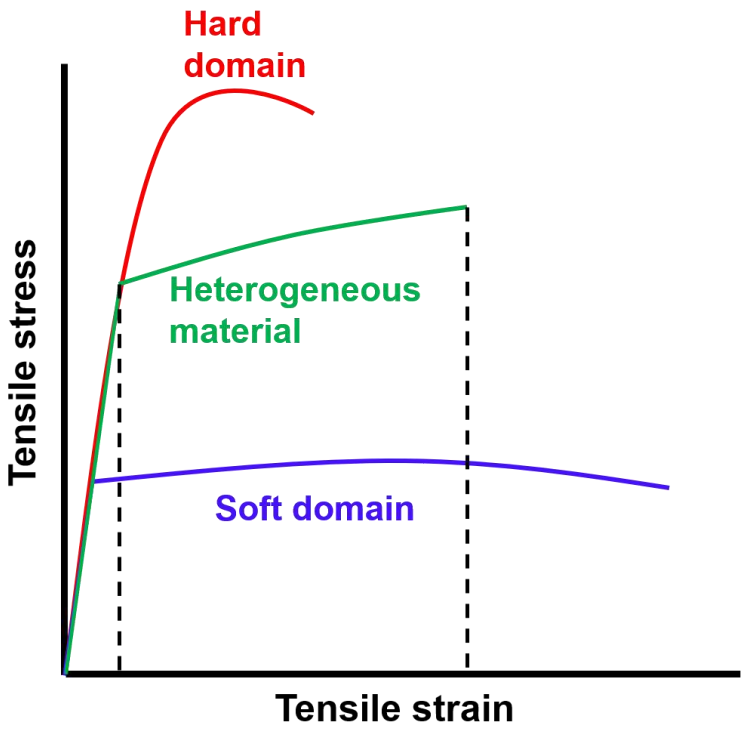

Figure 2. 5: Strength ductility trade-off curve

2.2 Effect of PHT on microstructure and microhardness of LPBF-manufactured Ti6Al4V

2.2.1 Need of PHT for LPBF-manufactured Ti6Al4V

LPBF process produces an anisotropic microstructure owing to the complex thermal events that occur during the process. A typical microstructure of LPBF-manufactured Ti6Al4V is shown in Figure. 2.6, where equiaxed grains are grown on the top plane of a sample (see Figure 2.6(a)) and columnar grains are grown along the build direction (see Figure 2.6 (b)). The prior β grains are visible due to the build direction's epitaxial growth owing to the build direction's temperature gradient and successive layer formations.

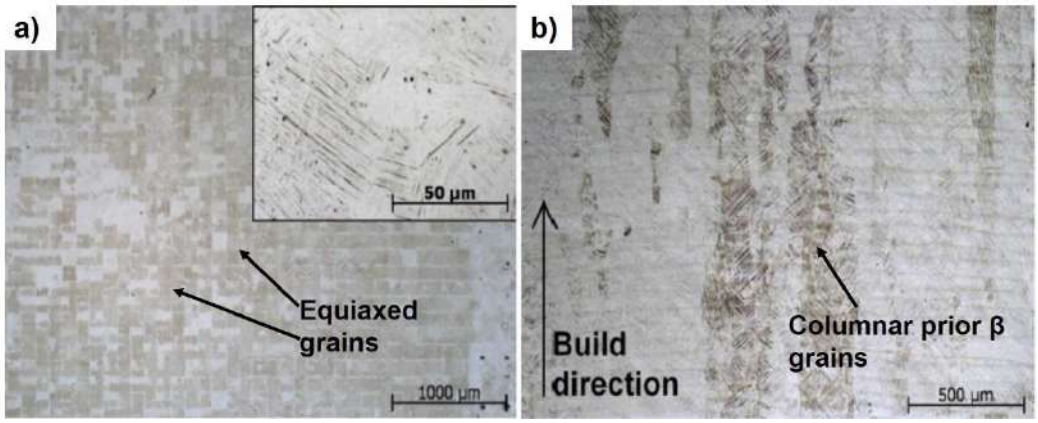

Figure 2. 6: LPBF-manufactured Ti6Al4V a) Transverse orientation; b) Longitudinal orientation [51]

The deposition of the next layer in the LPBF process on the previously formed columnar grains will re-melt and act as a nucleus for epitaxial grain growth with a strong texture development [52]. The shorter interaction time of laser with powder and high cooling rates (generally > 410°C/s) [53] leads to α' martensite formation. Due to high undercooling, the diffusion-less transformation forms α' martensite in prior β grains. It possesses very high strength and low ductility. In addition to α' martensite, the residual thermal stresses form in the LPBF process due to steep temperature gradients. The speed and power of a heat source can also affect the melt pool's thermal gradient (G) and solidification rate (R) [54]. During the LPBF process melting and re-melting of the material's layer co-occurs. This event generates a rewarm and cooling behaviour resulting in thermal cycling in both transverse and longitudinal directions in a non-uniform manner. Therefore, it leads to the development of a complex anisotropic microstructure. Moreover, the directional microstructures obtained in different directions (i,e transverse and longitudinal) under the LPBF process creates an anisotropy in a material's

properties [55]. In addition, the low thermal conductivity of Ti6Al4V (7.2 W/m °C) encourages heat accumulation and is presumed to promote directional microstructure development.

Moreover, the high heating and cooling rates involved in the LPBF process lead to significant thermal gradients. It generates anisotropic microstructure, tensile residual stresses, and low ductility in LPBF-manufactured Ti6Al4V[56]. It is important to note that these characteristics differ from cast or wrought parts of Ti6Al4V. Therefore, PHT becomes inevitable. It facilitates the relief of undesirable residual stresses and alters the anisotropic microstructure. The PHT is the most effective process to improve functioal properties and attain good strength and ductility.

2.2.2 Effect of α and β volume fractions and morphology on the mechanical properties of Ti6Al4V

The microstructural features of α and β phases, such as volume fraction and morphology, significantly impact the mechanical properties of Ti6Al4V alloys. Ti6Al4V consists of lamellar, bimodal and equiaxed microstructures, as shown in Figure. 2.7. The lamellar microstructure of Ti6Al4V possesses a high strength in which α and β+α' phases varies around 34% and 66%, respectively. The size of the α-lamellar is decisive for strength. Further the bigger lamellae cause slower fatigue crack propagation. The bimodal microstructure consists of around 72% of α and 28% of β+α', which shows moderate ductility and strength[11]. The size of the lamellae and volume fraction of α-phase affect the strength. The equiaxed microstructure of Ti6Al4V shows high ductility where α is found around 84% and β is around 16%. A grain size of less than 2 mm is achievable in an equiaxed microstructure to attain strength.

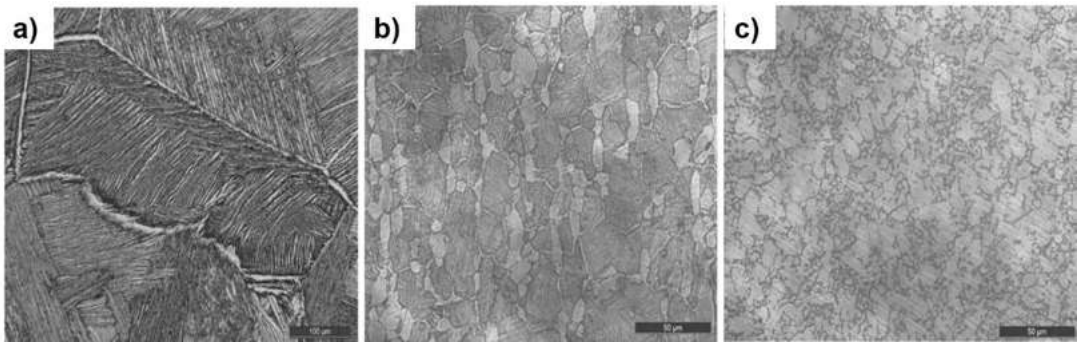

Figure 2. 7: Microstructures of Ti6Al4V [11]: a) lamellar; b) bimodal; c) equiaxed

2.2.3 Effect of cooling rate in PHT

PHT's cooling rates significantly affect the microstructure's final morphology and phases, which eventually dictates the material's mechanical performance. A phase transformation of Ti6Al4V as a function of cooling rate is shown in Figure. 2.8, where different cooling rates form distinct phases[53].

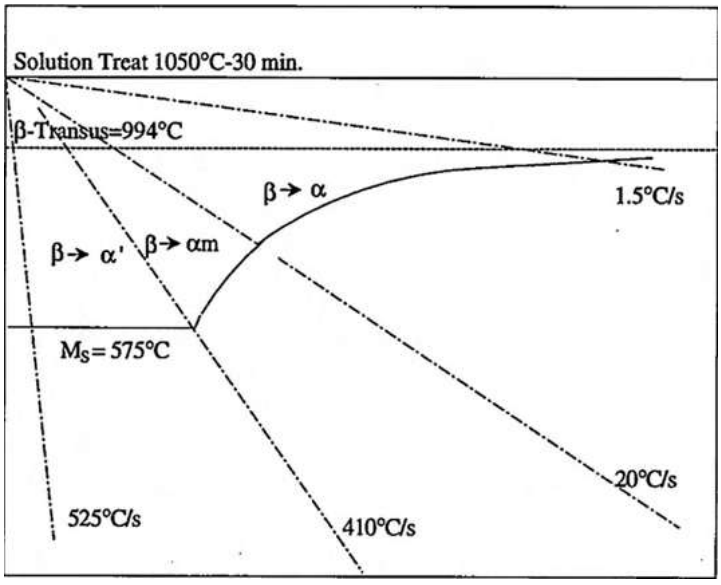

Figure 2. 8: Phase transformation as a function of cooling rate **[53]**

Wu et al. [57] studied the correlation between microstructural evolution and micro-hardness of the as-printed Ti6Al4V upon PHT. Ti6Al4V samples exhibited a higher hardness at a lower temperature (500 °C) due to sub-structural refinement and at a higher temperature (1000 °C) due to martensitic refinement. The samples were heat-treated from 300 °C to 1000 °C, followed by water quenching. The increased volume fraction of α martensite due to water cooling leads to higher hardness. Vrancken et al. [51] showed a comprehensive study of the microstructural evolution of LPBF-manufactured Ti6Al4V alloy. The LPBF-manufactured Ti6Al4V was heat-treated above β transus temperature to obtain different properties. The different microstructures obtained under furnace, air cooling, and water quenching were lamellar α + β, Widmanstatten, and α′ martensite, respectively. Holding time, cooling rates, and PHT temperatures on the microstructure were reported. The heating rate and holding time are minorly significant when LPBF parts are heat-treated below β transus temperature. It is because the α and β phases will prevent each other from growing, affecting grain growth. Sabban et al. [58] have chosen an intermittent heat treatment process for LPBF-manufactured Ti6AlV to obtain globularised

bimodal microstructure to enhance ductility and toughness. According to Zhang et al. [59], the LPBF-manufactured brittle, porous structure of Ti6Al4V changes to ductile material after a heat treatment at 800 °C for two hours, followed by furnace cooling.

2.2.4 Effect of PHT on α lath thickness

Researchers conducted many studies to understand the effect of PHTs on microstructure evolution and the mechanical properties of LPBF-manufactured Ti6Al4V samples.

X.Yan et al. [60] investigated PHT on the tensile properties of as-printed Ti6Al4V samples. The PHT performed at 1080 °C contributes to the highest hardness owing to the formation of Widmanstatten microstructure, and PHT attained high ductility at 900 °C. Zhang et al. [61] studied the effect of sub-β transus temperature heat treatment on the mechanical properties of additively manufactured Ti6Al4V. The researchers noted that the size of the α lath was affected by PHT. There is an apparent growth in α lath of around ~ 4 μm while exceeding 900 °C, enhancing the deformability of Ti6Al4V alloy.

Further, they recommended that PHT temperature plays a more vital role than cooling rate in improving mechanical properties. It is because, at low temperatures, the α phase content is reasonably large. Li et al. [62] showed the effect of α lath thickness on mechanical properties due to PHT from 650 °C to 950 °C. The fine needles of α' martensite were embedded in α + β stabilized microstructure. Further, the reduction of residual stresses was noted. However, at 850 °C and 950 °C, α' martensite was converted to α + β microstructure and resulting in a decrease in the hardness. It was reported that the α lath thickness was increased from 2.27 μm to 4.46 μm during PHT from 650 °C to 950 °C. With the increase in PHT temperature, the fracture strain of the samples increased due to microstructural coarsening phenomena.

The existing literature lacks quantifying different phases (due to PHTs) of the LPBF-manufactured Ti6Al4V and their effects on the mechanical properties. A comprehensive structure–process–property correlation is needed for better insight and understanding. In addition, it has been found from the open literature that the PHTs are not exploited effectively to harness their effects to enhance the isotropic mechanical properties of LPBF parts. Furthermore, the deficit in the appreciative and detailed correlation efforts on the effect of microstructural features such as α and β phase volume fractions and lath sizes on LPBF-manufactured Ti6Al4V alloy's mechanical properties is scary. Moreover, the PHTs

investigated by various researchers appear to be more generic and suitable for simple LPBF parts made from Ti6Al4V alloy. However, critical applications such as aerospace and biomedical involve more complex geometries having thick and thin sections. Therefore, the cooling conditions employed while performing PHTs can considerably affect the geometrical dimensional accuracies of the LPBF parts, mainly made out of thick and thin sections. Further, the material's thermal conductivity will influence the heat transfer behaviour in components with thick and thin sections during PHT.

2.3 Effects of PHT on the densification behaviour of LPBF-manufactured Ti6Al4V

2.3.1 Type of porosities in LPBF-manufactured parts

LPBF process is carried out through the rapid melting, solidification of materials, microstructural evolution, molten pool flow, and material evaporation. The numerous factors mentioned earlier that affect the LPBF process include the formation of porosities and the lack of fusion (LOF) holes and cracks. These defects are detrimental to a part's mechanical properties. Furthermore, other blemishes like residual stresses, inclusions, and metallurgical imperfections may also affect the mechanical properties of LPBF-manufactured material[59].

The inevitable porosities induced during the LPBF process can affect this material's mechanical strength and functional performance. Porosity is a small cavity that has a spherical or irregular shape. It usually occurs in less than 100 μm size[63]. The spherical shape porosities generally formed due to the inert gas entrapment in the molten pool during the LPBF process, as shown in Figure. 2.9(a). The packing density of metal powders must be high enough to prevent the gas between powder particles from dissolving in a molten pool [64]. A large volume of dissolved gas cannot escape from the molten pool during the solidification process, resulting in the formation of porosities.

Moreover, during the preparation of powder materials, the gas atomization caused the particles to get entrapped in them, and during melting, they escaped, which introduced porosity [65]. The lack of energy input causes the LOF defects during the LPBF process, as shown in Figure.2.9(b). They usually form when the metal powders are not completely melted to sufficient overlap [66]. If the laser's energy input is low, then the width of the pool is too small, which causes insufficient overlap between the tracks, as illustrated in Figure.2.9(c). During

forming a new layer, the melt is difficult to re-melt, which causes the LOF holes to develop in part[67]. In the LPBF process, metal powders can rapidly melt and be solidified under high local laser energy input. The high-temperature gradient and the residual stress can cause cracks, which deteriorate the mechanical properties [5]. These defects act as stress raisers, thus reducing a material's tensile and fatigue strength.

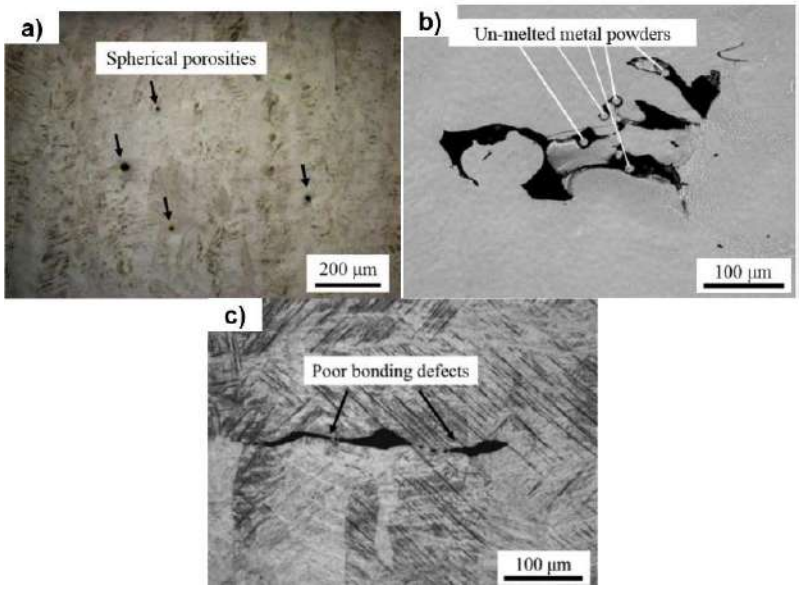

Figure 2. 9: a) Spherical porosities due to gas entrapment; b) LOF porosity with un-melted metal powder; c) LOF porosity with poor bonding defect [67]

2.3.2 Drawbacks of the hot isostatic pressing (HIP) process

Hot isostatic pressing (HIP) is a process commonly used in the AM industry to improve the mechanical properties by reducing porosities. However, HIP can only work on certain kinds of material. It can also have severe consequences when misused. The defects that extend from the part's inner side to the part's surface, the external gas medium isostatic pressing, will not eliminate such defects [68].

Moreover, HIP may also cause severe distortion of a part. In most cases, this process can thin the part's wall thickness and coarsen its grain size, resulting in poor material properties [69]. The advantages of the LPBF process allow complex shapes to be produced. For example, in Figure 2.10, the thicker flange is designed with, the thicker section as it bears a higher load during practical applications than the thinner web section. Interestingly, the HIP process can also distort contrasting shapes with thick and thin sections of a component. The thinner (web) ones will cool faster than the thick (flange) ones, resulting in distortion [70].

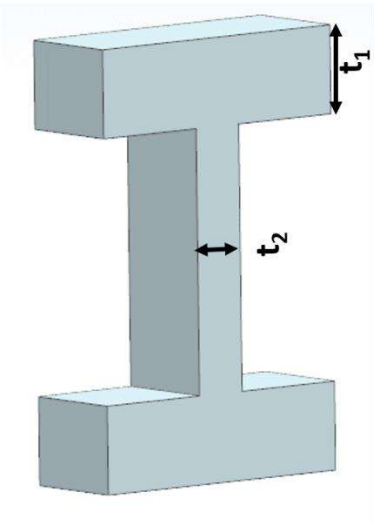

Figure 2. 10: Schematic of the "I" section part with varying thicknesses

Furthermore, HIPing can form liquefaction cracks for eutectic materials due to the significant differences in the melting points of various elements. Due to certain limitations of the HIP process owing to the material properties and geometry, it cannot always be used to eliminate the porosities. Even after the HIP treatment, the surface remains prone to plastic deformation. The surface roughness of a component after HIPing increases due to the depressions and dimples formed owing to plastic deformation, which affects the fatigue life. Moreover, an additional surface improvement process is required after HIP treatment since HIP only affects the internal porosities and does not affect the surface pores [71].

Further, it has been found that the HIP process is effective for the isolated and closed pores within the material; the connecting irregular shape pores cannot be closed effectively through this technique [72]. Additionally, a detailed inspection of X-ray computed tomograpgy (X-CT) data identifies various essential features, such as the emergence of a surface defect caused by the HIP process, as shown in Figure 2.11. The poor efficiency of the pore closure technique was demonstrated for LOF and excessive contour porosity [72].

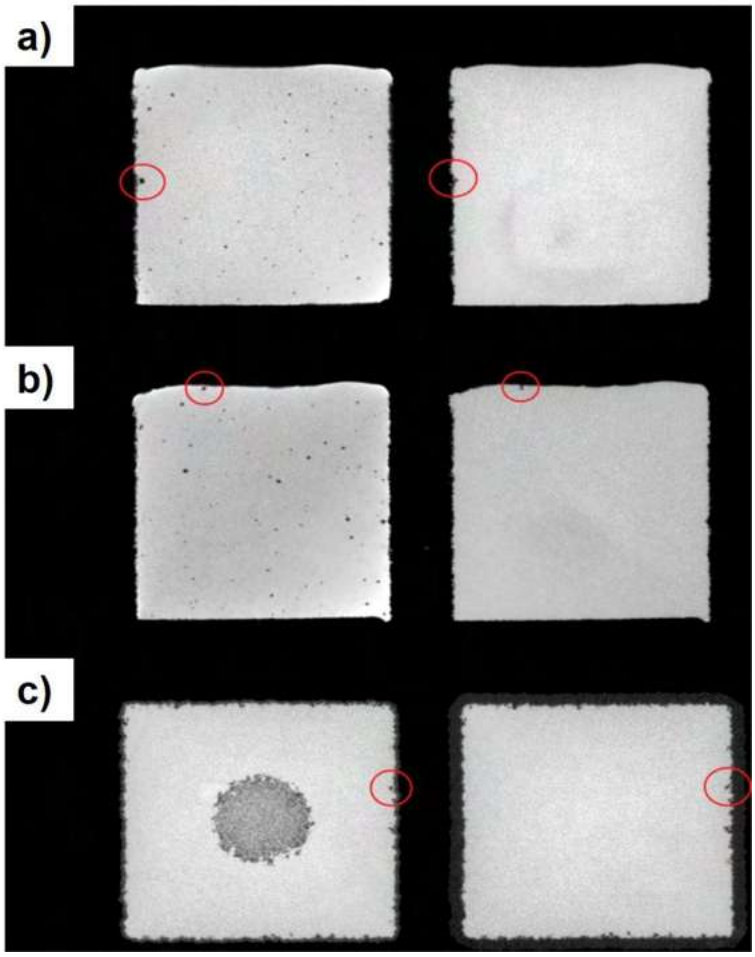

Figure 2. 11: Near-surface pores opened by HIP, creating a new surface notch defect [72]

2.3.3 Effect of PHTs on porosity reduction

Few studies reported a reduction in the external porosities of the LPBF-processed Ti6Al4V by re-melting the deposited layer thrice, thus increasing the material's mechanical properties [67,68]. However, re-melting a deposited layer may increase the localized temperature, which could evaporate the aluminium (Al) owing to its low melting temperature. Al as an α stabilizer will decrease due to vaporization, and the β ratio will increase, affecting the mechanical properties of LPBF-processed Ti6Al4V[75]. Moreover, due to re-melting, the undesirable Ti_3Al intermetallic brittle phase at high temperatures may form owing to the less solubility of Al in Ti[76]. Further, due to the less thermal conductivity of Ti6Al4V (7.2 W/m°C), re-heating may accumulate heat which could enhance the thermal gradients resulting in the formation of residual stresses[77] affecting part geometrical accuracy.

Various researchers have studied the effect of HT and HIP on the porosity level of LPBF-processed Ti6Al4V. HT of 800ºC/2hr/FC and HIP at 800ºC/2hr/1000bar was carried out by

Günther et al.[78] where lamellar microstructure with recovered α and a minor amount of β was observed after HT. The maximum stress intensity factor is lowered due to the HT at 800ºC due to a reduction in pore size, and HIP treatment improves the fatigue life by reducing the internal porosities. Zhang et al.[59] performed HTs at 950ºC/3hr, 950ºC/12hr, 950ºC/24hr, 950ºC/48hr and HIP at 800ºC/2hr/200MPa. The sharp edges were spherodize due to high-temperature HT.

Moreover, Zhang et al.[63] studied the effect of HT and HIP on pore morphology and size of pores of additively manufactured Ti6Al4V. The HIP at 820ºC /2hr/200MPa and HTs at 950 ºC/3hr, 950 ºC/6hr, 950 ºC/12hr, 950 ºC/24hr and 950 ºC/48hr were performed. The HIP reduces the pore size from 50µm to 500 nm, and the HT at 950 ºC blunts the sharp-formed LOF pores. Furthermore, Qiu et al.[79] carried HTs on LPBF processed Ti6Al4V 600ºC and 700ºC/2hr/FC, HT at 920ºC/4h, and HIP at 920ºC/4hr/103MPa. The HT performed on as-built samples at 600 ºC and 700 ºC reduces the residual stresses. Further, Post HT at 920 ºC shows no effect on porosity level. In a study conducted by Tammas-Williams et al.[80], porosity regrowth after HIP was observed. They carried a HTs at 1035ºC/10 min, 1035ºC/10 hr, 1200ºC/10 min and HIP at 920ºC/2hr/100MPa. The LOF pores were reduced through the HIP process by 100%. However, the few pores regrow after HIP at HT at 1035 ºC/10 min with a volume fraction of 0.007% compared to the as-printed 0.0397% volume fraction. However, the irregular shape pores can be effectively reduced by HT owing to the spherodization of uneven pores because of diffusion, and spherical is the stable morphology of pores [81]. Further, a reduction in porosity was observed for LPBF-manufactured AlSi10Mg after T4 and T6 heat treatments due to the change in micro structure [82].

Moreover, the PHTs investigated by various researchers are more generic and suitable for simple LPBF parts made from Ti6Al4V alloy. However, critical applications such as aerospace and biomedical involve more complex geometries from thick and thin sections. Therefore, the after-effects of PHTs can considerably affect the geometrical dimensional accuracies of the LPBF parts, mainly made out of thick and thin sections (as shown in Figure 2.10). Further, the material's thermal conductivity will influence the heat transfer behaviour in components with thick and thin sections during PHT.

2.4 Influence of PHT on the Tensile behaviour of LPBF-manufactured Ti6Al4V

2.4.1 As-printed Ti6Al4V parts

The mechanical properties of as-built Ti6Al4V samples show a high degree of strength and yield strength[83]. Their fully α' martensitic structure contributes to this. The high strength contributes to the low ductility (typically less than 10%), which is not recommended according to ASTM F2924-12 standard specifications. In this regard, appropriate PHTs are essential to improve the ductility of LPBF-manufactured Ti6Al4V[84]. On the contrary, some researchers have improved the material's ductility by varying the energy density (ED) and base plate preheating temperature during the LPBF process. Xu et al. [85] reported that the ductility increased by up to 11.4 %, and they also noted that the varying ED values resulted in an ultrafine microstructure. Moreover, the effect of preheating temperature of the base plate around (570°C) showed the formation of β precipitates (see Figure 2.12), resulting in ductility of ~ 10% as-printed Ti6Al4V reported by Ali et al. [86]. According to the same authors, the samples produced using preheated base plate at 670°C and 770°C encountered a premature failure due to the varying cooling rates during the printing process, which caused the products to fail.

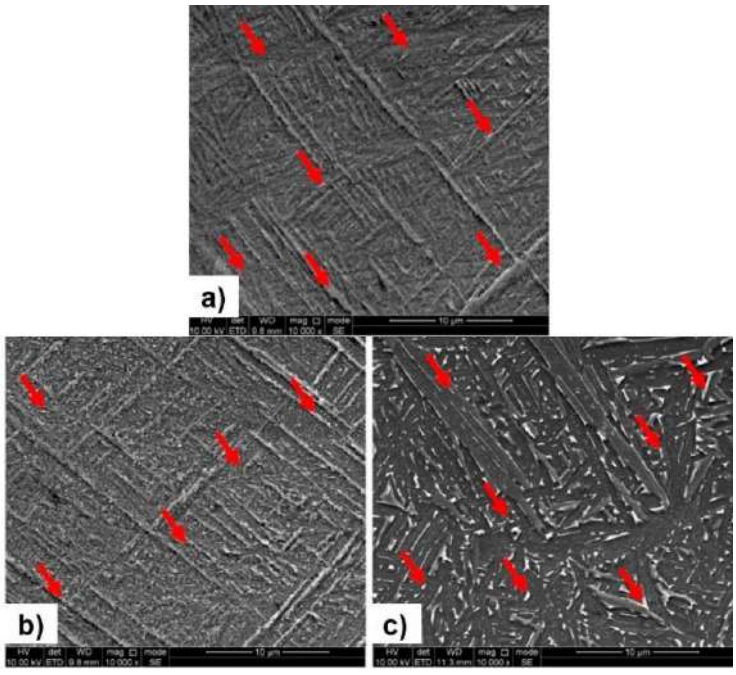

Figure 2. 12: Microstructure of as-printed Ti6Al4V with different base plate preheating temperatures a) 570°C; b) 670°C; c) 770°C. Red arrows showing the β precipitation and its growth [86]

Nevertheless, if ED and base plate temperature influence the mechanical properties of LPBF-manufactured Ti6Al4V, then build orientation within a build chamber also substantially affects the mechanical properties of Ti6Al4V.

2.4.2 Effect of build orientation and PHT on tensile properties

Various researchers studied the effect of build orientation on tensile properties, where few have reported that sample manufactured under horizontal orientation provides superior mechanical properties [87, 88]. Some researchers have shown better mechanical performance under vertical orientation [89, 90] and inclined orientation [91]. The LPBF-manufactured material's properties are sensitive to process parameters and result from porosities distribution. Therefore, process parameters and porosities resulted in different tensile properties for horizontal, inclined, and vertical-oriented samples. In addition, the anisotropy in as-printed condition of LPBF-manufactured Ti6Al4V also shows a significant difference in the tensile properties due to the anisotropy in the microstructure.

Moreover, the different build orientations also affect the fracture mechanism, as illustrated in Figure 2.13 (a-c). The horizontally oriented sample subjected to tensile load generally shows the Mode-1 type of fracture. On the contrary, the vertically oriented sample exhibits an intergranular fracture much more torturous than the horizontally oriented sample. Besides, the Inclined oriented sample is characterized by a transgranular crack propagation with tensile load subdivided into normal and shear stress. In this scenario, the mechanical properties of a material are usually affected by the build orientations.

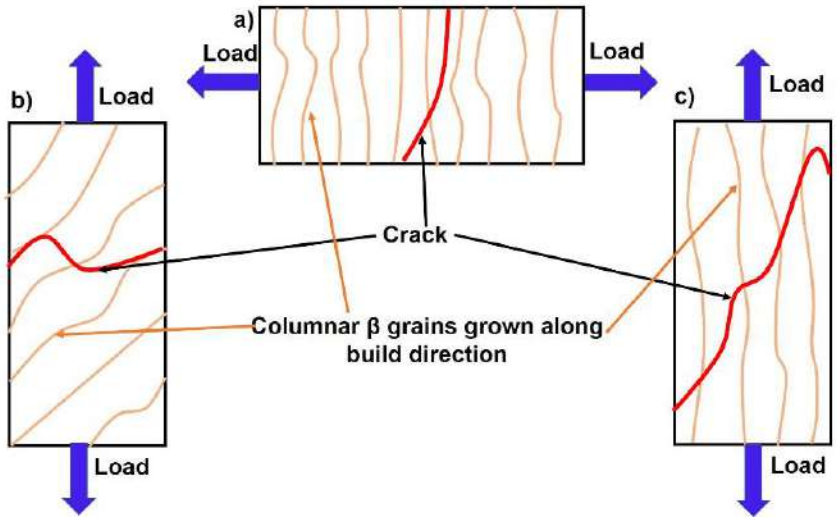

Figure 2. 13: Schematic representation of different build orientations and their load directions a) Horizontal build (0°); b) Inclined build (45°); and c) Vertical build (90°)

In this regard, the PHTs are the most convenient way to reduce the anisotropy and enhance the tensile properties of LPBF-manufactured Ti6Al4V samples. Lütjering [92] has shown an increase in yield and tensile strength at high cooling rates because of variation in colonies size of α and β. The following consolidated literature in Table 2.1 shows the effect of different PHTs on the tensile properties of LPBF-manufactured Ti6Al4V.

Table 2. 1: Tensile properties of LPBF-manufactured Ti6Al4V subjected to PHT

PHT Conditions	Microstructural characteristics	Orientation	UTS (MPa)	YS (MPa)	E (%)	Ref.
650°C+3hr+FC	α', α and β precipitates	V	1101±5	1040 ± 7	7.8±0.7	[93]
700°C+3h+AC	α', α+β	V	1082±34	1026 ± 35	9.1±2.1	[51]
700°C+2h+FC	α', α+β	H	1046±6	965 ± 16	9.5±1	

800°C+2h+AC	α' and α+β in columnar β	-	1073±9	1010 ± 11	17±1	[94]
850°C+2h+FC	α' and (α+β)	V	1004±6	955 ± 6	11.8±1	[41]
850°C+5h+FC	α' and (α+β)	V	965±22	944 ± 8	-	
950°C+1h+WQ followed by 700°C+2h+AC	(α+β)	H	1036±30	1010 ± 11	8.5±1	[52]
		V	1040±4	924 ± 14	7.5±2	
950°C+2h+AC	Bilamellar (α+β)	-	945±4	893± 3	14±1	[94]
1020°C+2h+FC	(α+β); Ti_3Al	V	840±27	760± 19	14±2.5	[41]
1050°C+1h+FC	(α+β); α_P along the β grains	V	869±3	787± 4	11.5±1	[95]
1050°C+1h+WQ followed by 990°C+30 min+ AC	Basketweave (α+β)	-	962±12	838± 6	12±0.1	[94]
1200°C+1h+AC	(α+β)	-	988±8	878± 7	11.2±1.2	[94]
950°C+1h+WQ	α', (α+β)	H	951±55	836±64	7.9±2	[52]

950°C+1h+WQ	α', (α+β)	V	1019±11	913± 7	8.9±1	

UTS: Ultimate Tensile Strength; YS: Yield Strength; E: Elongation; H: Horizontal; V: Vertical

The cooling rates affect the mechanical properties of LPBF-manufactured Ti6Al4V parts. Etesami et al. [96] showed a considerable improvement in the tensile strength of a Ti6Al4V after PHT at 930°C for 2 hr, followed by water quenching due to the diffusion less transformation α' martensite of the formed β. It is worth to mention that furnace cooling allows the grains to grow substantially, thus enhancing the ductility. However, grains grow at high temperatures under air cooling, though they are limited and have moderate ductility.

2.4.3 Effect of α lath width on tensile properties of LPBF-manufactured Ti6Al4V

Cooling rates are the deciding factor for the α lath thickness, which eventually affects the mechanical performance. The slow cooling rates cause enormous growth in the α lath, and fast cooling limits its growth, as discussed in section 2.2.4.

Considering the as-printed condition, Akram et al. [97] demonstrated the validity of the Hall Petch equation concerning the lath thickness in horizontal and vertical-oriented LPBF-manufactured Ti6Al4V. The horizontally oriented samples showed high tensile strength compared to the vertically oriented samples showing a faster enhancement in the yield strength with an inverse square root of α width as shown in Figure. 2.14.

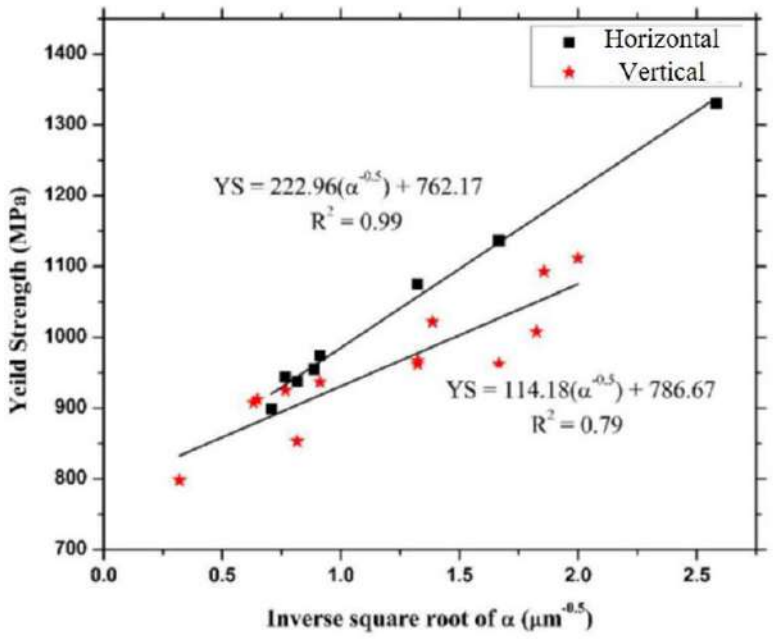

Figure 2. 14: Yield strength vs inverse square root of α lath of horizontal and vertical oriented LPBF-manufactured as-printed Ti6Al4V samples [97]

In this regard, the bimodal structure has better yield strength than the equiaxed and lamellar structures due to its greater resistance to dislocation. This is because the crystallographic distortion of the α phase, β phase, and secondary α phase prevents dislocation [98]. The dislocation movement and strength decrease exhibited by the β phase following the α'martensite decomposition during HTs have been studied by Zheng et al. [99]. The β phase is located between two α lamellae, which can be regarded as a barrier preventing dislocations from moving. This causes a pile-up which generates stress concentration. It is affirmed by Zheng et al. [99] and Kohn et al. [100] that the Hall-Petch mechanism did not consider the contribution of the β phase due to the α phase's laths and platelets were responsible for its control.

2.4.4 Effect of α and β volume fraction on tensile properties of PHT performed LPBF-manufactured Ti6Al4V

The volume fraction of α and β drives the mechanical strength of Ti6Al4V alloy. After performing the PHTs, the α and β volume fractions vary, which finally dictates the tensile properties. T. Mishurova et al. [101] performed a PHT at 900°C for 2 hours, followed by furnace cooling, which resulted in a 7% volume fraction of β phase. The resulting microstructure after PHT was α- Widmanstätten showed less ductility and strength compared to as-printed counterpart. The reduction in ductility was owing to the lower β content after

PHT. Moreover, Vrancken et al. [51] subjected LPBF-manufactured Ti6Al4V to different PHTs resulting in different α and β volume fractions. The authors performed PHT with furnace cooling for 850°C and 950°C for 2 hours, respectively. The sample subjected to 850 °C PHT showed around 73% α volume content. In contrast, the sample heat-treated at 950°C showed about 23% of α volume content. It is worth mentioning that as the PHT temperature increases, the α volume fraction decreases [61]. Furthermore, the same authors performed the tensile tests for different PHT performed samples, and yield strength decreased with increased PHT temperature. At high temperatures, β volume fraction increases, which possesses a BCC crystal structure responsible for increased ductility. Further, Jimenez et al. [102] performed PHT at the α-β domain for 1.5 hours, causing the formation of about 10% β phase content. The PHT sample showed an equiaxed microstructure with less strength than the as-printed sample. It is well established from the literature that as the PHT temperature increases, the α fraction decreases, which acquires an HCP crystal structure resulting in a decrease in tensile strength. Moreover, the effect of the volume fraction of α on tensile strength and ductility is shown in Figure. 2.15.

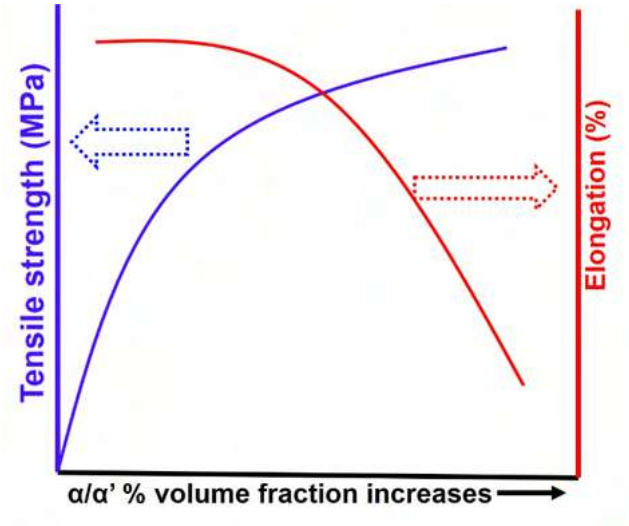

Figure 2. 15: α/α' volume fraction vs tensile strength and ductility

2.4.5 Effect of microstructural morphology on tensile properties of PHT performed LPBF-manufactured Ti6Al4V

The morphology of a microstructure of Ti6Al4V alloy also plays a crucial role in deciding the mechanical performance. Different PHTs lead to the formation of distinct microstructural morphologies. Moreover, a morphology could be decisive in delaying crack propagation, thus enhancing the mechanical performance. X.Yan et al. [60] performed PHTs at 800°C, 950°C,

and 1080°C for 2 hours, respectively, followed by furnace cooling. The heat-treated sample at 1080°C showed a coarse lamellar microstructure which offers high ductility than printed and other PHT-performed samples. Moreover, there was a decrease of around 2% in tensile strength and an increase of approximately 12% ductility for the 800°C heat-treated sample compared to the as-printed sample. Further, a decrement of about 35% in tensile strength and an increment of around 50% ductility was observed for the 950°C heat-treated sample compared to the as-printed sample. X.Y Zhang et al. [61] showed a basketweave type of microstructure for 950°C PHT performed for 2 hours, followed by furnace cooling on LPBF-manufactured Ti6Al4V.

Further, the same research group performed 800°C for 2 hours, followed by furnace cooling, resulting in columnar prior β grains. The basket weave microstructure showed about a ~13% decrease in tensile strength and around a 60% increase in ductility compared to the as-printed sample. Further, coarser prior β grains achieved after 850°C PHT showed approximately a ~16% decrease in tensile strength and ~76% increase in ductility. Another study by M. Simonelli et al. [90] performed a PHT at 730°C for 2 hours, followed by furnace cooling on LPBF-manufactured Ti6Al4V samples. A coarse columnar prior β grains type of microstructure has resulted after performing PHT. Interestingly, no significant change in tensile strength and ductility was observed after applying PHT because almost similar microstructural morphology was there as it was in as-printed Ti6Al4V samples. Therefore, it is well recognized from the literature the morphological changes in microstructure after PHTs resulted substantially in the mechanical performance. Moreover, the morphology effect on tensile strength and ductility is given in Figure. 2.16.

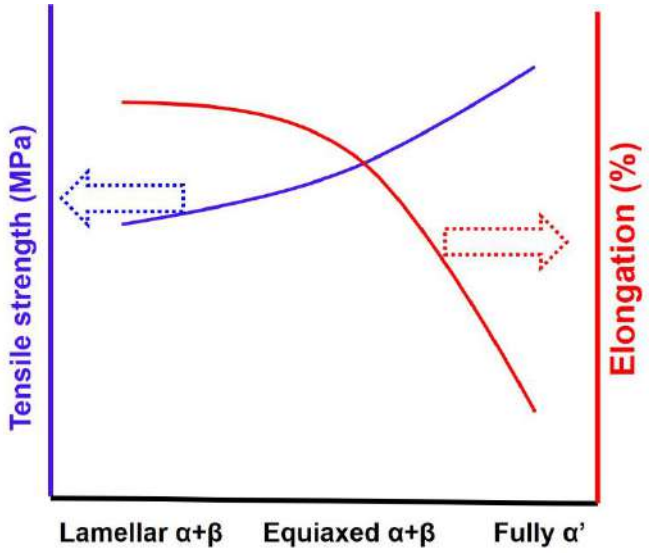

Figure 2. 16: Microstructural morphology vs tensile strength and ductility

2.4.6 Effect of α lath width on fractography

As the PHT temperature decreases, the α lath width increases, which affects a material's final tensile properties. The fractured surface of a tensile specimen can be seen to understand the behaviour of a fracture. The fractured surface of α lath width of ~0.42µm is shown in Figure. 2.17 (a) where brittle-type fracture can be observed. However, the fracture surface of α lath width of ~1.643 µm shows a ductile behaviour (Figure. 2.17 (b)) of a fracture owing to the growth in α lath width favouring easy movement of dislocations. Furthermore, the increased α lath width of ~2.87 µm also exhibits the ductile type of fracture (Figure. 2.17 (c)) resulting from grain growth favouring high ductility. Therefore, it can be assumed that despite of increase in α lath width at high temperature PHTs, the fracture behaviour of different microstructures obtained through different PHTs is similar.

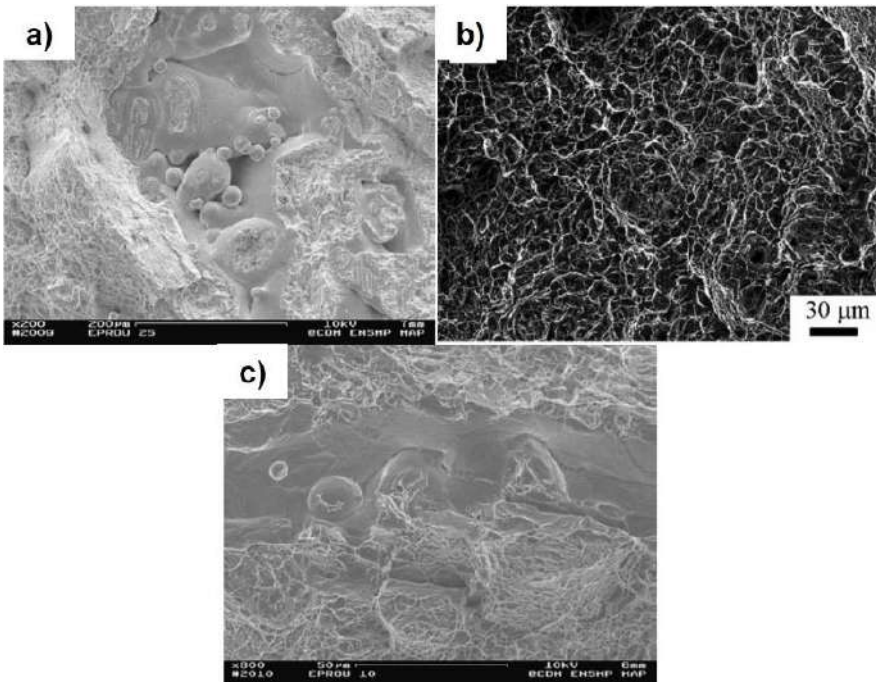

Figure 2. 17: Fracture surfaces of a) lower α lath width (0.42µm); b) intermediate α lath width (1.64µm); c) high α lath width (2.87 µm) [52]

The as-printed sample exhibits fully α' martensite microstructure which acts as a barrier for the movement of the dislocations resulting in a brittle type of fracture as shown in Figure 2.18(a). However, the sample heat treated to 800°C-850°C microstructure shows a ductile fracture surface, as shown in Fig.2.18(b). A similar feature was also observed in the basketweave-type microstructure fracture surface (see Figure. 2.17) and lamellar α+β fracture surface.

2.4.7 Effect of volume fraction on fractography

The fractured surface of a tensile sample is characterized to see the effect of the volume fraction of different phases on the fracture behaviour. Figure. 2.18(a) shows a fractography of as-printed Ti6Al4V samples where stair-like and layered cracks occur along grain boundaries with a combination of ductile dimples and brittle intergranular fractures. The α' martensite formed in as-printed Ti6Al4V samples is responsible for the brittle fracture. However, the LPBF-manufactured Ti6Al4V sample heat treated at 800°C-850°C exhibits 23% of α/α' volume fractions have shown ductile fracture as shown in Figure. 2.18(b). Moreover, PHT executed LPBF-manufactured Ti6Al4V consisting of 73% of α/α' also showed a similar kind of ductile fracture feature as shown in Figure 2.18 (c). Therefore, it can be said that after performing PHTs, the volume fraction variation does not show any significant differences in fracture behaviour.

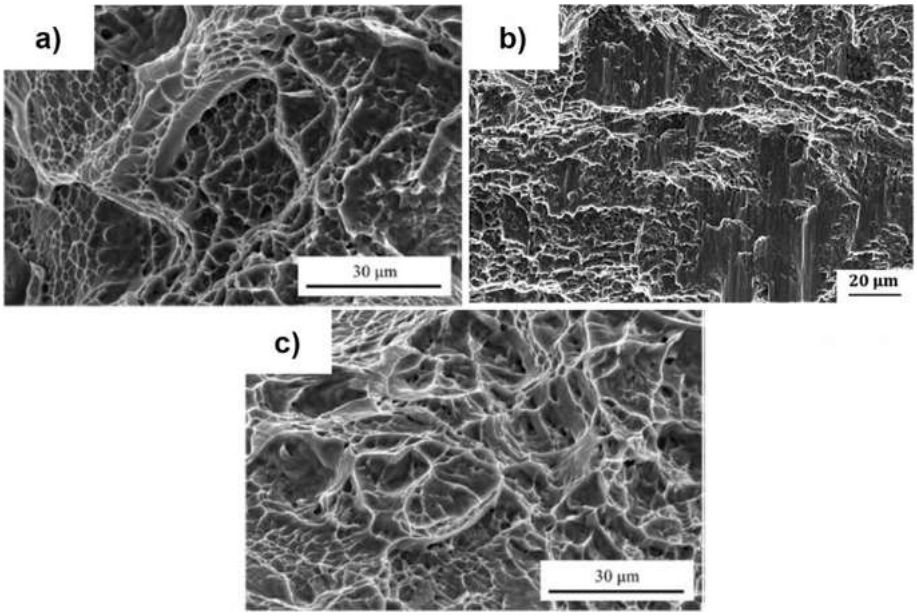

Figure 2. 18: Fracture surfaces of a) as-printed sample (α' martensite dominant); b) α/α'- 23% volume fraction; c) α/α'- 73% volume fraction [60]

Moreover, the effect of PHT in the literature shows non-uniformity in the tensile properties of LPBF-manufactured metallic materials [103–106] and, in particular, Ti6Al4V alloy[52]. There is scope and opportunity to understand the effect of different build orientations on the tensile behaviour of LPBF-manufactured metallic materials suitable for load-bearing applications. Consequently, understanding the various effects of build orientation and PHT on tensile properties is essential for meeting applications under an industrial environment.

2.4.8 Fractal dimension analysis of fractured surfaces subjected to tensile loading

Further, the plastic deformation during tensile tests leads to fracture events due to micro-mechanisms. They reveal inherent specific details on the fractured surface. Interpretation of those details could be helpful to understand the failure and precluding them. In contrast, experience shows that the fracture surfaces are irregular microstructures, and quantitative measurements cannot predict the mechanical properties of fracture features because of the challenges in arriving at a numerical characterization of the fractured surface. Most researchers have discovered that the fracture profiles do have a fractal character [107–109] and can be characterized by their linear fractal dimension (FD), which has a non-integer value between 1 and 2 [110].

Moreover, researchers are recently been exploiting FD analysis on complex surfaces to correlate and understand well for better designing microstructure to cater towards functional performance efficiently. Benoît Mandelbrot familiarised the name "Fractal" in 1960 [107]; it is exploited for surface analysis. The FD is interconnected to self-similarity; fractals are infinitely intricate patterns that are self-similar across various scales and are used to describe the surface. The techniques for FD analysis include the box-counting method, differential box-counting method, covering method, and prism method[108]. Among them, the box-counting method is popularly employed [109].

2.5 Influence of PHT on the fatigue behaviour of LPBF-manufactured Ti6Al4V

2.5.1 As-printed fatigue behaviour of Ti6Al4V

As-printed Ti6Al4V manufactured through LPBF process shows superior strength due to α' martensite, which is not suitable for its practical applications. The high cycle fatigue (HCF) behaviour of LPBF-manufactured Ti6Al4V must be high enough to enhance the lifespan of a component. Moreover, the anisotropy in the microstructure of as-printed Ti6Al4V sample also not makes it suitable for cyclic loading applications. There is a significant difference in the fatigue life of the as-printed samples due to anisotropic microstructure at the same stress levels reported by various researchers [111–113].

Researchers have shown that the microstructure of AM materials can affect their fatigue characteristics. Due to the build direction and the change in the grain boundary, the microstructure of LPBF-manufactured Ti6Al4V alloy has different morphology. This can result in lower ductility in the longitudinal direction. This is because the grain boundary of the phase tends to fracture when subjected to a tensile opening mode. Some researchers have revealed that the porosity of LPBF Ti6Al4V can affect its fatigue properties. This issue is usually caused by the complexity of the process [114]. The difference in fatigue behaviour among horizontal, vertical and inclined directions is due to the difference in microstructures (in transverse and longitudinal directions), defects and porosities distribution which dictates the material's structural integrity. The porosities in vertical build orientation are considered higher owing to the high number of interlayer porosities. Moreover, the anisotropy in the microstructure in different build orientations leads to the difference in the fatigue lives of a

material. Therefore, an appropriate PHT is essential because of making an isotropic microstructure and enhances a material's fatigue behaviour.

2.5.2 Effect of PHT on HCF behaviour of Ti6Al4V

The applied PHT could homogenize the microstructure and enhance the fatigue behaviour. Wu. Xu et al. [115] performed a PHT at 400°C followed by furnace cooling and found that from a crack propagation point of view, an ultrafine lamellar microstructure is not as sensitive to porosity as a martensitic microstructure. Moreover, PHT-performed samples in horizontal and vertical orientations have shown similar fatigue lives because of isotropic microstructures. Leuders et al. [116] showed a HCF life of PHT-performed samples compared to as-printed samples. A combination of increased ductility and reduced residual stresses resulted in higher fatigue lives in PHT samples. X.Yan et al. [60] performed a PHT at 900°C chased by furnace cooling and showed higher fatigue strength than as-printed samples. Comparison of fatigue strength between as-printed and heat-treated samples showed a limited effect on the number of cycles to the failure. In another study, there was a slight improvement of around 40 MPa of the PHT executed sample compared to as-printed sample owing to the change in microstructure. Y.Yang et al. [117] conducted different PHTs and found that all the performed PHTs showed higher fatigue lives compared to the as-printed sample due to the formed β phase improving the plasticity. Moreover, Table 2.2 summarizes the effect of different PHTs on the HCF behaviour of LPBF-manufactured Ti6Al4V samples.

Table 2. 2: Effect of different PHTs on fatigue behaviour of LPBF-manufactured Ti6Al4V

Sr. No.	PHT Conditions	Orientation	Stress Level (MPa)	Frequency (Hz)	Stress ratio (R)	Number of cycles	Fatigue limit (MPa)	Ref
1.	400°C+2h+FC	H	400	10	0.1	1000000	400	[115]
	400°C+2h+FC	V	400	10	0.1	1000000	400	
2.	800°C+2h+FC	V	400	40	-1	93000	-	[118]

	1050°C+2h+FC	V	400	40	-1	290000	-	
3.	900°C+2h+FC till 200°C + AC till RT	V	340	130	-1	1000000	340	[60]
4.	920°C+30 min + FC till 700°C + AC till RT	V	390	50	-1	10000000	390	[119]
5.	850°C+2h+FC	V	500	110	-1	3588800	-	[117]
	950°C+2h+FC	V	500	110	-1	570500	-	
	1050°C+2h+FC	V	500	110	-1	78700	-	

2.5.3 Effect of α lath width on fatigue behaviour of Ti6Al4V

The width of α lath has no substantial effect on the fatigue crack initiation[120]. However, it has a significant impact on fatigue crack propagation. It is well established that the coarser α lath width shows high fatigue crack growth resistance [89, 117]. The α lath width increases with increasing PHT temperature and is discussed in detail in section 2.2.4.

2.5.4 Effect of α and β volume fraction on fatigue behaviour of Ti6Al4V

The volume fractions of α and β at different PHTs are detailed in section 2.4.4. It is well recognized that as the PHT temperature increases, the β volume content increases and the α volume content decreases. The increase in β content could be favourable for high ductility because of the BCC crystal structure. A sample heat-treated at 850°C followed by furnace cooling has shown high fatigue lives compared to the as-printed samples owing to the optimal combination of α and β where higher α delayed the crack initiation, and β helps in crack propagation resistance[117]. In another study, the higher β formed by applying duplex PHT does not resist the crack initiation; however, the crack propagation delay enhances the fatigue

strength. Moreover, a PHT at around 900°C showed a higher fatigue life than the as-printed sample because the high β content resulted in high ductility, which was a dominating factor in enhancing the fatigue life [50].

2.5.5 Effect of microstructural morphology on fatigue behaviour of Ti6Al4V

Many studies have shown that a sample heat treated at 850°C for 2 hr followed by furnace cooling resulted in equiaxed α+β microstructure has shown higher fatigue life compared to the lamellar α+β and fully α' martensite microstructures [60, 61, 121]. However, in a few studies, lamellar microstructure has shown higher fatigue strength than the as-printed sample [122, 123]. Moreover, the morphology effect on the fatigue lives of LPBF-manufactured Ti6Al4V is shown in Figure. 2.19. It is worth to mention that the fatigue lives are very sensitive to the porosities and can reduce its fatigue life despite having a distinct microstructure.

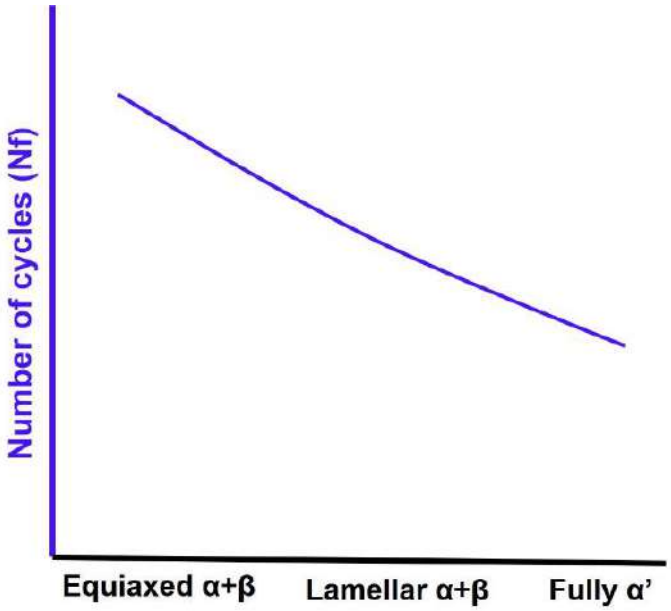

Figure 2. 19: Microstructural morphology vs fatigue lives of LPBF-manufactured Ti6Al4V

2.5.6 Effect of α lath width on fatigue tested fractography

A fatigue fracture fractography is the key to evaluating a material's fracture behaviour. The α lath will increase with an increase in temperature, and higher α lath width will resist the crack propagation. However, the fractography at temperatures increasing from 850°C, 950°C to 1050°C show similar kinds of ductile fracture features as shown in Figure. 2.20 (a), 2.20 (b) and 2.20 (c), respectively.

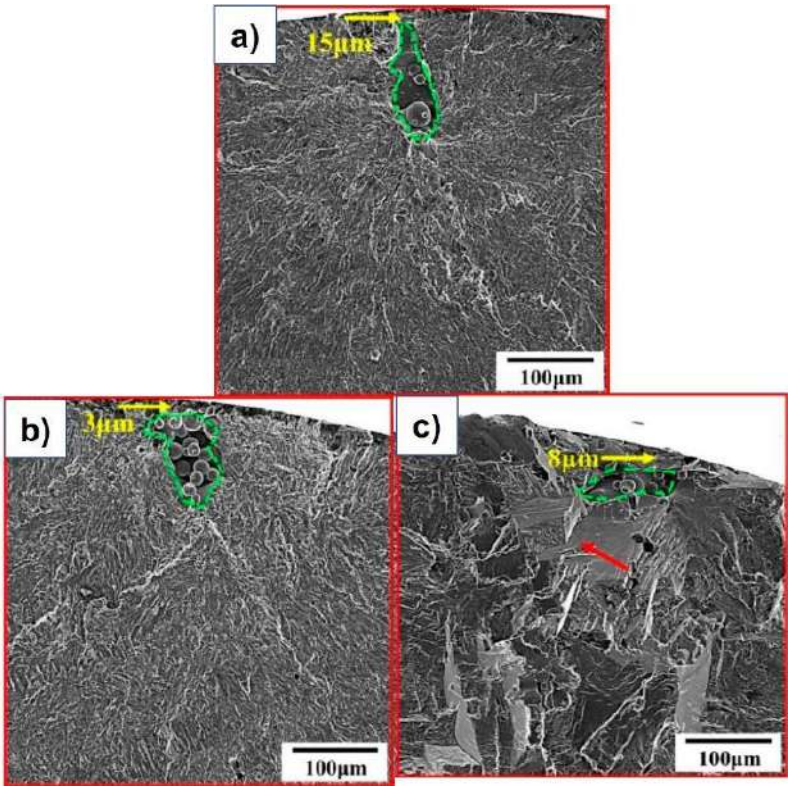

Figure 2. 20: Fracture surfaces of different lath widths (a-c) lower to higher [117]

2.5.7 Effect of microstructural morphology on fatigue fractured Ti6Al4V surfaces

The as-printed fractography is shown in Figure. 2.21 exhibiting facets features showing brittle fracture due to α' martensite. However, the α' martensite transforms into α+β in equiaxed and lamellar microstructures with different volume fractions of α, and β are showing a similar type of ductile fracture a scan is seen in Figure 2.20(a) and (c).

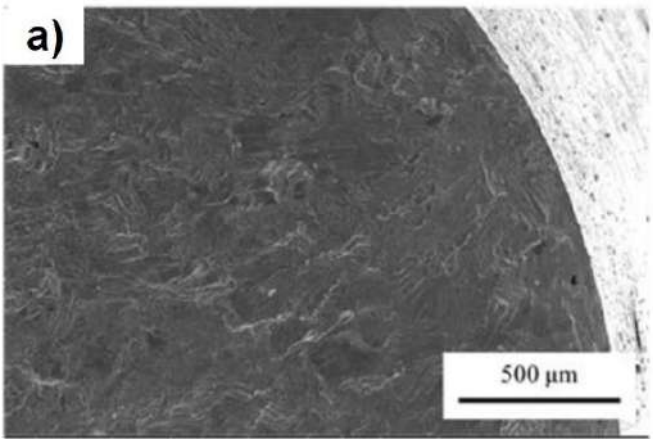

Figure 2. 21: Fracture surfaces of as-printed Ti6Al4V (fully α' microstructure) [60]

2.5.8 Effect of α and β volume fraction on fatigue fractured Ti6Al4V surfaces

Figure 2.20 (a-c) shows the different α and β volume fraction microstructures' fractography. Interestingly, all the fractography shows an almost similar type of ductile fracture behaviour. It is important to mention that as the β phase is increasing at higher temperature PHTs, the fractographs are showing almost similar ductile fracture features. Moreover, the α phase is decreasing at higher temperature favouring in enhancement of ductility which is evident in SEM fractography as shown in Figure 2.20 (a-c).

2.5.9 Fractal dimension analysis of fatigue fractured Ti6Al4V samples

Currently, limited research is available on the relationship between FD and fatigue-fractured surfaces. Hilders and Zambrano discovered a linear correlation between the FD increment and fracture toughness for duplex stainless steel [124]. W. Macek et al. [125] showed a correlation between FD and different fatigue loading conditions for S355J2 and 10HNAP steels and the 2017-T4 aluminum alloy. They found that the maximum and minimum fractal values exhibited the same behavior under various loading conditions regardless of the material. In another study, W. Macek et al. [126] investigated the topography of a fracture surface in relation to its susceptibility to multiaxial loading and fatigue behavior of S355J2. The analysis of fracture surfaces showed that specimens with a survival time of more than 105 seconds had higher average values of the surface roughness and lower average values of the FD, although the latter was found to be less sensitive. As a result, the FD approach used to measure the fatigue fracture topography was deemed appropriate, and it can be considered a reliable and efficient method for analyzing the fracture surface of the tested component. Additionally, a separate study also determined that measuring the entire topography of the fatigue fracture is an appropriate method based on the analysis of the FD of the fracture surface. The fatigue loading type affects the fracture's surface topography, specifically the various mean stresses expressed in the loading ratio, which influences the fracture surface morphology[127]. Krivonosova and Gorchakov [128] developed a relationship between FD and fatigue fracture surfaces and discovered that FD decreases with an increased crack propagation rate. Yun et al. [129] reported that the fracture surface profile of the fatigue crack in the initiation zone is smaller compared to the growth zone due to the compression loading of the fracture's FD. Tanaka and Kato [130] also reported that FD indicates microstructure characteristics and the damage caused by fatigue loading for SUS631 steel. Furthermore, Usov et al. [131] reported that an

increase in the FD of the fracture surface during the transition from a ductile to a quasi-brittle fracture is related to its fatigue life, and as the fatigue life decreases, FD increases.

The FD approach is an engineering tool that relates a given structure's material properties and geometrical irregularities. In the field of fracture, research has shown a correlation between microstructure features and fracture characteristics [108, 110]. During fatigue tests, various fracture events can occur due to plastic deformation. Analyzing the data can reveal details about these events. However, fracture surfaces are typically composed of irregular microstructures. Therefore, the FD technique provides a convenient and fast method to evaluate a material's fracture behavior in less time, making it beneficial for inexperienced researchers.

2.6 Effect of PHTs on damping behaviour of LPBF-manufactured Ti6Al4V parts

The rotary components, like rotor blades due to vibrational loads in an aero engine, may have premature catastrophic failure [132]. Therefore, it is essential to suppress these vibrations to increase the component's performance and service life.

Damping is imperative to rotatory components of an aero engine in view of dissipating vibrations[133]. Therefore the selection of a damping mechanism may vary depending on the nature of vibration, magnitude and complexity of the component's geometry[134]. Among various damping mechanisms, material damping is established to be simpler and offers a scope to tweak the material's microstructure as per the requirement without modifying the component's geometry. The release of strain energy (between slip planes) through the microstructure's anelastic behaviour of different phases enhances damping behaviour [135].

Hence, it is important to note that the microstructure and its morphology play an essential role in describing the energy absorption within the material resulting in different damping capacities [136]. The PHT is considered a practical scheme to impart desired microstructure for damping requirements at the component scale. Ti6Al4V ($\alpha+\beta$) alloy is used in compressor rotor blades in an aero engine system. The rotor blades experience fluctuating loads owing to the compression and expansion of the air in an aero-engine under operating conditions [137].

Ti6Al4V has high strength, low density and corrosion resistance properties. Due to the presence of both α and β phases, properties like strength, ductility, and functional properties, including

damping, can be tailored as per requirement[83]. It has been shown in the literature that a simpler and specific heat treatment technique (with varying cooling rates) can achieve various types of microstructures with varying phases and morphology. It is well established that the high content of β phase after water quenching in α and α' matrix plays a predominant role in enhancing the material's damping[138]. For instance, Ti6Al4V with various PHT schemes are employed by numerous researchers, taking into consideration studying the effect of microstructure and phases [57, 61, 139, 140]. The specific PHTs can induce bimodal, equiaxed, and Widmanstatten microstructures [136]. Moreover, it was observed that the high damping capacity was shown by equiaxed microstructure followed by Widmanstatten and bimodal microstructures[136].

The cooling rate in PHTs will influence the type of microstructure. For instance, the Ti6Al4V sample exhibited a higher damping capacity under a PHT at 800°C followed by water quenching and ageing treatment at 200°C for 100 hours due to the anelastic deformation of the metastable phase (α''+β) [138]. Similarly, another study noted that the β phase exhibited a high damping capacity under PHT subjected to a temperature of 1050°C for 2 hours, followed by water quenching[141]. It was reported that, the highest damping of Ti6Al4V is in the order of β>α'>α phases. The low damping capacity of Ti6Al4V alloy is typical of their stable α+β phase mixtures. These are commonly produced through a slow cooling rate during PHT [138].

Moreover, an optimized PHT can enhance a material's damping behaviour. In addition to the conventional Ti6Al4V damping performances, few studies have been conducted on the damping properties of AM-manufactured materials. In particular, the damping test was evaluated for lattice structured Ti6Al4V[142], 316L[143] and AlSi10Mg[144] using dynamic mechanical analysis (DMA), universal tensile testing machine (UTM) and impact hammer test (IHT), respectively. It was observed that the lattice structure had shown high damping compared to the bulk solid material. More studies have yet to be conducted to understand the damping properties of AM-manufactured materials to deploy efficiently in industrial environments.

Moreover, it is well established that a lattice structure shows higher damping capacity than solid material owing to better energy dissipation and lightweight. However, specific issues are involved in fabricating the lattice structure, like challenges to remove support due to inaccessibility issues, poor surface roughness and dimensional accuracy. Therefore, the use of

a lattice-structures to enhance the damping is limited and in its early stages to exploit at full potential.

Furthermore, the PHT's effect on mechanical performance (damping) of LPBF-manufactured component level is very limited, which opens the scope to carry out this present study. No component scale evaluation and performance of LPBF-manufactured component are found in the literature.

Chapter - 3

OBJECTIVES AND SCOPE

The strength and ductility trade-off are the serious concern in the LPBF process of Ti6Al4V alloy. The optimum combination of strength and ductility can be achieved through LPBF process parameters optimization. However, the anisotropy is still the major challenge in LPBF-manufactured Ti6Al4V which limits its usage in industrial applications. Therefore, PHTs are inevitable to reduce the anisotropy and achieve the optimum combination of strength and ductility. In view of detailed literature survey, the following objectives were arrived:

3.1 Objectives of this work

- To study the effect of PHTs and their cooling conditions on the microstructure morphology, microstructural constituents (lath thickness and volume fraction of phases) and microhardness of LPBF-manufactured Ti6Al4V parts.
- To study the effectiveness of PHT on the tensile properties and fatigue resistance of LPBF-manufactured-Ti6Al4V parts under three build orientations (viz. horizontal, vertical and inclined).
- To perform fractal dimension analysis on the fractographs of Ti6Al4V samples subjected to tensile and fatigue loadings.
- To investigate the influence of PHTs on the damping behaviour of LPBF-manufactured Ti6Al4V parts and examine the damping performance of rotor blades subjected to PHT.

3.2 Scope of this study

The challenges pertaining to anisotropic microstructure and porosities in LPBF-processed Ti6Al4V restrict its practical usage. The appropriate PHT can be applied to overcome these challenges. In addition, the PHTs can be optimized to enhance mechanical performance. Much published literature is available on the PHT of LPBF-processed Ti6Al4V; however, the microstructural studies are inconsistent with applied PHTs. Moreover, there is a lack of α and β phase volume quantification; hence a comprehensive process-property relation is deficient. The present work deals with the effect of PHT on densification, tensile, HCF and damping

behaviour of LPBF-processed Ti6Al4V parts. Further, the component scale damping test is also investigated in this study. The methodology followed in this work is shown in Figure 3.1.

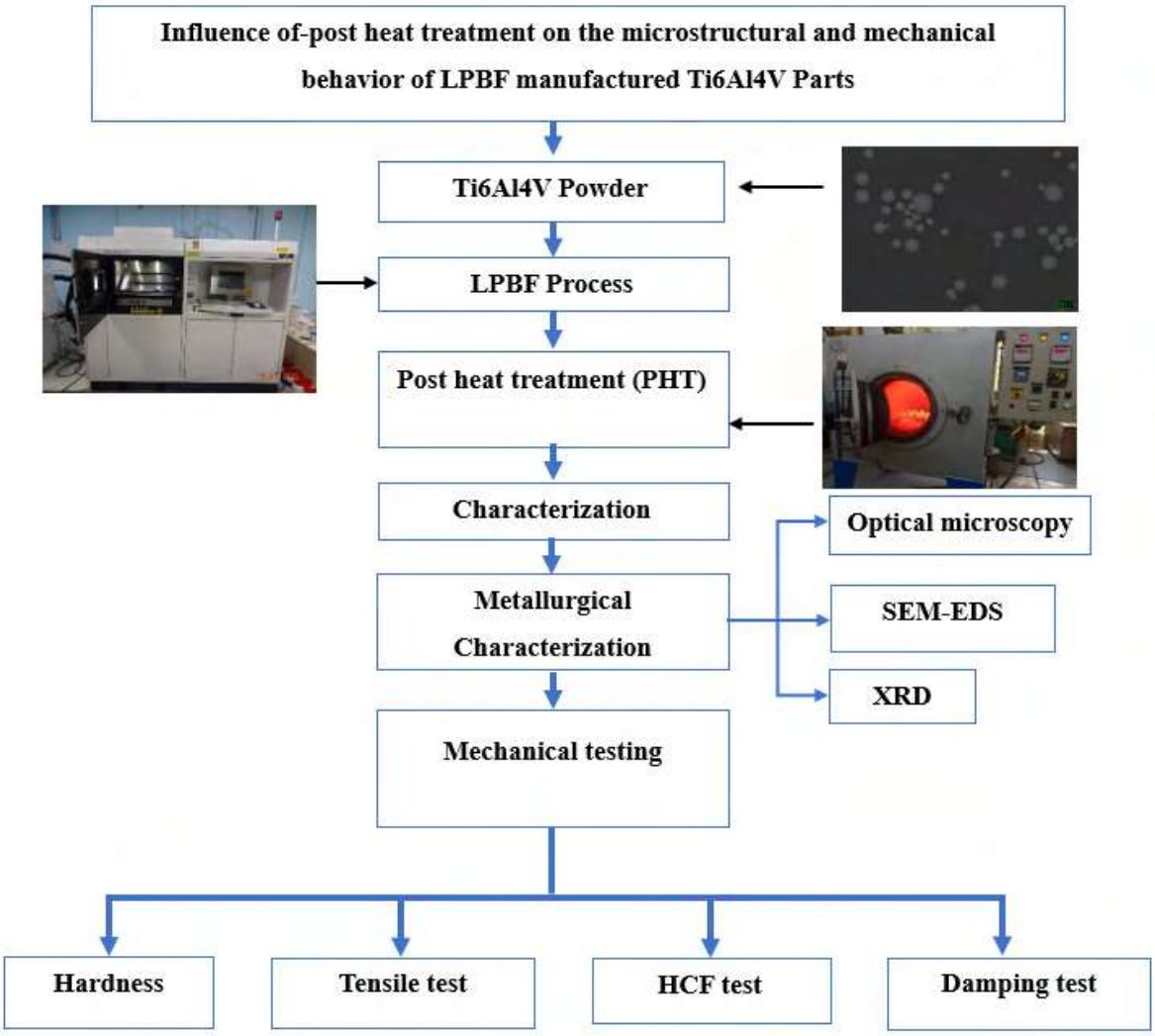

Figure 3.1: Methodology of the present work

Chapter - 4

EXPERIMENTAL PROCEDURE

4.1 Support structure manufacturing optimization studies

FEM simulations were carried out for different process parameters of support structures using Ansys Additive 2021. The mechanical properties of Ti6Al4V alloy were assigned using a bilinear isotropic-hardening J2-plasticity model given in Table 4.1. Further, the voxel size was kept as 0.3 mm to compute the distortion and residual stresses. The parameters used for the simulation of samples 'A', 'B', 'C', and 'D' are shown in Table 4.2. Moreover, a correlation between experimental and simulation distortion results has arrived.

The process parameters in the LPBF process were varied (as per Table 4.2) based on FEM simulations for support structure fabrication to evaluate distortion behaviour and assess the support strength at the interface of the base plate and part. The block type of support used in the present work was designed in magics software, as shown in Figure 4.1 (a). The CAD model of the gear-type part is presented in Figure 4.1 (b). The Ti6Al4V gear-type parts were built with different support structure process parameters, shown in Figure 4.1 (c). The 3D printed parts were removed using a mechanical torque wrench to evaluate the torque required to remove the part from the base plate as per [ISO 6789]. Similar type of technique was used for LPBF processed parts[43]. The overall process followed for the present work is shown in Figure 4.2.

Table 4. 1: Material input data of Ti6Al4V**[145]**

Input	Values
Stress mode	J2 Plasticity
Hardening factor	0.0198
Yield strength (MPa)	1100
Elastic modulus (GPa)	110
Poisson ratio	0.3
Strain scaling factor (SSF)	1
Anisotropic strain coefficient (‖)	1.5
Anisotropic strain coefficient (⊥)	0.5
Anisotropic strain coefficient (Z)	1
Gas convection coefficient	12.5 W/m^2K
Base plate temperature	35°C

Table 4. 2: LPBF process parameters used for support structure fabrication

Sample	Laser Power (W)	Scanning speed (mm/sec)	Hatch distance (µm)	Layer thickness (µm)
Sample A	140	700	100	30
Sample B	120	600	100	30
Sample C	100	500	100	30
Sample D	80	400	100	30

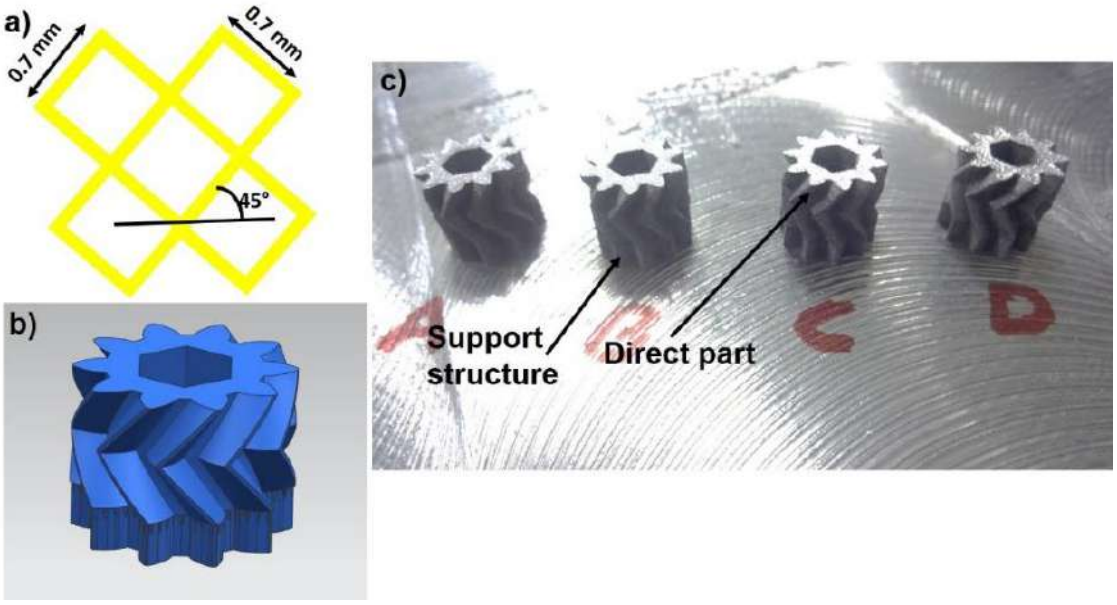

Figure 4. 1: 2D block type support; b) CAD model of gear-type part; c) LPBF-manufactured parts with different support structure process parameters

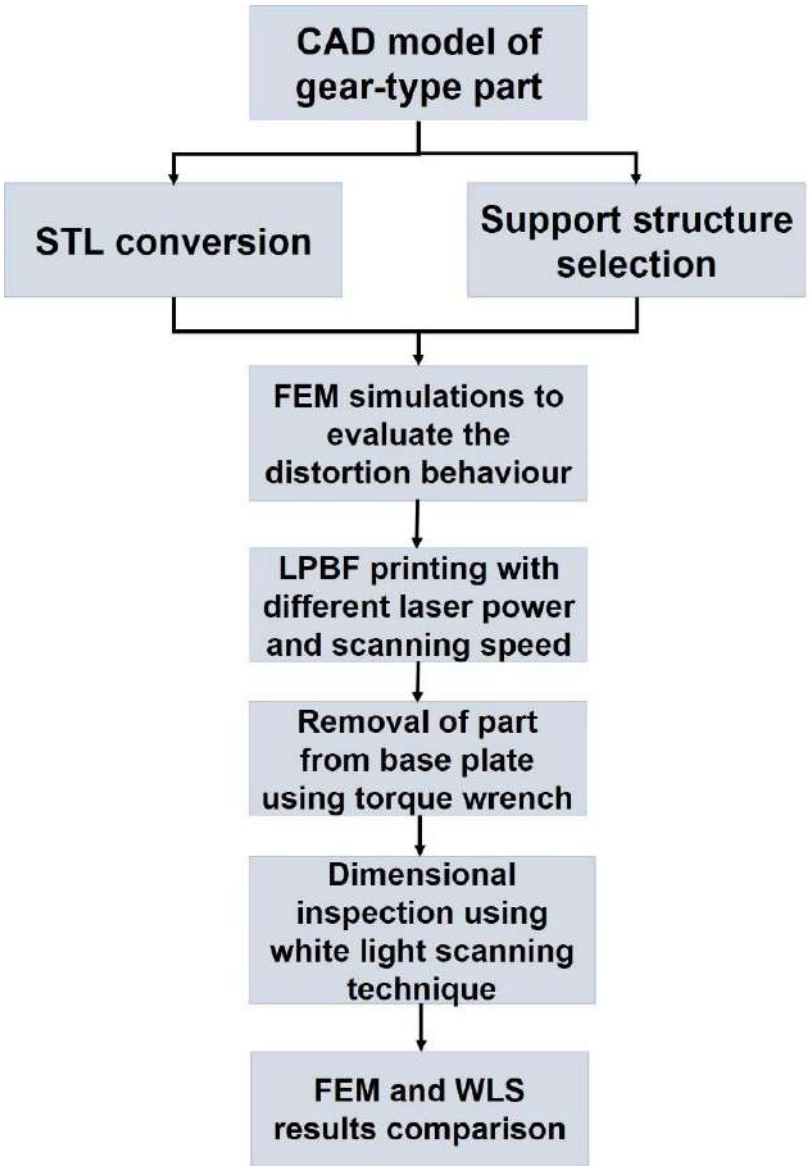

Figure 4. 2: A process flow adopted in the present work

4.2 Strength and ductility trade-off studies

The skin and core strategy adopted sample was prepared using the LPBF process shown in Figure 4.3. The process parameters used in fabricating the skin and core sample are given in Table 4.3.

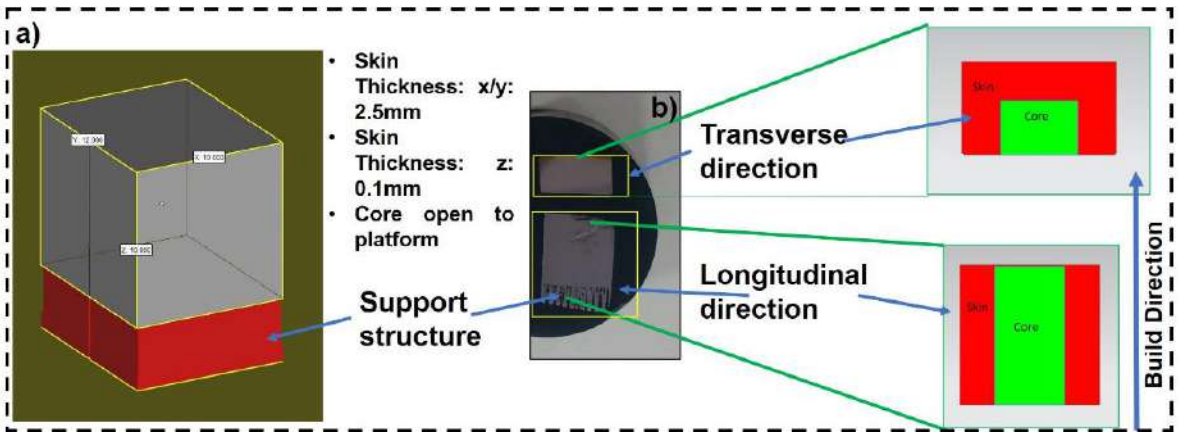

Figure 4. 3: Sample prepared for microstructural characterization

Table 4. 3. LPBF-Process parameters for skin and core strategy study

Feature	Laser Power (W)	Scanning speed (mm/s)	Hatch distance (mm)	Beam offset (mm)	Stripe width (mm)
Skin	170	1450	0.1	0.015	5
Core	170	1020	0.1	0	5

The samples were etched through Kroll's reagent. The microstructural characterization was carried out using an optical microscope. The samples were subjected to Vickers's microhardness tester with a load of 500 grams and 10 seconds dwell time.

4.3 Ti6Al4V powder feed stock characterization

The Ti6Al4V powder material supplied by EOS Germany was used to fabricate all the specimens for microstructural characterization, tensile, HCF, and damping tests. Moreover, the rotor blade fabrication for damping test evaluation was carried out from the same powder. The powder size ranges from 20 µm to 50 µm, and no aggregation was observed in the SEM image of the powder shown in Figure. 4.4. Moreover, the average powder particle size was 20-50 µm with a mean of 27.43 µm and a standard deviation of 9.41 µm. The chemical composition of the Ti6Al4V powder particles is shown in Table 4.4.

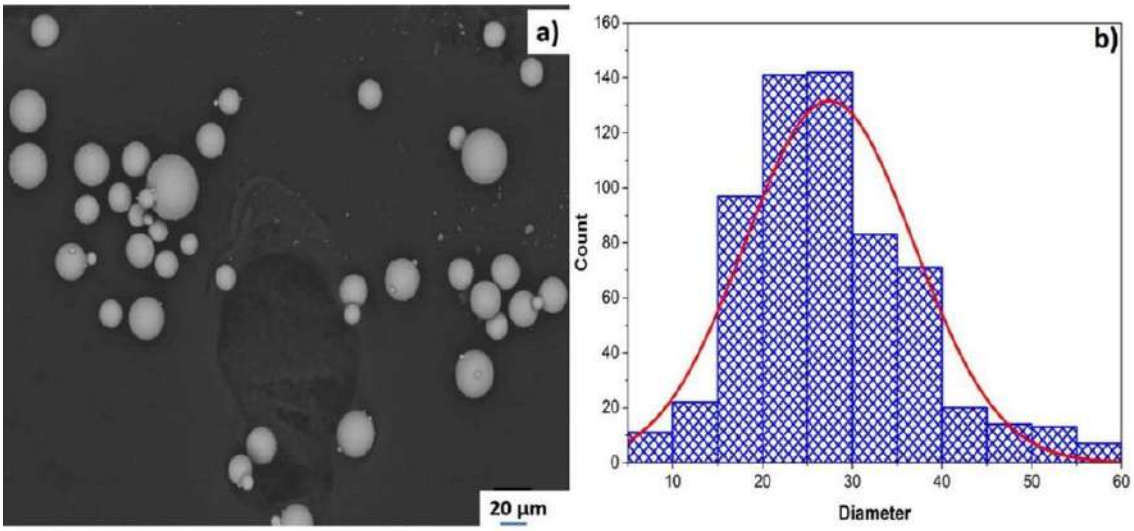

Figure 4. 4: a) SEM image of Ti6Al4V powder; b) Powder particle size distribution

Table 4. 4: Elemental composition of Ti6Al4V powder

Element	Ti	Al	V	Fe	C	O	N	H
wt%	Balance	6.47	4.08	0.24	0.005	0.08	0.008	0.003

All the specimens and rotor blades used for this study were fabricated using an EOS M280 machine equipped with a Ytterbium fiber laser, as shown in Figure. 4.5. The Argon gas is supplied during the LPBF process to maintain an inert atmosphere. The process parameters used to fabricate the samples are given in Table 4.5.

Figure 4. 5: EOS M280 LPBF machine employed in the present work

Table 4. 5: LPBF process parameters used in the present study

Laser power (W)	Scanning speed (mm/s)	Hatch distance (µm)	Layer thickness (µm)	Laser beam dia (µm)	Beam offset (mm)	Stripe width (mm)	Scanning strategy
170-200	500-1250	100	30	100	0.015	5	67° rotated stripe

The stress-relieving heat treatment at 650°C for 3 hours, followed by furnace cooling, was performed for all the samples and components. Moreover, different post-heat treatments (PHTs) were carried out at different temperatures and cooling rates. The PHTs were performed using a muffle furnace, as shown in Figure 4.6, equipped with an Argon gas supply to maintain the inert atmosphere.

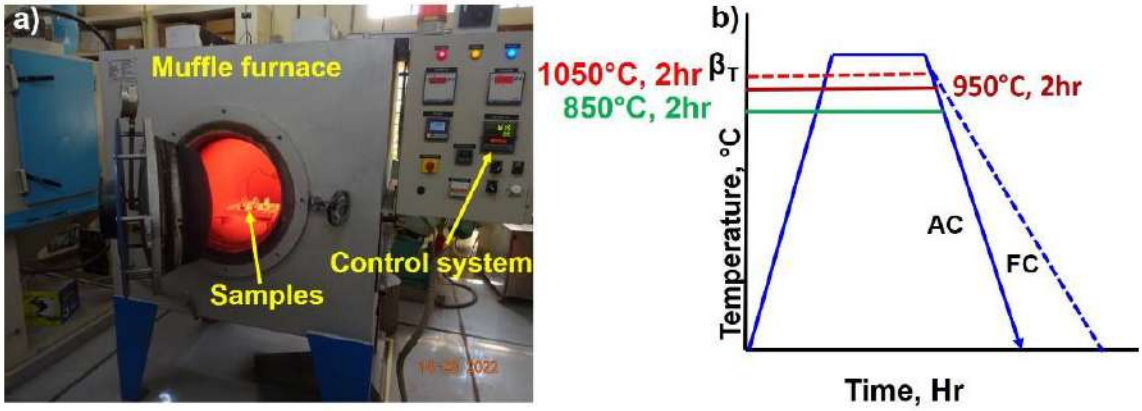

Figure 4. 6: a) Muffle furnace; b) PHT scheme

4.4 Microstructural characterization of LPBF-manufactured Ti6Al4V parts

After completing the LBPF process, the as-printed samples were cut using a wire EDM process from the base plate. The cubical samples with 3×3×3 mm^3 dimension were prepared as shown in Figure. 4.7 for PHTs. The as-printed LPBF-manufactured Ti6Al4V samples were prepared for PHTs. The samples were heat-treated in a muffle furnace at 850 °C, 950 °C, and 1050 °C under air and furnace cooling conditions. The corresponding PHTs at different temperatures and cooling conditions, termed samples A, B, C, D, and E, are shown in Table 4.6. The process parameters used to manufacture the samples are given in Table 4.5.

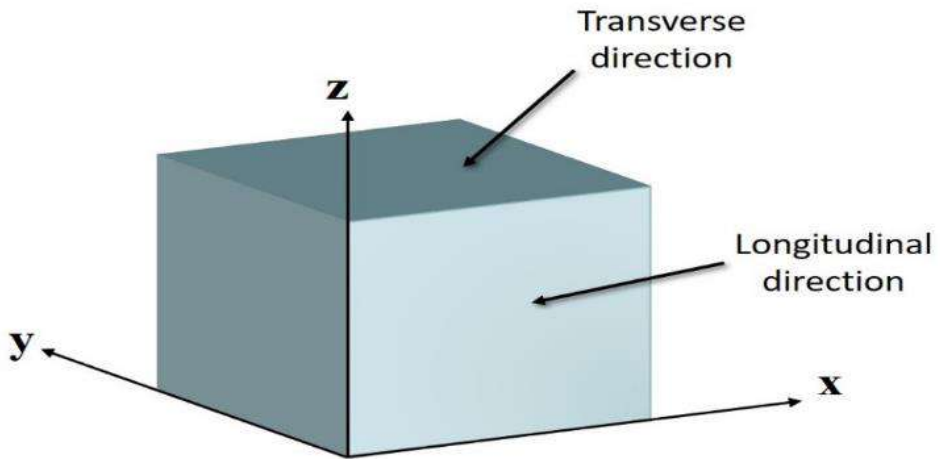

Figure 4. 7: Schematic illustration of LPBF-manufactured sample

Table 4. 6: Post-heat treatment conditions employed in the present study

Sr. No.	Nomenclature	Temperature (°C)	Time (hour)	Cooling condition
1	Sample A	850	2	Air
2	Sample B	950	2	Furnace
3	Sample E	950	2	Air
4	Sample D	1050	2	Furnace
5	Sample E	1050	2	Air

The as-printed and PHT samples oriented in horizontal and vertical directions were mounted and polished through emery papers ranging from 200-2000 μm, followed by diamond polishing (size 1μm) used for porosity evaluation. The polished samples were etched using Kroll's reagent (50 ml distil water, 25 ml HNO3 and 10 ml HF) for microstructural characterization. The microstructural observations were performed using an optical microscope (Olympus-DSX-510) and FESEM (Zeiss GeminiSEM 300). The chemical composition of the samples in as-printed and heat-treated conditions was evaluated using EDS (attachment to FESEM) technique. The lath thickness was measured using Image-J software, and the average value of three measurements was reported. The X-ray diffraction (XRD; make: Panalytics) equipment with Cu Kα was used to analyze as-printed and heat-treated samples. Vicker's micro-hardness tester (INNOVA Falcon-400) evaluated the micro-hardness under a load of 500 grams as per the ASTM-E384 standard. The average value of six measurements was reported in the present study.

4.5 Densification studies of LPBF-manufactured parts

The Ti6Al4V samples of around 18x5x5 mm^3 in size in horizontal and vertical orientations were produced using an EOS M280. The orientation of the built samples is shown in Figure

4.8. The samples were then subjected to a post-heat treatment (PHT) at 1050 ºC for two hours, then air cooling in a muffle furnace. The PHT temperature is higher than the β transus temperature, which is a high temperature that helps in the diffusion of pores. The as-printed and PHT samples oriented in horizontal and vertical directions were polished through emery papers ranging from 200-2000 μm, followed by diamond polishing before microscopic analysis. The micrographs were captured using the Nikon Eclipse LV100 optical microscope. The porosity was observed at an interval of 2150 μm on the horizontal and vertically built direction of as-printed samples and PHT samples. The process parameters used to manufacture the horizontal and vertical oriented samples are given in Table 4.5.

In the current practice of the LPBF process, the researchers quantify the defects, such as porosities, as metallurgical and irregular shape pores which is a conventional approach to defining them. However, there is a scope for further classification and quantification of porosities in order to correlate with the parts subjected to dynamic, impact, or coupled loading conditions and their interplay on the part's performance. Therefore, a facile approach is essential for the porosity classification is a need of the hour. Hence, in literature, the classification of pore size is classified by Mays[146] as shown in Figure 4.9, in which less than 10 μm pore size is considered as inter-micropore, whereas more than 10 μm is regarded as a super-micropores. Therefore, May's approach is used in the present study. In addition to it, similar approach of pore classification is also used in laser additive manufacturing by other researchers[147].

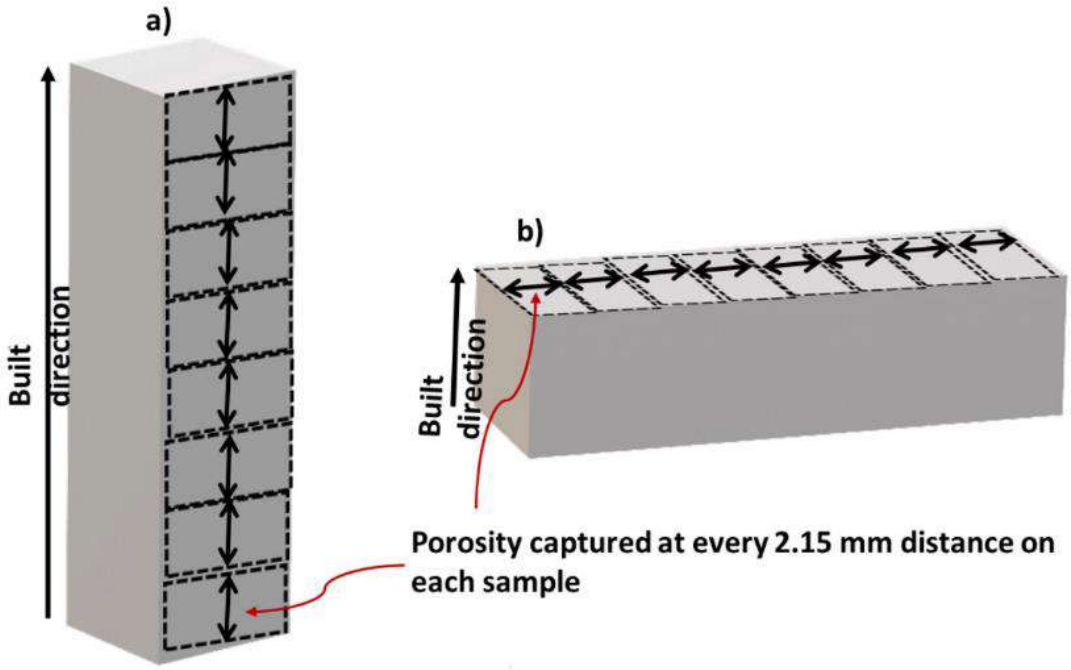

Figure 4. 8: Schematic of porosity measurement: a) Vertical build sample; b) Horizontal build sample

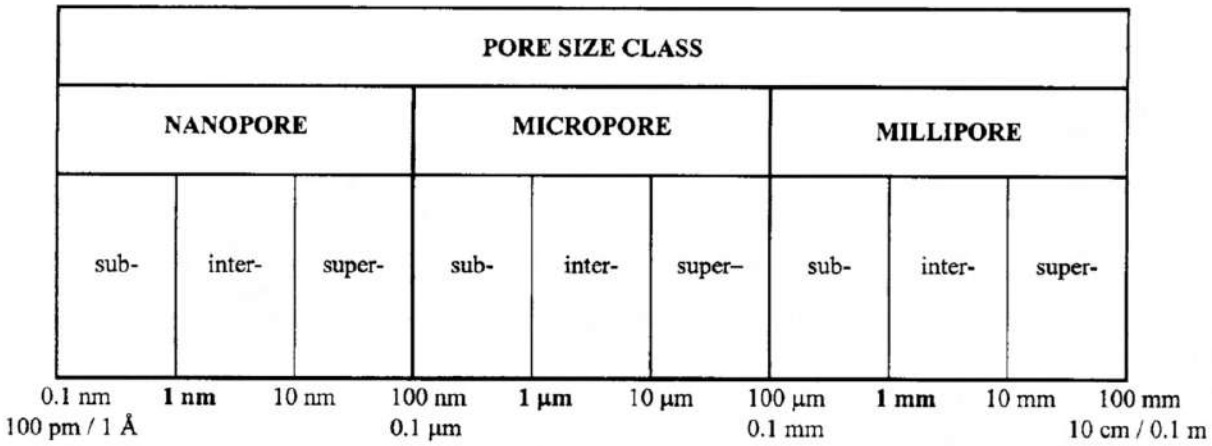

Figure 4. 9: Pore size classification [63]

4.6 Tensile tests specimen fabrication

Ti6Al4V cylindrical samples of size ϕ=20 mm and length = 145 mm were printed. The samples were fabricated in three different orientations viz 0°, 45°, and 90°, as shown in Figure. 4.10. The process parameters used to manufacture the tensile samples are given in Table 4.5.

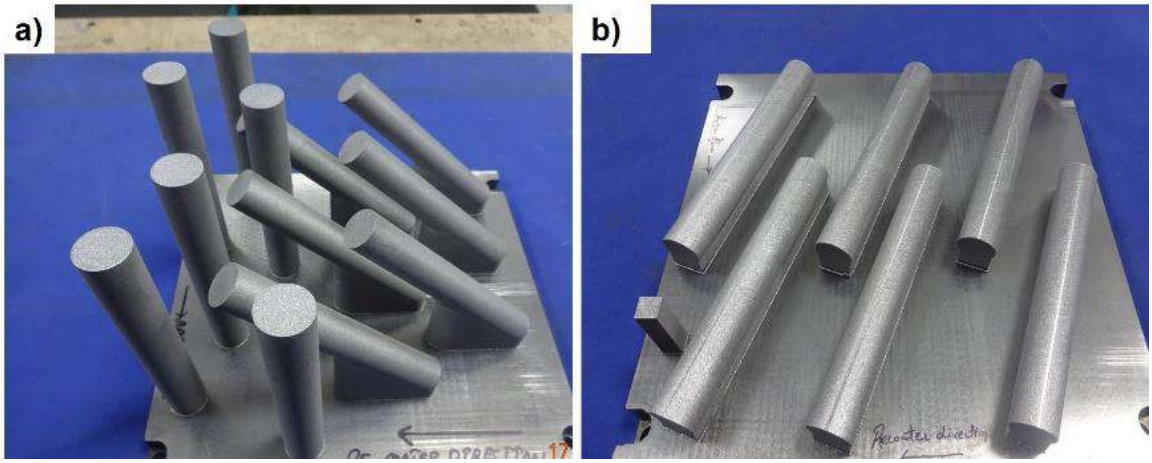

Figure 4. 10: Photographic images of LPBF-manufactured Ti6Al4V cylindrical samples in three orientations: (a) vertical and inclined; (b) horizontal

All the samples were machined to attain the ASTM E8 standard, as shown in Figure 4.11. The samples' dimensions were the total length of a sample = 143 mm, gauge length = 60 mm, grip dia = 16 mm, and gauge radius of curvature = 10 mm. Tensile tests were performed at a 0.003/s strain rate using a Universal testing machine (UTM; make: Walter+Bai). The fractography analysis was performed using an SEM.

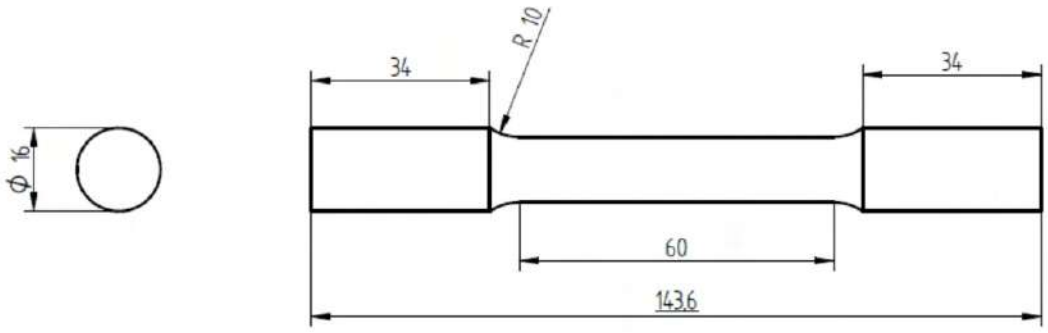

Figure 4. 11: ASTM-E8 standard machined specimen for tensile tests

4.7 HCF test specimens fabrication

Ti6Al4V cylindrical samples of size ϕ=12 mm and length = 100 mm were printed. The samples were fabricated in three different orientations viz 0°, 45° and 90°, as shown in Figure 4.12. The process parameters used to manufacture the HCF samples are given in Table 4.5.

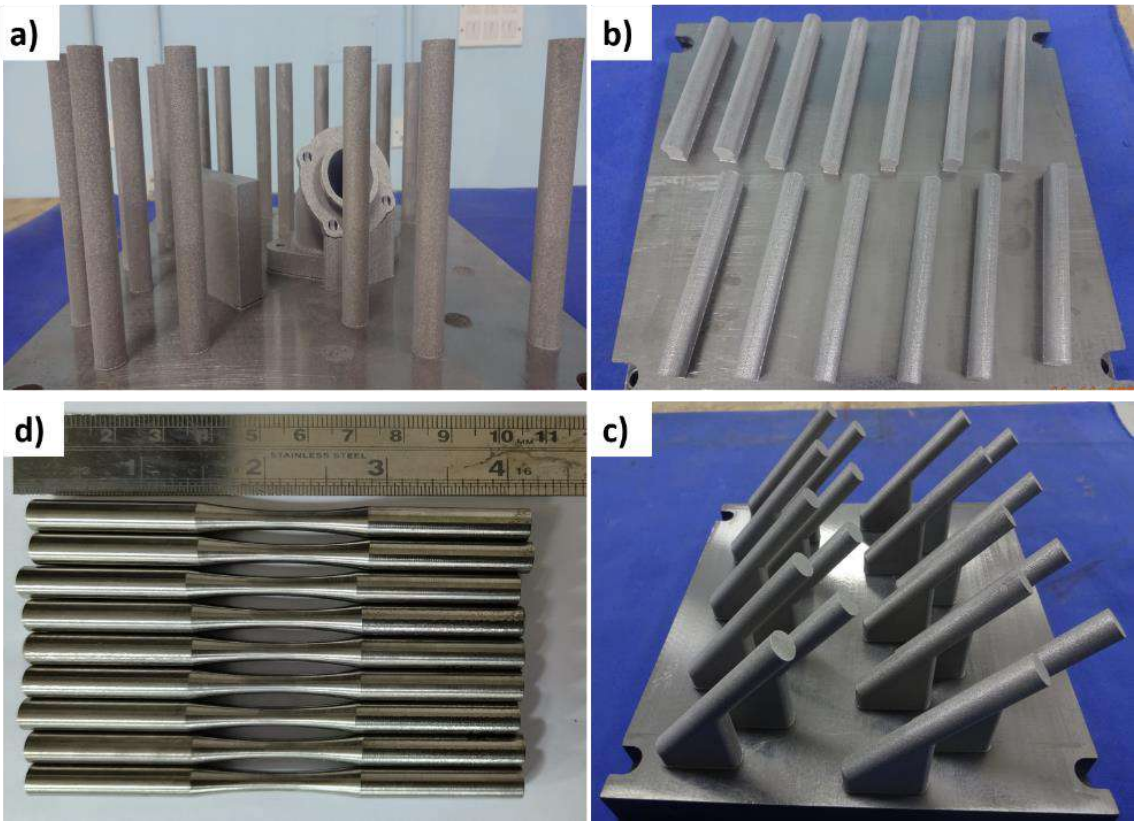

Figure 4. 12: Photographic images of LPBF-manufactured Ti6Al4V cylindrical samples in three orientations: (a) vertical; (b) horizontal; (c) inclined; (d) machined samples for HCF testing

All the samples were machined to ASTM E466 standards, as shown in Figure 4.13. The HCF test was performed at a load ratio of 0.1 and frequency of 15 Hz using uniaxial dynamic loading UTM machine (make: Walter + Bai). The dimension of the hour-glass samples was the total length of a sample = 100mm, gauge length = 25 mm, grip dia = 10 mm, and gauge radius of curvature = 72 mm. The fractography analysis was performed using an SEM. ImageJ software measured the crack initiation location length on the fractured surface.

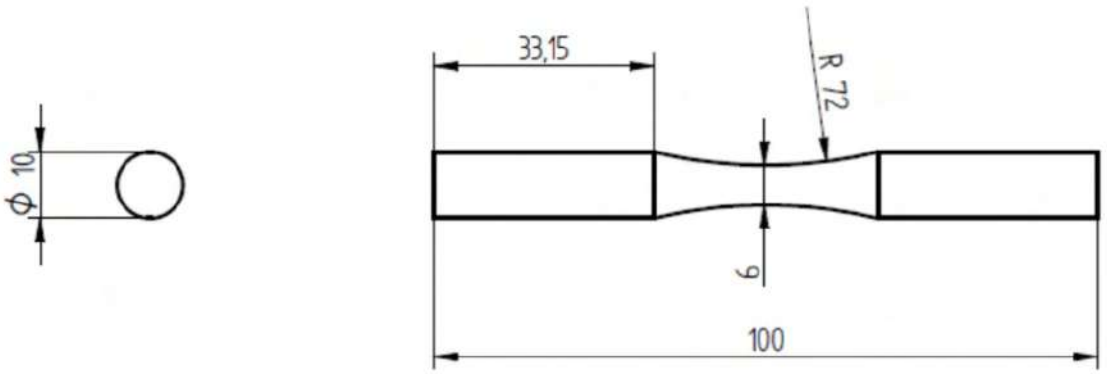

Figure 4. 13: ASTM E-466 standard machined samples for HCF tests

Further, FD analysis was performed for the fractured surface of tensile and HCF samples. The techniques for FD analysis include the box-counting method, differential box-counting method, covering method, and prism method[108]. Among them, the box-counting method is popularly employed[109]. The multifrac plug-in used to calculate FD value uses the fracture surface converting them into a binary image. FD is calculated using the equation 4.1.

$$D = \lim_{l \to 0} log \frac{N(l)}{\log l} \tag{4.1}$$

where l is the length size of non-overlapping boxes/cubes and N(l) is the number of boxes/cubes necessary at each scale l to cover the mass area (black or white)[148]. ImageJ software was employed to measure the FDs. The images were converted to 32-bit image types per the plug-in. Multifrac plug-in for Image-J was used to calculate the FD of all the samples using the 2D box-counting method. The maximum box size used for the box-counting FD was 16, and the procedure adopted for FD analysis is shown in Figure 4.14.

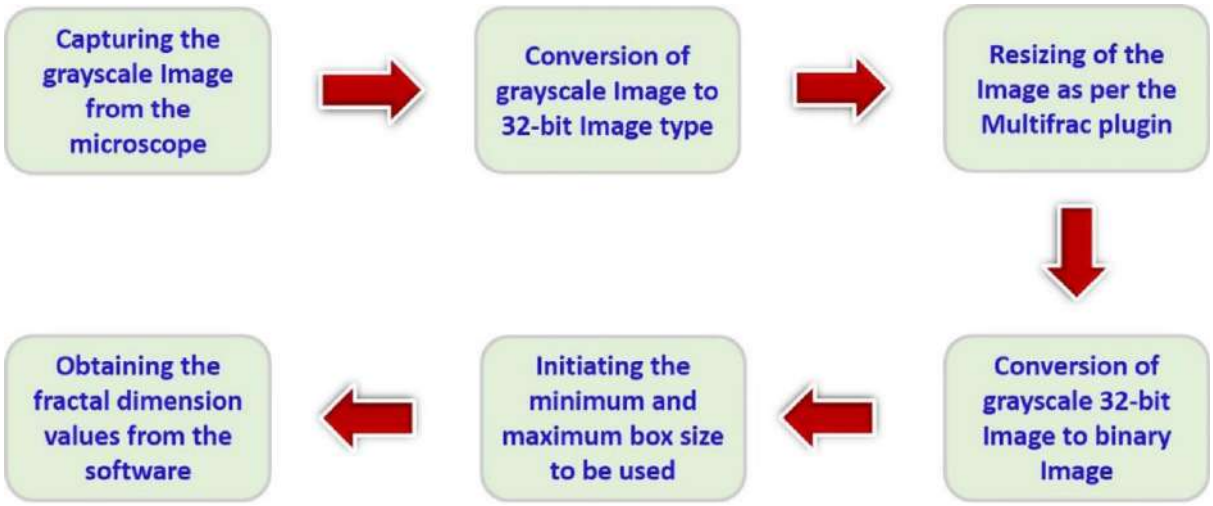

Figure 4. 14: Procedure adopted for FD analysis in the present study

4.8 Damping test of LPBF-manufactured Ti6Al4V specimens and rotor blade

Ti6Al4V samples of size 118 x 28 x 4 mm^3 in thickness were printed. Moreover, the rotor blade printing was fabricated using the LPBF process for evaluating the damping behaviour. The blade-like samples and rotor blade were printed vertically, as shown in Figure 4.15. The process

parameters used to manufacture the samples and rotor blade for the damping test are given in Table 4.5.

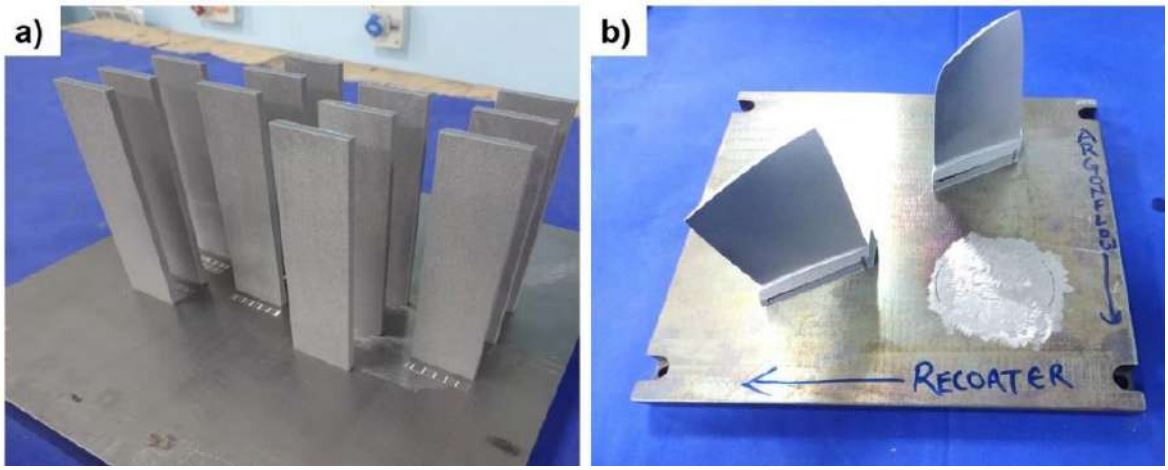

Figure 4. 15: Photographic images of LPBF-manufactured Ti6Al4V a) thin flat samples and b) rotor blades

The damping behaviour of as-printed PHT samples and rotor blades was evaluated using an experimental impact hammer modal analyzer (make: PCB) (given in Figure. 4.16). The accelerometer (PCB-353C22) is attached to the sample and connected to the data acquisition system (PCB-SN15267). The impact hammer (PCB-086C03) excites the material to obtain the response through the data acquisition system. Moreover, the modal analysis was carried out using FEM and compared with the experimental natural frequencies.

The damping ratio for two-mode shapes of as-printed and PHT samples was evaluated using the half-power bandwidth at peak by first computing the amplification factor Q using equation (4.2).

$$Q = \frac{fn}{\Delta f} \tag{4.2}$$

Where fn is natural frequency, Δf is f2 - f1 (frequency width between half power points). For clarity, f1 and f2 are determined from an amplitude of $\frac{A\,max}{\sqrt{2}}$ of the frequency range of fn. Thus, the resulting damping ratio is given in equation (4.3).

$$\text{Damping ratio } (\xi) = \frac{1}{2Q} \tag{4.3}$$

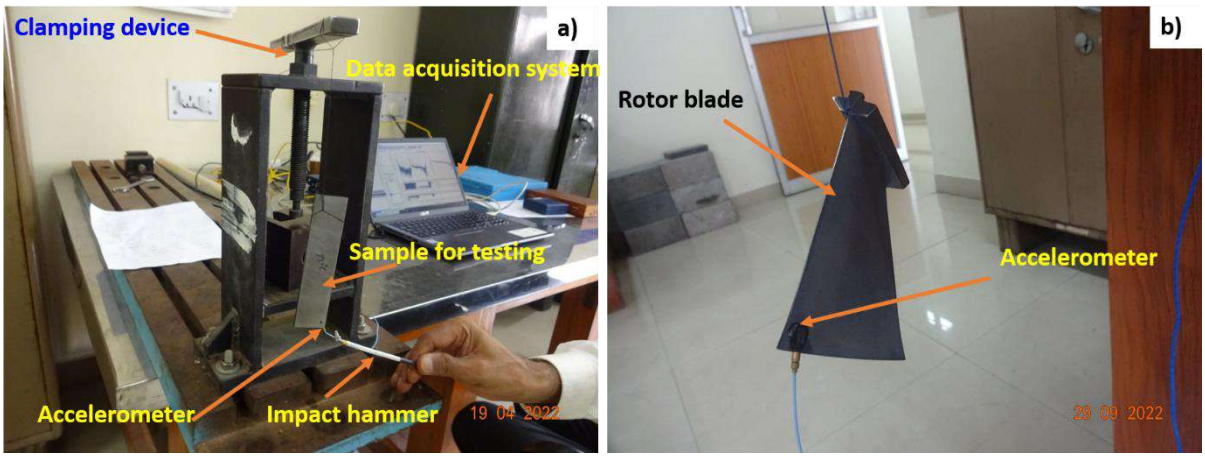

Figure 4. 16: Experimental setup of modal analysis; a) thin flat sample; b) rotor blade

Chapter - 5

RESULTS AND DISCUSSION

5.1 LPBF process parameter optimization studies for support structure

5.1.1 Post-Processing of support structures of LPBF-manufactured Ti6Al4V part

5.1.1.1 FEM simulation studies

In the present study, FEM simulations were performed to obtain insight into understanding the effect of process parameters on the distortion behaviour and thus aid in minimizing the use of experimental samples required, which are usually time involved and expensive. The residual stress distribution of different parameters for samples 'A,' 'B,' 'C,' and 'D' was computed for SSs using Ansys Additive and is shown in Figure 5.1. The response of distortion on the SSs will influence the part's printed layers, eventually affecting the build dimensional accuracy. It can be observed that stresses are higher at locations 3 and 4. Moreover, the corresponding distortion due to stresses is shown in Figure 5.2, comparable with WLS results (see Figure 5.3). The residual stresses on the inner surfaces of all four samples are not reaching the yield strength (see Figure 5.1) owing to the heat accumulation and restriction by surrounding material leading to a distortion-free inner surface, as shown in Figure 5.2. Moreover, the sharp corners of gear-type part in all four samples are the high heating and stress accumulation zones leading to the distortions in locations 3 and 4. Similar results were found in another study by Chen et al.[149], where localized overheating occurs at the sharp corners of a part resulting in higher residual stresses. Further, the stresses at the outer surfaces of the gear-type part show residual stress that exceeds the yield strength of a material due to high thermal gradients causing the surface distortion, as seen in Figure 5.2, which is comparable with WLS results (see Figure 5.3).

Moreover, the percentage reduction of stresses computed through simulation in sample D compared to samples 'A,' 'B' and 'C is given in Table 5.1. It can be observed that less laser power in sample 'D' SS generates less heat input, resulting in less temperature gradient leading to reduced stresses. Subsequently, the lesser stresses in sample 'D' help reduce the overall distortion compared to samples 'A,' 'B,' and 'C,' as shown in Table 5.1.

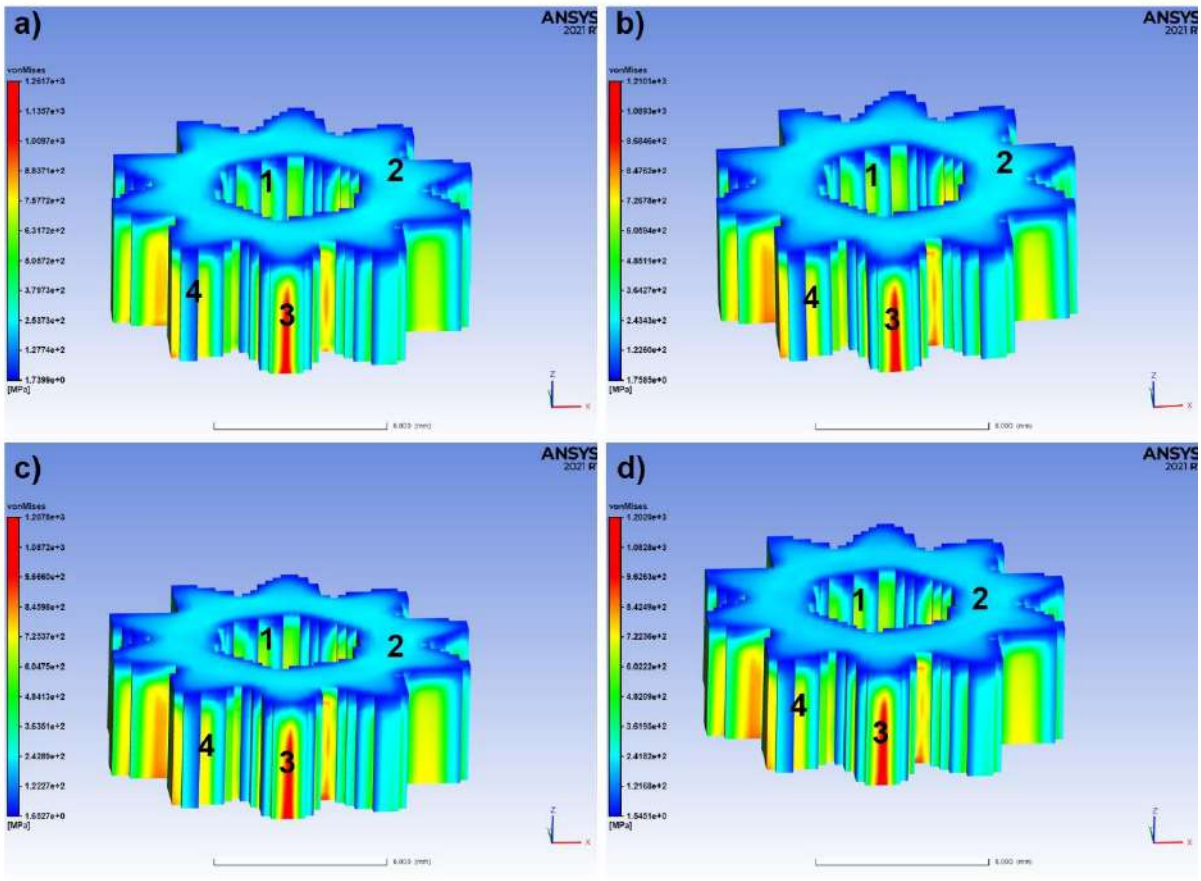

Figure 5. 1: Ansys simulation of SSs residual stress: a) Sample 'A'; b) Sample 'B'; c) Sample 'C'; d) Sample 'D.'

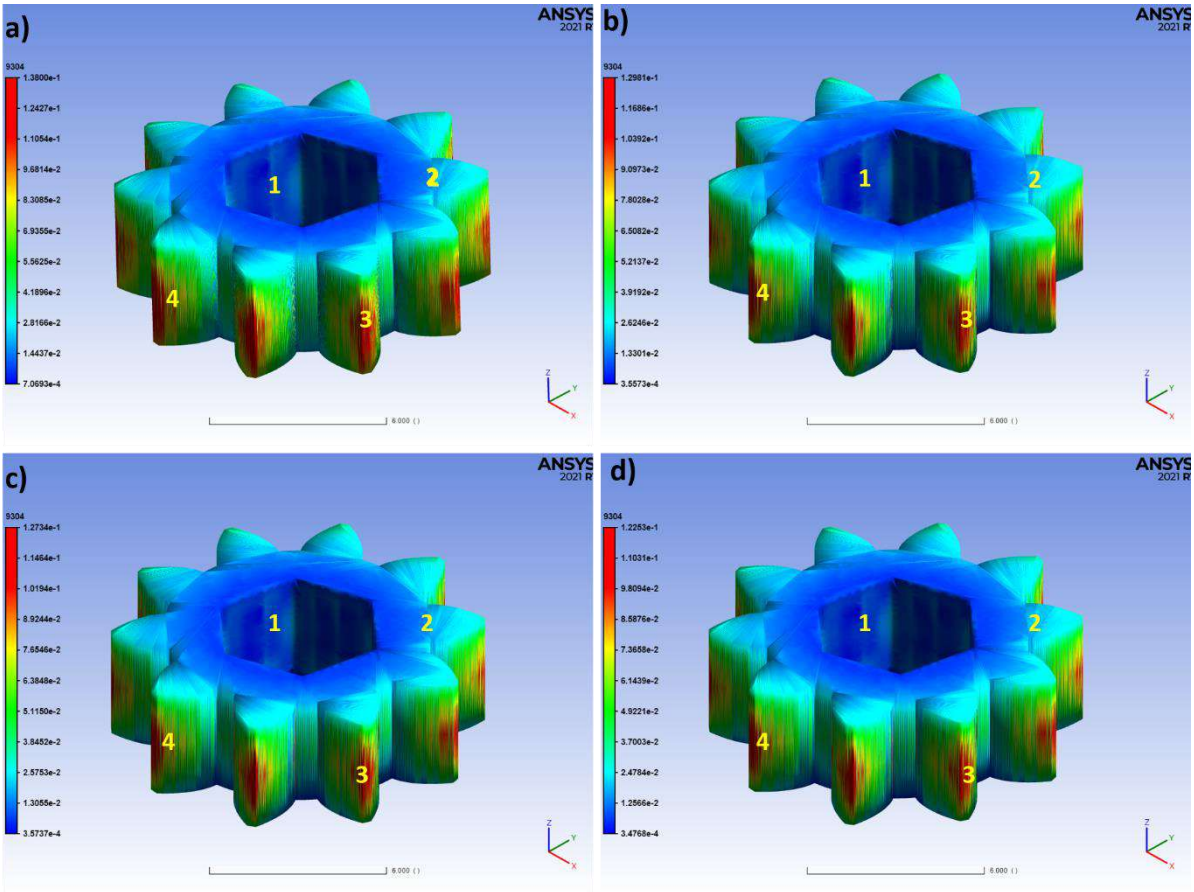

Figure 5. 2: Ansys simulation of SS distortion: a) Sample 'A'; b) Sample 'B'; c) Sample 'C'; d) Sample 'D.'

Table 5. 1: Percentage reduction in residual stress and distortion for sample 'D' compared to samples 'A,' 'B' and 'C.'

Sample	Stress with base plate (MPa)	%age reduction in residual stress for sample D	Distortion with base plate (µm)	%age reduction in distortion for sample D
Sample A	1261.7	5%	138	11%
Sample B	1210.1	0.7%	130	6%
Sample C	1207.8	0.4%	128	4%

Sample D	1202.0	-	123	-

The obtained results in simulations showed lesser distortion in Sample' D' among all the samples. Although the distortion using FEM was evaluated for SSs; the distortion at SS will influence the part and subsequently affect the dimensional accuracy of a part. Therefore, the gear-type parts were fabricated using the same process parameters for SSs.

5.1.1.2 Dimensional inspection studies

After printing, the base plate with LPBF parts was investigated for dimensional inspection with the WLS technique. 3D WLS is a technique that uses a non-contact scanning method. This method works by projecting a fringe projection onto the surface of the scan. The WLS measurement takes place on the surface of an object to collect the coordinates of its various points. This process is carried out using a combination of digital image processing and optical technology. The samples (A-D) were scanned through 3D WLS, and obtained scanned data was compared with the CAD model, as shown in Figure 5.3 (a-d). It is observed that the dimensional variation was within the acceptable limits, i.e., below 100 µm. However, the dimensional variation of ~200 µm between the CAD model and the part may be due to the applied developer making a part as a white object, adding a few microns of thickness due to human error. The overall dimension deviation concerning the different processing parameters for SS was insignificant. The inspection results obtained from WLS confirm that changing the SS's process parameters does not affect a part's dimensional accuracy.

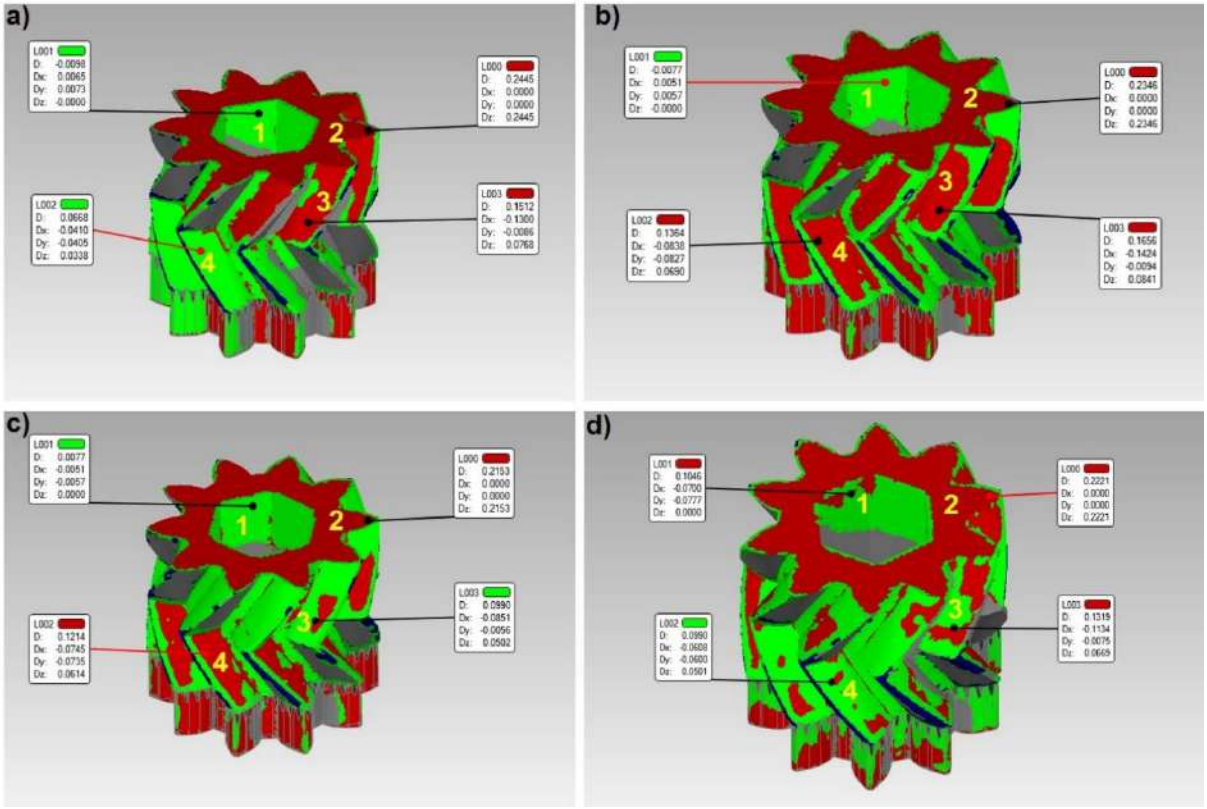

Figure 5. 3: 3D WLS model compared with CAD model: a) Sample 'A'; b) Sample 'B'; c) Sample 'C'; d) Sample 'D.'

The dimensional deviation between WLS and simulation of different locations for Sample 'A,' 'B,' 'C,' and 'D' are shown in Figure 5.4. Location 1 in all four samples offers a dimensional accuracy of less than ~10 µm, which is close to the CAD model dimensions. Further, location 2 in simulation results in all samples shows a minor deviation due to fewer stresses developed there. However, Location 2 in WLS, a top surface, offers an expansion and dimensional variation of ~200µm for all four samples from the CAD model. Such top surface's dimensional deviation is characterized by surface quality due to the combined effect of surface roughness and waviness[150]. The surface roughness of the top face is high due to the heat accumulation around it[151]. The powder bed in LPBF acts as an insulator, and the heat accumulates surrounding the melt pool. In the LPBF process, inserting a fresh powder layer keeps the previous layer farther away from the molten pool. As a result, the top surface's maximum temperature rises along with heat accumulated in the surroundings. Eventually, the temperature rises to a point where surrounding powder particles begin to stick partially, and the surface becomes rougher. This impact could become more noticeable as more layers are added. Researchers report similar dimensional deviations in LPBF[152] and EBM-manufactured[151]

parts. Moreover, the dimensional deviation in locations 3 and 4 in all four samples between WLS and experimental was observed between 100µm to 150µm. It may be attributed to the large thermal gradient between L3, L4, and the surrounding powder, which pulls the material at the sharp corner edges of the gear-type part due to thermal stresses.

Further, it should be noted that L3 and L4 have sharp edges facilitating thermal stress concentration and leading to dimensional distortion. Moreover, Ti6Al4V's lower thermal conductivity (7.2 W/mK) will increase a thermal gradient. However, interestingly, the location 1 inner surface is smooth and shows an almost closer values with CAD dimensions in all samples due to a lesser thermal gradient than L3 and L4 due to heat accumulation. Moreover, a further detailed study is desirable to evaluate the dimensional deviation of such surfaces in the LPBF-manufactured part.

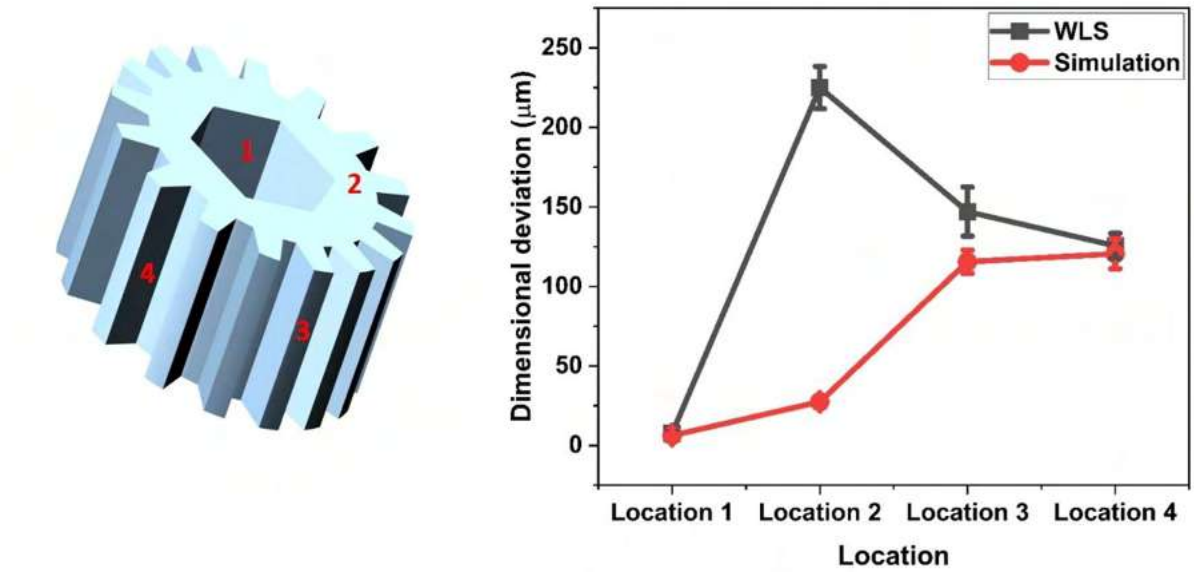

Figure 5. 4: Dimensional deviations at different locations of a part experimental vs simulation

5.1.1.3 Interface shear strength (ISS) evaluation studies

The gear-type parts were separated from the base plate using a mechanical torque wrench, as shown in Figure 5.5, to evaluate the torque required to remove the support from the part and base plate. The torque wrench was rotated manually to separate the part from the SS, and the torque required to remove the part was evaluated for each sample as per [ISO 6789]. Table 5.2 comprises the measured torque values to separate the part from the SS. The resulting torque values were in the range from 145-230 Kgf-cm, signifying that LPBF process parameters have a greater influence on the part removal. Interestingly, sample 'A' requires a relatively large

torque value to remove the part from the support. It could be attributed to high laser power enabling complete melting of the powder and resulting in a stronger SS.

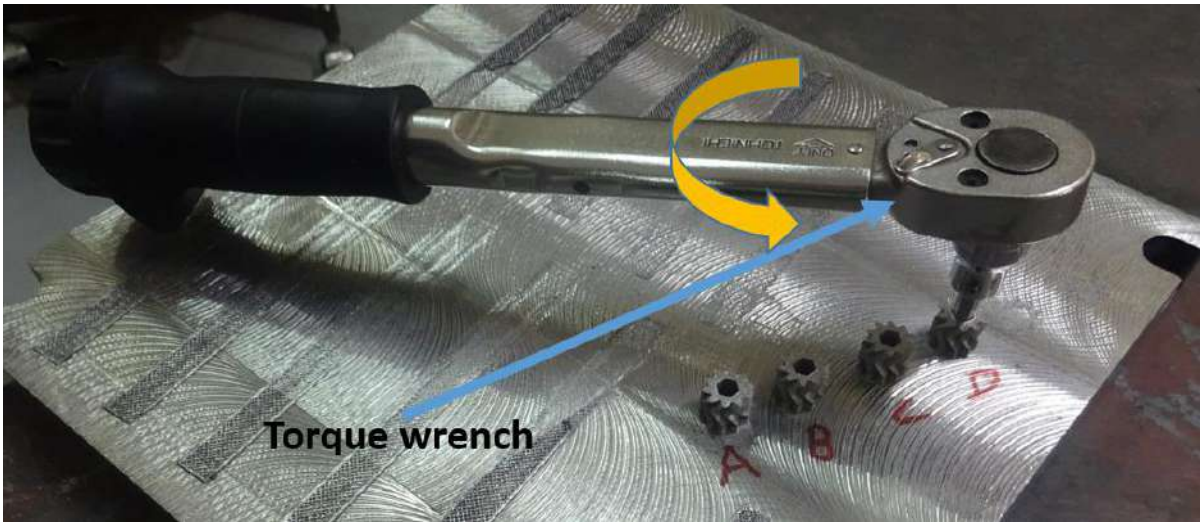

Figure 5. 5: LPBF part separation from a SS and base plate

In contrast, sample D showed the marginally most minor torque value required to separate the sample from the SS. The least laser power was used in sample D to fabricate the SS, due to the partial melting of powder resulting in less ISS enabling less effort for part removal. These results open an insight into effectively using the SSs to remove the part easily by preserving the dimensional and structural integrity of the LPBF part. The partially melted powders due to using lesser laser power (80 W), might enable easier removal of a SS. Moreover, it is reported that as the laser power increases from ~80 W to 140 W, the porosity in LPBF fabricated Ti6Al4V reduces from ~5% to 0.07% respectively[153]. In view of the above it is presumed that in the present work, highest laser power (i.e, 140 W) was employed for sample A resulting a high ISS between SS and part owing to less porosity. It is also reported that laser speed and layer thickness has insignificant effect on the ISS[43].

Table 5. 2: Torque measurements

Sample	Laser Power (W)	Scanning speed (mm/sec)	Hatch distance (µm)	Layer thickness (µm)	Torque (Kgf-cm)

Sample A	140	700	100	30	230
Sample B	120	600	100	30	190
Sample C	100	500	100	30	155
Sample D	80	400	100	30	145

In present work, the ISS between SS and part is shown in the form of schematic representation in Figure 5.6.

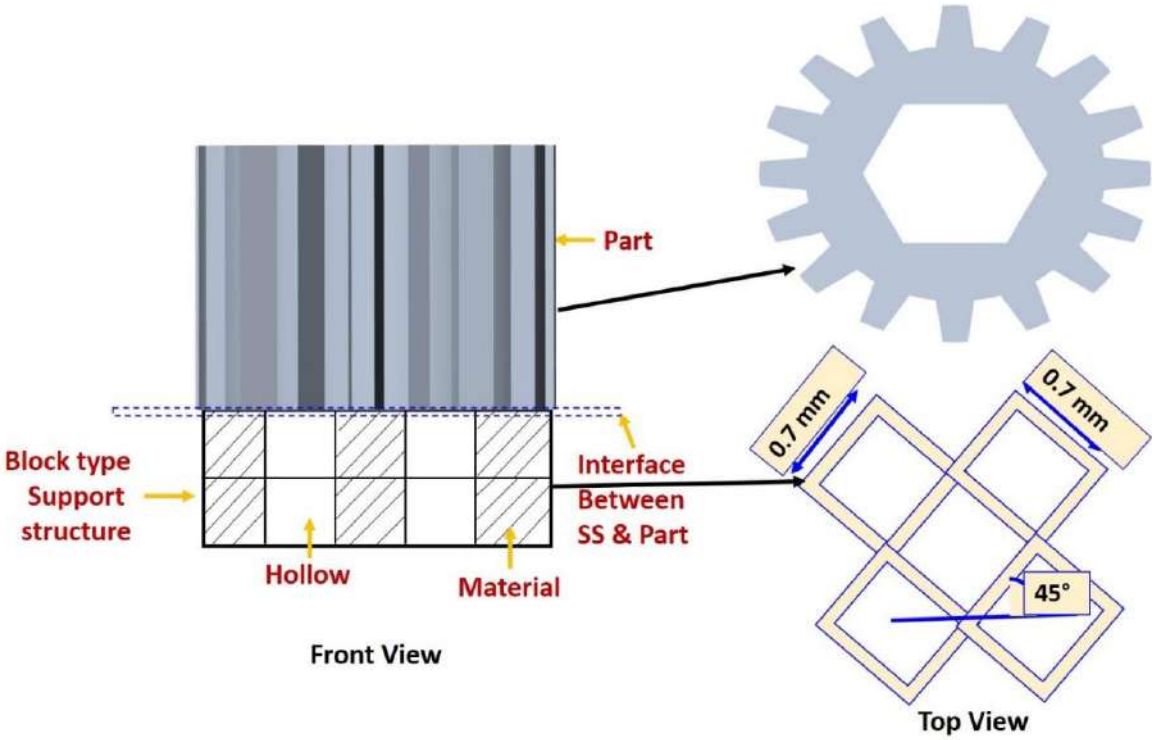

Figure 5. 6: Interface between SS and part

Moreover, the torque values obtained to remove the base plate's support was converted to the ISS using equation 5.1[154] and 5.2. The ISS developed during support removal for samples A, B, C, and D is shown in Figure 5.7. Sample D shows the least ISS required to remove the SS. Further, sample D showed ~60% less ISS value compared to sample A, ~34% less torque value compared to sample B, and ~9% less torque value compared to sample C.

$$\tau = \frac{T}{K_p} \tag{5.1}$$

$$K_p = \frac{\pi D^3}{16} - \frac{5}{4}\frac{\sqrt{3}}{D}S^4 \tag{5.2}$$

Where τ = shear stress, T = torque, and K_p = Polar section modulus, D is the outer diameter, and S is the side length of the inner hexagon of a gear-type part.

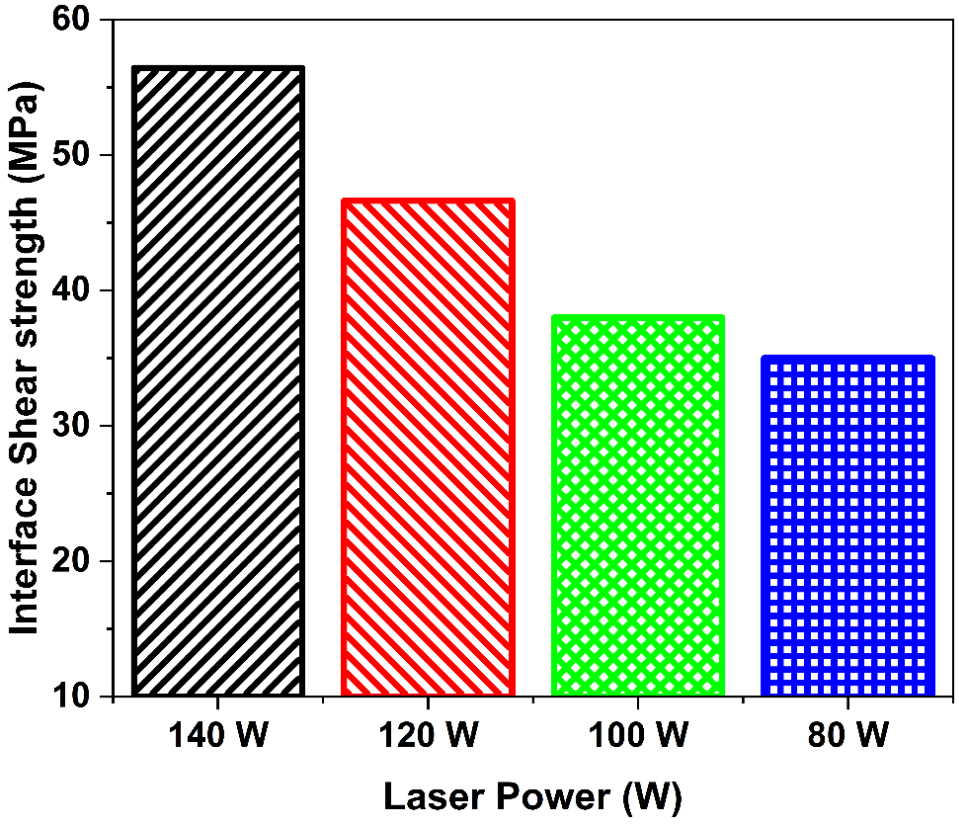

Figure 5. 7: Interface shear strength evaluation

The SSs play an essential role in deciding the final quality of a build component in terms of its structural and dimensional integrity. In this study, the ease of removal of SS is the outcome derived from optimal LPBF process parameters. Further, the SSs process parameters were employed for all the LPBF manufactured samples and parts in the present study.

5.1.2 Skin-core scanning strategy in LPBF-manufactured Ti6Al4V parts

The strength and ductility trade-off are a major road-block in LPBF-manufactured Ti6Al4V parts, which is not suitable for its end-use applications. Therefore, by varying the process

parameters, the goal is to obtain optimal strength and ductility in LPBF-manufactured Ti6Al4V parts.

The equiaxed grains are observed in the transverse direction, where α' martensite appears in the form of needles, as shown in Figure. 5.8 (a-f). The columnar grains are visible along the longitudinal direction due to the thermal gradients, as shown in Figure. 5.8 (d-f). The α' martensite is embedded in these columnar grains, formed due to the high cooling rates involved in the LPBF process [53]. LPBF process consists of the re-melting and melting of the material's layer. This event results in cooling and rewarms behaviour and can cause thermal cycling [56].

The α’ martensite formed in LPBF of Ti6Al4V is responsible for exhibiting high strength with poor ductility. However, the skin-core strategy could be useful to induce architectured microstructure at the required part’s location to ensure improved functionality.

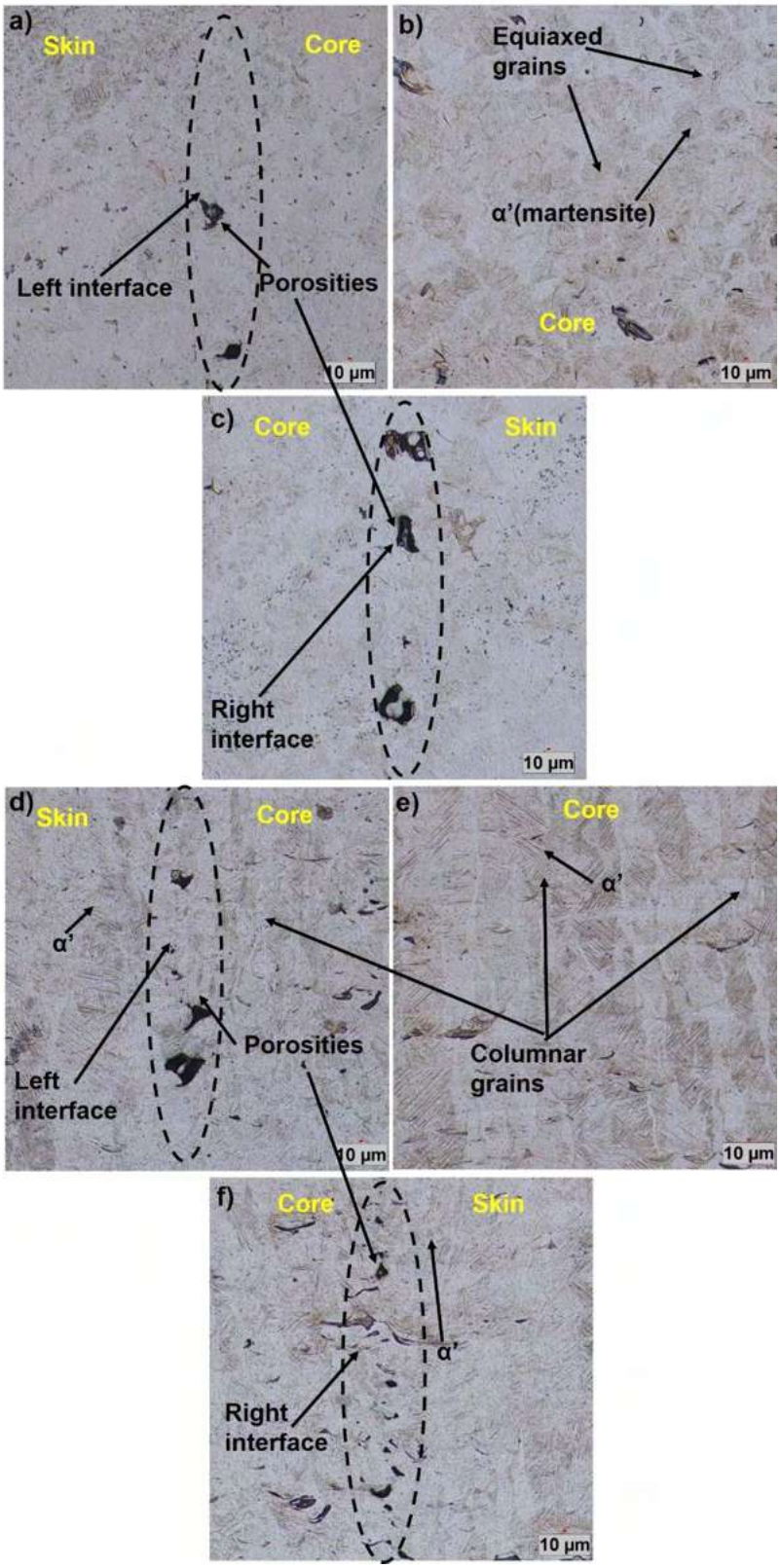

Figure 5. 8: Optical microstructures: a) left interface of TD; b) core of TD; c) right interface of TD; d) left interface of LD; e) core of LD; f) right interface of LD. Transverse Direction (TD); Longitudinal Direction (LD)

Despite varying scanning speeds, the columnar and equiaxed microstructure contains α' martensite in the skin and core regions. However, there was a difference in the grain size in both columnar and equiaxed skin and core regions, owing to the difference in scanning speed. The grain boundaries observed in the skin region are smaller than those observed in the core in transverse and longitudinal directions. These results are well corroborated with the literature, where it is reported that the microstructure contains smaller grains with high tilt angles at higher scanning speeds. In contrast, the low speed will give large grains with low tilt angles [50]. However, a detailed study is required to confirm this. The metal's grain structure plays a vital role in controlling its mechanical properties after laser melting. After solidification, the grains are characterized by anisotropic properties. This is due to the formation of columnar and elongated grains.

The heat flow direction can control the growth direction of these grains. The heat from the laser is extracted from the melt pool and then to a cooler part of the sample. This allows the grains inside the fusion zone to orient themselves according to the heat flow properties. During a competitive grain growth period, the grains that prefer a specific orientation during the heat flow can grow faster and produce more energy than those that prefer a non-specific orientation.

Interestingly, these findings open up an alternative way to change the material's grain size, enabling it to attain different mechanical behaviour, thus enabling location-specific functional properties. Moreover, grain size also dictates the material's strength. The larger the grain size, the less strength it will exhibit, as per the established Hall-Petch relation [155].

In Figure. 5.9(a), it is observed that the microhardness of the skin was relatively higher than the core due to the smaller grain size. The grain size of the skin and core in transverse direction was evaluated and shown in Figure. 5.9(b). The average grain size of the skin and core were ~77 μm and ~116 μm, respectively. The smaller grain size of the skin was responsible for higher microhardness owing to the Hall-Petch relation. The drop in hardness at the interface was due to the porosities present in the interface, as shown in Figure. 5.8(a, c, d and f).

Moreover, a marginally higher hardness in the transverse direction compared to the longitudinal direction due to the variation in grain sizes. Further, the hardness values of LPBF-manufactured Ti6Al4V samples obtained using the standard rot scanning strategy [7] were ~10 % lesser than those obtained using the skin-core scanning strategy along the longitudinal direction. The results of this study revealed the effects of changing parameters in the LPBF

process on the grain shape, size and porosities. However, the anisotropy in the microstructure was still retained (Figure.5.8). Therefore, a post-heat treatment is inevitable to reduce the anisotropic microstructure, thus making it suitable for end-use parts operating under industrial environments.

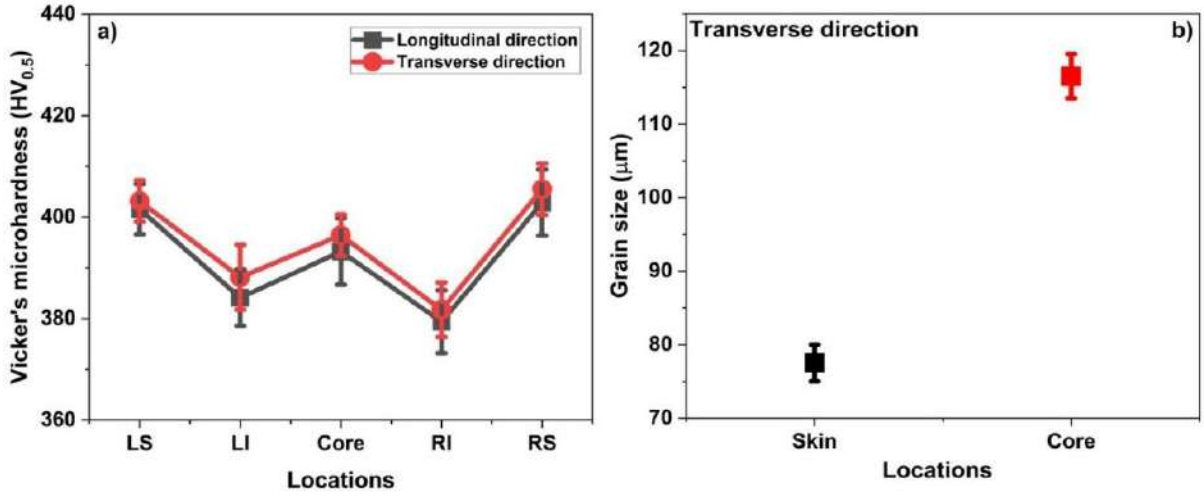

Legends: LS- Left side, LI- Left interface, RI- Right interface, RS – Right side

Figure 5. 9: a) Vickers's microhardness of sample; b) grain size of skin and core

5.2 Influence of PHTs on Microstructural and microhardness of LPBF-manufactured Ti6Al4V parts

5.2.1 Microstructural characterization

Microstructures of the as-printed Ti6Al4V samples in transverse and longitudinal directions are shown in Figure. 5.10 and 5.11, respectively. The reflected light from the etched Ti6Al4V surface under an optical microscope shows the dark phase as an α and the bright phase as a β phase; based on the contrast, the phases were distinguished in the micrographs. The arrows in the micrographs indicate different features and phases in the Ti6Al4V microstructure.

Figure. 5.10 shows the optical microstructure of the as-printed LPBF-manufactured Ti6Al4V in the transverse direction. The cellular prior β grains are visible in Figures. 5.10 (a) and (b), along with the fine needles of α' martensite phases. The rapid solidification of the melt pool in the LPBF process leads to the formation of the cellular microstructure. The obtained microstructure shows fine α' martensite (~ 0.5 μm thick) in slender β grains due to faster cooling rates and the small melt pool size, as seen in Figure.5.10 (b) and (c).

Figure 5. 10: Optical micrographs of the as-printed LPBF Ti6Al4V samples in the transverse direction (a); higher magnification micrographs (b-c)

Figure. 5.11 shows the microstructure in the longitudinal direction of the as-printed LPBF-manufactured Ti6Al4V sample. The prior β grains are visible (see Figure. 5.11a) due to the build direction's epitaxial growth owing to the build direction's temperature gradient and successive layer formations. The deposition of the next layer in the LPBF process on the previously formed columnar grains will re-melt and act as a nucleus for epitaxial grain growth with a strong texture development [52]. The shorter interaction time of laser with powder and high cooling rates (generally > 410°C/s) [53] leads to α' martensite formation. Ti6Al4V transforms (α+β) to β to liquid to β to (α+β/α') during the LPBF process. The formation of α' (martensite) phase depends upon the specific cooling rates. The cooling rate above 410°C/s leads to the form α' structure, whereas there is an incomplete transformation of α' between 410°C/s and 20°C/s and the cooling rate below 20°C/s will not produce α' phase. Due to high undercooling, the diffusion-less transformation forms α' martensite in prior β grains (see Figures. 5.11 (b) and (c)). It possesses very high strength and low ductility. In addition to α' martensite, the residual thermal stresses develop in the LPBF process due to steep temperature gradients. The speed and power of a heat source can also affect the melt pool's thermal gradient (G) and solidification rate (R) [54]. The columnar grain structure (houses α' martensite) is formed by the geometry and heat flow of the melt pool, as seen in Figure.5.11 (a). Figures 5.11 (b) and (c) show that the microstructure reveals features of α' martensite needles oriented at a particular angle. A larger, deeper melt pool should result in more columnar grains [156]. In the LPBF process, a smaller powder area interacts with the laser; therefore, it has a much higher laser power per area, directly influencing re-melting and epitaxial growth. The heat dissipation in LPBF is mainly due to the continuous heat conduction from the melted layer to the solidified material, which generates a columnar microstructure [56].

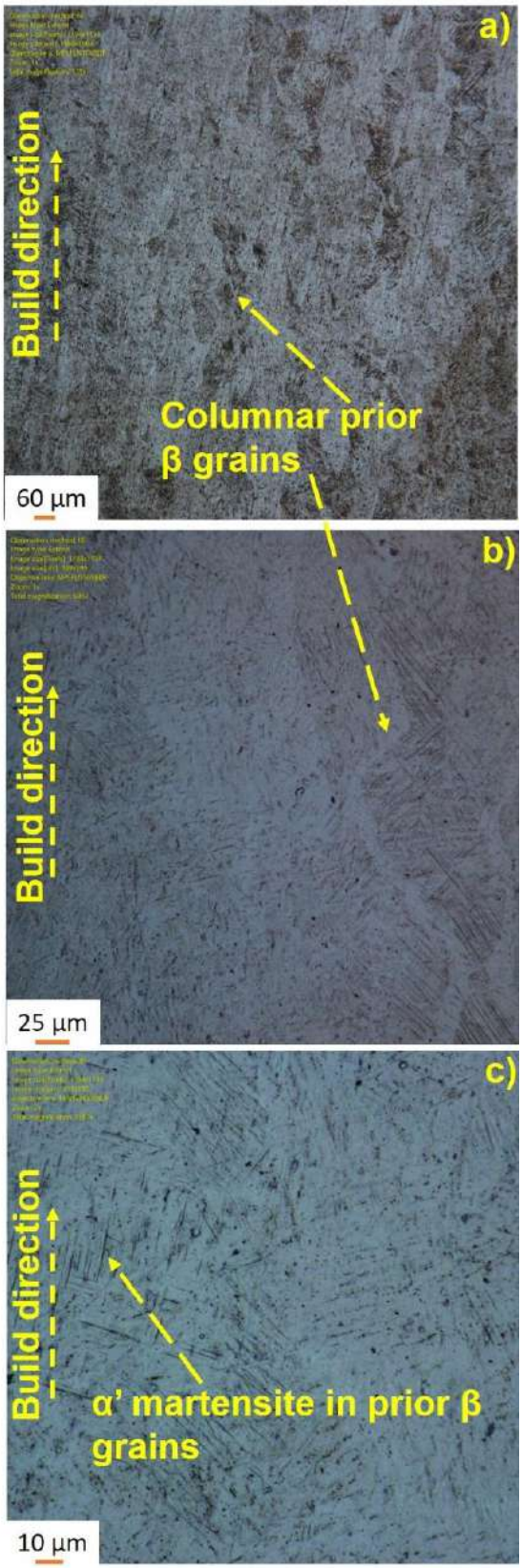

Figure 5. 11: Optical micrographs of the as-printed LPBF-manufactured Ti6Al4V sample in the longitudinal direction (a); higher magnification micrographs (b-c)

During the LPBF process melting and re-melting of the material's layer co-occurs. This event generates a rewarm and cooling behaviour resulting in thermal cycling in both transverse and longitudinal directions in a non-uniform manner. Therefore, it leads to the development of a complex anisotropic microstructure. Moreover, the directional microstructures obtained in different directions (i,e transverse and longitudinal) under the LPBF process create an anisotropy in a material's properties [55]. In addition, the low thermal conductivity of Ti6Al4V (7.2 W/m °C) encourages heat accumulation and is presumed to promote directional microstructure development. Interestingly, the α' martensite phase formed during the LPBF process differs from the α phase content in mill-annealed or forged Ti6Al4V alloy [157]. This anisotropic structure feature shows the burger's relationship between α' and the β phases of the hexagonal lattice [158].

The cross-sections of LPBF-manufactured as-printed samples are characterized by their longitudinal and transverse cross-sections in Figure 5.12(a). As revealed in Figure 5.12(b), the uniform distribution of cellular grains is apparent in the middle section of a laser track. In contrast, elongated β grains are visible perpendicular to the laser moving direction. The various microstructure characteristics can be comprehended in Figure 5.12(b) shows the Gaussian energy distribution induced by the laser source. The Gaussian energy dispersal caused by the laser was responsible for the heat input (Q_v) dissemination in the molten pool, as referred to in equation (5.3) [159].

$$Q_v = \frac{f P_v}{\Pi d^2 h} \exp\left(-3\frac{r^2}{d^2}\right)\left(1-\frac{z}{h}\right) \quad (5.3)$$

Where f is the factor of heat dissemination, P_v is the engrossed laser power, d is the laser ray radius, r is the radial dimension from the centre of the laser source, h is the energy source depth, and z is the current depth in the thickness direction. The heat input decreases exponentially in the transverse plane when the r increases.

The temperature at the centre of a laser track will be higher than the boundaries of the melted regions. It causes the thermal gradients to increase. Therefore, a thermal flux sets at the boundaries due to heat dissipation. The heat dissipation and, thus, cooling rate cause the liquid temperature (T_L) in the melt pool to be lesser than the melting temperature (T_M) in the centre of the melt pool. Therefore, it results in higher undercooling ($\Delta T = T_M - T_L$), leading to the

nucleation of new grains [54]. Thus, the liquid metal will undergo simultaneous nucleation and orient randomly [160].

Further, steady growth rates in all directions of the crystal nucleus make forming a cellular grain structure possible. The columnar β grains are grown in a longitudinal direction perpendicular to the laser movement. It is due to a lesser degree of undercooling defeating the precipitation of new grains. The formation mechanism of such heterogeneous microstructures in LPBF-manufactured material is shown schematically in Figure. 5.12 (b) and (c), which is determined by the thermal gradient (G) and solidification rate (R) ratio. It corroborates with Figure 5.10(a) and 5.11(a). Similar results were also reported by Acharya et al. [161].

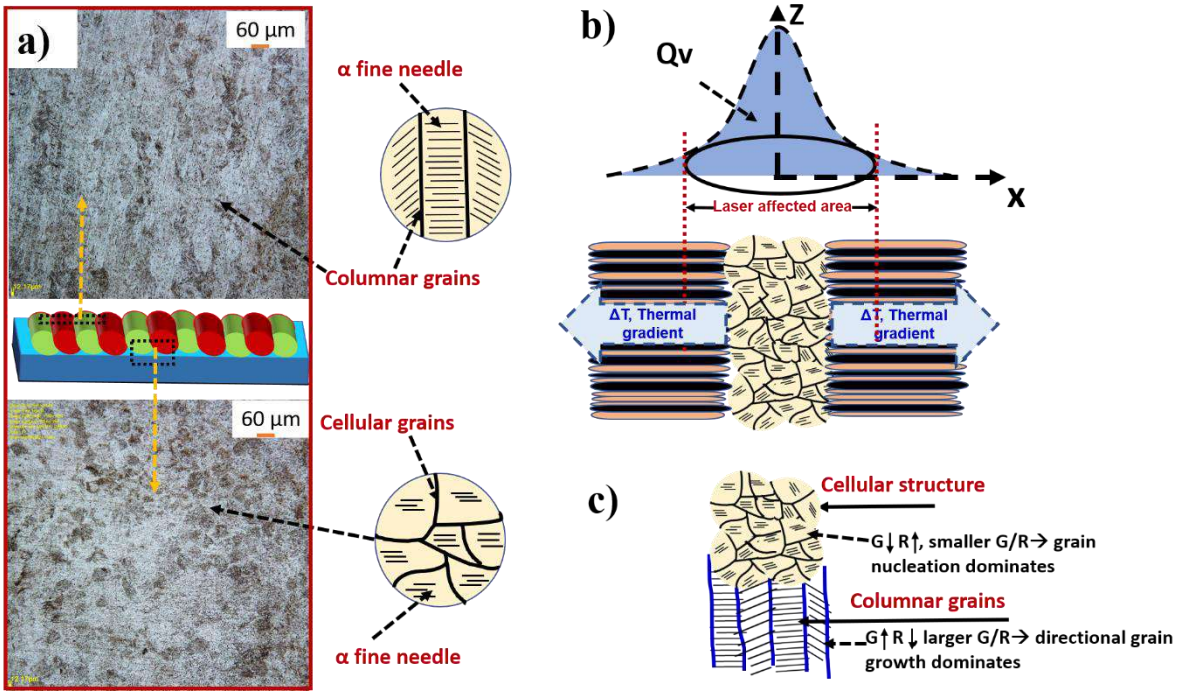

Figure 5. 12: Microstructural evolution of as-printed samples: (a) The characteristic morphologies in the TD and LD; (b) the schematic and formation mechanism of cellular structure; (c) the schematic and formation mechanism of the columnar grains in the microstructure

Figure. 5.13 depicts sample A's micrographs, which underwent PHT at 850 °C for 2 hours and was subjected to air-cooled conditions. Sample A exhibits a decomposition of fine α' into α+β phase in which α phase is visible as fine needles, as shown in Figure. 5.13(a). The columnar β grain boundaries are visible in the longitudinal direction (along the build direction), as shown in Figure. 5.13(b). At 850 °C, the volume fraction of the α phase is high; therefore, the impact of the cooling rate under air cooling is minimal, which corroborates nicely with XRD pattern results (see Figures 5.27 and 5.28). Moreover, the high-volume fraction of the α phase at 850

°C hinders its growth during cooling, and the cooling rate does not affect the microstructure [51]. Therefore, only air cooling is performed for sample A in the present work.

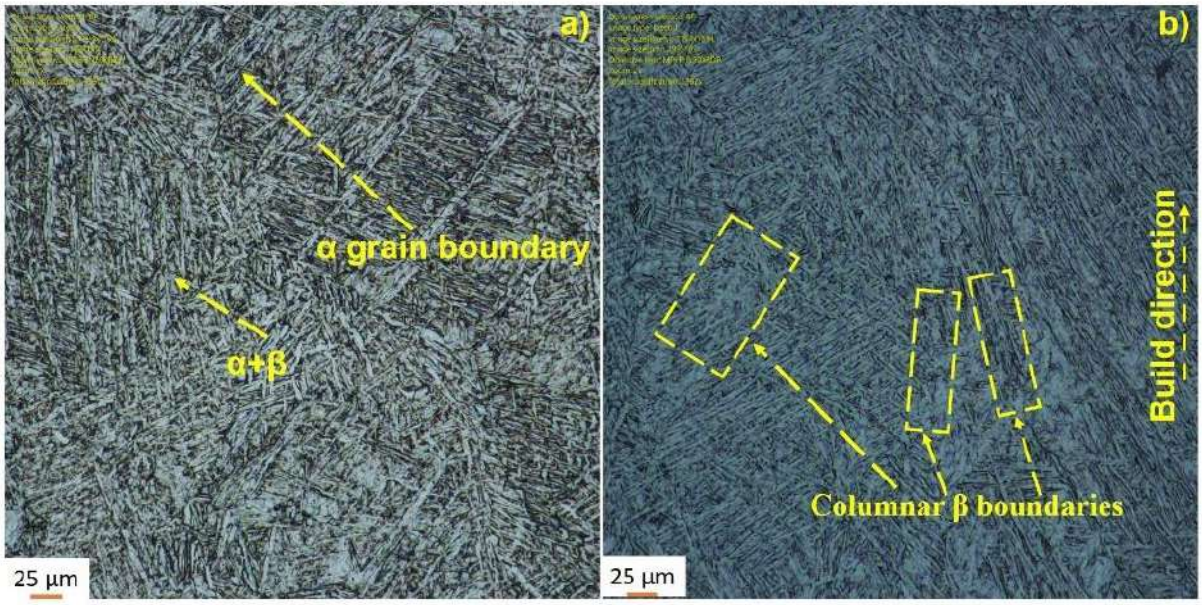

Figure 5. 13: LPBF-manufactured Ti6Al4V sample 'A' a) transverse direction; b) longitudinal direction

Figures. 5.14 and 5.15 reveal microstructures of samples B and C under transverse and longitudinal directions. Figs. 5.14 (a) and (b) depicts the size of α lath due to PHT performed at 950 °C under air and furnace-cooled conditions. Under higher temperatures, the volume fraction of α decreases due to the nucleation of β phase around the β transus temperature [162]. Therefore, PHT performed at 950 °C allows α laths to grow at different cooling rates [61]. A similar microstructural observation was noted for B and C samples in longitudinal directions (see Figures. 5.15 (a) and (b)). It is observed in Figures. 5.14 (a) and 5.15 (a) that the samples heat-treated under air-cooled conditions induce thinner α laths (~3.38 µm in transverse and ~2.85 µm in the longitudinal directions). Further enhanced growth of α laths (~5.56 µm in transverse and ~5.10 µm in the longitudinal direction) due to slow furnace cooling experienced by samples are shown in Figures. 5.14 (b) and 5.15 (b).

In addition, the PHT above β transus temperature is the most crucial parameter, as it decides the size and morphology of the α lath. The PHT performed at 950 °C vanishes the β grain boundaries, and α grains become shorter and slender. Further, PHT at 950 °C in samples B and C reduced the volume fraction of α phase compared to sample A.

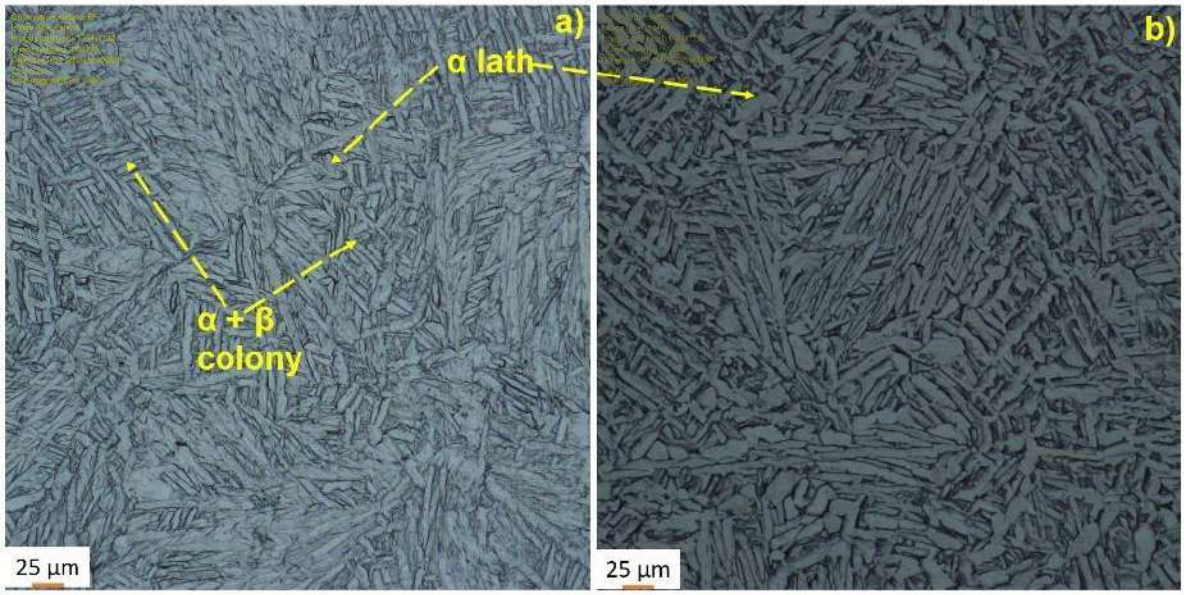

Figure 5. 14: LPBF-manufactured Ti6Al4V samples in the transverse direction; PHT at 950 °C for 2 hours: (a) sample 'C'; (b) sample 'B'

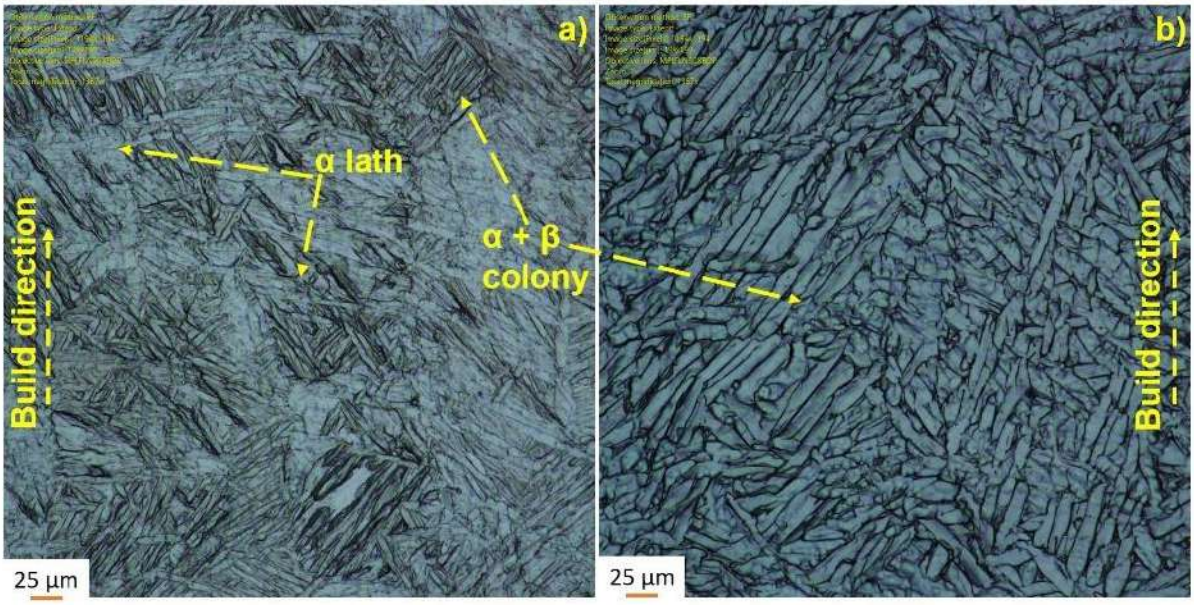

Figure 5. 15: LPBF-manufactured Ti6Al4V samples in the longitudinal direction; PHT at 950 °C for 2 hours: (a) sample 'C'; (b) sample 'B'

Figures. 5.16 and 5.17 illustrate the microstructures of samples D and E under transverse and longitudinal directions. The samples in the transverse direction that underwent PHT at 1050 °C (above β transus temperature) are shown in Figure. 5.16. The extent of grain growth and the tendency for homogeneous microstructural formation is enhanced compared to the other heat-treated samples such as A, B, and C.

The lamellar α + β features are seen in Figure. 5.16 (a) and retained β phases under air-cooled conditions, similar to the casted Ti6Al4V [11]. The β will retain because upon slow cooling from above β transus temperature β will decompose to α+β phase, which is a diffusional transformation [53]. The cooling rates are significantly crucial in deciding the size of the lamellar α+β, which dictates the final property. In addition, coarse β plates with α grain boundaries are observed in Figure. 5.16 (b) under furnace-cooled conditions consistent with EBM and LPBF-manufactured Ti6Al4V [163]. The extent of homogenous microstructure development led to isotropic mechanical properties in the LPBF-manufactured Ti6Al4V samples.

The PHT performed at 1050 °C transforms α' and α into β phases, and different cooling rates determine the microstructural morphology (as seen in Figure. 5.16 and 5.17). Furthermore, it should be noted that the α+β lamellar has grown significantly in furnace-cooled conditions, as shown in Figures. 5.16 (b) and 5.17 (b). However, it is observed that the effect of cooling rate on microstructure below the β transus temperature is insignificant in LPBF-produced Ti6Al4V (see Figure. 5.13). It is because, below β transus temperature, α and β phases hinder each other's growth so no substantial lath growth occurs. In addition, the holding time in PHT also affects the morphology and volume fraction in the material's microstructure. The holding time affects grain growth; therefore, significant growth was reported at a more considerable holding time [51]. A comprehensive microstructural evolution in different heat-treated LPBF-manufactured Ti6Al4V samples is shown in Figure. 5.18.

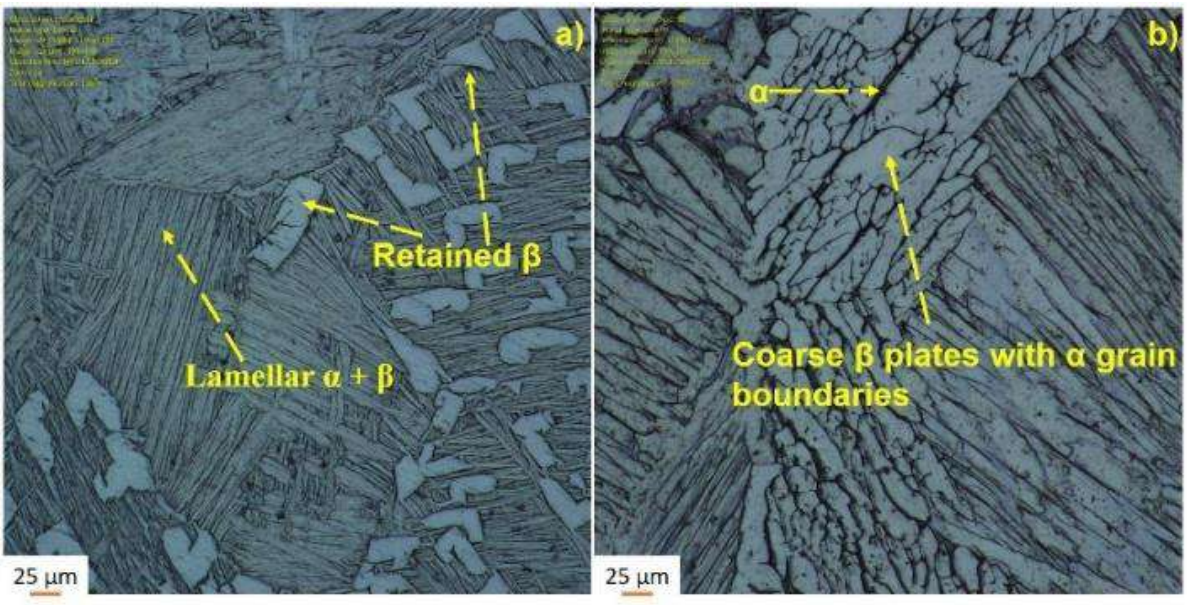

Figure 5. 16: LPBF-manufactured Ti6Al4V PHT samples in the transverse direction at 1050 °C for 2 hours: (a) sample 'E'; (b) sample 'D'

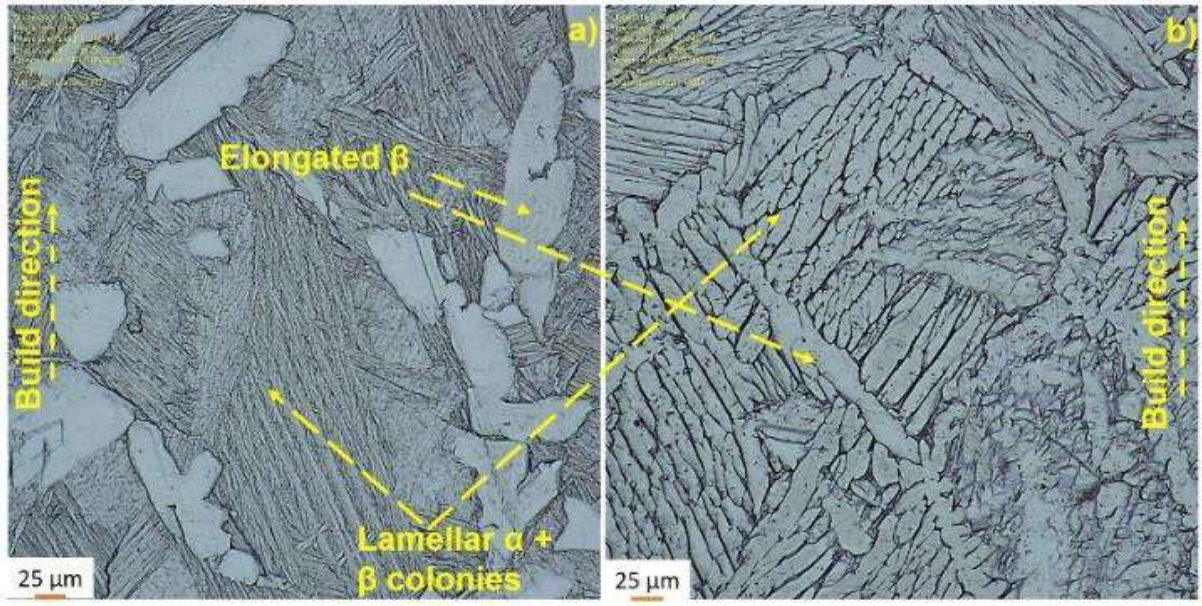

Figure 5. 17: LPBF-manufactured Ti6Al4V PHT samples in the longitudinal direction at 1050 °C for 2 hours: (a) sample 'E'; (b) sample 'D'

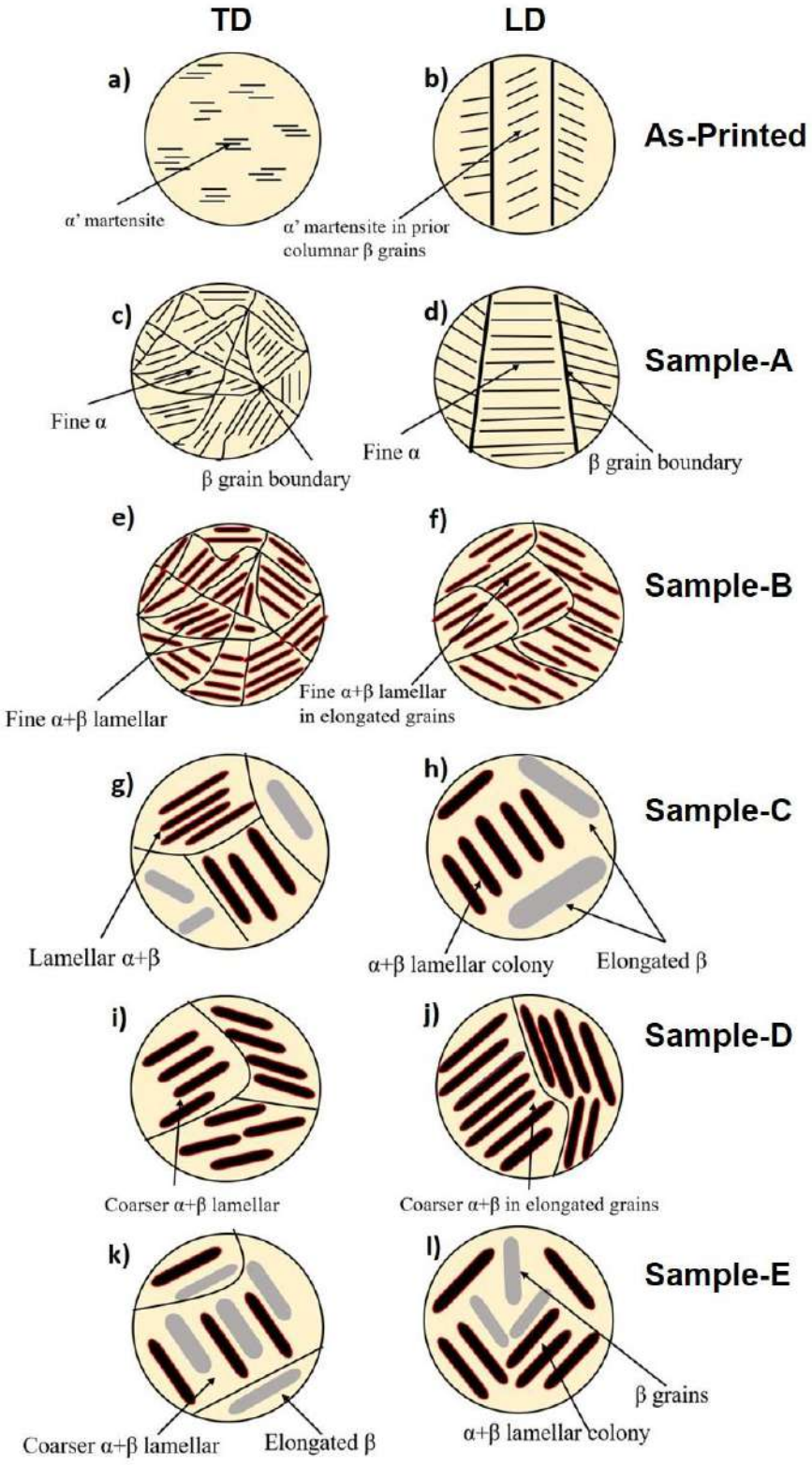

Figure 5. 18: Microstructure evolution: a) As-printed sample in TD; b) As-printed sample in LD; c) sample 'A' in TD; d) sample 'A' in LD; e) sample 'B' in TD; f) sample 'B' in LD; g) sample 'C' in TD; h) sample 'C' in LD; i) sample 'D' in TD; j) sample 'D' in LD; k)

(TD: Transverse direction; LD: Longitudinal direction)

The samples in as-printed conditions in both transverse and longitudinal directions were examined using SEM. It was confirmed through optical microstructures that heat-treated samples possess similar microstructures in both directions. Therefore, the heat-treated samples were analyzed in one direction only using SEM, shown in Figure 5.19 (c-g). It is important to note that similar features are observed in the SEM microstructures as were in the optical microstructures. The microstructure in Figure 5.19 (a) exhibits the cellular type of β grains containing α' martensite of fine needles in the transverse direction. A similar observation could be seen in the LPBF-manufactured Ti6Al4V study [164]. Further, the microstructure in Figure 5.19 (b) shows the columnar prior β grains parallel to the build direction due to the epitaxial grain growth in the longitudinal direction. Comparable microstructural features for LPBF-manufactured Ti6Al4V are reported in [165].

The samples subjected to PHT show significant morphological changes in the microstructures due to the transformation of α' to α, lamellar α+β, and retained β (Figure 5.19 (c-g). These features agree with the works of literature on EBM and LPBF-manufactured Ti6Al4V [163].

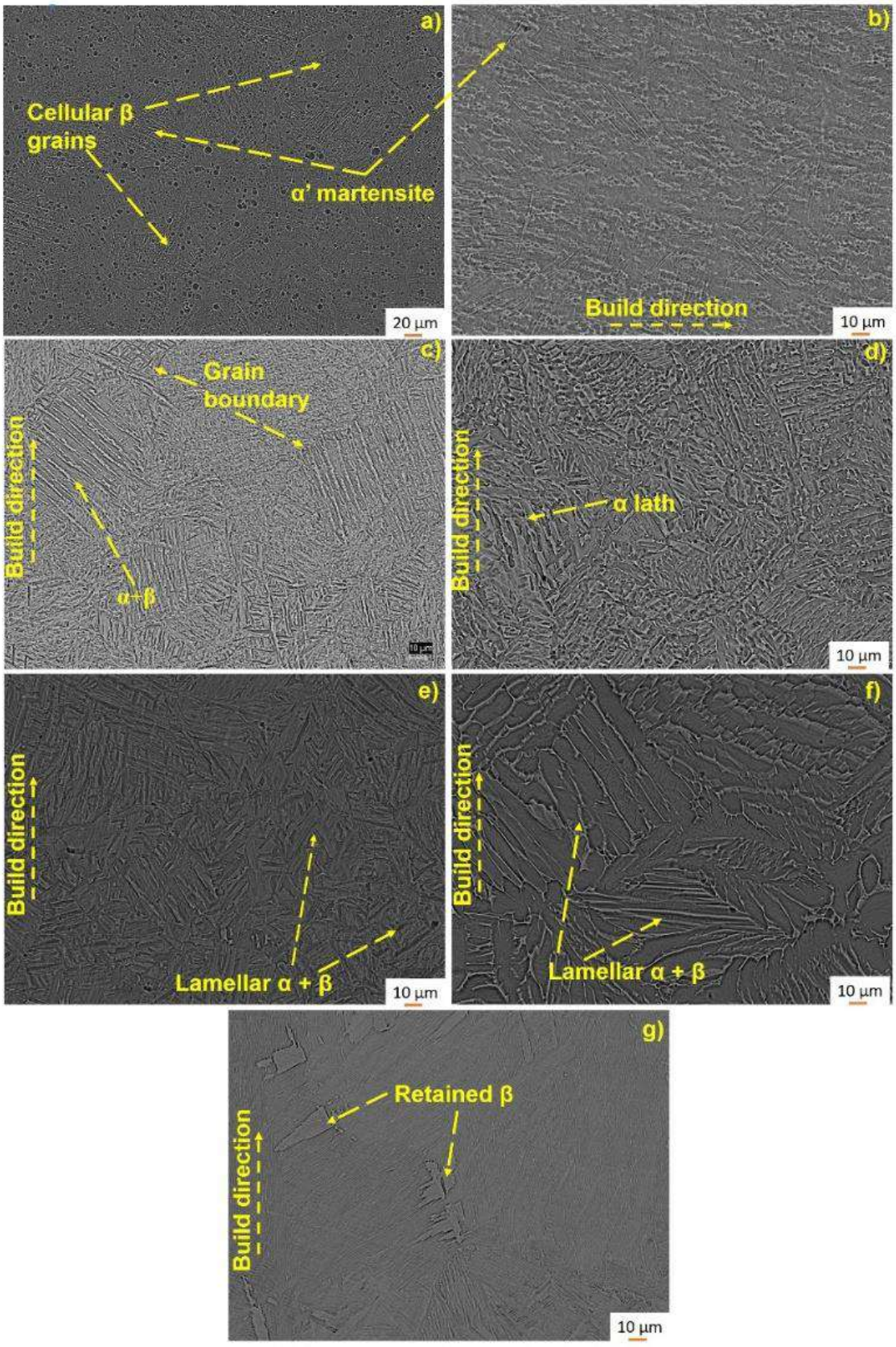

Figure 5. 19: SEM images of LPBF-manufactured Ti6Al4V as-printed samples: (a) TD; (b) LD; and PHT samples: (c) sample 'A'; (d) sample 'B'; (e) sample 'C'; (f) sample 'D'; (g) sample 'E'

The LPBF-manufactured Ti6Al4V samples are characterized using the EDS technique to evaluate the chemical composition at different conditions (Figures. 5.20-5.23). The results of the experiments indicate that the chemical composition of Ti6Al4V remains the same under different PHT conditions. Hence, it could be inferred that the corresponding mechanical properties are preserved, and other researchers reported similar observations for EBM and LPBF-manufactured Ti6Al4V [166].

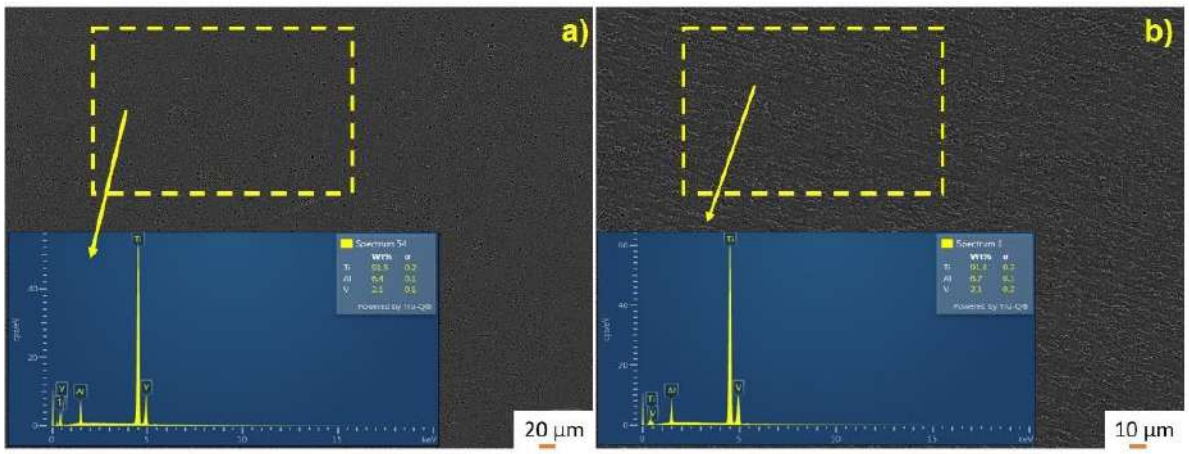

Figure 5. 20: SEM-EDS of LPBF-manufactured Ti6Al4V as-printed samples: (a) transverse direction; (b) longitudinal direction

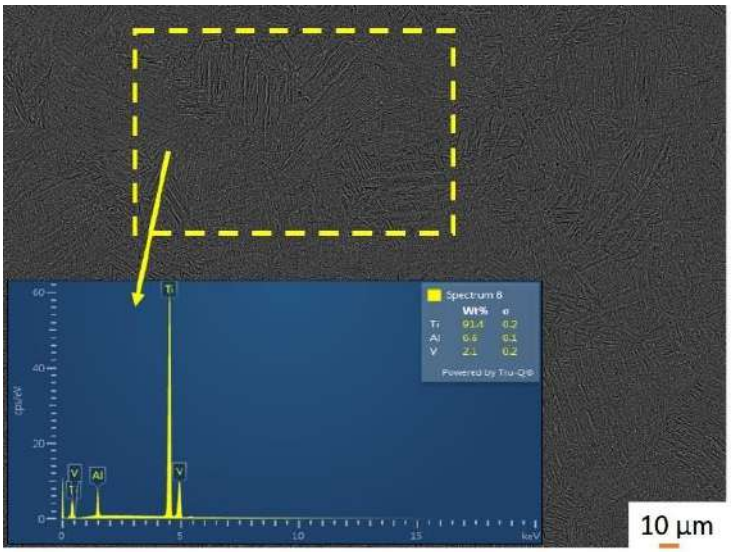

Figure 5. 21: SEM-EDS of LPBF-manufactured sample 'A'

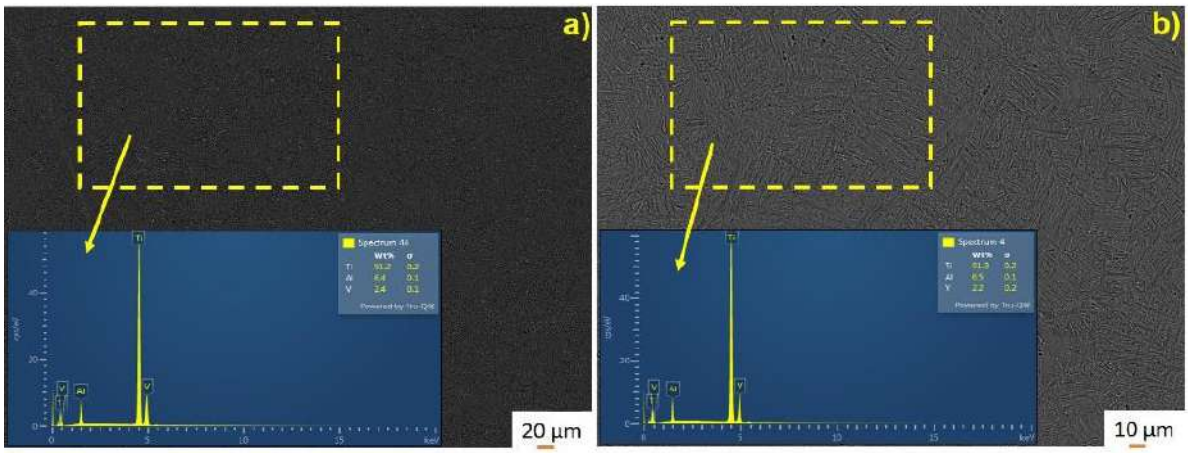

Figure 5. 22: SEM-EDS LPBF-manufactured Ti6Al4V subjected to PHTs: (a) sample 'B'; (b) sample 'C'

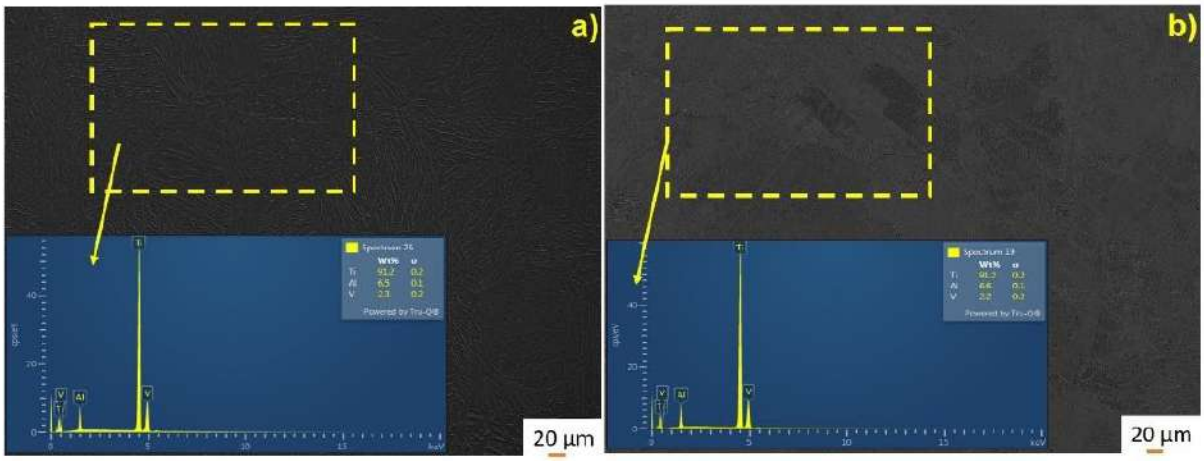

Figure 5. 23: SEM-EDS of LPBF-manufactured Ti6Al4V subjected to PHTs: (a) sample 'D'; (b) sample 'E'

5.2.2 Influence of PHTs cooling conditions on α and β lath thicknesses

Figures. 5.24 and 5.25 show the PHT influence on the α lath growth behaviour in the transverse and longitudinal directions. The width of α lath is lesser under air-cooled samples than in furnace-cooled samples. However, the slow cooling rate in furnace-cooled conditions allows α lath to grow substantially in transverse and longitudinal directions than in air-cooled conditions (see Figures. 5.24 and 5.25). Further, upon cooling above β transus temperature, the cooling rate was a crucial factor that decides the phase's morphology and size (refer to Figures. 5.16 and 5.17) in both directions. It is well established that the α lath size is a significant factor that dictates the mechanical properties of lamellar Ti6Al4V α+β alloy. As the α lath size decreases, the yield stress, percentage of elongation, and crack initiation and propagation resistance are significantly enhanced [92].

Also, with an increase in PHT temperature, almost a linear trend in the growth of α lath width under air-cooled samples in transverse and longitudinal directions is observed in Figures. 5.24 and 5.25. Interestingly, a strong correlation exists with the increase of α lath width and different PHT temperatures employed.

It is reported by Zhang et al. [61] that the increase in α lath width with the rise in PHT temperature is owing to the lesser volume fraction of the α phase at high temperatures (23 % at 950 °C compared to 73 % at 850 °C) [61]. The higher the volume fraction of α phases, the more obstruction for α lath growth from each other. Hence α laths grow effortlessly due to a lesser amount α phase hindrance and thus become coarser. Therefore, it is presumed that a similar α lath growth behaviour would have operated in the heat-treated LPBF-manufactured Ti6Al4V under higher PHT temperatures. However, detailed microscopic investigations are required to confirm this. It is essential to emphasize that no lath growth occurs for sample 'A' heat treatment performed at 850°C with different cooling rates. At low temperatures, α and β phases obstruct each other, limiting the lath growth [51]. Therefore, the present study's sample A, heat-treated at 850 °C, was air-cooled. It is interesting to note that the α lath grows (~ two times) in air-cooled conditions from 2.3 μm at 850 °C to 4.30 μm at 1050 °C in the transverse direction. Further, α lath grows from 2.4 μm at 850 °C to 4.20 μm at 1050 °C in the longitudinal direction.

It signifies no appreciable difference in α lath width in both directions under air-cooled conditions, suggesting that the microstructure is transforming to its isotropic nature. Further, it could be corroborated with microstructures of samples A, C, and E in Figures. 5.13, 5.14 (a), 5.15 (a), 5.16 (a), and 5.17 (a).

Under the furnace-cooled condition, the α lath width is 5.56 μm at 950 °C and 7.92 μm at 1050 °C in the transverse direction and 5.10 μm at 950 °C and 12.59 μm at 1050 °C in the longitudinal direction, respectively, which can be correlated with microstructures of samples B and D in Figures. (5.14b), (5.15b), (5.16b) and (5.17b). Interestingly, the α lath width varies drastically from transverse to longitudinal direction, which could be attributed to the large colony size of α in columnar grains exhibiting higher length and width [167]. Furthermore, the fracture toughness and macro-crack propagation resistance increase with a thicker/larger α lath size because of the crack-closure effect and higher crack roughness [92].

The PHT, carried out at 1050 °C above β transus temperature, transforms α' martensite into a fully β phase and subsequently, after air and furnace cooling, α lath grows in the retained β phase. The volume fraction and lath width of β phases were found to be higher under PHT performed at 1050 °C, and the α+β lamellar and retained β phases were present in both transverse and longitudinal directions under air and furnace cooled conditions.

The sample heat-treated at 1050 °C grows extensively, and further, the slow cooling rate in the furnace gives time for β lamellae to grow. The samples heat-treated at 1050 °C above β transus temperature do not show any prior β columnar grains. Subsequently, the width of β lamella above β transus temperature for sample D is ~ 19.30 μm in the transverse, and ~ 26.95 μm in the longitudinal direction. Whereas for sample E, it is ~ 9.65 μm in the transverse direction and ~ 17.59 μm in the longitudinal direction, which signifies that β grows enormously at a high temperature of 1050 °C.

It is observed that the feature size of the lamellar structure is more sensitive to the heating temperature and cooling rates. In air cooling, the thin α width is obtained for all the heat-treated samples subjected to PHT, favouring the higher hardness of LPBF parts. Therefore, the marginal improvement in micro-hardness was observed in air-cooled samples rather than the furnace-cooled (see section 5.2.4 micro-hardness). Moreover, samples D and E heat-treated above β transus also exhibit higher hardness than as-printed samples. Given the above, it could be understood that the air cooling favours in generating desirable thinner widths of α and β laths achieving the higher hardness and strength of LPBF-manufactured parts.

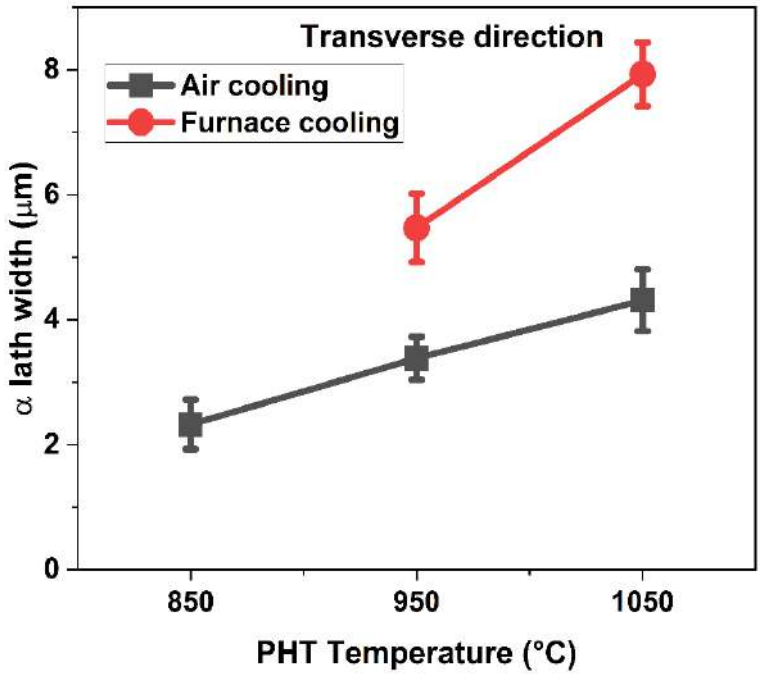

Figure 5. 24: α lath width thickness in the transverse direction

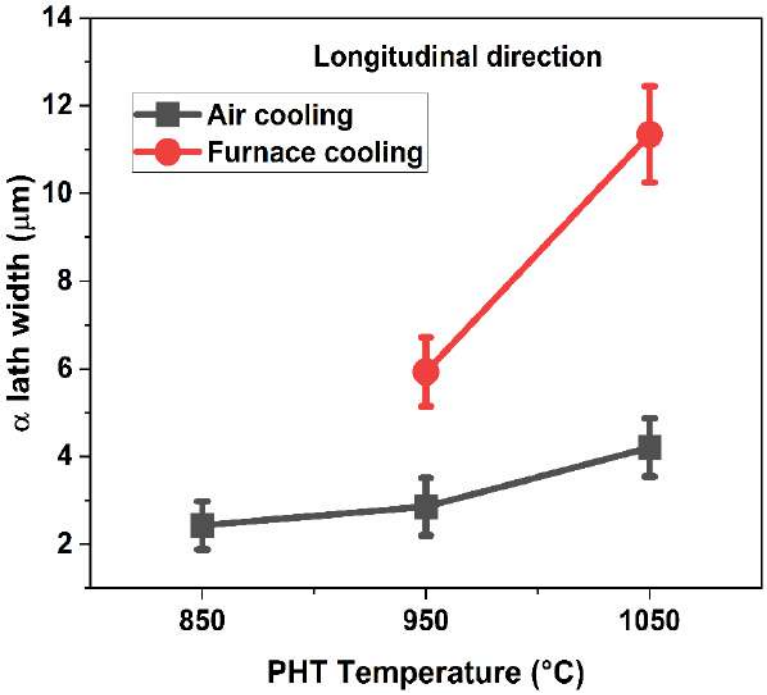

Figure 5. 25: α lath width thickness in the longitudinal direction

It is well established that as the thickness of α lath decreases, the resistance to long plastic slip bands increases, leading to higher resistance in fatigue crack initiation. Therefore, the lath size of α also significantly impacts defining the mechanical properties [10]. The correlation between the PHT temperature and the α lath width shows a strong connection, as shown in Figure. 5.26

[51, 52, 94, 118, 168, 169]. It is important to note that the cooling rate also plays a substantial role in deciding the α lath width and the PHT temperature. The growth of α lath at below 850°C was moderate but increased significantly at higher temperatures.

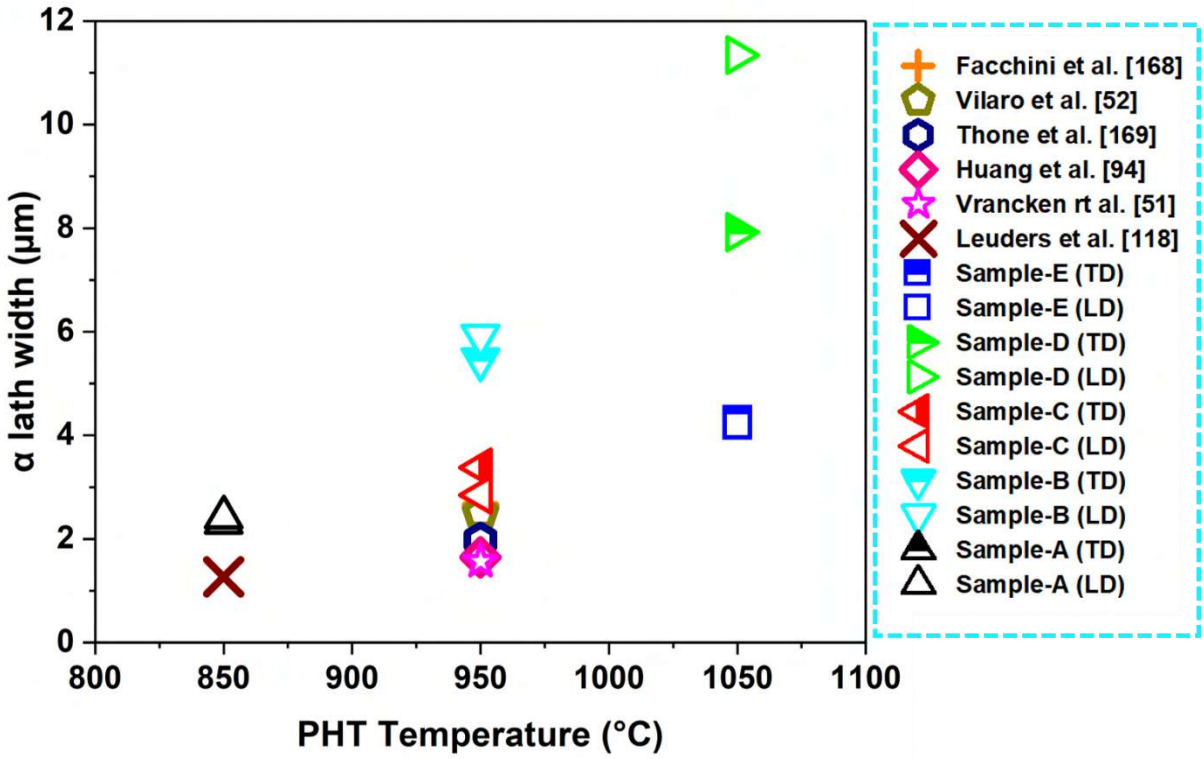

Figure 5. 26: α lath sizes of LPBF-manufactured Ti6Al4V alloy subjected to PHT at different PHT temperatures

5.2.3 X-ray Diffraction Characterization

5.2.3.1 Phase characterization and analysis

The XRD pattern of the as-printed LPBF-manufactured Ti6Al4V and PHT samples in transverse and longitudinal directions are shown in Figures. 5.27(a) and 5.28(a). It is evident that in as-printed LPBF-manufactured Ti6Al4V, due to fast cooling, there is a formation of α' martensite, which possesses the HCP crystal structure and an absence of the β phase as seen in Figures. 5.10 and 5.11. However, after PHT, the α' transforms to α+β, and a tiny β phase peak is reflected due to less content corresponding to the (110) plane in the heat-treated samples at 1050 °C and 950 °C.

Figures. 5.27(b) and 5.28(b) shows the detailed XRD pattern between 2θ = 33° to 42°. It is noted that the HCP α phase peaks are shifting towards the lower angles predominantly in the

transverse direction samples due to the transformation experienced by α' martensite to (α+β) equilibrium phases [62, 170].

Moreover, Figure. 5.29 shows the full-width half maximum (FWHM) of as-printed and PHT-executed sample extracted from XRD plots at around 2θ~40.2°. It is apparent from Figure 5.29 that as-printed samples show high FWHM values in both transverse and longitudinal directions owing to the residual stresses present in them. In contrast, PHT-executed samples showed less FHWM resulting from residual stresses relieved at high temperatures [140].

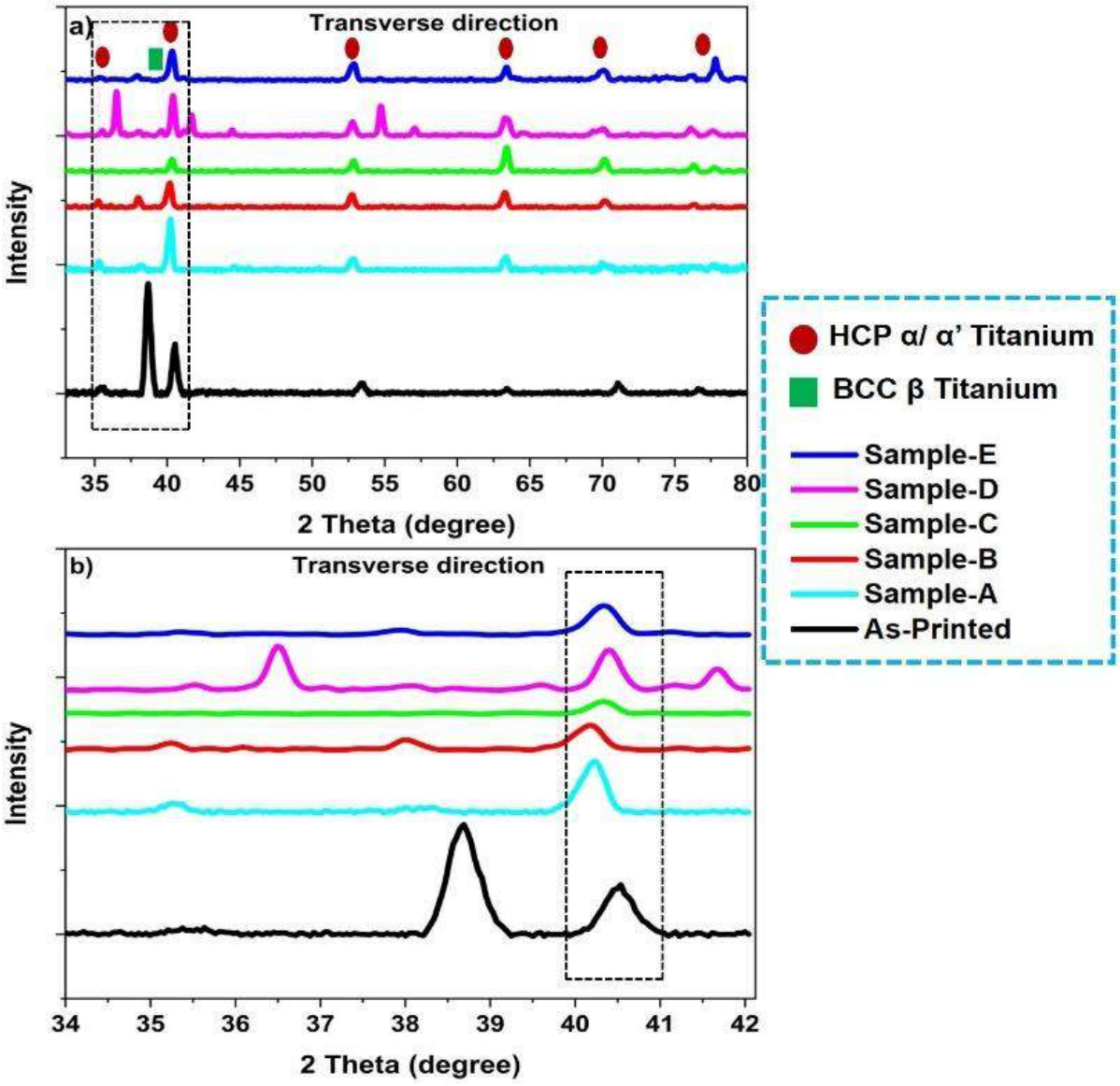

Figure 5. 27: XRD pattern of LPBF-manufactured Ti6Al4V in the transverse direction: (a) a wide range of 2θ; (b) details between 2θ = 33°- 42°

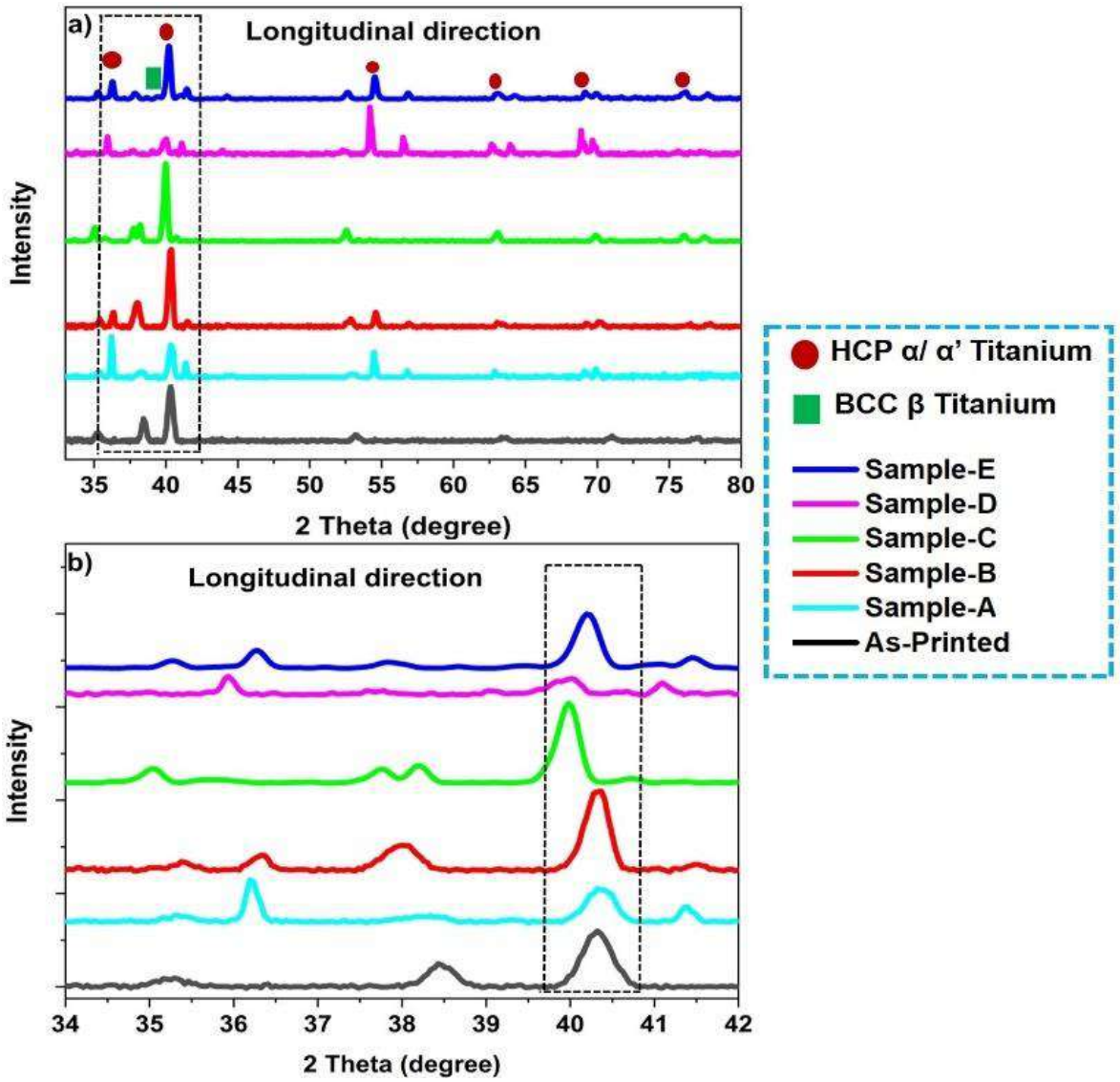

Figure 5. 28: XRD pattern of LPBF-manufactured Ti6Al4V in the longitudinal direction: (a) a wide range of 2θ; (b) details between 2θ = 33°- 42°

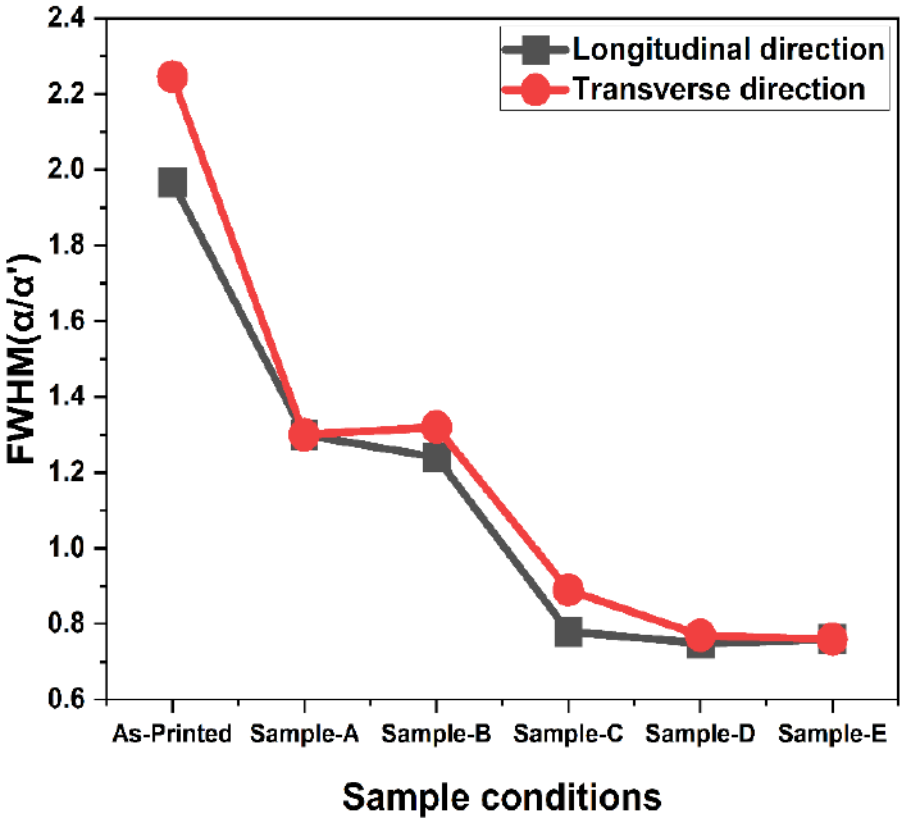

Figure 5. 29: Relationship between FWHM values and LPBF-manufactured Ti6Al4V samples in different conditions

5.2.3.2 Basal plane characterization

The higher intensity of the peak corresponding to the 2θ signifies the strong texture of crystallographic planes. Figures. 5.30 and 5.31 show the higher intensity of α phase (101) peaks, indicating the significant texture of α phase in all as-printed and PHT samples.

The (0001) basal plane exhibited a higher atomic packing density and was termed a closed pack plane (CPP) in the HCP crystal structure. It is well established that the CPPs are more amenable to plastic deformation under mechanical loads [171]. The intensities corresponding to the (002) CPPs are shown in transverse and longitudinal directions (Figures. 5.30 and 5.31). It is observed that samples D and E have CPP peak intensities significantly lesser than samples A, B, and C in both transverse and longitudinal directions. The effect of intensities of CPPs on the micro-hardness of the LPBF-manufactured Ti6Al4V samples at different heat-treated conditions is discussed in detail in section 5.2.4.

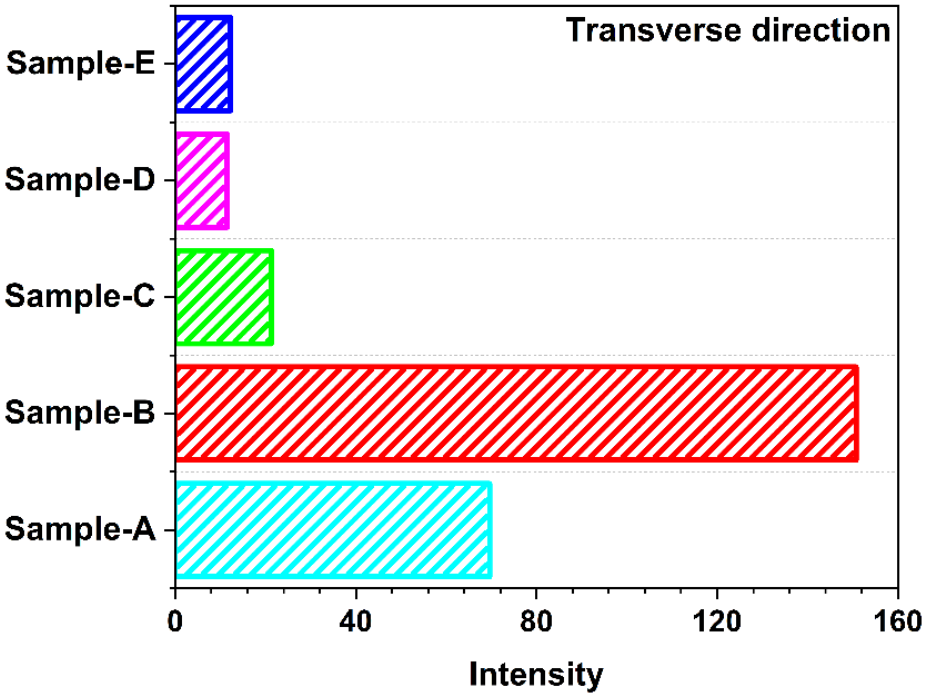

Figure 5. 30: Intensities of (002) CPP under different PHT conditions in the transverse direction

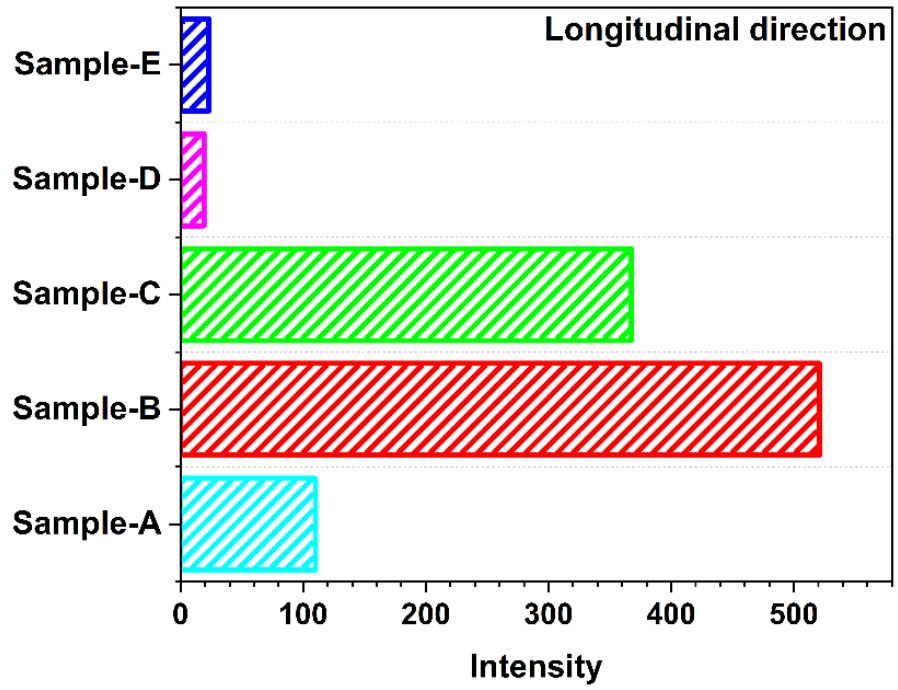

Figure 5. 31: Intensities of (002) CPP under different PHT conditions in the longitudinal direction

5.2.3.3 Characterization of volume fractions of α and β phases

Figures 5.27 and 5.28 show phases of α and β peaks were used for phase volume fraction quantification. The weak β phase peak was obtained in the XRD pattern due to a lesser amount,

as shown in Figure 5.27(b) and 5.28(b). However, a tiny peak of the β phase is observed in samples 'B', 'C', 'D', and 'E', used to quantify the volume fraction of α and β phases using equation (5.4) proposed by Pedersen et al. [172]. The relative integrated intensities of α and β peaks are estimated using equation (5.4):

$$\mathbf{R = F^2 \times p \times \frac{1}{v^2} \times \left(\frac{1+\cos^2 2\theta}{\sin^2\theta \times \cos\theta}\right) \times \exp^{-2m}} \quad (5.4)$$

where F^2 is the structure factor that describes the effect of crystal structure, P is a multiplicity factor that describes the number of family of planes contributing to reflection, v is the volume of a unit cell, Lorentz polarization factor is used in the term parenthesis and $\exp^{-2m}$ is the temperature factor [173]. In the present work, the integrated intensity of the β phase is represented by the ratio ($R = \frac{R_\alpha}{R_\beta}$) at an angle around ($2\theta = 39$) is 1.4 times stronger than α phase intensity at an angle around ($2\theta = 40$). Therefore, the corrected β phase intensity to estimate the phase fraction is represented by equation (5.5)

$$\mathbf{I_{\beta c} = \frac{I_\beta}{A}} \quad (5.5)$$

$V_{\alpha c}$ and $V_{\beta c}$ are the corrected phase volume fractions of α and β, respectively, as shown in equations (5.6) and (5.7)

$$\mathbf{V_{\alpha c} = \left(\frac{I_\alpha}{I_\alpha + I_{\beta c}}\right)} \quad (5.6)$$

$$\mathbf{V_{\beta c} = I - V_{\alpha c}} \quad (5.7)$$

The volume fractions of α and β phases are shown in Figures. 5.32 and 5.33 in both transverse and longitudinal directions. The β phase volume fraction ($V_{\beta c}$) is higher at 1050 °C for samples D and E compared to 950 °C for samples B and C. It correlates well with the microstructures observed in Figures 5.16 and 5.17, where retained β phase is present along with α+β lamellar microstructure.

The size of the α lath also dictates the fatigue resistance. The fine α laths obtained during the air-cooled condition (Figures 5.24 and 5.25) exhibit higher resistance to crack initiation due to long plastic slip band increases in finer microstructure [174]. Moreover, the coarser α lath

attained during the furnace cooling enhances the crack propagation resistance due to the disorientation of the cracks [175].

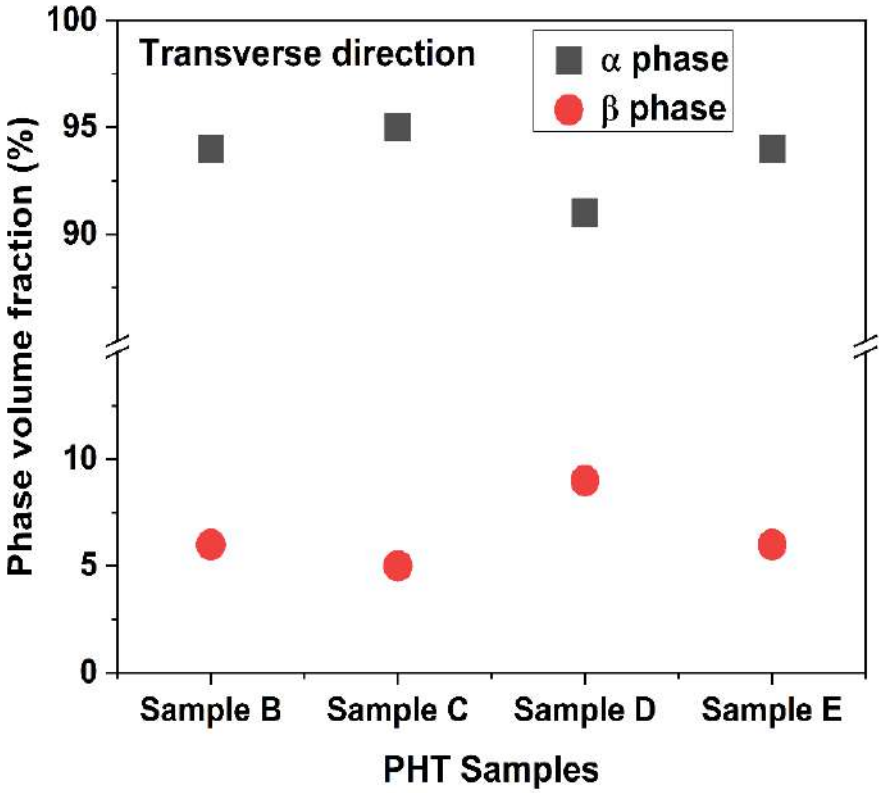

Figure 5. 32: Volume fraction of phases α and β in the transverse direction

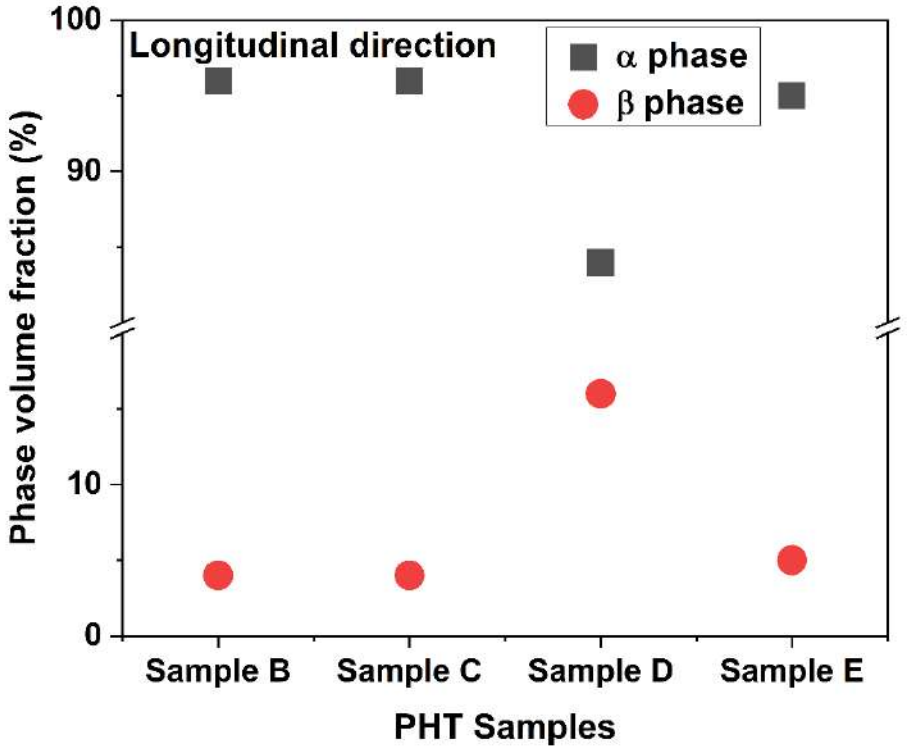

Figure 5. 33: Volume fraction of phases α and β in the longitudinal direction

5.2.4 Micro-hardness Characterisation

The micro-hardness of the as-printed LPBF-manufactured Ti6Al4V and PHT samples are shown in Table 5.3 for transverse and longitudinal directions. It is evident that the PHT strongly influences the micro-hardness of LPBF-manufactured Ti6Al4V samples.

The micro-hardness of the as-printed LPBF-manufactured Ti6Al4V samples were 362±9.9 $HV_{0.5}$ and 378±7.1 $HV_{0.5}$ in both transverse and longitudinal directions. The difference in hardness values between transverse and longitudinal are attributed to the anisotropic microstructure obtained in the LPBF process (see Figures 5.10 and 5.11). The higher hardness of the as-printed sample is due to the fine α' martensite, which possesses a high density of dislocations [176]. Moreover, during the LPBF process, the residual stresses occur due to the high cooling rates, which exhibit a high hardness value [120]. The PHT samples under temperatures of 850 °C and 950 °C show a reduction in hardness value (for sample A – 10% reduction, sample B – 14% reduction, sample C – 13% reduction in the transverse direction and sample A – 14%, sample B – 16% and sample C – 15% reduction in longitudinal direction compare to as-printed samples) significantly due to coarsening of the grains, which corroborates well with micrographs in Figures. 5.13, 5.14 and 5.15. As a consequence of PHT

under elevated temperatures, the grain size increases, due to which the strength of the material decreases owing to the Hall-Petch relation [155]. The martensitic α' exhibits a higher hardness due to high dislocation density than the α phase obtained after conversion of α' martensite under PHT.

Also, the α phase volume fraction is higher in PHT conditions performed under 850 °C and 950 °C, which is evident from the obtained XRD pattern (see Figures.5.27 and 5.28). Furthermore, it is interesting to note that samples D and E, heat treated at super β transus temperature (1050°C), have shown higher hardness among other PHT-performed samples.

However, the micro-hardness of samples D and E was marginally low (Sample D- 7% and Sample E- 9%) compared to as-printed samples in the transverse direction. Moreover, the reduction in microhardness for sample D was about ~14%, and E was about ~9% for sample E compared to as-printed samples in the longitudinal direction.

During the mechanical load applications on the LPBF-manufactured Ti6Al4V sample, the dislocations are piled up at the α lamellae and retained β phase interface causing the stress field, which is considered a reason for the higher strength [177]. The large β grains formed during the PHT under 1050 °C resist the plastic deformation and provide higher hardness for LPBF parts.

Further, samples D and E had higher hardness among PHT samples due to the development of the α-Widmanstatten (lamellar) microstructure. The slip length in α layers on β grain boundaries will be restricted during the application of mechanical loads [60, 178]. The micro-hardness of sample ‘A’ is relatively higher than sample ‘B’. It could be attributed to the fine microstructure of sample A with α/α' present in α+β phase as seen in Figure. 5.13(a), which hinders the dislocation movement compared to sample B having the coarser α and β laths. The slow cooling rates under furnace cooling provide ample time for the different phases to grow, due to which the coarsening of grains is promoted.

In addition, the increase of microhardness values in samples D and E is due to the lesser availability of the CPPs in the HCP crystal structure. The XRD patterns in Figures 5.27 and 5.28 showed the CPPs (0002) of α phase intensities at ~ 38 ° for different PHT samples. The ease of slip and plastic deformation are favourable in CPPs since the CPPs will have a higher atomic density. Therefore, lesser strain energy is sufficient to initiate the slip mechanism [171].

Figures 5.30 and 5.31 show the intensities of ~ 38° for the CPP of the α phase (002). Samples D and E show lower intensity values, indicating that the sample PHT above β transus temperature has limited CPPs. Therefore, the micro-hardness values of samples D and E are higher, which can be attributed to the less resistance to deformation during mechanical load applications.

Table 5. 3: Microhardness of as-printed and PHT subjected Ti6Al4V samples in transverse and longitudinal directions

Sample Conditions	**Vicker's microhardness ($HV_{0.5}$)**	
	Transverse direction	**Longitudinal direction**
As-Printed	362.00±9.9	378.00±7.1
Sample A	328.40± 6.3	325.00±6.5
Sample B	312.10±32	318.00±2.4
Sample C	318.00± 9.4	321.00±8.9
Sample D	332.00±4.2	331.00±3
Sample E	338.00±7.5	348.00±6.6

5.2.4.1 Effect of α lath thickness on micro-hardness

A thin α lath width is responsible for a material's high hardness and strength in the case of Ti6Al4V. More barriers for moving dislocations will be there as α lath width will decrease, and high dislocation densities around fine α lath will enhance the micro-hardness of the material. However, samples D and E behave differently when above β transus temperature. The β content is higher in samples heat-treated at 1050°C, and there is extensive growth of α lath thickness

at high temperatures. Interestingly, intense slip bands are formed upon mechanical loading in the α phase [179]. The slip length in α laths on β grain boundaries will be restricted[60].

This instructive result endorses that PHT at above β transus temperature (1050 °C) under air cooling conditions is well suited for LPBF parts with complex and intricate thick and thin sections enabling superior and isotropic mechanical properties i,e, without part distortion during PHTs. Cooling rates under air cooling conditions are expected to offer parts (with distinct thick + thin sections) to undergo uniform and homogeneous microstructural development resulting in better functional properties. Therefore, during practical applications, air cooling conditions may be preferred over furnace cooling for distinctive parts made from material with low thermal conductivity, such as Ti6Al4V (7.2 W/m °C) employed in the present work.

5.3 Influence of PHT with super β transus temperature on the densification behaviour of LPBF manufactured Ti6Al4V

The representative image of porosity using SEM in an as-printed sample in a horizontal direction is shown in Figure 5.34. However, optical microscopy is used to obtain detailed analysis of porosities in as-printed and Sample E conditions in both horizontal and vertical directions.

The optical micrographs of as-printed LPBF manufactured Ti6Al4V samples in horizontal and vertical built conditions are shown in Figures. 5.35 and 5.36, respectively. The inter-micropores can be observed (Figures 5.35-5.38), attributed to the argon gas entrapment during the LPBF process[64]. Moreover, the irregular shape of super-micropore porosities (Figures 5.35-5.38) found in the micrographs could be due to the lack of fusion. The optical micrographs of Sample E Ti6Al4V samples in horizontal and vertical directions are shown in Figures 5.37 and 5.38, respectively. The microscopic images reveal that the inter-micropores are merged due to PHT and reduces the porosities. Therefore, inter-micropores were less noticeable in both horizontal and vertical directions under Sample E than in the as-printed condition.

The energy density for fabricating horizontal and vertically oriented samples was used around (45-113) J/mm^3. In the present work, the average porosity evaluated for as-printed samples using an optical microscope (OM). The purpose of Figure 5.39 is to validate the present work's

OM technique used to measure the average porosity against the as-printed condition with that of the reported average porosity values using OM technique for as-printed Ti6Al4V samples processed by LPBF[180] and DED[181]. In the present work, average porosity values were found to be ~0.06% and ~0.07% in horizontal and vertical orientations, respectively. The as-printed sample pores of less than 10μm were observed to be ~85% in the horizontal and ~83% in the vertical orientations. In a study conducted by Promoppatum et al.[180], they found through OM technique that the average porosity was about ~0.04% in as-printed Ti6Al4V processed by LPBF technology. In addition, the average porosity of DED-Laser processed Ti6Al4V was about ~0.04% using the OM technique[181]. The evaluated average porosities values of different AM techniques are of comparable magnitude with the current work's average porosity values (see Figure 5.39).

The measured average porosity values for LPBF-processed Ti6Al4V samples for as-printed and sample E under horizontal and vertical directions are shown in Figure 5.40. It is evident from the obtained results that the porosity values under samples E were reduced two times than as-printed samples. The goal of Figure 5.41 is to show the independent quantification of inter micro pores (<10μm) and super micropores (>10μm). The desirable target is to achieve the higher densification of the part and least average porosity (inter micro pores + super micropores) after PHT executed for sample E as depicted in Figure 5.41. Furthermore, the porosity values are high for samples built under a vertical direction. Interestingly, inter-micropores are still present in the samples E, as shown in Figure 5.41 (a and b). The distribution of the number of pores, inter-micropores, and super-micropores are represented through a box chart in horizontal and vertical directions, as shown in Figure 5.42 (a and b), respectively.

The reduction in super-micropores may be attributed to the size decline of super-micropores to transform them into inter-micropores after PHT (see Figures 5.37 and 5.38). The super-micropores observed in the as-printed samples were significant, whereas some of the super-micropores transformed into the inter-micropores in samples E. Moreover, the inter-micropores merged due to the sintering phenomenon at high temperatures and reduced micropores in the samples E (see Figures 5.37 and 5.38).

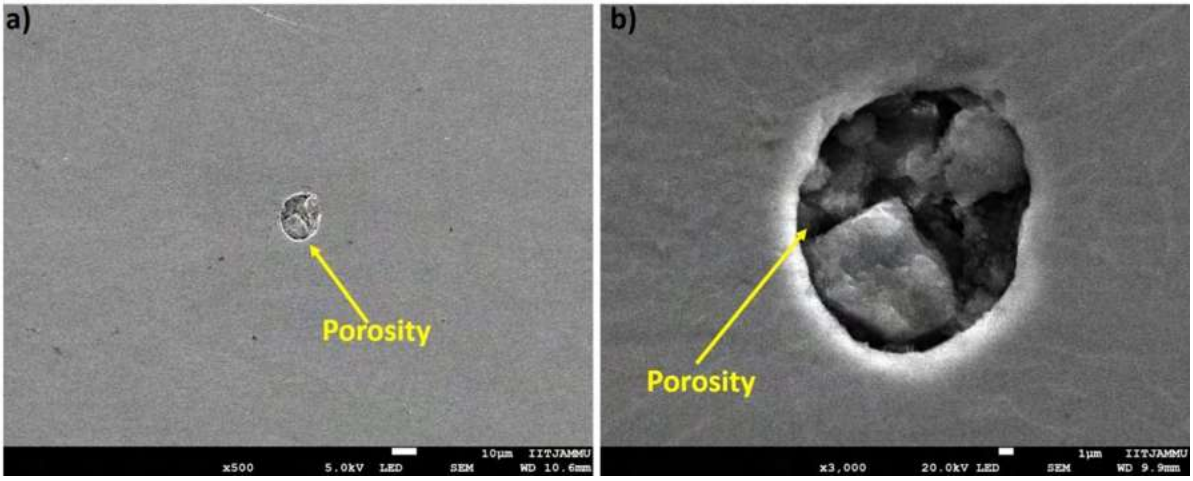

Figure 5. 34: SEM image of porosity in as-printed sample under horizontal direction: a) Low magnification; b) High magnification

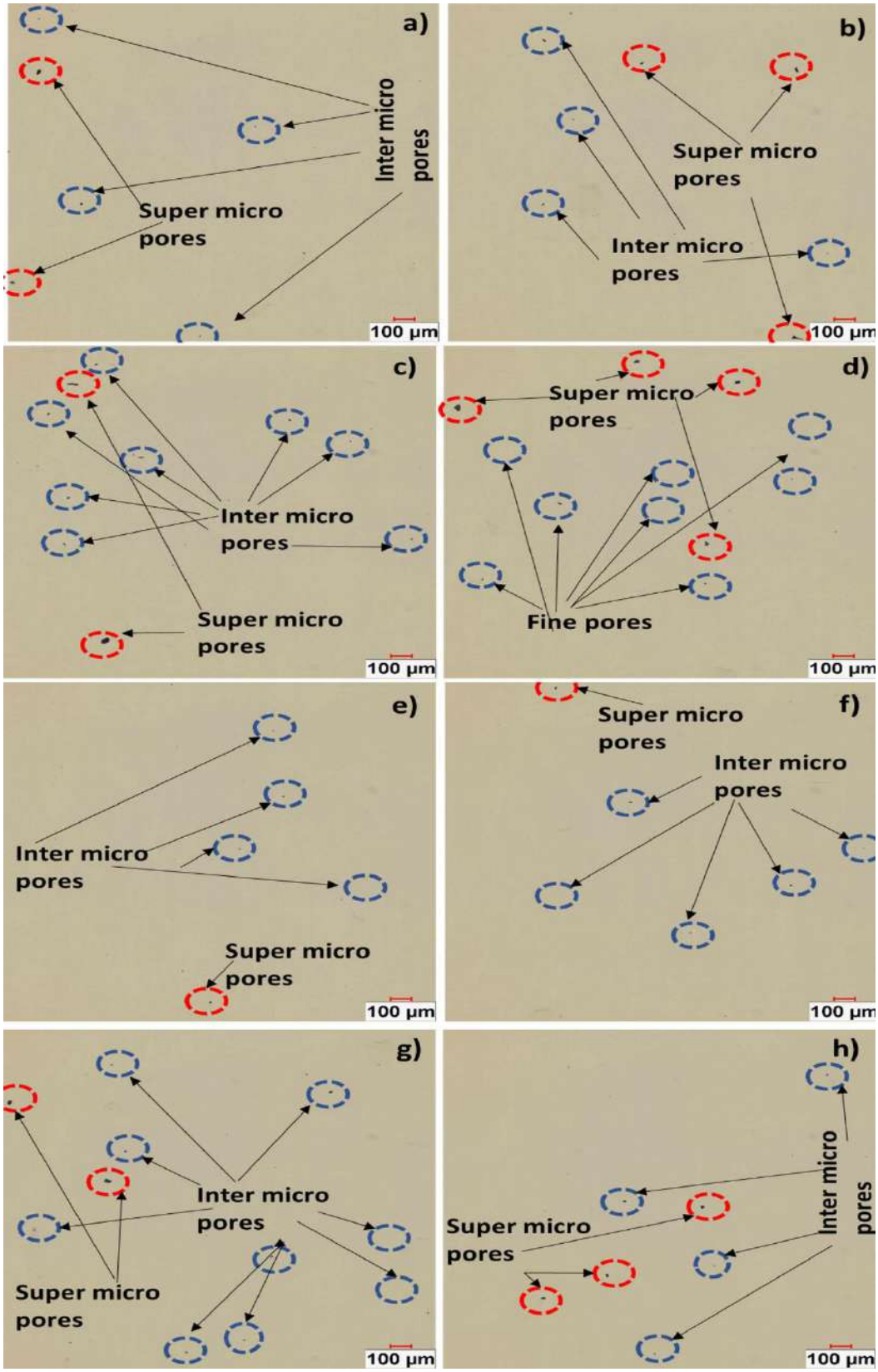

Figure 5. 35: Optical micrographs of as-printed Ti6Al4V sample under horizontal direction at different distances: a) 2.15 mm; b) 4.30 mm; c) 6.45 mm; d) 8.60 mm; e) 10.75 mm; f) 12.90 mm; g) 15.05 mm; h) 17.20 mm

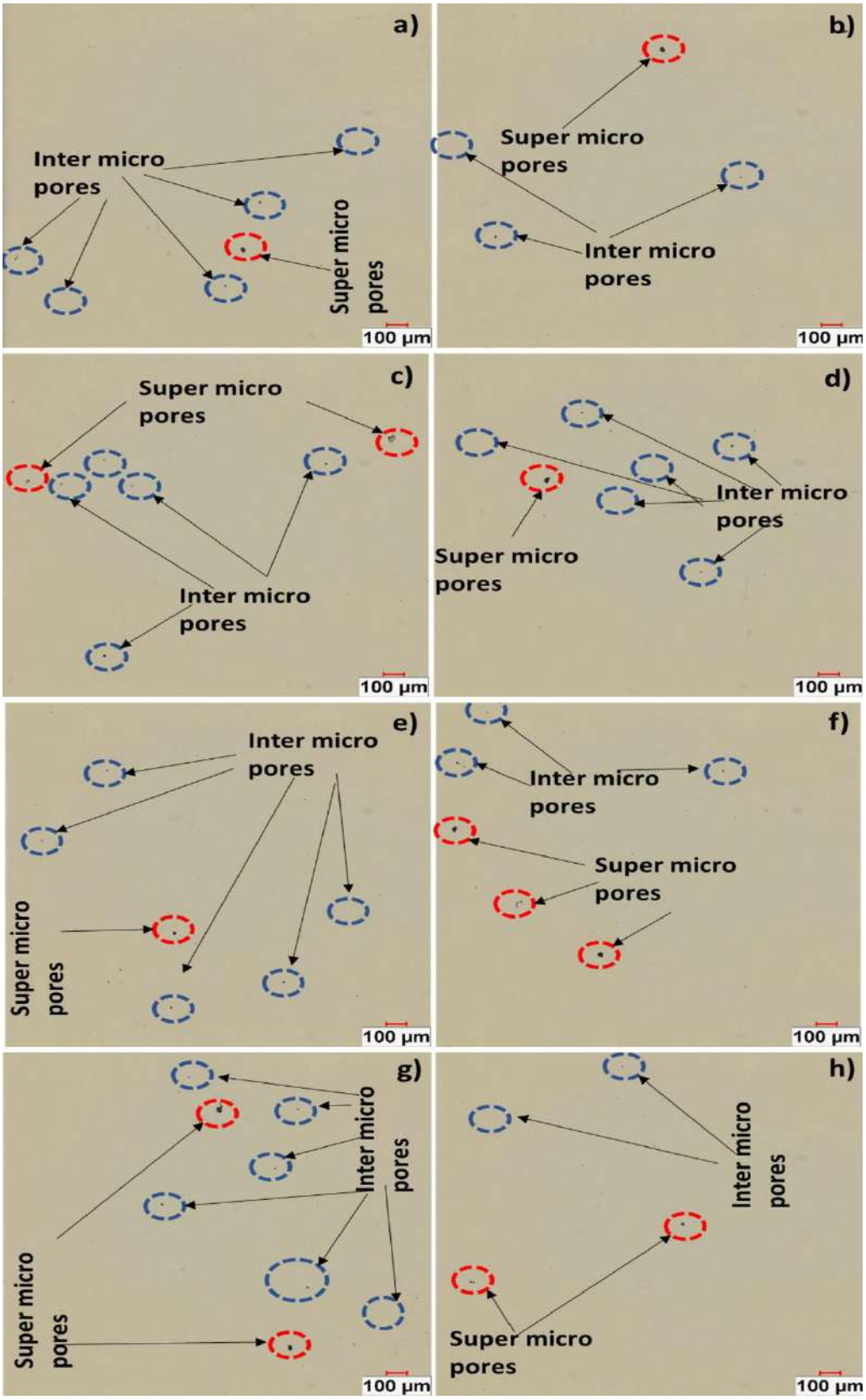

Figure 5. 36: Optical micrographs of as-printed Ti6Al4V sample under vertical direction at different distances: a) 2.15 mm; b) 4.30 mm; c) 6.45 mm; d) 8.60 mm; e) 10.75 mm; f) 12.90 mm; g) 15.05 mm; h) 17.20 mm

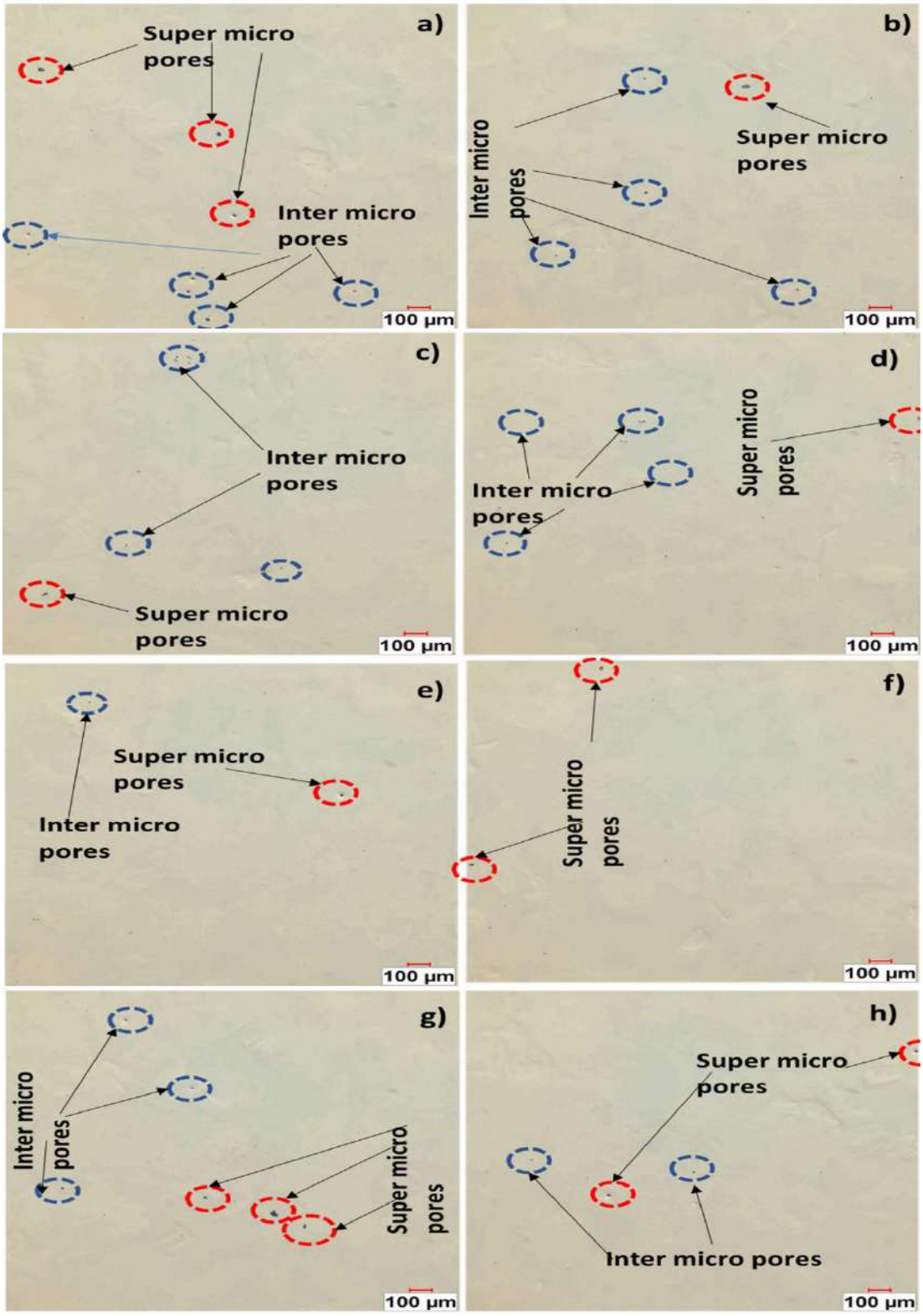

Figure 5. 37: Optical micrographs of sample 'E' under horizontal direction at different distances: a) 2.15 mm; b) 4.30 mm; c) 6.45 mm; d) 8.60 mm; e) 10.75 mm; f) 12.90 mm; g) 15.05 mm; h) 17.20 mm

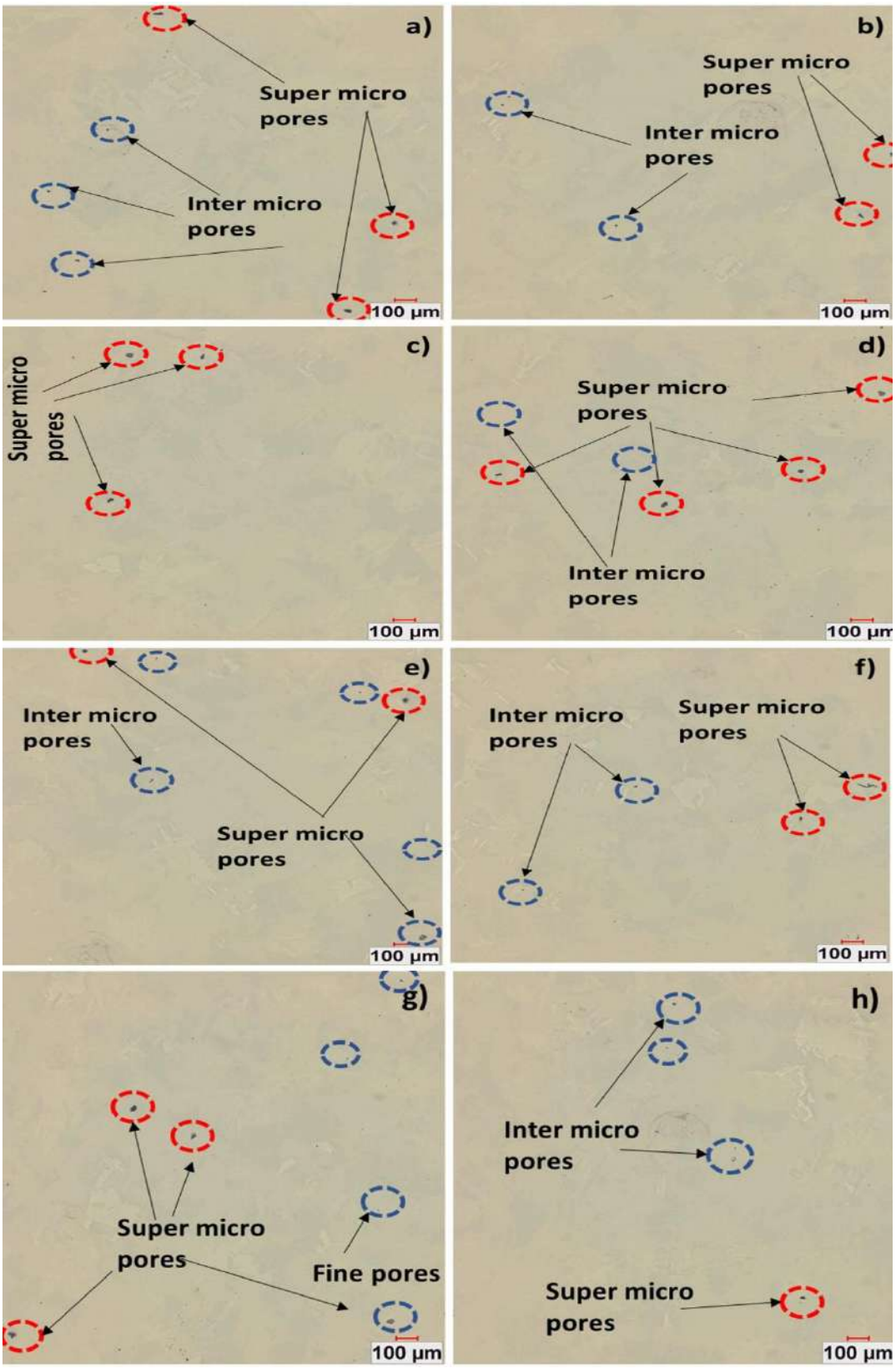

Figure 5. 38: Optical micrographs of sample 'E' under vertical direction at different distances: a) 2.15 mm; b) 4.30 mm; c) 6.45 mm; d) 8.60 mm; e) 10.75 mm; f) 12.90 mm; g) 15.05 mm; h) 17.20 mm

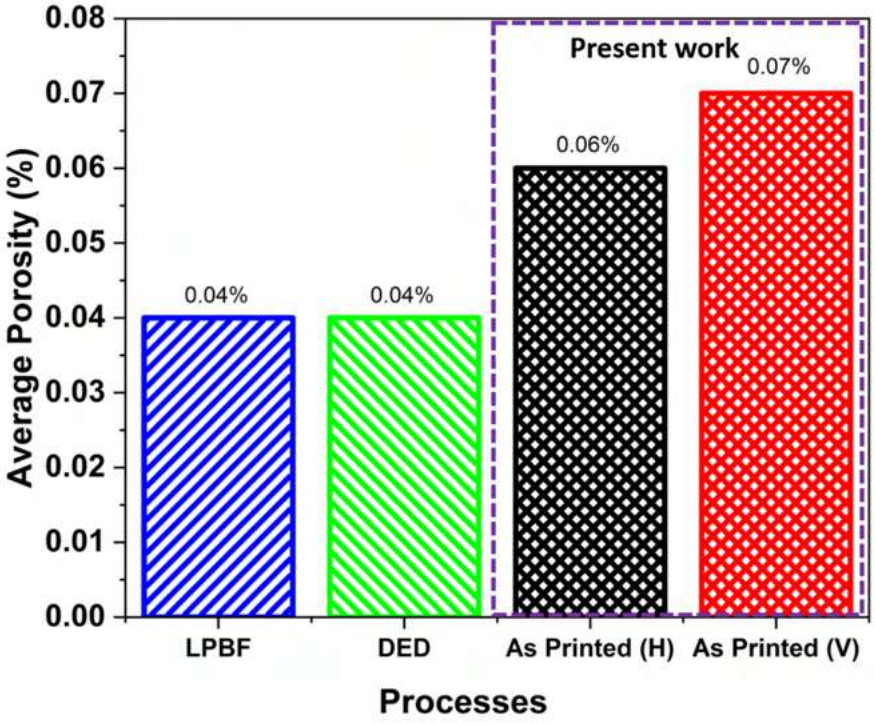

Figure 5. 39: OM measurement of average porosity comparison between different AM processes and present work [158–160]

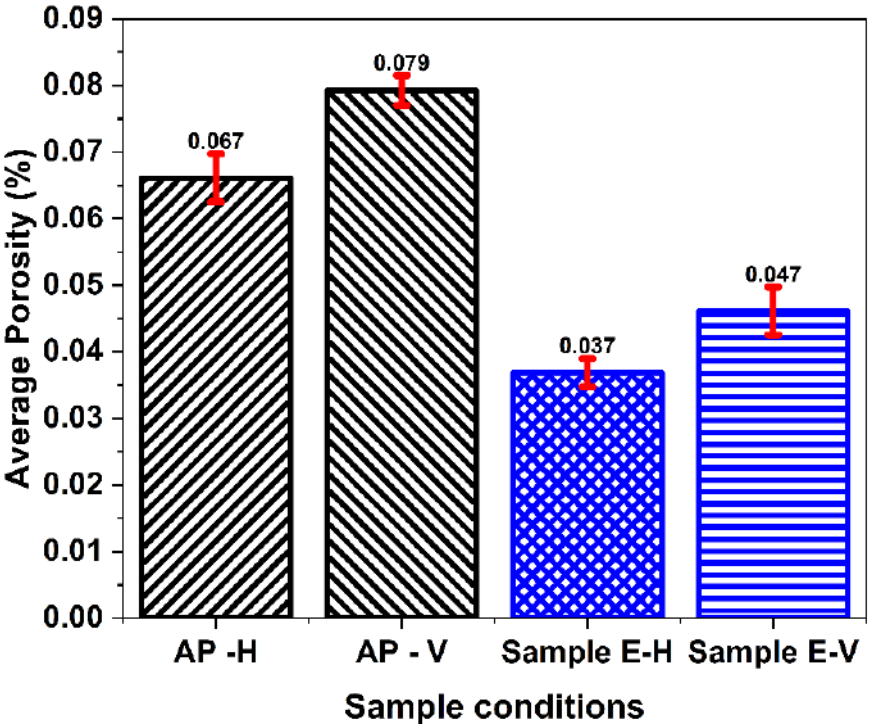

Figure 5. 40: Average porosity in different conditions of LPBF-manufactured Ti6Al4V samples

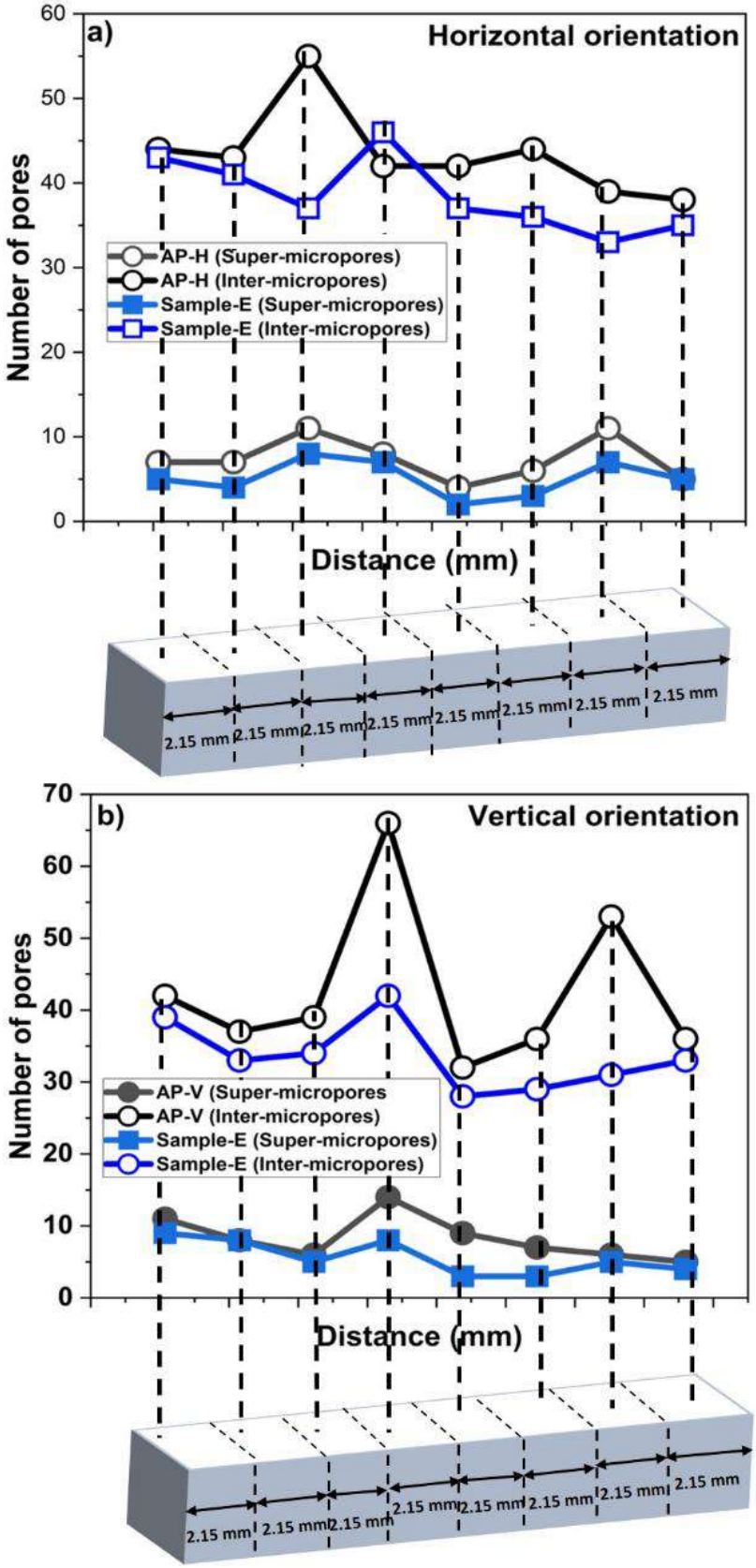

Figure 5. 41: Quantification of pores in the as-printed sample and sample 'E': (a) horizontal direction; (b) vertical direction

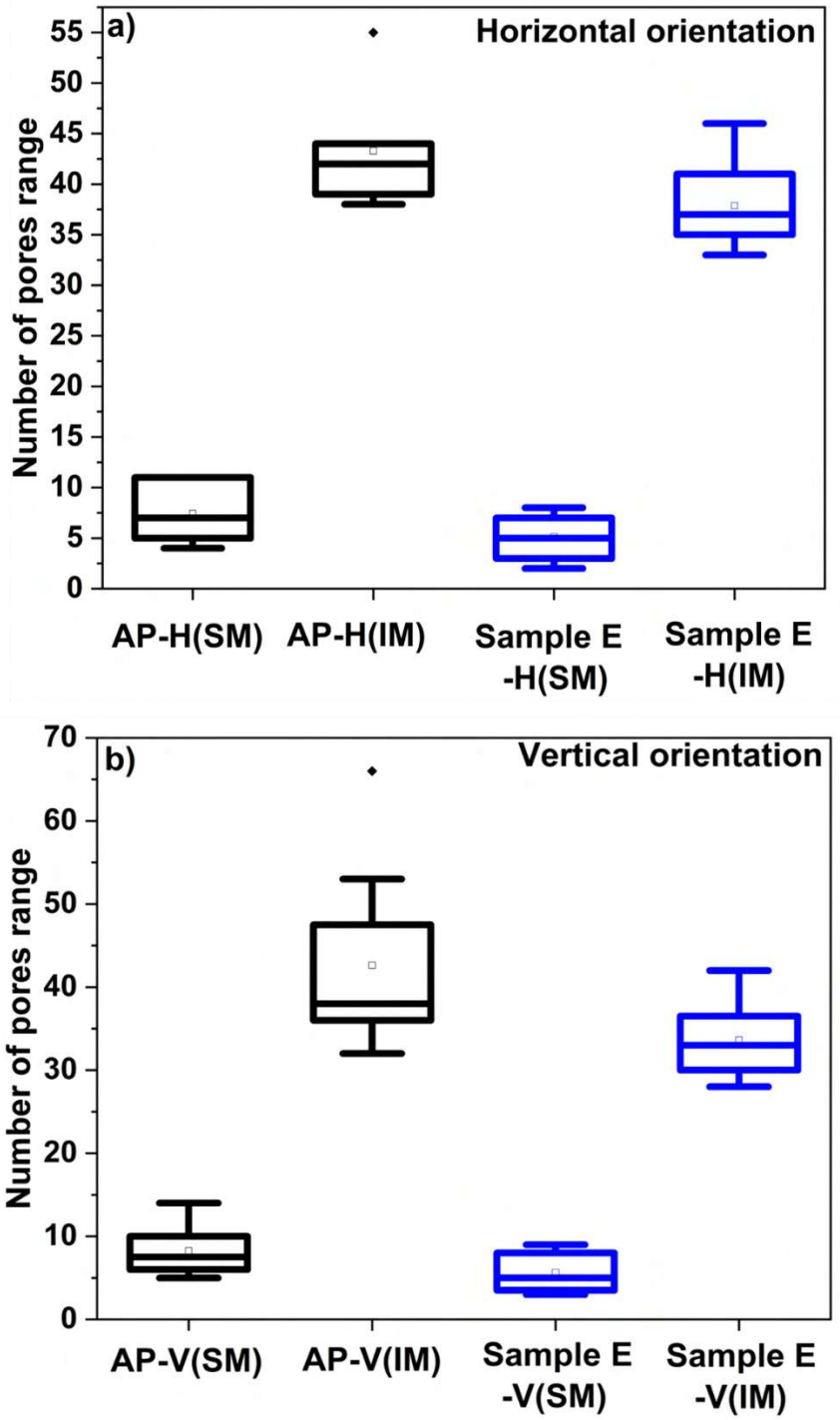

Figure 5. 42: Box plot showing the distribution of the number of pores in as-printed and sample 'E' for (SM: super micropores and IM: inter micropores): a) horizontal build; b) vertical build

The microstructures of as-printed samples and sample 'E' conditions are shown in Figures 5.10, 5.11, 5.16(a) and 5.17(a). The microstructures of the as-printed Ti6Al4V sample were anisotropic due to complex thermal events during the LPBF process, as shown in Figure. 5.10

and 5.11 [182]. A re-melting process in the LPBF process occurs when a material layer completely reheats and cools, promoting columnar grain growth towards the build direction. Moreover, the shorter interaction time between a laser and a powder leads to a faster transformation to α' martensite. Due to the high undercooling, the α' martensite phase was formed, as shown in Figures 5.10 and 5.11

The PHT transforms the as-printed sample's anisotropic microstructure into a homogenous microstructure. Furthermore, the α' martensite formed in as-printed samples (Figures. 5.10 and 5.11) converts to (α+β) lamellar (Figures 5.16 a and 5.17 a) at elevated temperature through the PHT process. The uniform microstructure obtained by the PHT technique also reduces the porosity [183]. The detailed microstructural evolution in context to porosity reduction of as-printed and PHT conditions is shown in Figure 5.43.

The α and β volume fractions play a significant role in dictating the mechanical properties of Ti6Al4V. The α phase is considered hard due to the HCP crystal structure, whereas the β phases possess a BCC crystal structure and are regarded as soft phases [184]. After PHT, the formed α+β phases provide optimum strength and ductility favourable for achieving superior fatigue strength [83].

The XRD pattern for as-printed and sample 'E' is shown in Figure 5.27 and Figure 5.28. After PHT, the α' transforms to α + β, and a tiny β phase peak is reflected due to less content corresponding to the (110) plane in sample E.

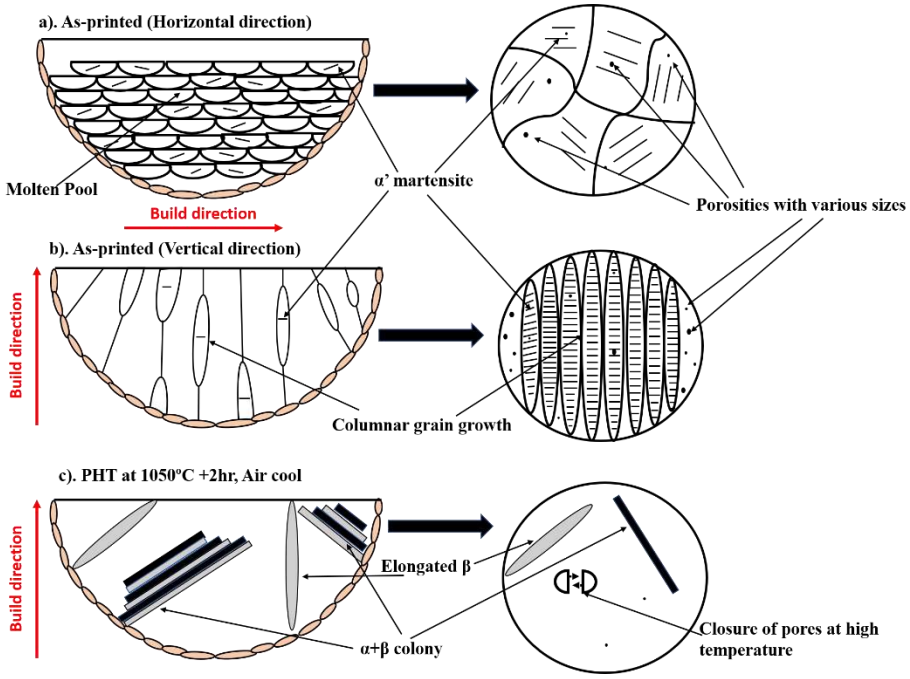

Figure 5. 43: Schematic showing microstructural evolution of LPBF-manufactured Ti6Al4V: (a) as-printed (horizontal direction); (b) as-printed (vertical direction); (c) sample 'E'

Furthermore, in the present work, the pore size classification is carried out by considering the size of the inter-micropores and the super-micropores, as shown in Figure 5.41. The pore size classification helps understand the pore closure phenomenon in PHT and its effects on mechanical properties [146, 147]. In addition, the box chart for the number of porosities is shown in Figure 5.42 where it is evident that the super-micropores are reduced to inter-micropores, and some of the inter-micropores are closed owing to the sintering phenomenon after PHT.

The selection of optimum parameters in the LPBF process helps reduce the porosities in as-printed samples. The laser power, scanning speed and laser spot size play a significant role in dictating the densification of a material. The selection of an optimal laser source for vaporization reduction is expected to be based on the energy density thresholds indicated during laser-matter interaction [185]. The energy thresholds were calculated by taking into account the evolution of the melt-pool penetration and the normalized enthalpy ratio between input laser energy (ΔH) and melt enthalpy (h_s) [186]. The specific enthalpy (ΔH) and the energy required to melt the material during fusion (h_s) are given in equations (5.8) and (5.9).

$$\mathbf{\Delta H} = \frac{\mathrm{A.P}}{\sqrt{\pi \alpha \mathrm{V} r^3}} \tag{5.8}$$

where A is the coefficient of absorption of powder, P is laser power (W), α is thermal diffusivity of a material (m^2/s), V is scanning speed (m/s), and r is laser spot size (m).

$$\mathbf{h_s} = \delta Cp\ (T_m - T_0) \tag{5.9}$$

where δ is the density of a material (Kg/m^3), Cp is the specific heat capacity of a material (J/Kg K), T_m is the melting temperature of a material (K), and T_0 is the ambient temperature of a powder bed (K).

If the ratio of $\Delta H/ h_s$ around 10 results in conduction mode melting, greater than 25 leads to keyhole defects [187]. However, Fabbro et al. [188] obtained an analytical model where threshold ($\Delta H/ h_s$) = 16 - 20 forms the keyhole mode defects. In the present study, the $\Delta H/h_s$ for as-printed Ti6Al4V is around 13.2, which signifies the conduction mode melting of the layers during the LPBF process. However, the observed irregular shape pores could be due to the improper bonding between the layers. Spherical porosities arise due to the gas entrapment under the optimized conditions, as observed by other researchers [189, 190].

Further, the HIP technique has shown significant improvements in the reduction of porosities of LPBF-manufactured Ti6Al4V samples [191, 192]. It is interesting to note that in a study by Kasperovich and Hausmann [81], the OM evaluated porosity of as-printed LPBF-manufactured Ti6Al4V was decreased from its as-printed porosity of 0.077% to 0.012% using the HIP process, which is comparable to the reduction in porosity achieved in the current study where Sample 'E' showed porosities ~0.046% compared to the as-printed sample porosities ~0.079%. Therefore, these instructive results suggest that PHT can be used as an alternative way to reduce the porosity in LPBF-manufactured Ti6Al4V parts.

Moreover, there could be components where the HIP technique cannot be used effectively for which PHT could reduce the porosities. HIP could be ineffective in eliminating irregular internal and interconnecting pores [193], can distort thin-walled parts and inferior mechanical properties (due to grain coarsening) [194], can form liquefaction cracks (in eutectic materials), can induce rougher surface due to gas pressure. Therefore, the positive benefits of HIP are masked due to the above-mentioned ill effects.

In the LPBF process, inevitable porosities during the part fabrication are addressed via the HIP technique with carefully optimized parameters for end-use parts with specific geometries.

However, the HIP process is expensive and time-consuming, and other factors limit its use in many practical cases. A study by Zhang et al. [59] reported that the effect of PHT on the hot isostatic pressed LPBF-Ti6Al4V alloy aggravates the regrowth of pores, and sharp-edged, and slit-shaped pores were formed. Further, they exhibited a detrimental effect on plain fatigue resistance. Moreover, components due to heat treatment at elevated temperatures reduced the sharpness and size of a pore due to the diffusion process.

Another study of selective electron beam melted Ti6Al4V conducted by Tammas et al. [80] revealed that the heat treatment after the HIP process facilitates the regrowth of spherical shape pores that were less in size than the defects formed during the as-printed condition. However, there was no change in the size of a lack of fusion pores after heat treatment. Only those gas pores that are identified as spherical can appear to regrow after annealing. They can be explained by the origin of the gas particles that make up these pores. Although argon gas employed during the LPBF process cannot diffuse out of the material during the HIP process, it remains in the sample within the collapsed pores. This high internal pressure will cause the regrowth of these pores during the heat treatment process [195]. Furthermore, the surface roughness after the HIP process increases due to the depressions and dimples formed on the material's surface undergoing high pressure and heat treatment. The HIP process does not improve the fatigue strength if surface roughness is not enhanced; since the treatment only affected the internal porosity, it did not affect the surface finish's fatigue strength [71]. A study by Uzan et al. [196] revealed that stress-relieving heat treatment provides superior fatigue strength to the stress-relieving and HIP processes. LPBF-manufactured rotor blades in an aero-engine have thin profiles for which PHT could be beneficial to reduce the porosity.

In addition, HIP cannot remove surface-connected porosity. It can still expose subsurface pores because pressurized gas penetrates the porous surface during HIP and pushes against the subsurface pores [197]. Majeed et al. [194] reported that the solution treatment and artificial ageing reduced the porosity levels of thin materials to less than 2.5 mm. However, the relative density was lowered for the specimens with a thickness between 2.5 mm and 5 mm. Indeed, there is an improvement in the density of thin sections after solution treatment and artificial ageing; still, there are no significant and proposed explanations for the reported differences in porosities.

The inter-micropores' closure at elevated temperatures can also be attributed to the sintering process. Tascioglu et al. [183] showed similar results as observed in the present work. The 316L stainless steel fabricated through the LPBF process was examined for porosity in as-printed and PHT conditions. The PHT sample exhibited a significantly lower porosity than the as-printed samples. The reduction in porosity was attributed to the formation of a homogeneous microstructure [183]. A group of researchers led a study on the PHT effect on the porosity measurement of thin-walled AlSi10Mg manufactured using the LPBF and showed that densification was achieved using HTs. This process alters the grain structure and microstructures of the part to improve its densification [194]. In another study [198], the heat-treated AlSi10Mg showed less porosity than the as-printed AlSi10Mg due to microstructural refinement. The current study evaluated the microstructures of as-printed and PHT samples. A homogeneous microstructure originated for the PHT samples discussed in the section 5.2.1. The homogenization of the specimen makes it hard to maintain its natural porosity. This is because the high-temperature homogenization produces a uniform structure within the specimen.

The positive effects of PHT on the densification behaviour are reported in the thermal spray coating process, in which powder feedstock is melted (similar to the LPBF process) and deposited on a part surface with a high velocity. The high nickel thermal spray coating produces a deleterious porosity to the fatigue life. The pores in thermal spray coatings are due to insufficient melt source and un-melting of powder, identical to the pores produced in the LPBF process [199]. These developed pores during the thermal spray coating were reduced through heat treatment. Through a process known as sintering, the porosity of a thermal spray coating was decreased by high-temperature treatment. This process involves raising the metal or ceramic particles to an elevated temperature, reducing the particles' spaces [200]. Another study on 316L stainless steel thermal spray coating conducted by Mangour et al. [201] showed the beneficial effect of heat treatment on reducing porosity levels. The decrease in porosity caused by increasing annealing temperature in N_2-sprayed coatings can be attributed to the usual sintering models. However, it is also possible that the inter-microporosity observed in He and N_2-treated samples is due to incomplete inter-particle inter-sintering.

In the present work, the reduction in porosities in sample ‘E’ is attributed to the sintering process and closure of the pores at elevated temperatures. However, the porosity level in vertically built samples is slightly higher than in horizontally built samples, attributed to many

layers in vertically built samples [90]. The higher the number of layers in the material, the more likely inevitable pores will develop. The possible mechanism for reducing porosity due to PHT is shown in Figure. 5.44, where the pore gap gets close to mitigate the void. Due to high temperature, the study revealed that only inter-micropores are closed after PHT. The increased surface energy of inter-micropores reduces them as much as possible, but not in the case of super-micropores [202]. This phenomenon is known as diffusion, which occurs at high temperatures and is also considered a self-healing of the porosities [203]. Further, the porosity size reduction in samples E compared to as-printed samples in horizontal and vertical orientation is shown in Table 5.4.

Table 5. 4: Maximum and minimum porosity sizes in LPBF-manufactured as-printed and samples E

Sample Conditions	Maximum Porosity size (µm)	Minimum Porosity size (µm)
AP-H	38.16±2.09	7.12±0.13
AP-V	44.76±2.03	4.47±0.75
Sample E-H	33.99±3.15	0.409±0.17
Sample E-V	37.25±0.73	1.32±0.45

Moreover, in inter-micropores, the high surface energy is the driving force for diffusion at high temperatures, resulting in the closure of pores. Further, elevated temperatures can cause morphological changes in the pores. For instance, pores may spheroidize the surface to

minimize the free surface energy. According to Young Laplace, equation (5.10) [59] is a simple calculation that shows the driving force for the closure of a pore.

$$\mathbf{\Delta p} = \frac{\gamma}{R} \tag{5.10}$$

where Δp is the pressure, γ is the surface energy, and R is the radii of the pore. The radius of an inter-micropore is less than the radius of a super-micropore. It increases the driving force for the closure of a pore. Therefore, the super-micropores with low surface energy prevent these pores from getting close effectively [204]. The solid-state sintering effect facilitates the closure of inter-micropores. The main challenge in solid-state sintering is to reduce surface energy. It can be achieved through various means, such as transporting materials and reducing the surface area [5]. There are three stages in solid-state sintering: (1) particles keep growing as they contact the neck. As they do so, neck growth occurs, and the pore shapes are also irregular; (2) with sufficient neck growth, the enlarged pore channels become cylindrical in this stage. The resulting curvature gradient is high enough for faster sintering; (3) in the final stage, the closure of the pore channel can occur when the porous region is isolated and the inter-connected portions are no longer necessary [205]. Moreover, it is found in literature that porosity size less than ~10μm does not affect significantly the fatigue resistance of a material thus reducing super-micropores by converting them to inter-micropores at high-temperature PHT may enhance fatigue resistance[115].

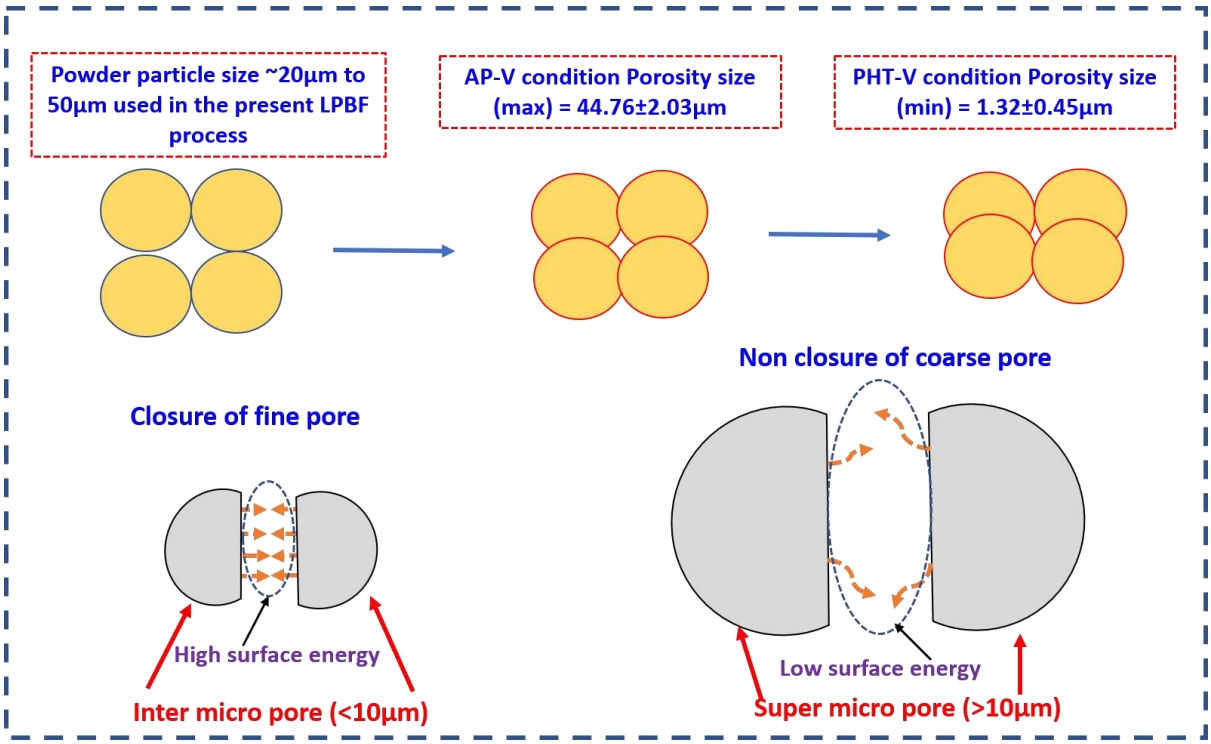

Figure 5. 44: Schematic of densification mechanism due to PHT

5.4 Influence of PHT with Super β transus temperature on the Tensile behaviour of LPBF-manufactured Ti6Al4V parts

5.4.1 Tensile properties of the LPBF-manufactured Ti6Al4V

The tensile properties of the as-printed and sample E in all three build orientations (0°, 45°, and 90°) are shown in Figure 5.45. It was observed that the as-printed samples in all three orientations show high yield strength (YS) and ultimate tensile strength (UTS). The high strength in the as-printed Ti6Al4V is due to the α' phase which provides increased strength owing to the high dislocation density around it [206]. Moreover, the sample under inclined orientation has shown high strength and ductility among all three oriented samples, which corroborates well with the results reported by [111].

Further, sample E in all three orientations shows low YS and UTS values; however, ductility in all three orientations of the sample is considerably high and nearly isotropic because of its high β phase content. It is important to note that the tensile properties of the as-printed Ti6Al4V sample in horizontal, inclined, and vertical orientations satisfy the minimum requirement for AMS4991 cast Ti6Al4V properties. The comparison of tensile properties in the as-printed

sample and sample E with wrought Ti6Al4V[207] and cast[208] tensile properties are given in Figure 5.46.

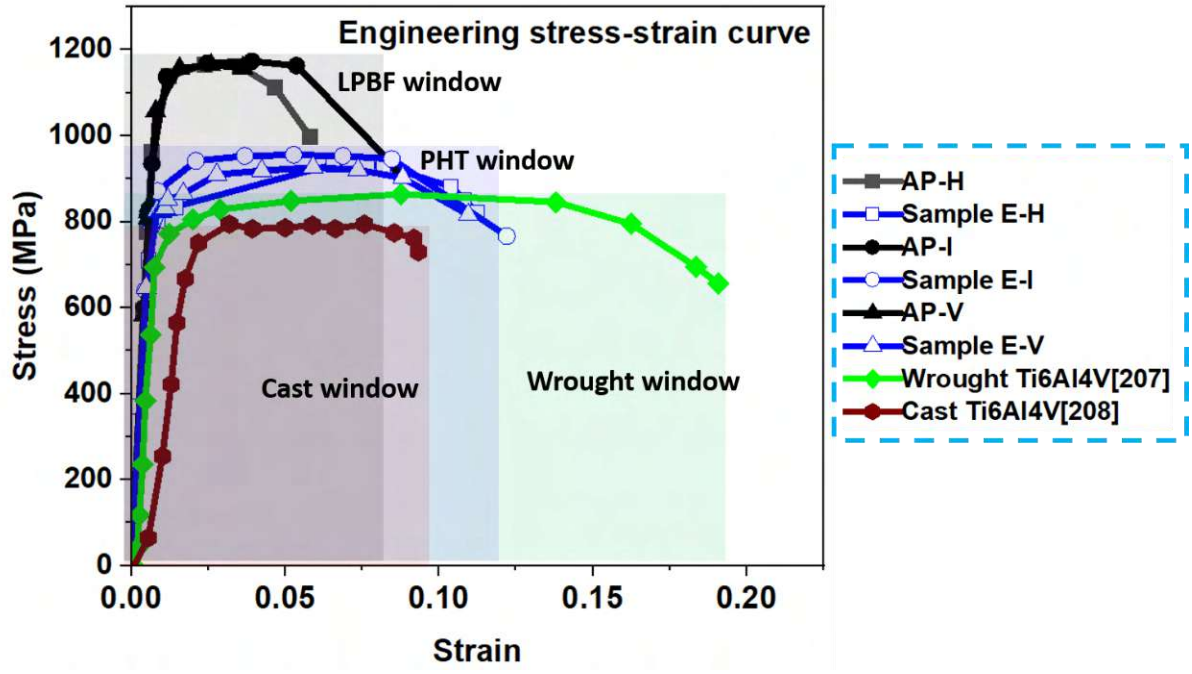

Figure 5. 45: Stress-strain curves for as-printed samples and sample E under different orientations

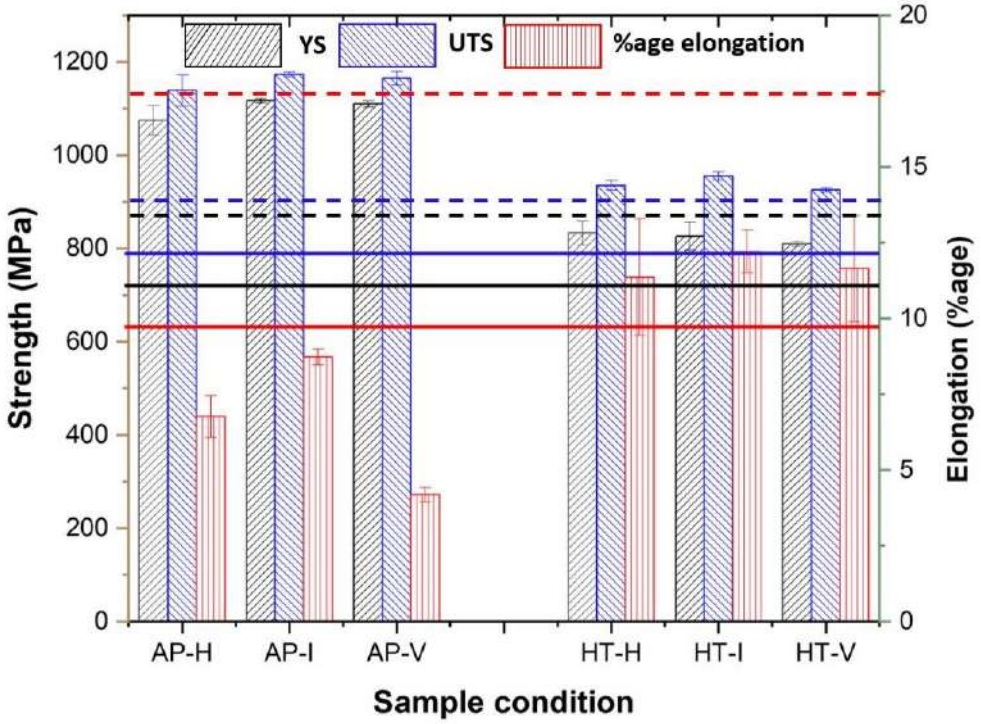

Figure 5. 46: Tensile properties values comparison of as-printed, sample subjected to PHT, wrought and cast Ti6Al4V samples. Horizontal dotted lines correspond to the wrought Ti6Al4V data [202] and Horizontal solid lines corresponds to the cast Ti6Al4V [203]

For predicting the yield strength of Ti-6Al4V, Galindo Fernandez-Fernandez[207] proposed a physics-based model. The yield strength under various test conditions is evaluated as given in equation (5.11).

$$\sigma_y = (\sigma_\alpha V_\alpha + \sigma_\beta (1- V_\alpha) + \frac{K_{HP}}{\sqrt{D_\alpha}}) * \left(\frac{\kappa \mu b^3}{K_\beta T ln(\frac{10^7}{\dot{\varepsilon}})} \right)^n \quad (5.11)$$

Where σ_y is yield strength, V_α is the volume fraction of α phase, σ_α is friction stress in α phase, σ_β is friction stress in β phase, K_{HP} is the Hall-Petch coefficient of a given material, D_α is the grain size of α, T is the temperature, ἑ is strain rate, K_β is the Boltzmann constant, b is burger vector, n and κ are constants taken from experimental data as given in Table 5.5. The shear modulus (μ) was determined as μ = (54-0.003T). All constant parameters used for the equation (5.11) are given in Table 5.5.

Further, the volume fraction of α was calculated, which is given in Figure. 5.33. The proposed model Y.S. is calculated using equation (5.11). Further comparison has been made between experimental YS and proposed model YS in horizontal and vertical oriented samples in as-printed and PHT executed sample E condition in Table 5.6. The grain size of the α lath was evaluated using ImageJ software, and a similar technique was followed by different researchers[209, 210]. It is worth mentioning that the proposed model and experimental results agree with each other. Therefore, the proposed model can be used to evaluate the yield strength of LPBF-processed Ti6Al4V for various lath thicknesses, temperatures, and strain rates.

Table 5. 5: Constant parameters employed in equation 5.11

Sr. No.	Constant	Value	Units	Reference
1.	K_{HP}	300	MPa	[211]
2.	σ_α	550	MPa	[207]
3.	σ_β	1350	MPa	[207]

4.	b	2.9×10^{-10}	m	[212]
5.	K_β	1.38×10^{-23}	J/K	[212]
6.	n	0.23	-	[213]
7.	ϰ	0.4	-	[213]
8.	έ	0.0003	/s	Used value

Table 5. 6: Comparison of model-predicted YS and experimental YS for sample E

Conditions	**YS in MPa (Experimental)**	**YS in MPa (Model)**
Sample 'E'-H	833.73	884.44
Sample 'E'-V	810.00	884.12

Further, the true stress-strain curve is shown in Figure. 5.47. The strain hardening coefficient (n) and strength coefficient (k) are derived from the true stress-strain curve, as shown in Table 5.7. The as-printed sample shows a higher strain hardening exponent (n) and strength coefficient (k) than sample E due to fine microstructure in the form of α' needles. The α' martensite obstructs the dislocation motion during mechanical loading, resulting in high strain hardening and strength coefficient [214]. Moreover, the comparison between different AM processes with our work is shown in Figure.5.48. It is apparent from Figure. 5.48 that PHT sample E is showing better tensile properties from wire arc additive manufacturing (WAAM) PHT [215], directed energy deposition (DED) [216], and electron beam melted AM (EBM) PHT [217].

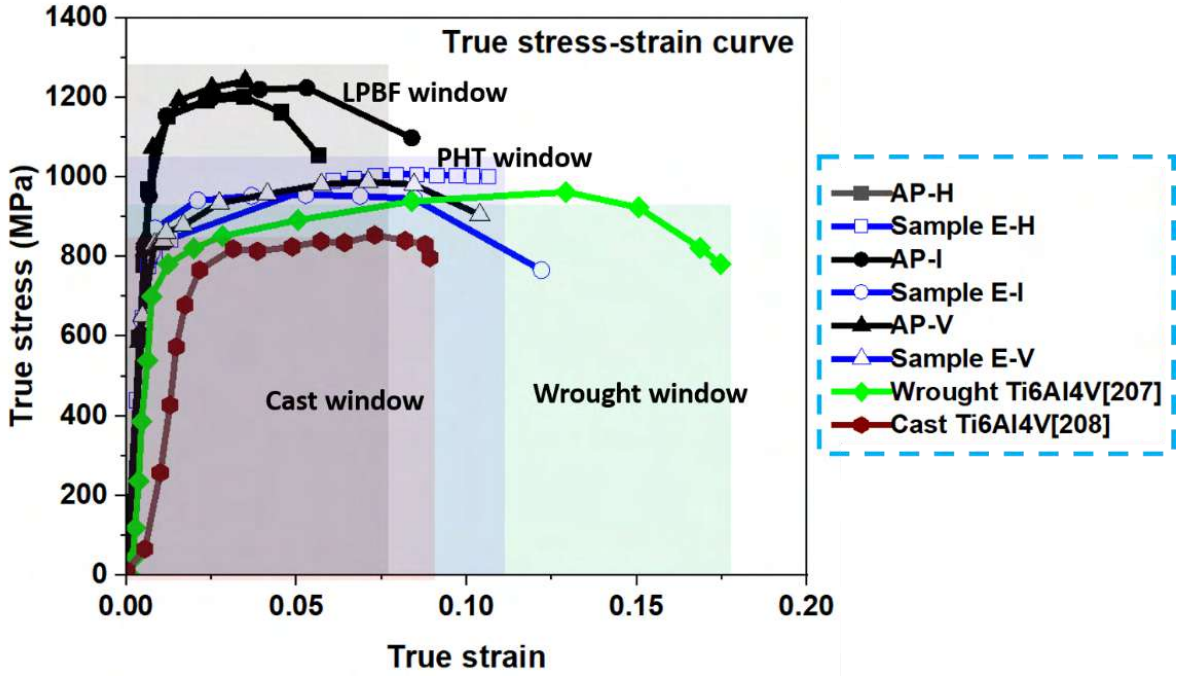

Figure 5. 47: True stress-strain curves for as-printed sample and sample E under different orientations.

Table 5. 7: Strain hardening exponent and strength coefficient of as-printed sample and sample 'E'

Conditions	Strain hardening exponent (n)	Strength coefficient (k)
As-printed-H	0.304	3283.68
As-printed -I	0.326	3612.83
As-printed -V	0.357	4819.99
Sample E-H	0.259	1875.99
Sample E-I	0.347	3046.21

Sample E-V	0.206	1781.54

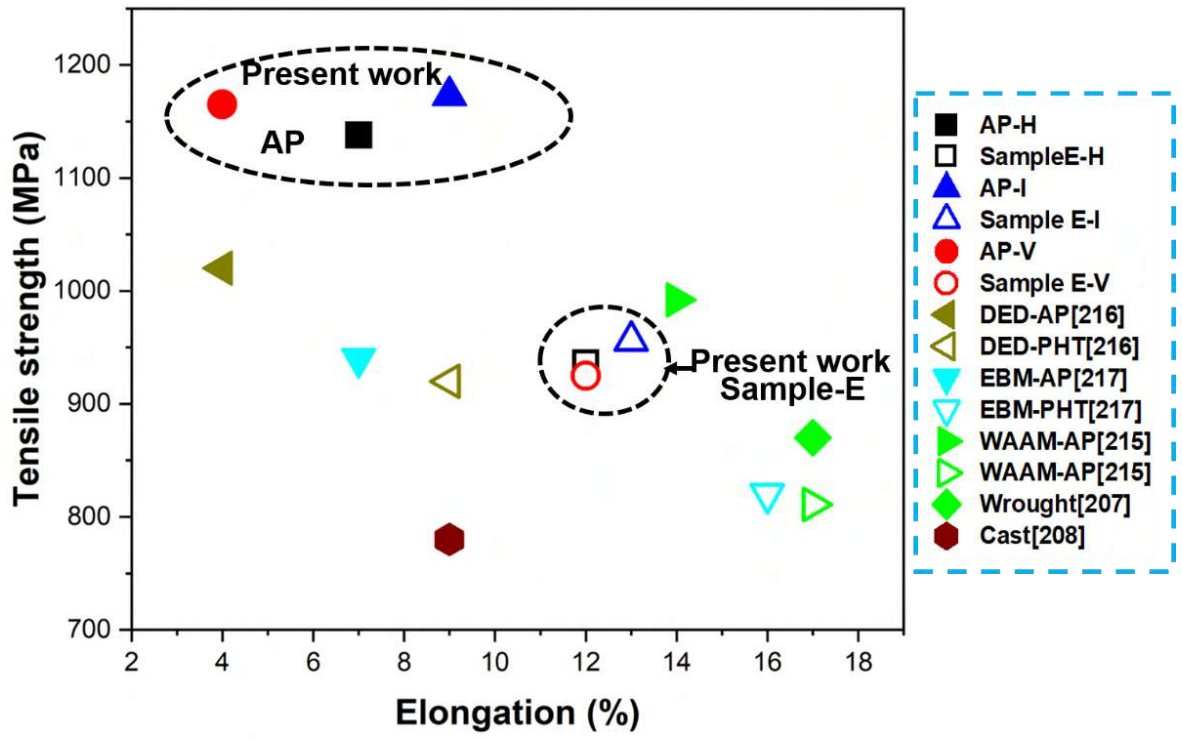

Figure 5. 48: Comparison of tensile strength vs elongation between different AM processes and present work results

5.4.2 Fractographic analysis of fractured surfaces

The fracture surface morphologies for horizontal, vertical and inclined samples for the as-printed condition are shown in Figure. 5.49-5.51, respectively. The fractographic image at different regions of the horizontally oriented as-printed sample is shown in Figure. 5.49. It is evident from Figure 5.49 that the presence of many micro-voids may convert into cracks after coalescence under tensile loading.

These defects play a predominant role during fracture in uniaxial tensile testing. Moreover, some facets and dimple features are also observed in Figure. 5.49(b), which could be attributed to the fracture's ductile and brittle mixed mode. It is important to note that the cracks in Fig. 5.49(b) are parallel, which can be associated with a parallel deposition of layers in horizontally oriented samples[111].

Further, the fractographic images of the as-printed Ti6Al4V sample under inclined orientation are given in Fig. 5.50 (a, b and c). The pores in Fig. 5.50 are considerably less than the horizontally oriented sample, possibly due to higher UTS. The small facets can be seen in Fig. 5.50 (b), which could be responsible for high ductility compared to the horizontally as-printed samples. The fibrous fracture observed in Fig. 5.50 (c) is similar to the cast and wrought Ti6Al4V fracture resembling the ductile fracture[218].

The fractography at different locations of the vertically as-printed Ti6Al4V sample is shown in Fig 5.51 (a, b and c). The tiny facets are observed in Fig.5.51 (b), and the fibrous fracture in Fig 5.51 (c) shows the mixed mode of ductile and brittle fracture as observed in the horizontally oriented sample. However, the number of pores is higher in vertically oriented samples, resulting in lower ductility than in the horizontal and vertically oriented samples. The porosities marked in Fig.5.51 (c) could be the gas porosities that negatively affect a sample's ductility.

In addition to high porosities, the lower ductility of vertical manufactured samples compared to their counterparts in the horizontal direction can be attributed to the orientation of inter-layered pores (Figure. 5.51 c). The anisotropy of the pores in the direction of the applied load could be a cause of mechanical properties anisotropy[164, 219]. During tensile testing of a vertical built sample, the layers will be perpendicular to its tensile loading axis. This means that any fabrication defect will be perpendicular to this axis and defects can potentially be opened to lower stress levels in a situation like this. A horizontal built sample that is subjected to tensile testing will have its layers parallel to the axis of the test resulting in higher ductility due to difficulty in opening of such pores during tensile loads. Similar type results are shown by Vilaro et al.[52] where thin flattened pores found in vertical oriented samples due to the lack of a fusion between the layers showed lower ductility. Furthermore, the interface between the successive layers may experience microstructural discontinuity. This occurs due to the change in the grain orientation after each successive layer which can weaken the interface[220]. The interface between layers that are vertically stacked can become perpendicular to the axis of the tensile loading. This can cause the and nucleation and coalescence of pores to occur faster, decreasing the elongation of a material.

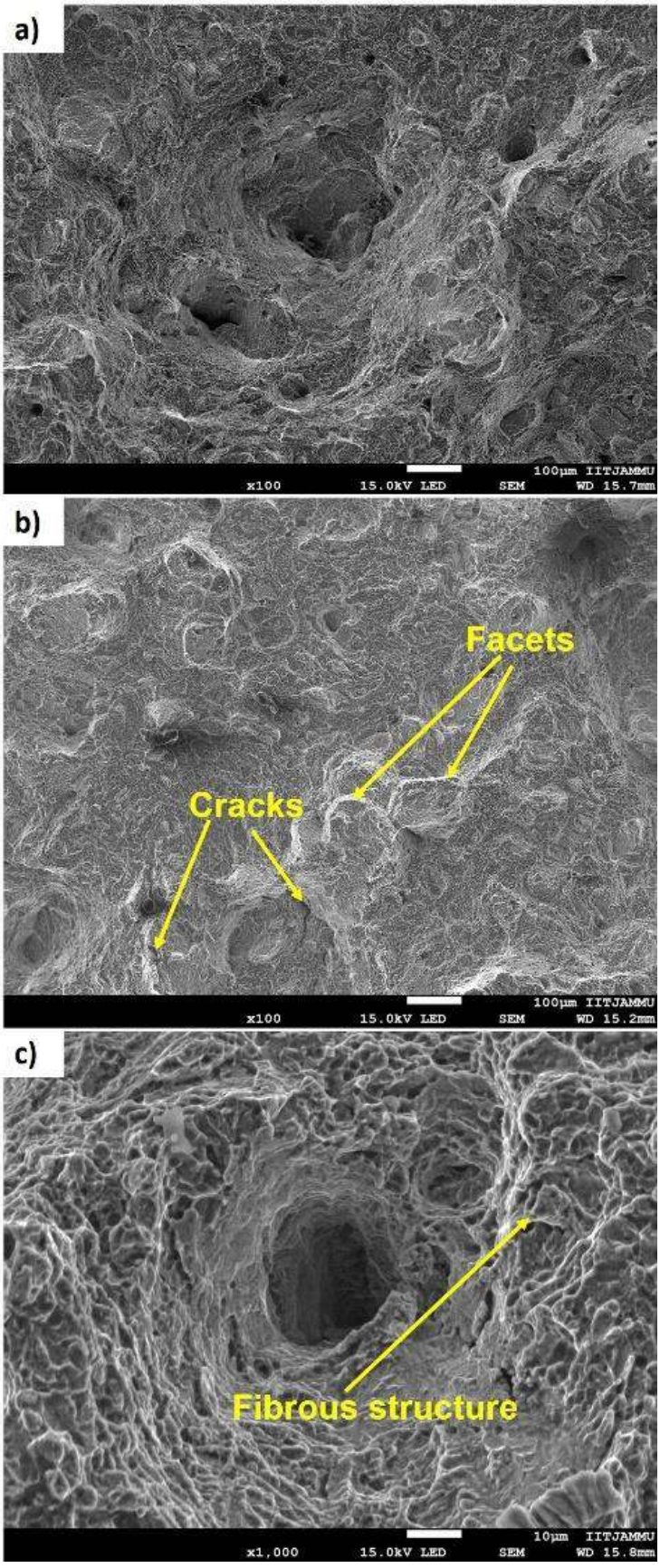

Figure 5. 49: SEM images of the fractured surface of the as-printed sample under horizontal orientation

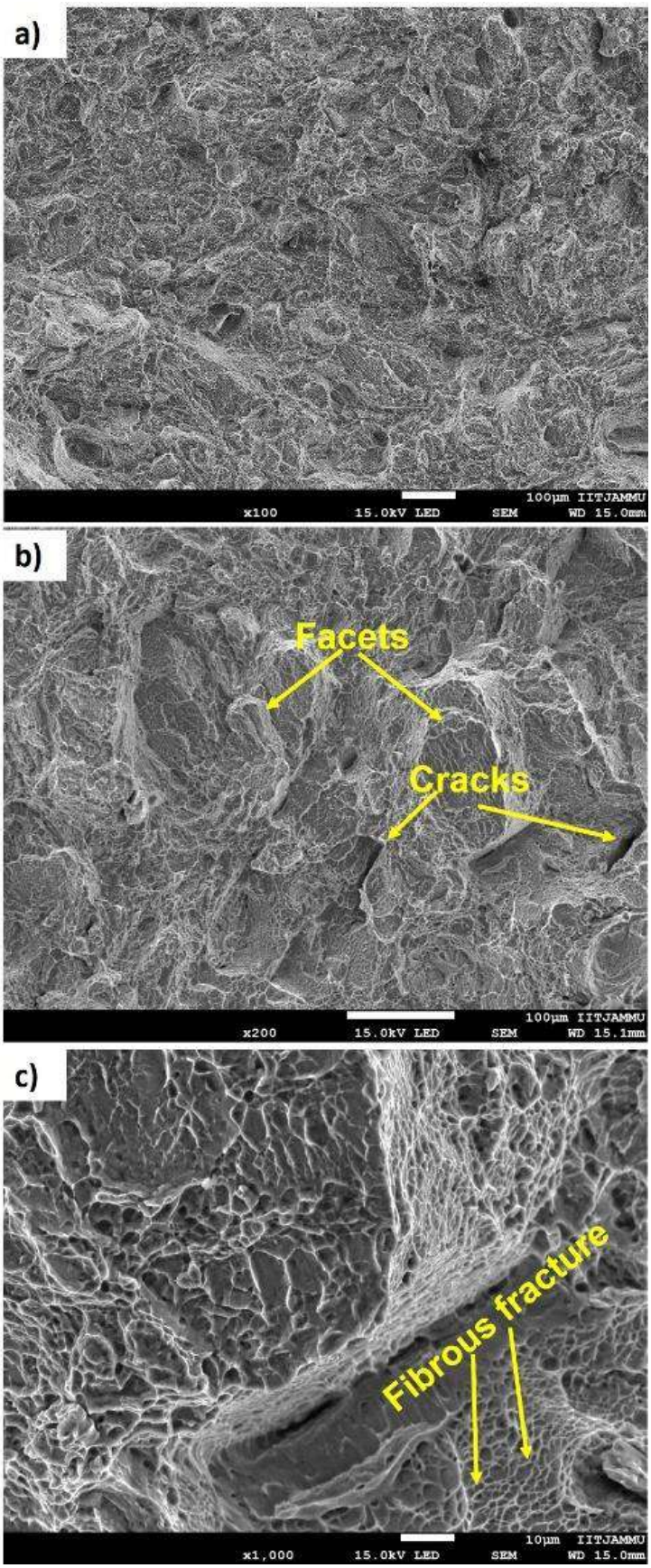

Figure 5. 50: SEM images of the fractured surface of the as-printed sample under an inclined orientation

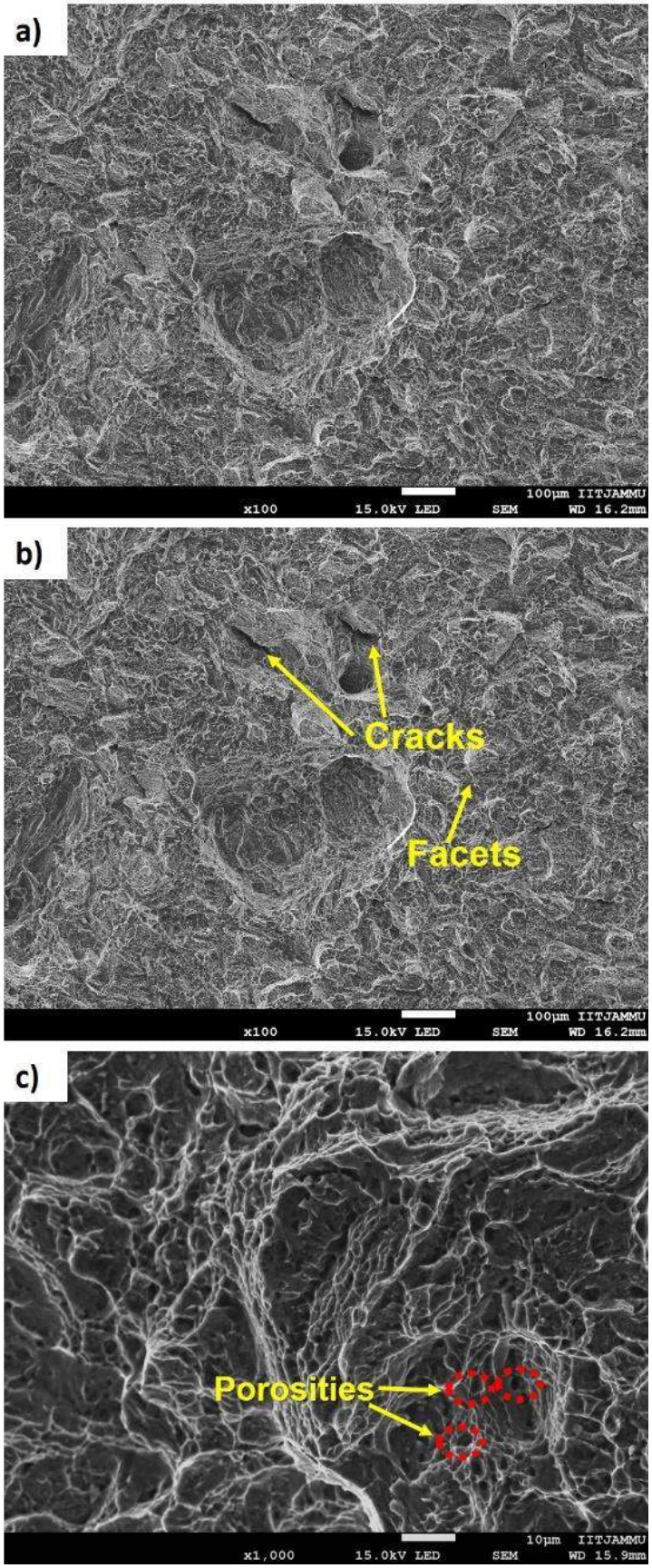

Figure 5. 51: SEM images of the fractured surface of as-printed sample under vertical orientation

The effects of build direction on the tensile performance of AM materials are complex due to their sensitivity to various process parameters. For instance, the scanning speed, hatch distance and laser energy are some factors that affect the performance of the as-printed material. Different LPBF process parameters can affect the pore distribution and microstructure of LPBF-manufactured materials[87]. These factors can influence the build direction. The ductility of LPBF-manufactured Ti6Al4V can be affected by the prior β columnar grains and the α phase grain boundaries. In addition, the presence of pores can negatively affect ductility. Therefore, the PHT is essential to make the microstructure homogenous in view of enhancing mechanical performance. There is a high possibility of several pores in the vertically oriented LPBF-manufactured sample owing to many interlayers compared to the horizontal and inclined oriented material. Moreover, it is evident from Figure. 5.51(c) that porosities in vertically oriented samples result in a loss in ductility.

Figure. 5.52(a-c) shows the fractography images for sample E under horizontal orientation. It is apparent from Figure. 5.52 that dimples are observed, which are attributed to the ductile fracture. The higher ductility is due to sample E's high β content.

Fig. 5.53 (a-c) shows the fractography of sample E in an inclined orientation. Similar features were also observed in Fig.5.52, resulting from the isotropic microstructure. It is interesting to note that Fig.5.53(b) reveals α+β lamellar structure, which is responsible for the high ductility. The fractography results for sample E under vertical orientation are shown in Fig. 5.54(a-c). The observed dimples and fibrous structure in Fig. 5.54(c) show the ductile fracture. It is important to note that all three oriented samples E have shown similar features; ductile fracture with little micro-voids and cracks. The reduction in mechanical strength and high ductility of sample E in all orientations is due to the β phase content because of super β transus temperature PHT. It should be noted that enhancing ductility in sample E after PHT could be favourable in increasing the fracture critical applications in cyclic loading scenarios.

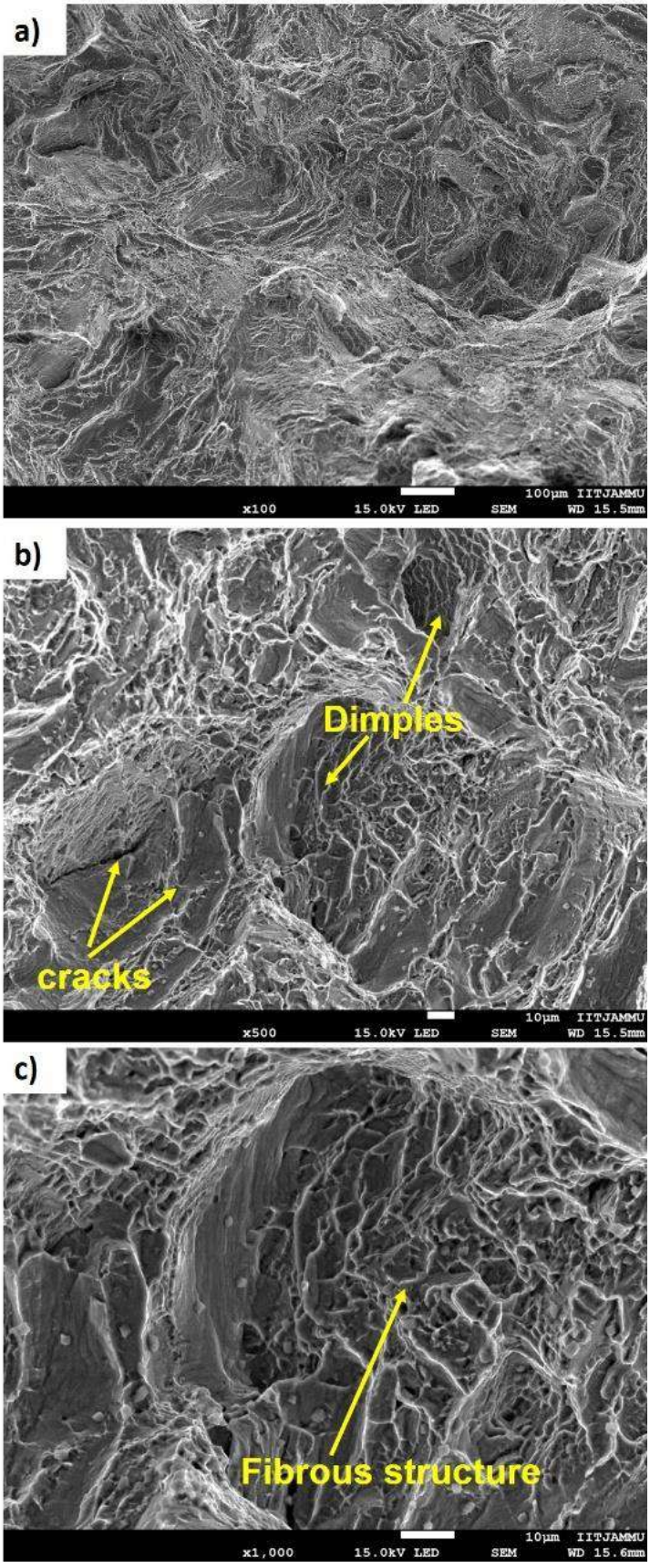

Figure 5. 52: SEM images of the fractured surface of sample E under the horizontal orientation

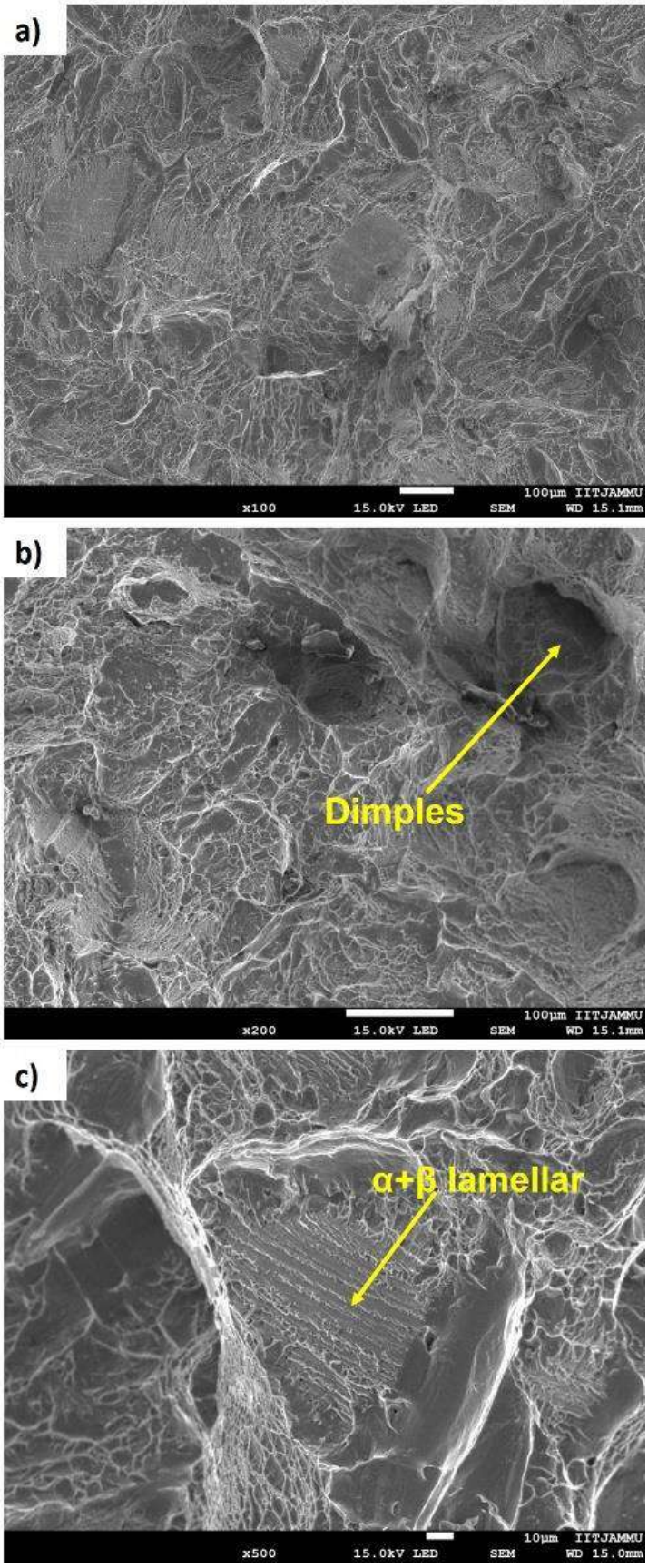

Figure 5. 53: SEM images of the fractured surface of sample E under an inclined orientation

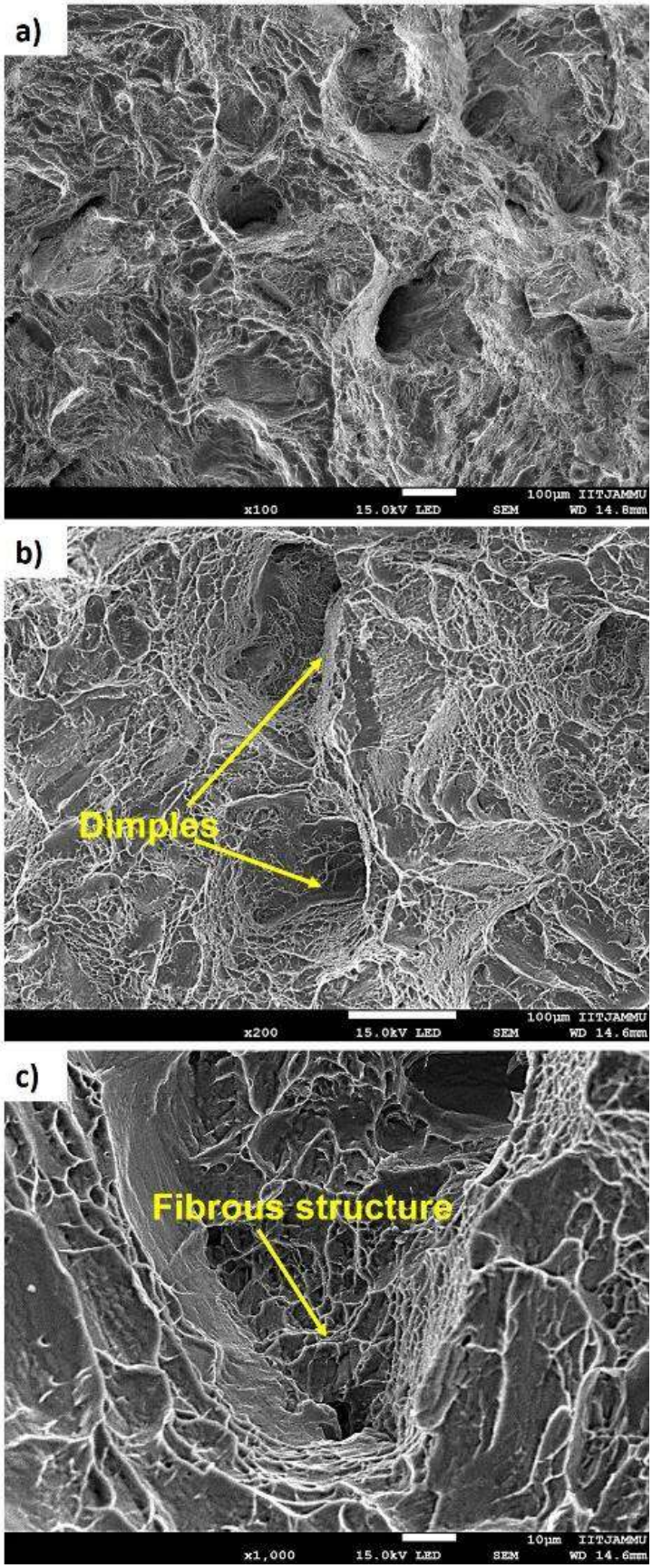

Figure 5. 54: SEM images of the fractured surface of sample E under the vertical orientation

Further, it was observed that vertically oriented samples in as-printed condition showed less ductility compared to horizontal and inclined build samples due to the orientation of pores with respect to the loading direction. Figure. 5.55 shows the LPBF machines utilized by different researchers [51, 52, 85, 90, 118, 219, 221, 222], whereas Figure. 5.55 (a and b) show the differences between the UTS and the elongation of the horizontal and vertical samples, respectively, compared with the results of the literature analysis for as-printed conditions. The data in Figure. 5.55 (a) shows the various characteristics of Ti6Al4V parts that were fabricated using different SLM machines. The UTS and ductility of these components are shown to be inversely related. This relationship is commonly found in other materials that are fabricated through other manufacturing methods. However, the differences between the mechanical strength and the vertical samples' elongation are shown in Figure. 5.55(b). Although the literature clearly states that ductility and UTS vary depending on the process and machine, it is not possible to tell from this that these two factors change regardless of the external conditions. The scattering of these properties might be caused by the orientation of the defects, which locally increases the applied stress to cause a fast fracture.

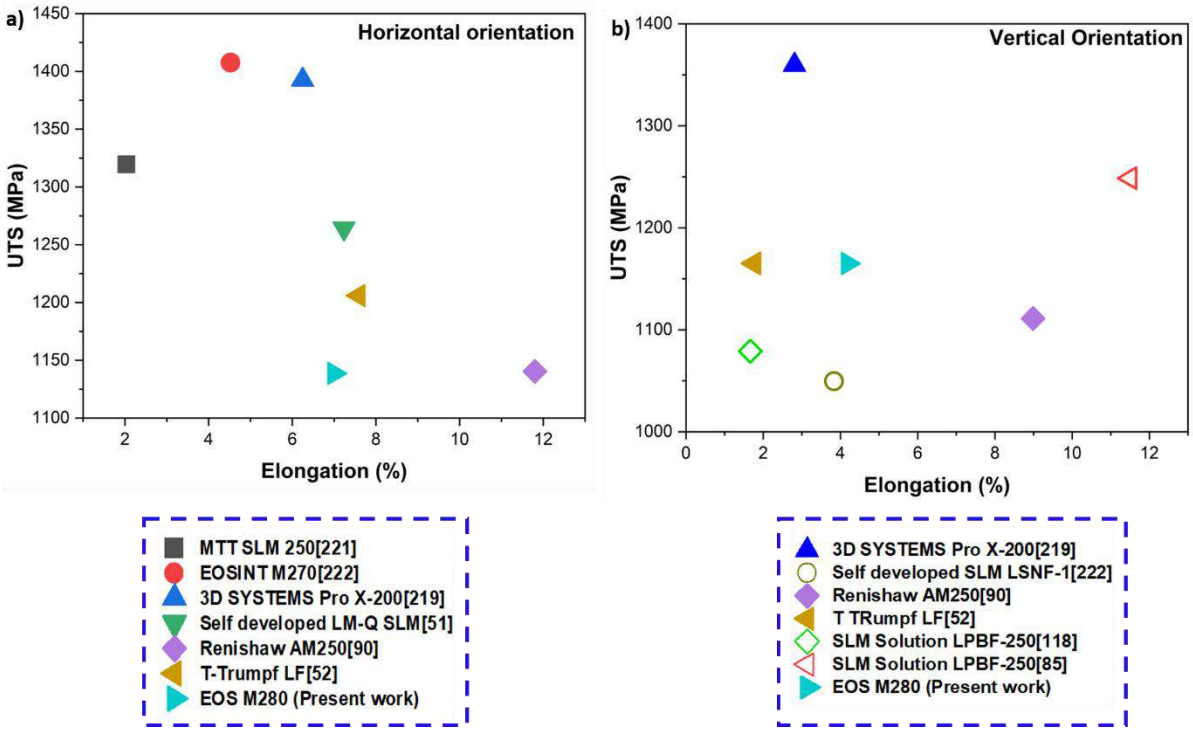

Figure 5. 55: UTS vs Elongation of LPBF-manufactured Ti6Al4V: a) Horizontal orientation; b) Vertical orientation

5.4.3 Fractal dimension analysis of fractured surfaces of Ti6Al4V

To characterize fractured surfaces, FD analysis was found to be promising and adopted invariably in practical situations. It is apparent from Figure. 5.56 that there is a mixed mode fracture in as-printed samples in all three orientations. However, Fig.5.57 shows the ductile fracture in all three orientations of sample E owing to the homogeneous microstructures. The calculated FD and ductility (% elongation) values are shown in Fig. 5.58, which shows that the FD value exhibiting a similar trend with the ductility value. The sample E FD result aligns with the result in the literature for 900°C heat treated LPBF-manufactured Ti6Al4V owing to high ductility [223].

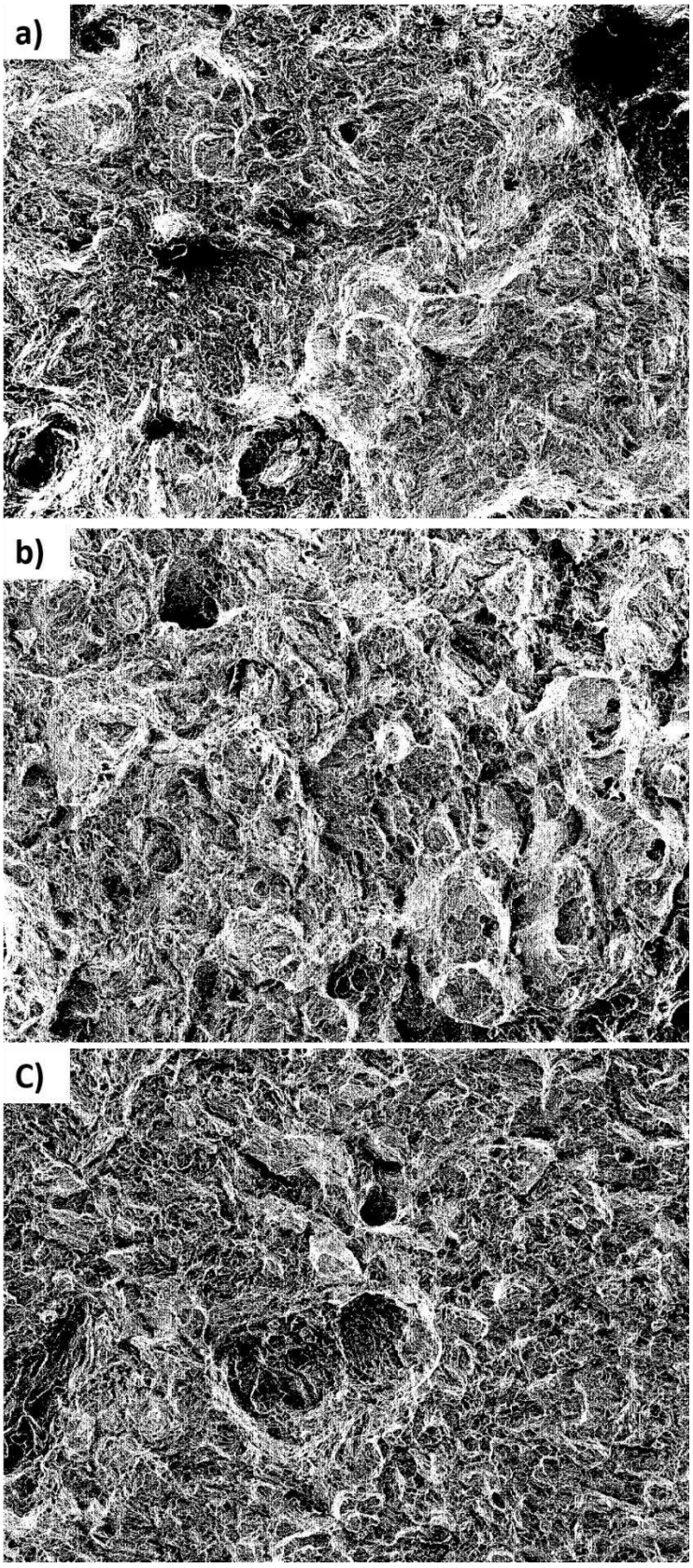

Figure 5. 56: FD analysis of as-printed fractured tensile samples: a) Horizontal orientation; b) Inclined orientation; c) Vertical orientation

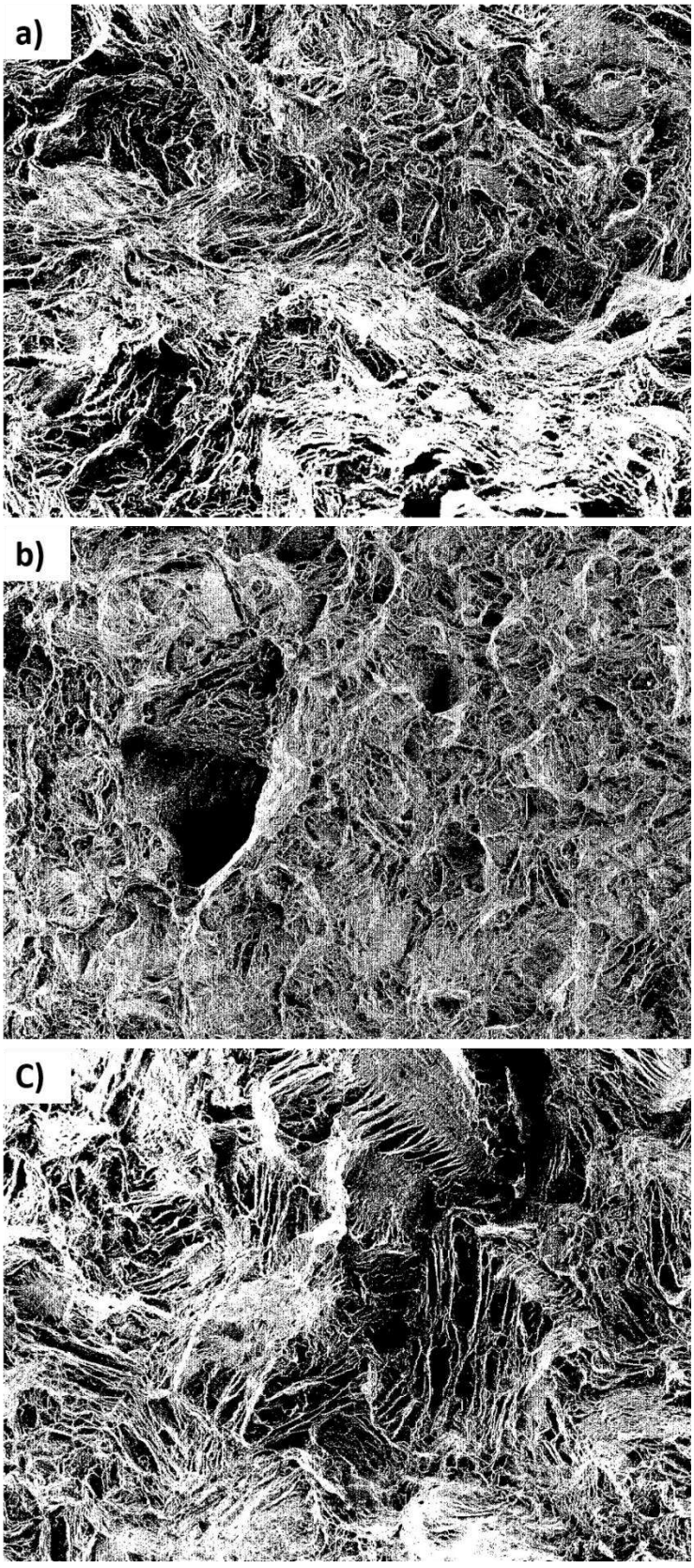

Figure 5. 57: FD analysis of sample 'E' fractured tensile samples: a) Horizontal orientation; b) Inclined orientation; c) Vertical orientation

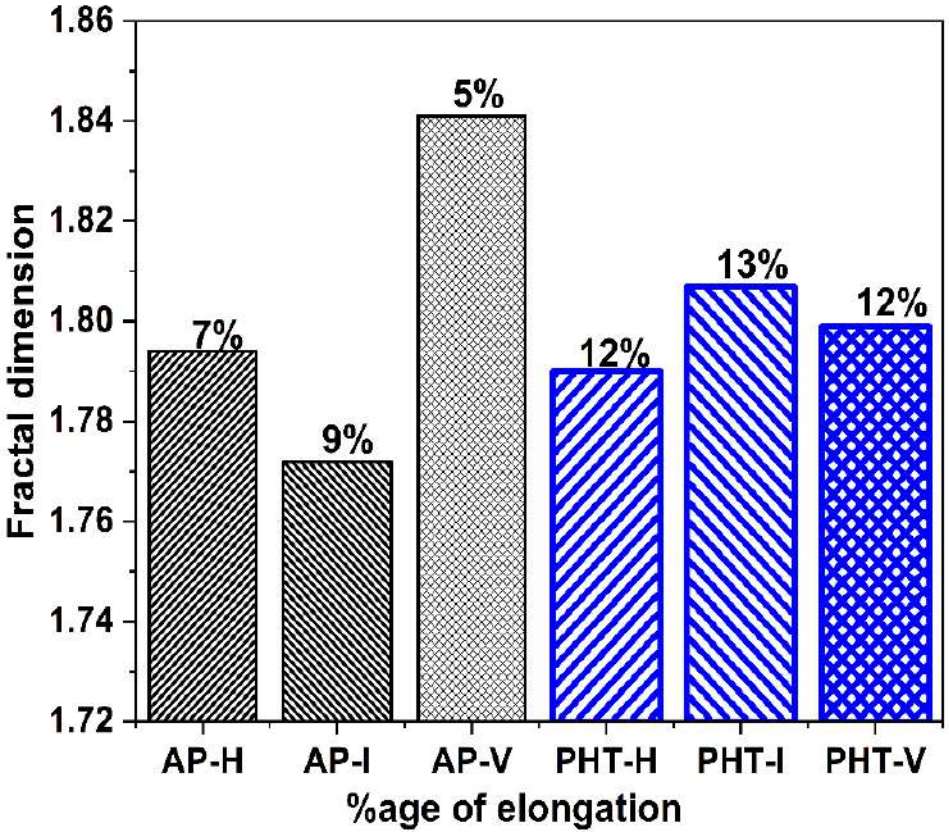

Figure 5. 58: Comparison of fractal dimensions with elongation (ductility) of LPBF-manufactured samples

Further, comparing the FD of LPBF-manufactured as-printed and heat-treated (900°C+2hr+FC)[60], Ti6Al4V fracture surfaces was compared with the present work (as-printed and PHT) FD values. It is interesting to observe that the results exhibited a similar and comparable trend as shown in Figure 5.59. The α lath width of LPBF-manufactured Ti6Al4V increases with increase in heat treatment temperature as shown in Figure 5.26. The α lath width of LPBF-manufactured Ti6Al4V 900°C heat-treated sample increased and showed a FD similar to sample E's FD (~1.7921). Therefore, it can be said that the FD is a quick and convenient way to analyse the fracture surfaces. Moreover, as the PHT temperature increases, the β content in Ti6Al4V also increases. It is important to note that at β grain size around 13.25µm of LPBF-manufactured Ti6Al4V at 900°C heat-treated showing similar FD of sample E whose β grains size 9.65 µm in transverse direction and 17.59 µm in longitudinal direction.

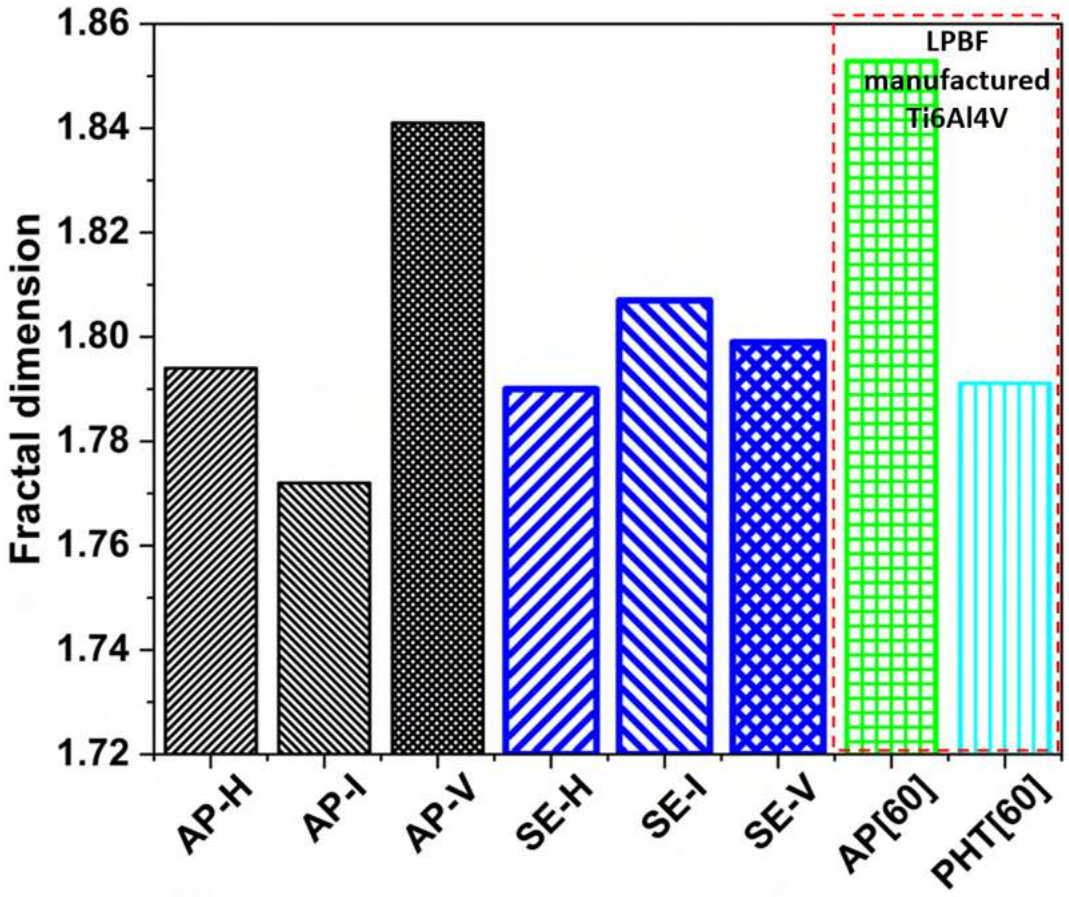

Legend: SE: Sample E

Figure 5. 59: Comparison of LPBF tensile fractured of as-printed and PHT sample [60] with present work

5.5 Influence of PHT with Super β transus temperature on the Fatigue behaviour of LPBF-manufactured Ti6Al4V parts

5.5.1 Fatigue behaviour of LPBF-manufactured Ti6Al4V samples

The fatigue lives for an as-printed sample and sample E in all three orientations are shown in Figure 5.60. It is observed that LPBF-manufactured Ti6Al4V is showing superior fatigue lives compared to the wrought [16] and mill annealed Ti6Al4V [224]. The as-printed sample under inclined orientation shows enhanced fatigue life compared to horizontal and vertical orientation samples due to the high UTS value compared to others. It should be noted that sample E in all three orientations shows better fatigue resistance at a high-stress level (600 MPa) compared to

as-printed samples due to pore size modification leading to the reduction in harmful super micro-pores after PHT at 1050°C.

Further, it is well established that lamellar microstructure showed better fatigue behaviour than bimodal microstructure[225]. The temperature increase of the PHT for sample E has resulted in the expulse of vanadium atoms, which nucleates the α phase at the boundaries. This also triggers the formation of a β phase at these boundaries. It is reported that while mechanical loading, the slip length formed in α is restricted by the formed β phase, which could enhance the mechanical loading bearing ability[60]. The super micropores having a pore size greater than 10 μm are detrimental to the fatigue performance[114]. It is observed that the fatigue limit for all the samples under as-printed and PHT conditions is 400 MPa, correlating with reported literature values[220, 226]. Moreover, sample E in three orientations have shown a relatively higher fatigue limit (of 450 MPa) compared to the as-printed samples (400 MPa) due to beneficial microstructural features and the pore size modification (reduction of super micro-pores) in sample E. Further, the comparison between different AM processes (like DED[215], WAAM[215] and EBM[217] with present work data is given in Figure 5.61, where sample E showed better fatigue behaviour compared to other AM and traditional manufacturing processes.

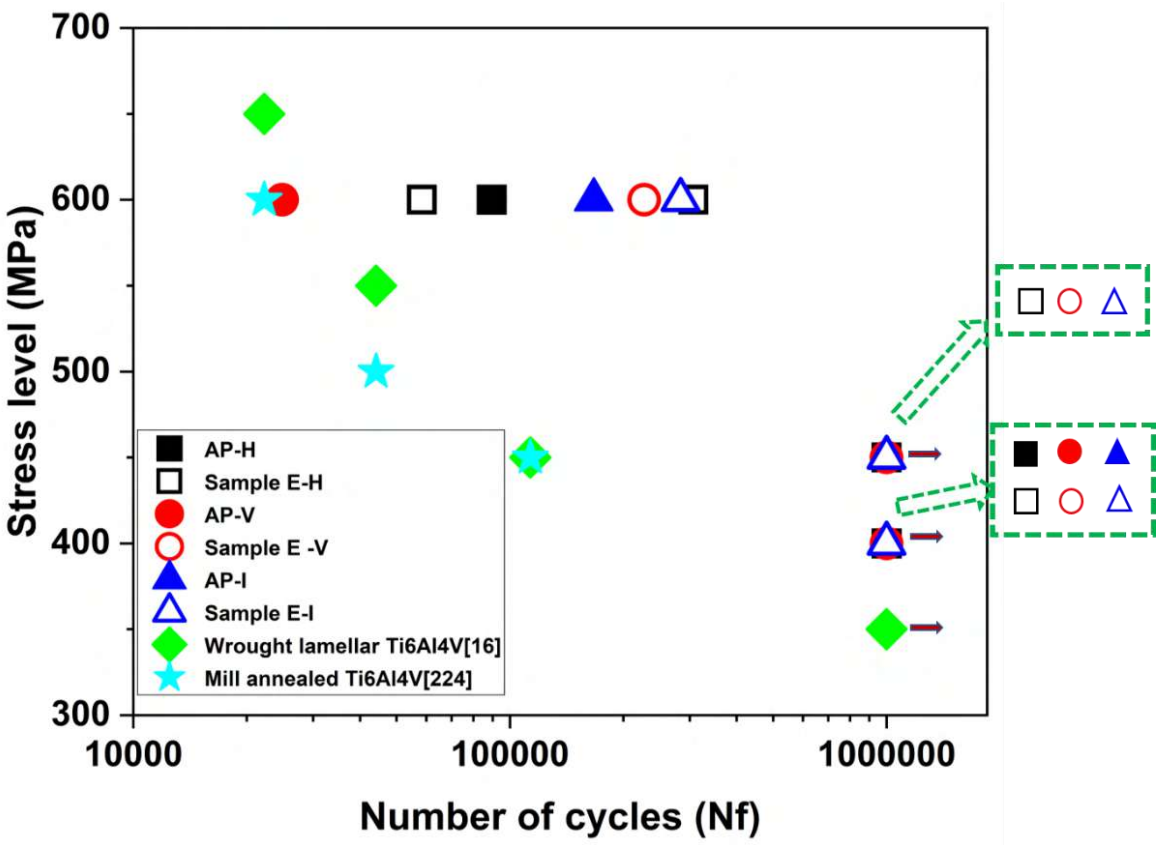

Figure 5. 60: Fatigue lives of as-printed and sample E under three build orientations, (Solid arrows: Run out; Hollow arrows: Magnified view of different sample conditions)

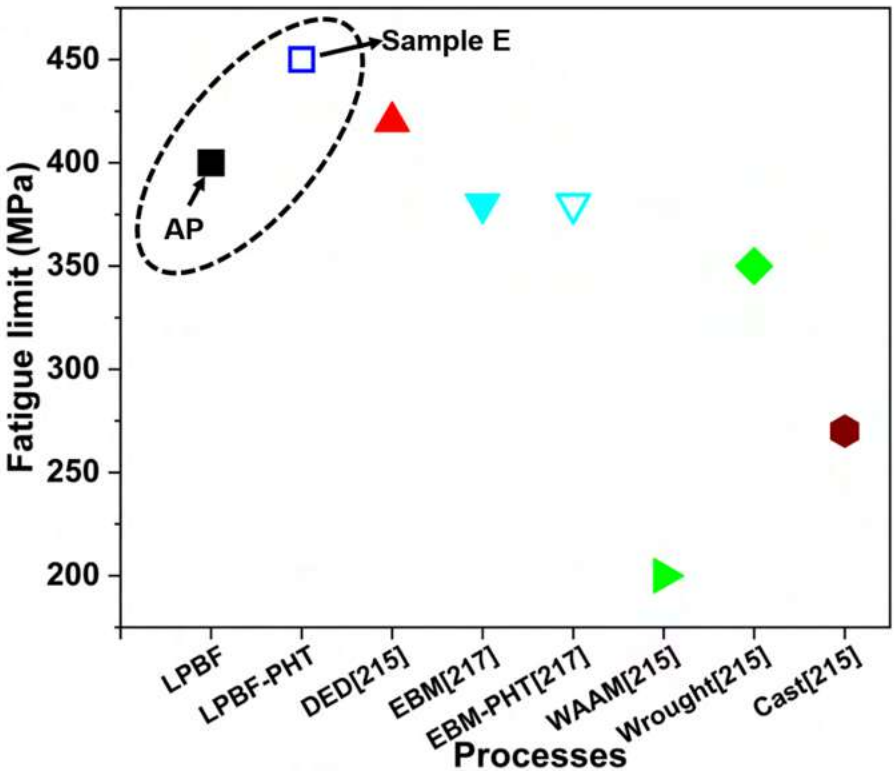

Figure 5. 61: Comparison of fatigue lives between different AM processes and present work results [215, 217]

Moreover, the porosities act as stress concentration sites where the crack initiates and degrades the fatigue life. However, there is no correlation between a material's fatigue life and defect size; Muhammad Shamir et al. [227] showed that large defect sizes reduce the fatigue life of wire arc additive manufactured (WAAM) Ti6Al4V alloy where porosity ranges from 40-220 µm. It was observed that a 20 % decrease in defect size enhances the 100% fatigue life. Nevertheless, this trend was not true for all the samples tested at different defect sizes. Furthermore, the location of pores also plays a key role, along with the pore size, in determining fatigue resistance [227]. Generally, surface defects are more prone to initiate cracks. A study by Williams et al. [228] showed the effect of pore size on fatigue crack initiation of electron beam melted Ti6Al4V alloy. The pore size ranging from 20 µm to 170 µm was observed, and the study revealed that the size of the pores affected the fatigue life. The researchers noted that the larger the pores, the less fatigue they exhibited. Moreover, Murakami [114] showed that defects found in pores are comparable to cracks in the same stress intensity. Murakami's equation exhibited the maximum stress intensity (K_{max}) caused due to the pores is given below as equation (5.12).

$$\mathbf{k_{max}} = 0 \cdot 5 \times \sigma_{\infty} \times \sqrt{\pi\sqrt{A}n} \qquad (5.12)$$

Where σ_∞ is the global applied stress, and A_n is the pore area normal to the applied stress. According to Murakami's equation, the constant 0.5 increases to 0.65 when the defect is on the surface, indicating that greater stress intensity arises from the surface defect [228]. It is important to emphasize that PHT has reduced the present study's super-micropores and inter-micropores. Therefore, it is presumed that PHT can offer superior fatigue resistance to LPBF Ti6Al4V. In addition, due to the low surface energy associated with super-micropores, they can still convert to inter-micropores and improve fatigue life. A comparison of fatigue lives with tensile properties of LPBF manufactured Ti6Al4V in as-printed and PHT conditions is presented in Figure 5.62 to elucidate the above statement. This Figure depicts that the fatigue strength does not essentially increase with tensile strength; however, there is a stronger correlation with ductility enhancement. Similar results are reported for the LPBF-manufactured aluminium alloys[229].

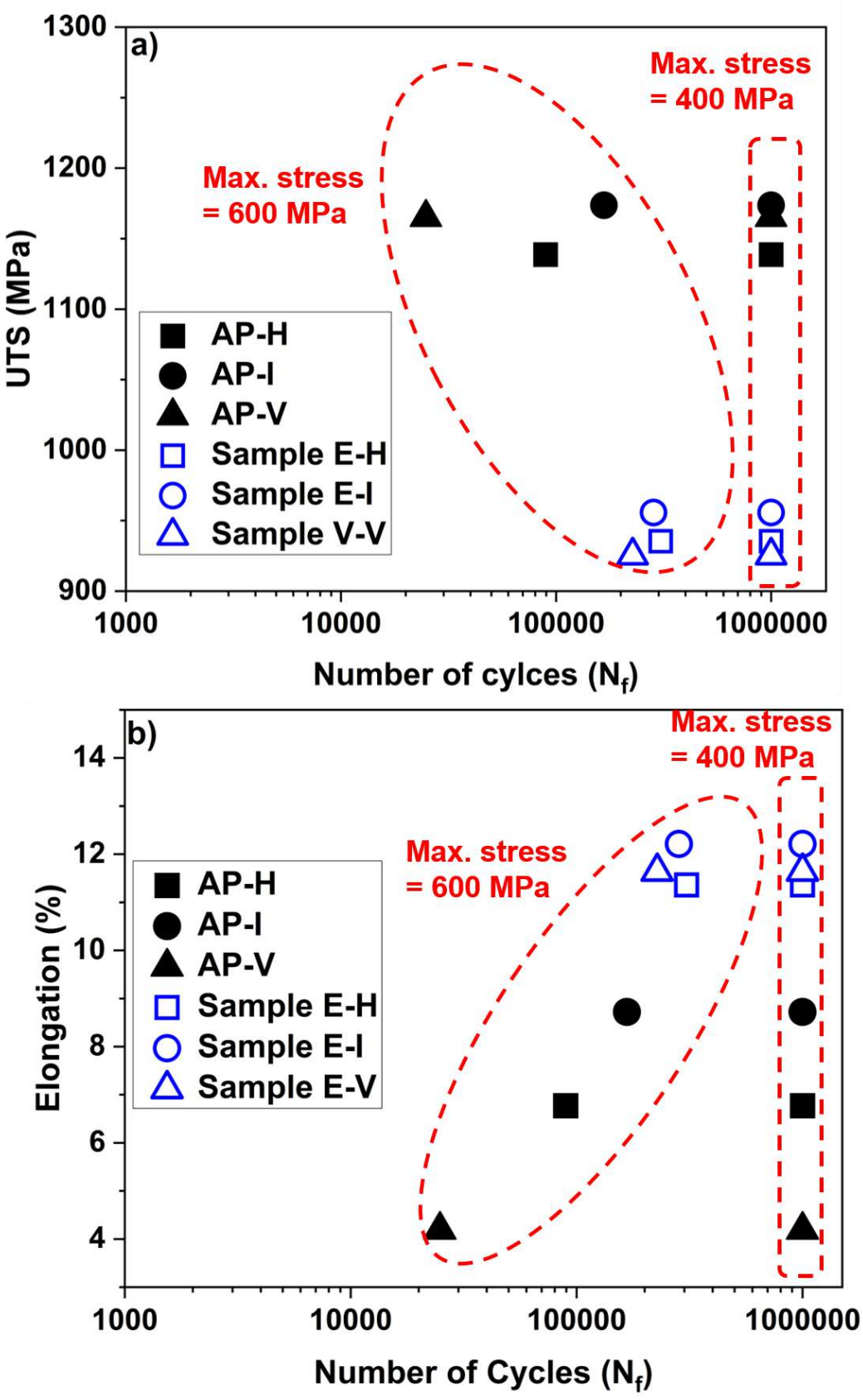

Figure 5. 62: Fatigue lives comparison of LPBF manufactured as-printed samples and sample E under three orientations: a) UTS; b) % age of elongation

5.5.2 Fractographic analysis of fatigue fractured surfaces of Ti6Al4V

ImageJ software measures the crack initiation location length from the sample surface for as-printed samples and samples 'E'. The fractography of the as-printed in the vertical orientation is shown in Figure 5.63. The crack initiated from the surface (~ 90 μm from the surface) could be attributed to the presence of a micropore/void. Moreover, the micro voids are observed samples.

Figure 5.64 depicts the fractography of the as-printed sample in an inclined orientation. It is noticeable from Figure 5.64 that the crack has initiated ~ 100 μm from the sample's surface and propagates inside as the fatigue cycles progressed. The facets-like features can be observed in Figure 5.64(b), which may be due to the brittle fracture of the as-printed inclined sample experienced owing to the α' phase. Further, the micro voids and partially melted particles are visible in Figure 5.64(c), acting as a stress concentration site and reducing the fatigue lives of the samples.

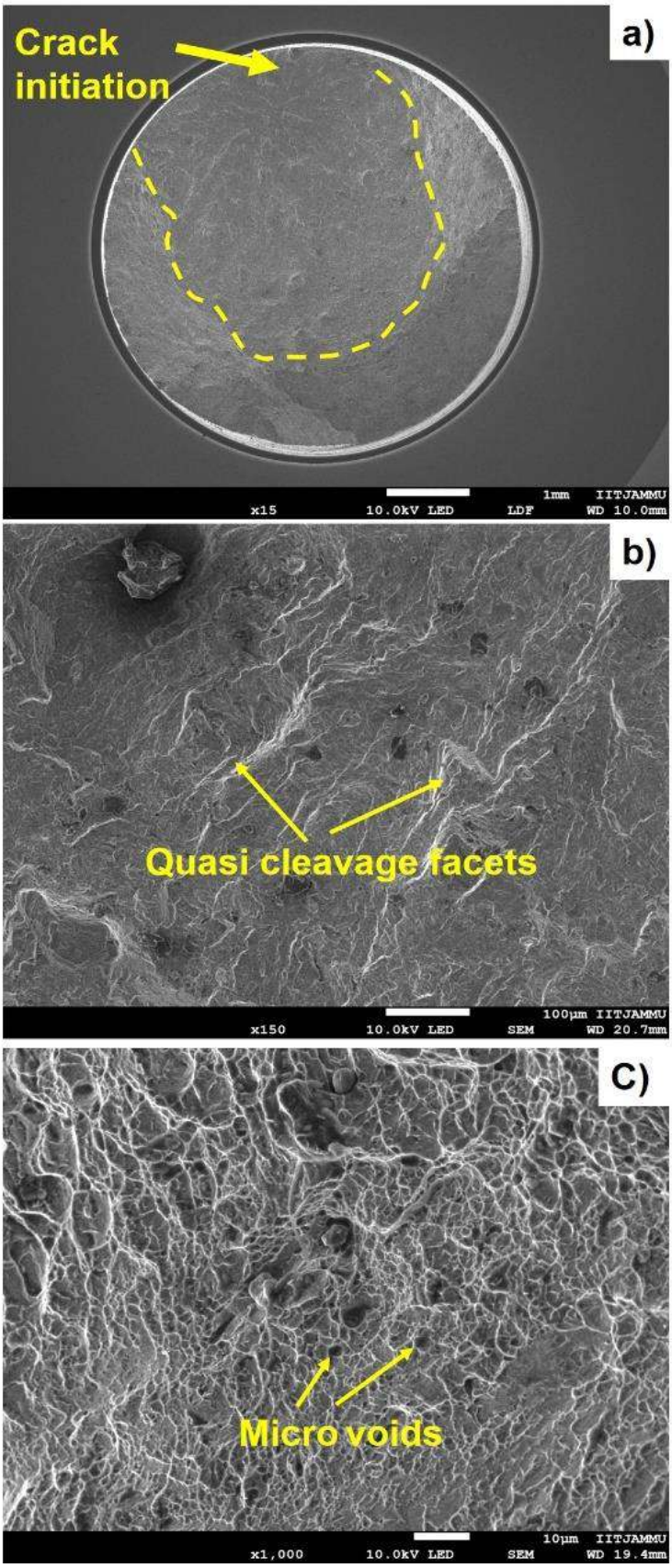

Figure 5. 63: SEM images of the fractured surface of the as-printed sample under vertical orientation

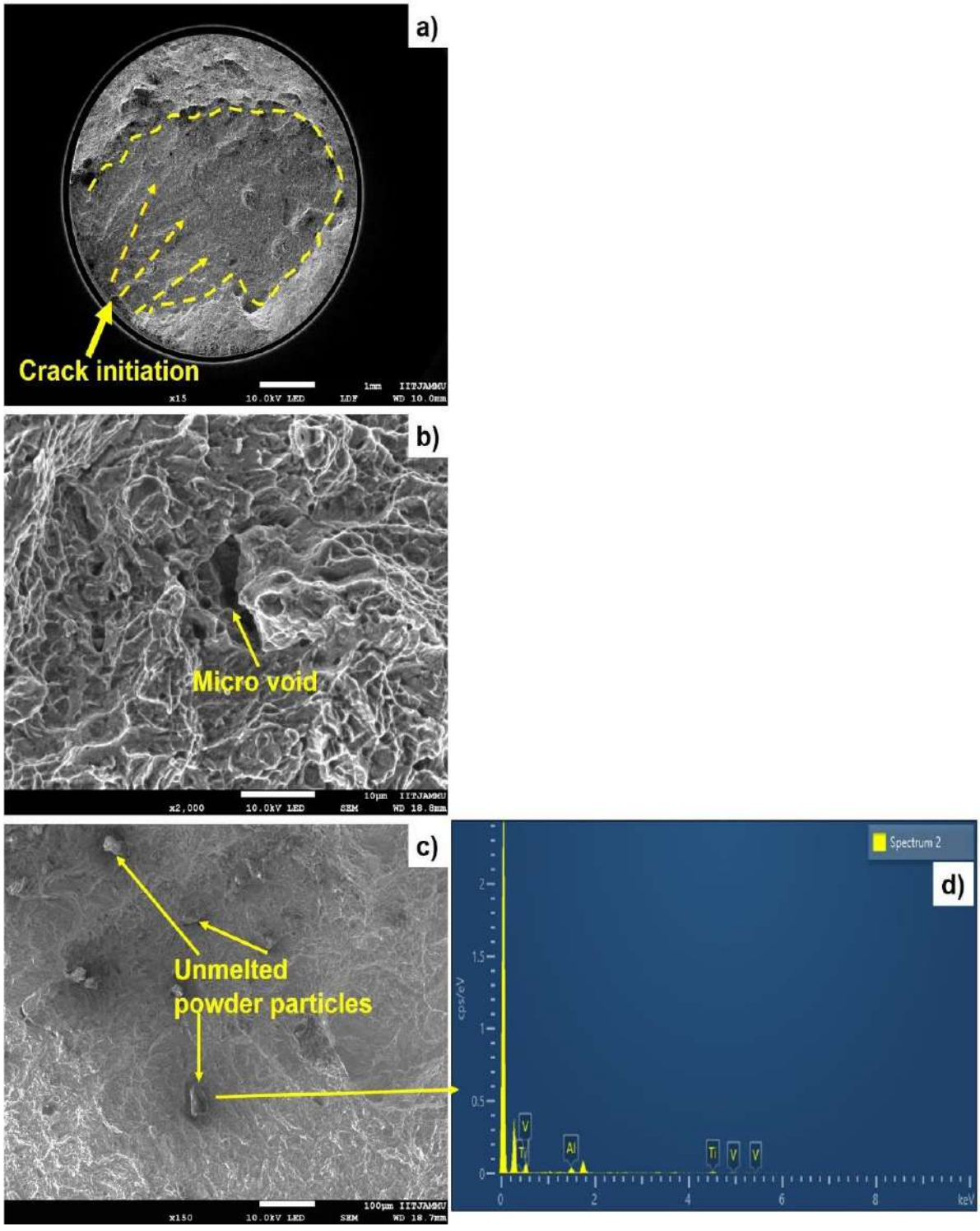

Figure 5. 64: SEM images of the fractured surface of as-printed sample under an inclined orientation: a) low magnification; (b-c) high magnification; d) EDS of un-melted powder particle

The fracture surface of sample E under vertical orientation is shown in Figure 5.65. The crack initiation site is observed at the sub-surface (~ 200 µm from the surface), which correlates to the microstructural features and reduced porosity in sample E due to PHT. It has been studied

that the presence of a fully-lamellar microstructure in Ti6Al4V alloy can also contribute to the formation of cracks in the subsurface[60]. The fatigue cracks can also start at the boundary between the α and β phases, depending on the factors that affect their formation[92]. Some of these include the presence of flaws in the matrix, the microstructural inhomogeneity of the surface, and the presence of secondary particles[218, 230, 231].

The striation marks are observed from the subsurface of the sample, which indicates the incremental growth of the crack towards the centre of a surface, as shown in Figure 5.65(b). The fracture surfaces for sample E in inclined orientation are shown in Figure 5.66. The crack initiation site on the subsurface (~ 250 μm from the surface) is similar to sample E in the vertical orientation. The PHT has reduced the surface porosities [183], thus increasing the fatigue resistance compared to the as-printed samples. However, few quasi-cleave facets are visible in sample E, as shown in Figure 5.66(c).

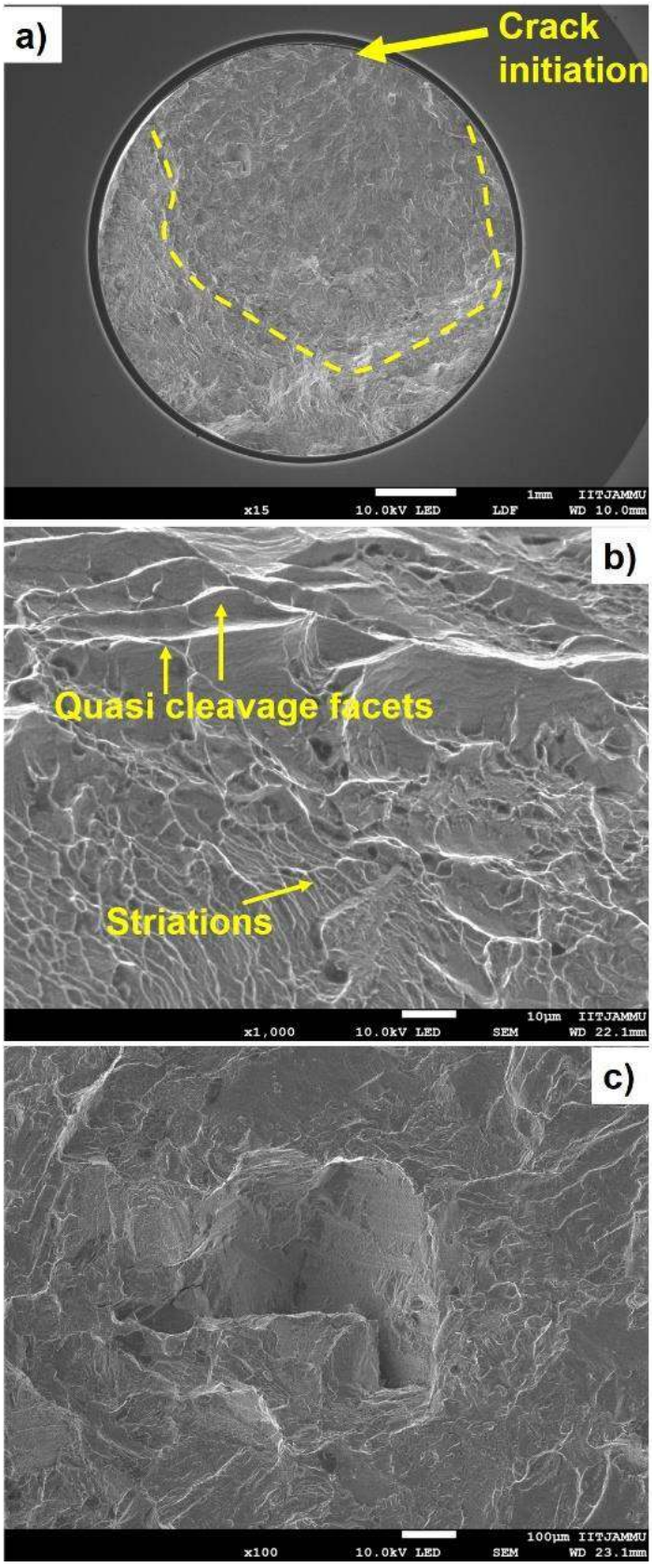

Figure 5. 65: SEM images of the fractured surface of sample E under vertical orientation: a) low magnification; b-c) high magnification

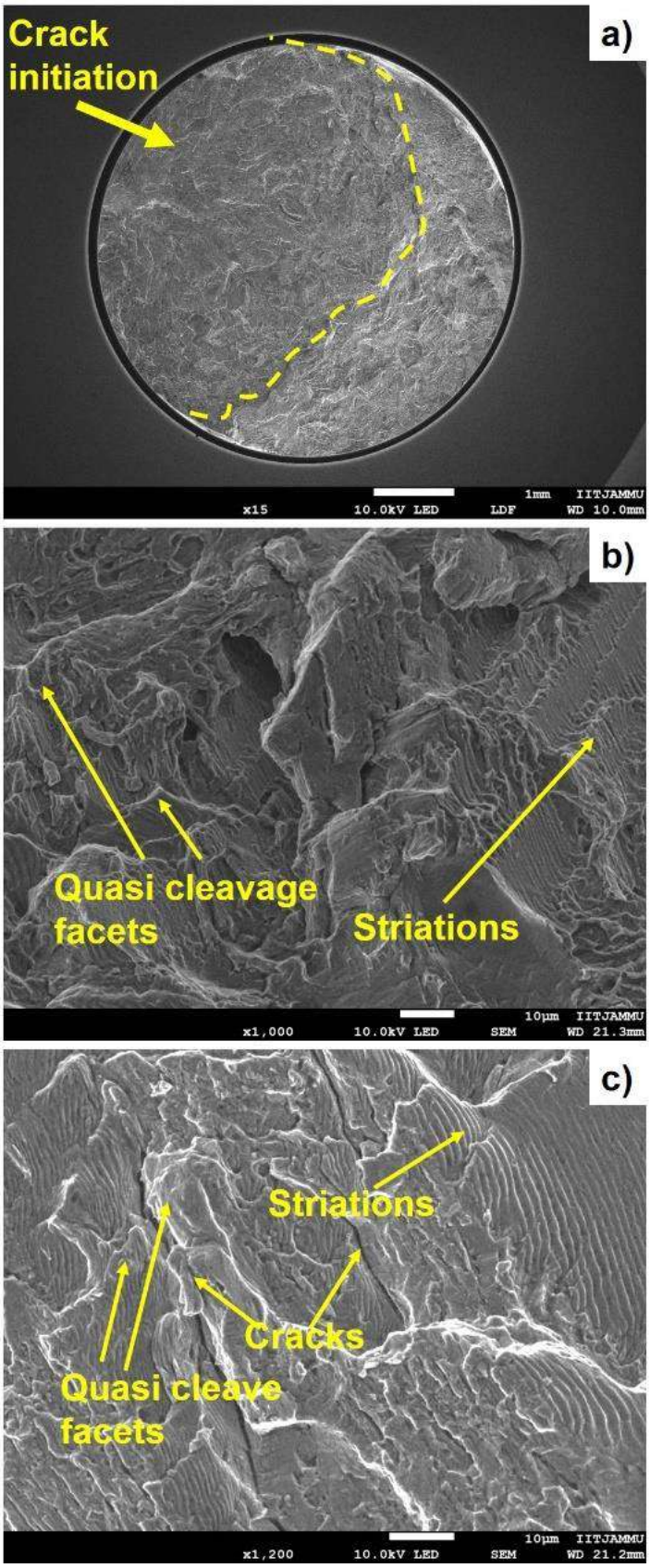

Figure 5. 66: SEM images of the fatigue fracture surface of sample E under inclined orientation: a) low magnification; b-c) high magnification

It could be expected that the residual pores in LPBF-manufactured samples do not alter the tensile strength considerably, provided the pore size is below a threshold value. In contrast, fatigue properties are greatly influenced by the presence of pores. Besides, LPBF-manufactured samples with high ductility may offer a superior fatigue crack propagation resistance rate through the grains. The microstructure and porosities are the two influencing factors for the HCF performance of a material. The as-printed Ti6Al4V samples show high strength because of α' martensite; however, it offers an inferior fatigue life compared to sample E despite high strength.

Similar results were observed in another study; compared to the as-printed sample, samples subjected to PHT exhibited better fatigue properties[118]. They noted that the reduced residual stresses and an increased β phase improved fatigue resistance. Moreover, the lamellar (α+β) microstructure observed in sample E is considered to have better HCF properties than the equiaxed and bimodal microstructure of Ti6Al4V samples [122]. In another study, due to defect-free microstructure, the heat-treated Ti6Al4V performed better in HCF properties[115].

The fatigue lives of sample E in all three orientations have improved and resulted in almost a similar number of cycles to failure (N_f) values, as shown in Figure 5.60. It suggests that sample E exhibits nearly isotropic fatigue behaviour. The difference in fatigue behaviour among horizontal, vertical and inclined directions is due to the difference in microstructures (in transverse and longitudinal directions), defects and porosities distribution which dictates the material's structural integrity. The porosities in vertical build orientation are considered higher owing to the high number of interlayer porosities. However, some studies showed the superior fatigue performance of LPBF-manufactured samples under vertical orientation[87, 88].

Further, the reduction of pore size (from super micropore to inter micropore) in sample E in all orientations enhances the fatigue behaviour compared to the as-printed samples. It is important to note that sample E has shown a quasi-cleavage fracture where the river patterns are parallel to the stable crack growth region during fracture, which is responsible for the higher fatigue propagation resistance. This type of fracture morphology reveals that heat-treated Ti6Al4V enhance fatigue performance by modifying the microstructure, which is well corroborated by X.Yan et al. [60].

Moreover, the fatigue limit of sample E is enhanced in all three orientations and is marginally improved by 50 MPa. A similar result was reported that heat-treated Ti6Al4V showed high

fatigue strength due to the microstructure change [119]. Figure 5.67 depicts the schematic representation of crack propagation and growth mechanism encountered by as-printed and PHT samples in the present work.

Widmanstatten microstructure exhibits a higher fracture toughness due to the lamellar grains performing as crack deflectors [232]. A fully lamellar α+β microstructure formed due to the subtransus heat treatments is anticipated to deliver superior performance in fracture-critical end-use applications.

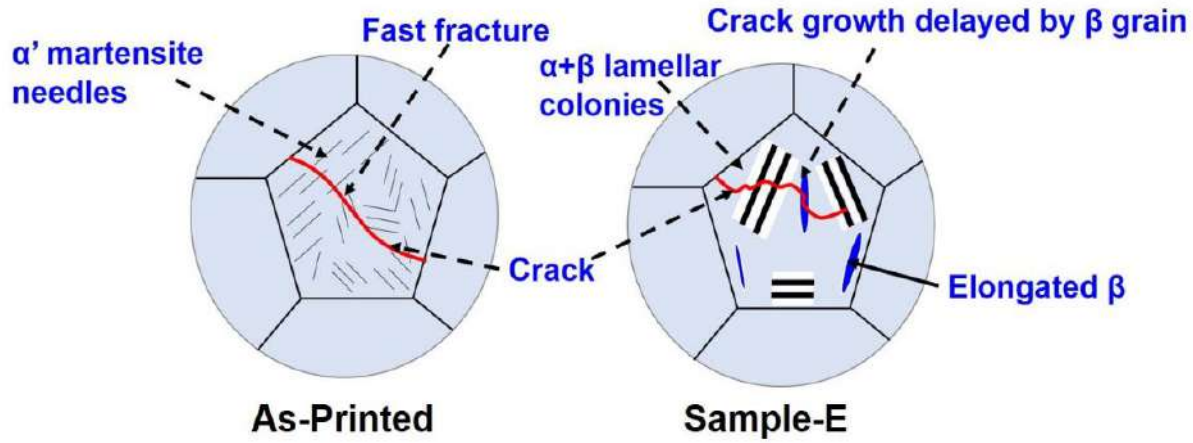

Figure 5. 67: Schematic shows the fatigue behaviour mechanism in as-printed sample and sample E

5.5.3 Fractal dimension analysis of fatigue fractured surfaces of Ti6Al4V

The FD analysis on fractured surfaces for as-printed samples and sample E under different orientations are shown in Figure. 5.68(a-c) and Figure 5.69(a-c), respectively. It is noticeable from Figure 5.68(a-c) that there is a difference in crack propagation between three oriented samples owing to the anisotropic behaviour for as-printed samples. However, the crack propagation behaviour is similar for sample 'E' in all three orientations, as indicated in Figure 5.69(a-c).

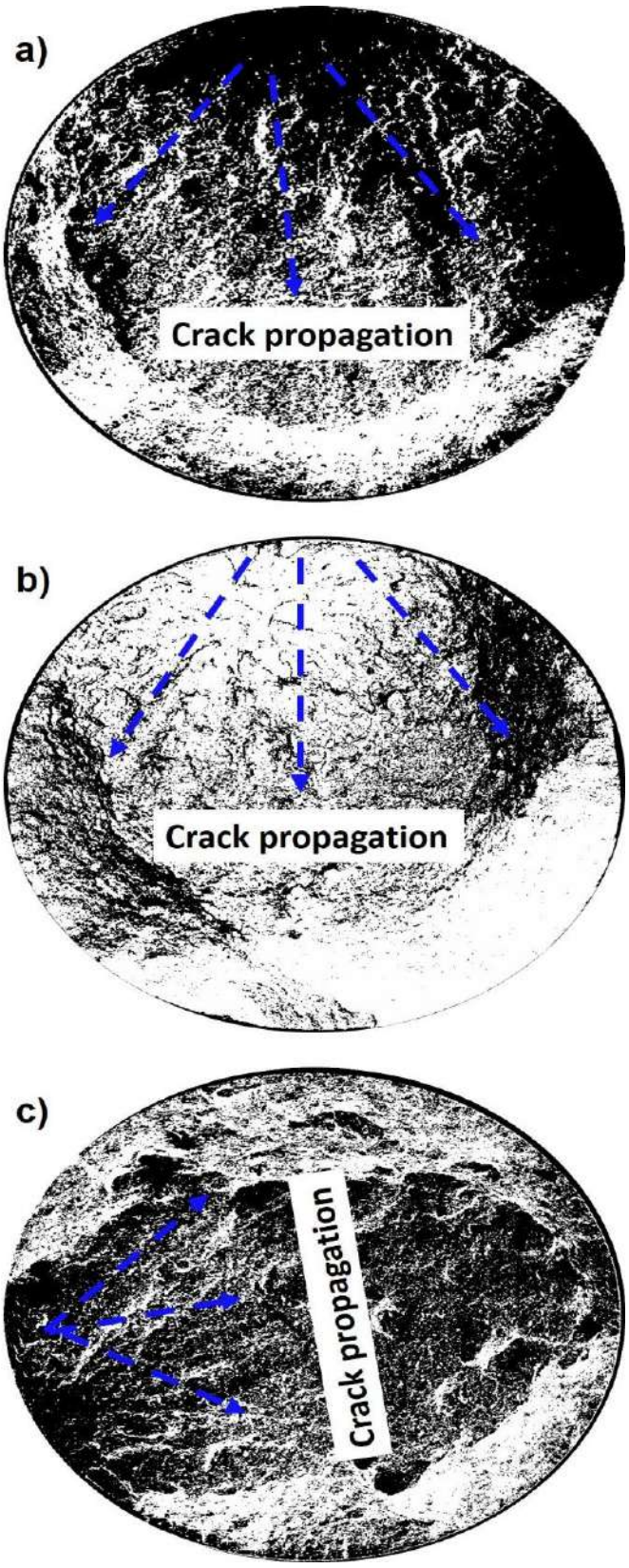

Figure 5. 68:FD analysis of as-printed samples: a) Horizontal orientation; b) Inclined orientation; c) Vertical orientation

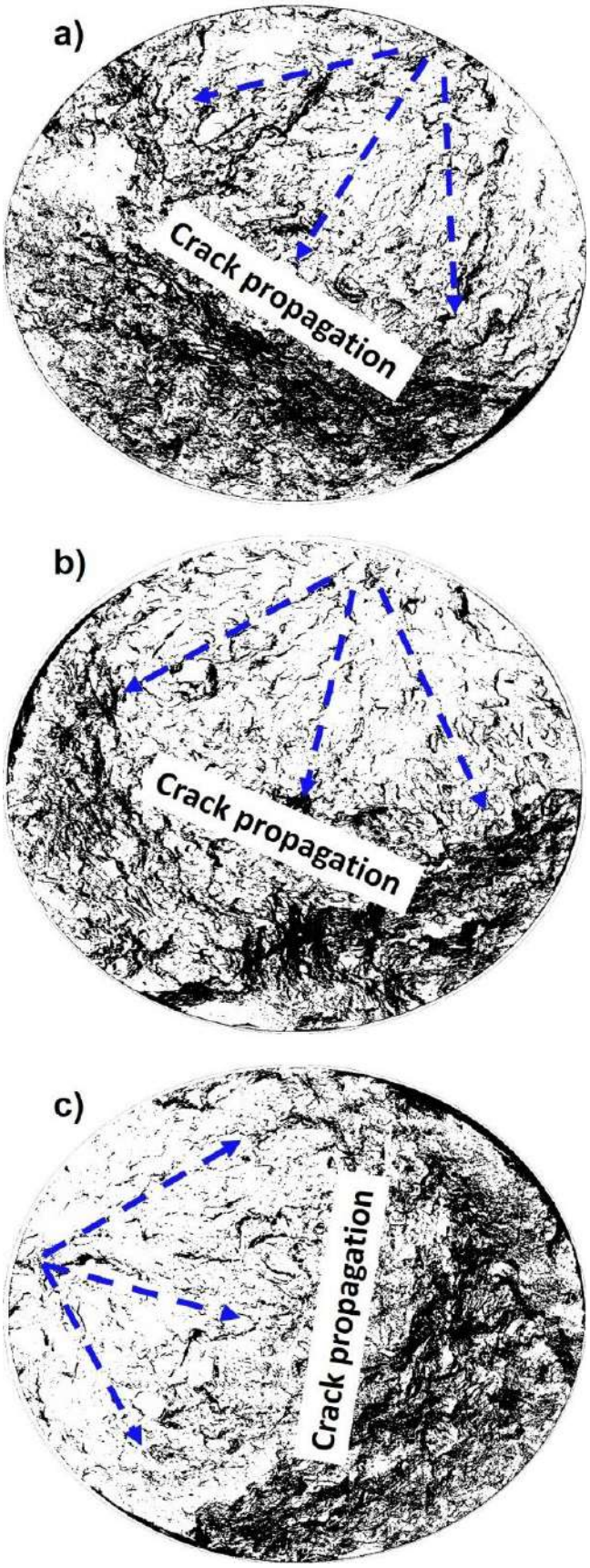

Figure 5. 69: FD of sample 'E': a) Horizontal orientation; b) Inclined orientation; c) Vertical orientation

Figure 5.70 shows the FD values for fractured surfaces under the different orientations of fatigue-tested conditions, where it can be seen that the as-printed samples show variations in the FD values. However, sample 'E' showed almost similar FD values irrespective of build orientations. It is important to mention that as the heat treatment temperature increases the α lath width decreases as shown in Figure. 5.26. However, the FD for LPBF-manufactured Ti6Al4V sample subjected to PHT at 1050°C were almost similar showing the ductile fracture despite of decreasing the α-lath width at higher temperatures. A similar kind of results were also found and well corroborated with the literature[233]. Moreover, the increased β size of mill annealed Ti6Al4V showed a ductile fracture and exhibits the FDs which were similar to the sample E FD in all three orientations.

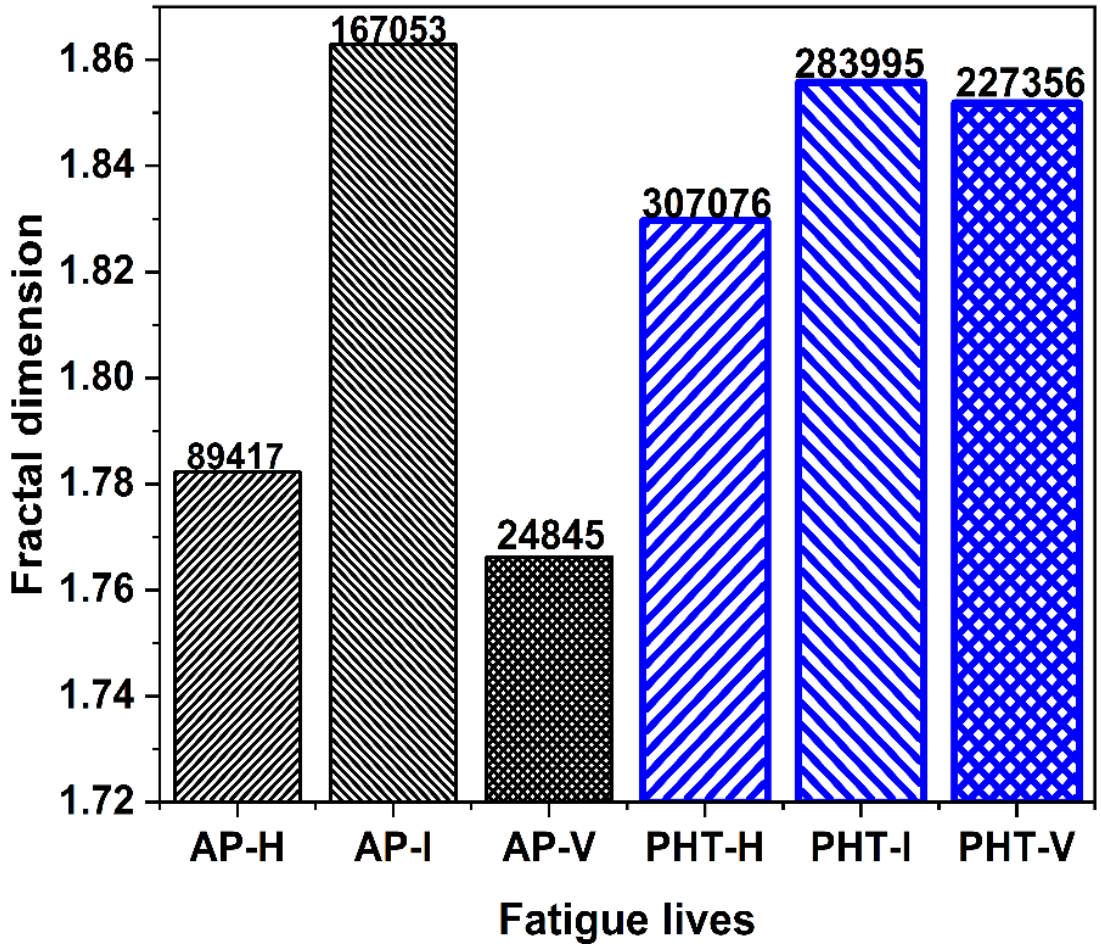

Figure 5. 70: FD values correlated with fatigue lives at different conditions of LPBF-manufactured Ti6Al4V samples

Further, it is considered that the FD increases as the distance from the surface of the sample increase [130]. In sample 'E', FD values are high (under horizontal and vertical) than in as-

printed samples, which shows that the crack propagation distance is longer, which could be due to delay by the β phase where the plastic zone ahead of a crack tip could create a tortuous crack length[234]. Moreover, the crack propagation rate in as-printed samples in all three orientations is considered high owing to the fast fracture due to the brittle behaviour of α' martensite. The FD values of as-printed samples are less compared to the samples subjected to PHT conditions, which shows that the crack propagation rate in as-printed conditions was high. It is well corroborated by the results reported by [128].

Moreover, the FD analysis was carried out for LPBF-manufactured Ti6Al4V in as-printed and heat-treated conditions [60] where the FD values was closely matching with present work FD value for fatigue fractures as shown in Figure. 5.71. Further, the FD value of as-printed fatigue fracture surface from literature were also following the similar trend with the present work [60, 121]. Therefore, the FD approach is convenient and reliable in analysing the fractography of the fractured surfaces. Moreover, it is interesting to note that the FD technique can capture the build orientation effect in the as-printed samples and isotropic behaviour in PHT sample 'E'.

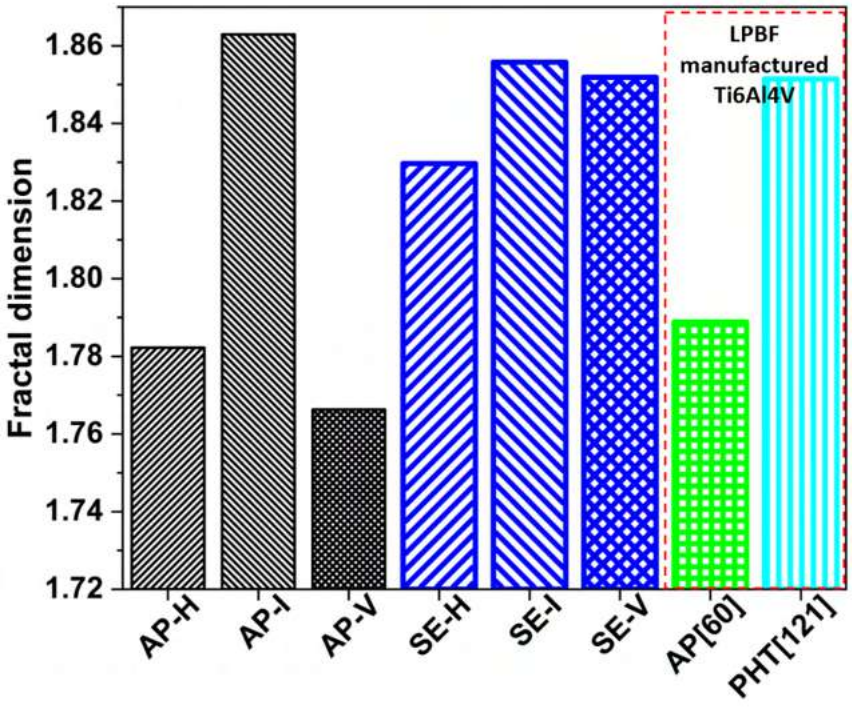

Figure 5. 71: Comparison of LPBF tensile fractured surface of the as-printed and PHT samples [60, 121] with present work data

5.6 Effect of PHT with Super β transus temperature on the Damping Behaviour of LPBF-manufactured Ti6Al4V Thin Rotor Blade

5.6.1 Damping behaviour of LPBF-manufactured Ti6Al4V thin flat samples

In present work sample E was chosen for damping evaluation owing to its high hardness and high β phase in it favourable for high ductility among other PHT executed samples. However, sample A, B and C were also evaluated for comparison with the thin flat geometry.

The damping ratio of the samples under as-printed and PHT conditions at mode shapes (1 and 2) was evaluated using the half-power bandwidth method, as shown in Table 5.8 and Figure 5.72. It is observed that sample E exhibited a higher damping ratio compared to the other PHT conditions. Sample E revealed 30% and 140% higher damping ratios than as-printed in mode shape one and two, respectively. Further, sample C showed 21% and 98% higher damping in mode shapes one and two compared to the as-printed samples. Interestingly, sample A displayed a marginally low damping ratio, around 12% in mode shape one compared to the as-printed sample. Similar results were observed where sample A showed less damping compared to the as-printed sample owing to the presence of α in (α+β) lamellar, whereas in the as-printed condition, α' in β grains favours the high damping [142]. However, mode shape 2 of sample A at high frequency showed a higher damping ratio of around 98% compared to mode two of the as-printed sample.

Table 5. 8: Damping ratio of as-printed sample and PHT executed Ti6Al4V thin flat samples

Conditions	Mode shape	Frequency	Damping ratio (ξ)
As-printed	Mode 1	1457	0.100
As-printed	Mode 2	3552	0.110
Sample A	Mode 1	1462	0.089
Sample A	Mode 2	3557	0.216

Sample C	Mode 1	1450	0.121
Sample C	Mode 2	3586	0.218
Sample E	Mode 1	1434	0.136
Sample E	Mode 2	3564	0.264

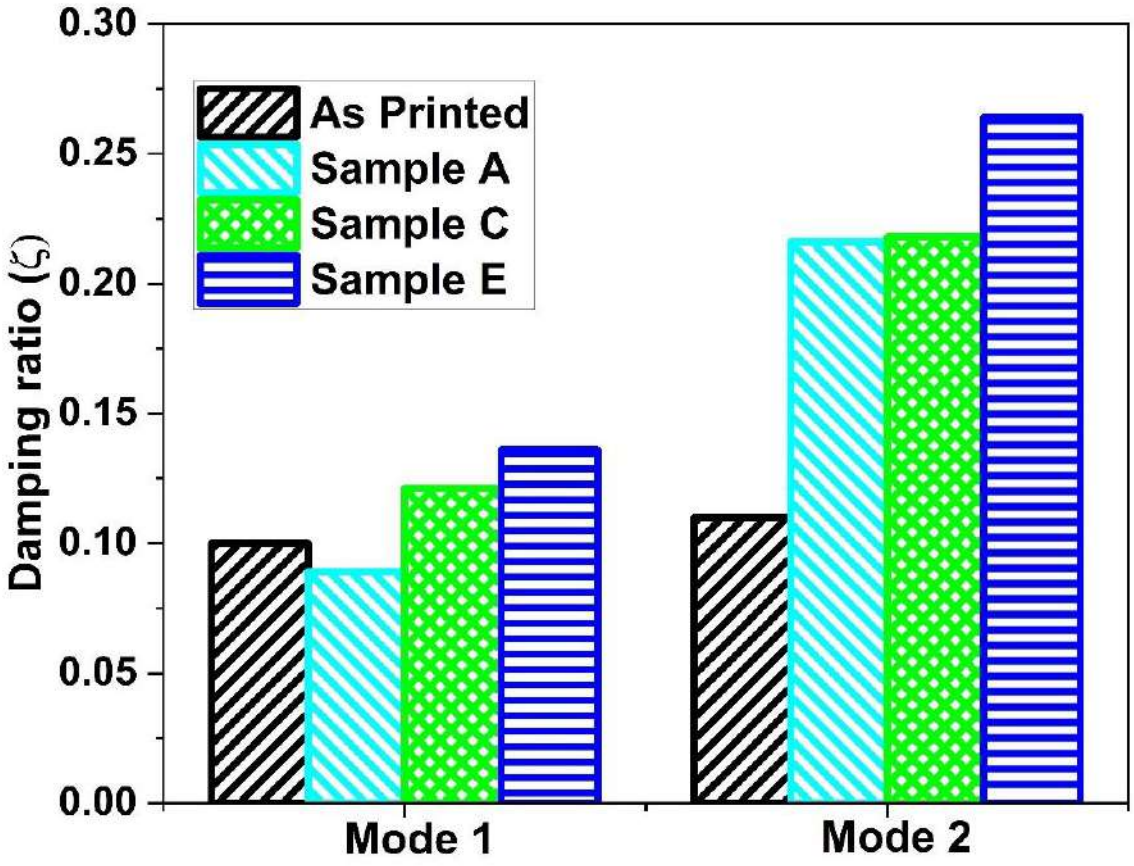

Figure 5. 72: Damping ratio vs frequency of thin flat Ti6Al4V samples

Figure 5.73(a-d) shows a frequency response function (FRF) of as-printed and heat-treated Ti6Al4V thin plate samples. The frequency response function (FRF) is a frequency-based measurement system used to find the resonant frequencies, damping ratio and different mode shapes of a vibrating system. Figure 5.73(a-d), shows peaks of natural frequencies of the LPBF-

manufactured Ti6Al4V. Damping is proportional to the width of the peaks; the wider the peak, the heavier the damping. It is apparent from Figure 5.73(a-d) that sample E shows the highest damping among all samples in all two mode shapes (1 and 2). A mode shape is determined by the phase and amplitude of multiple FRFs acquired to a standard reference.

Moreover, the logarithmic decrement diagrams for as-printed and PHT conditions are shown in Figure. 5.74(a-d). The amplitude dissipation for sample E occurs in around 0.3 seconds when the hammer impacts the specimens resulting in higher damping than the other samples. It is well established that the higher β content in Ti6Al4V is also helping in releasing the strain energy within the material[138].

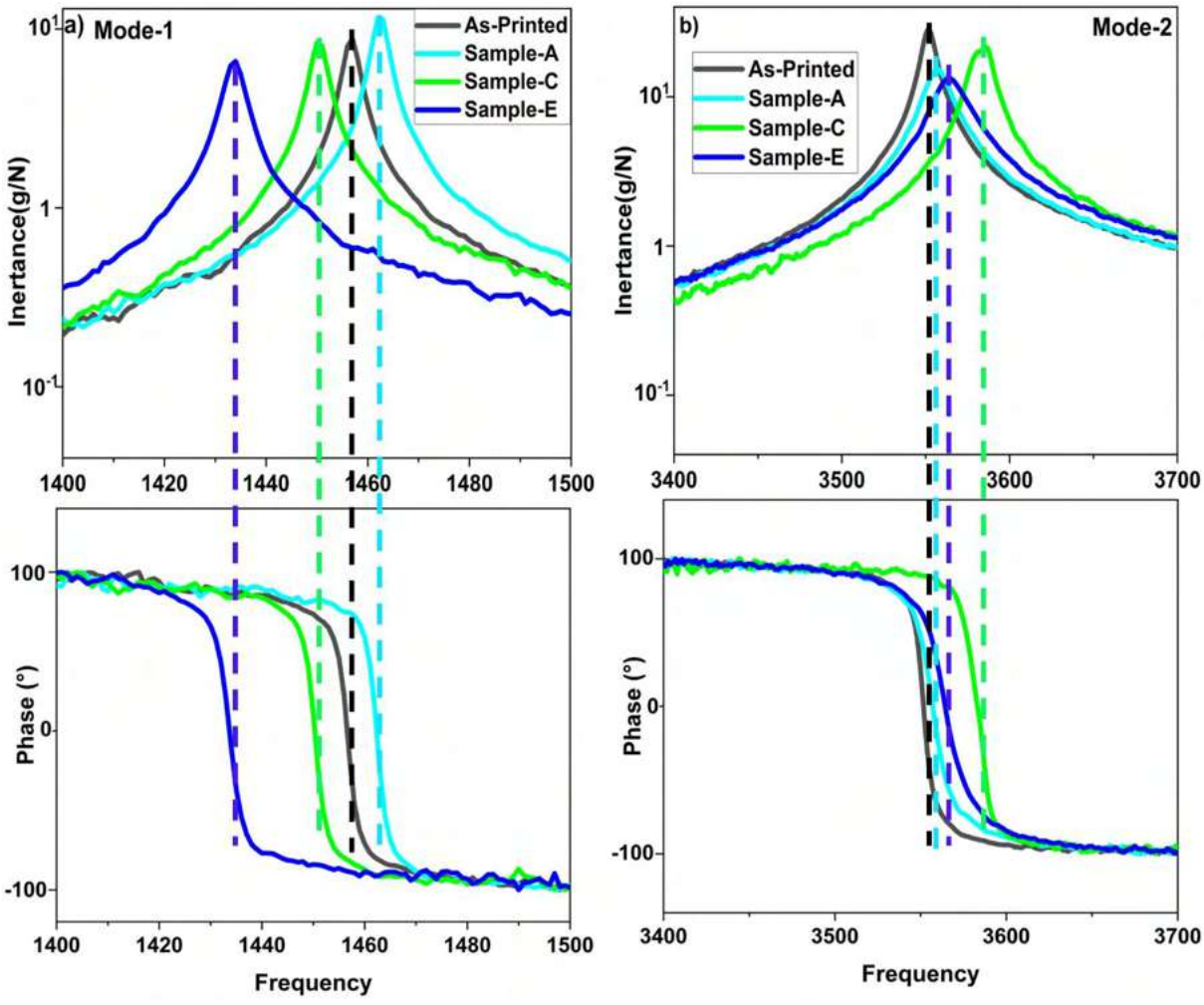

Figure 5. 73: FRF of as-printed and PHT thin flat samples: a) Mode 1; b) Mode 2

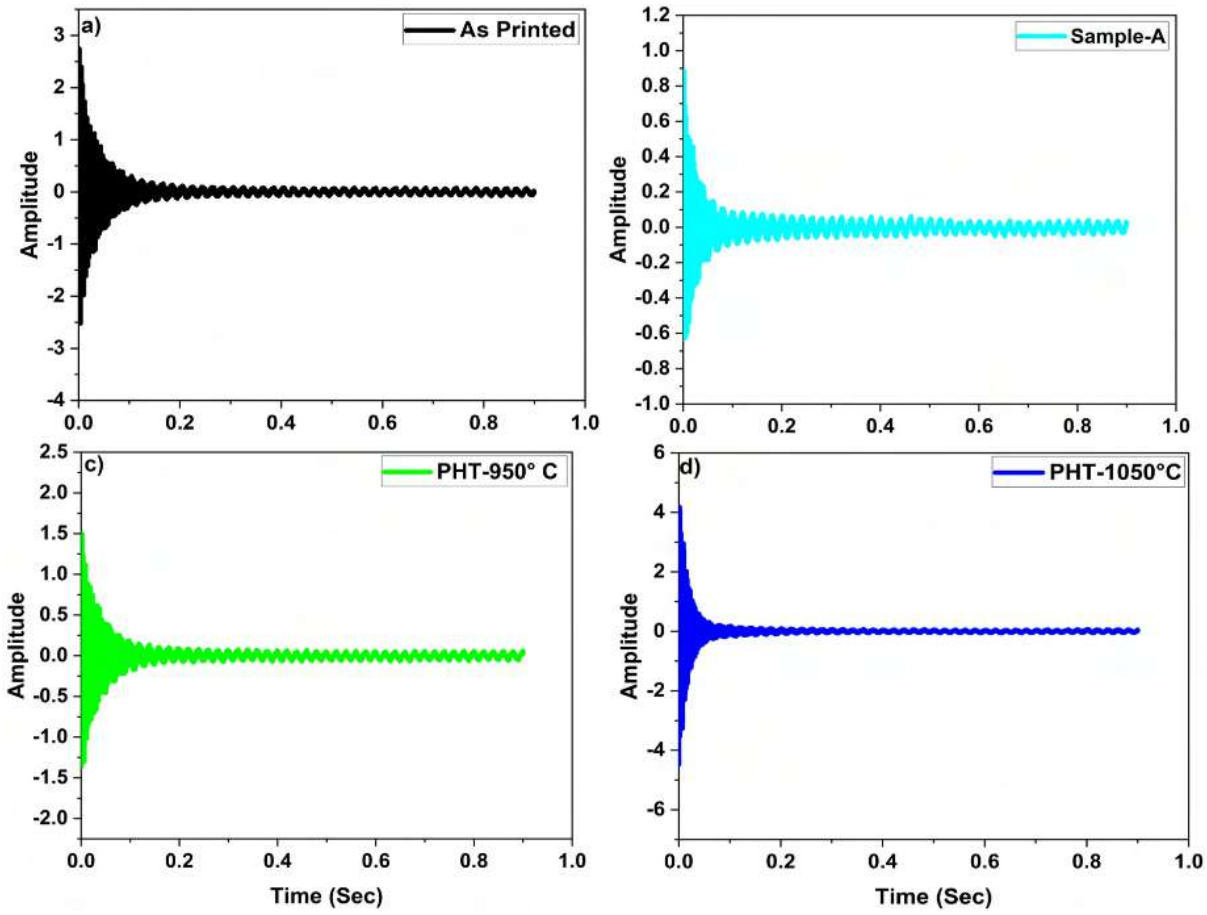

Figure 5. 74: Logarithmic decrement diagram of thin flat samples: a) as-printed; b) sample 'A'; c) sample 'C'; d) sample 'E'

5.6.2 Damping behaviour of LPBF manufactured rotor blade part

Different PHTs were performed on LPBF-manufactured Ti6Al4V thin flat samples, and it was observed that sample E showed higher damping compared to other PHT conditions. Hence rotor blades were printed, and super β transus PHT (1050°C) was performed for the damping behaviour evaluation. The damping ratio of a rotor blade under as-printed and PHT conditions for two mode shapes are shown in Table 5.9 and Figure 5.75. It is noted that the heat-treated rotor blade (at 1050°C) showed higher damping of around 348% in mode 1 and 118% in mode 2 compared to the as-printed blade. It is attributed to the high β content (soft nature). Hence favourable for energy dissipation resulting in higher damping. It is apparent in Figure 5.76 (a and b) that the heat-treated blade shows broader peaks than the as-printed blade indicating effective damping. Figure 5.77 (a-b) shows the logarithmic decrement diagram of a rotor blade under as-printed and heat-treated conditions. It is noteworthy that amplitude decay for heat

treated rotor blade was shorter than the as-printed blade. This result strongly demonstrated that the β phase in a heat-treated blade absorbs energy to dampen swiftly.

Table 5. 9: Damping ratio of rotor blades

Condition	Mode shape	Frequency	Damping ratio (ξ)
As-printed	Mode 1	1028.55	0.0037
As-printed	Mode 2	1835.26	0.0050
PHT-1050°C	Mode 1	1037.00	0.0166
PHT-1050°C	Mode 2	1855.00	0.010988

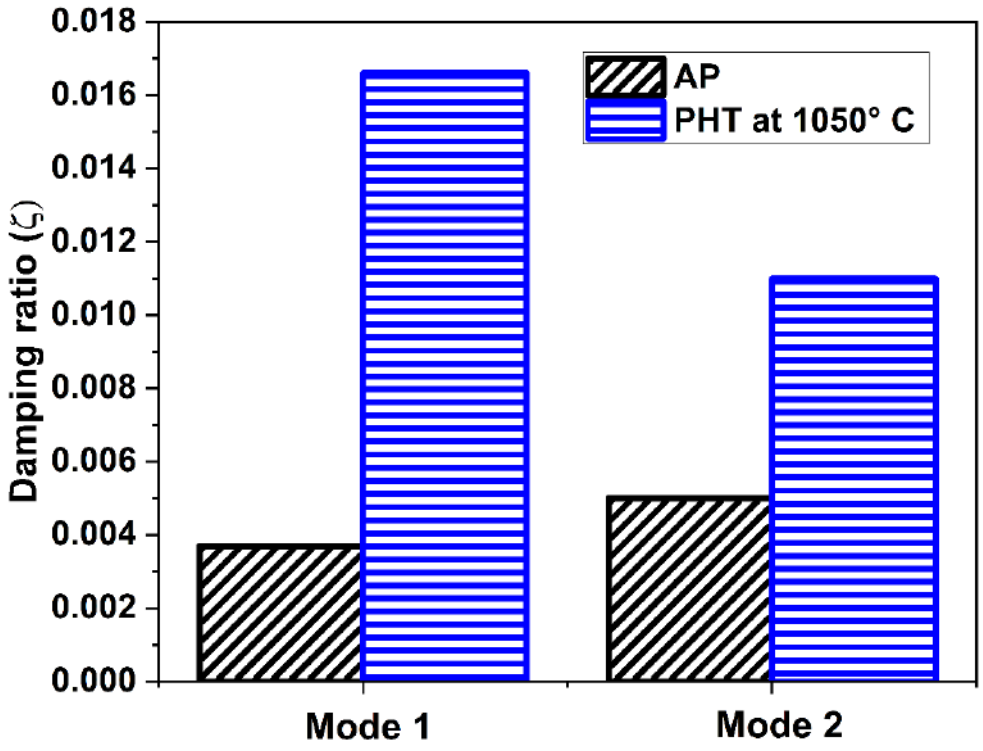

Figure 5. 75: Damping ratio vs frequency of Ti6Al4V rotor blades

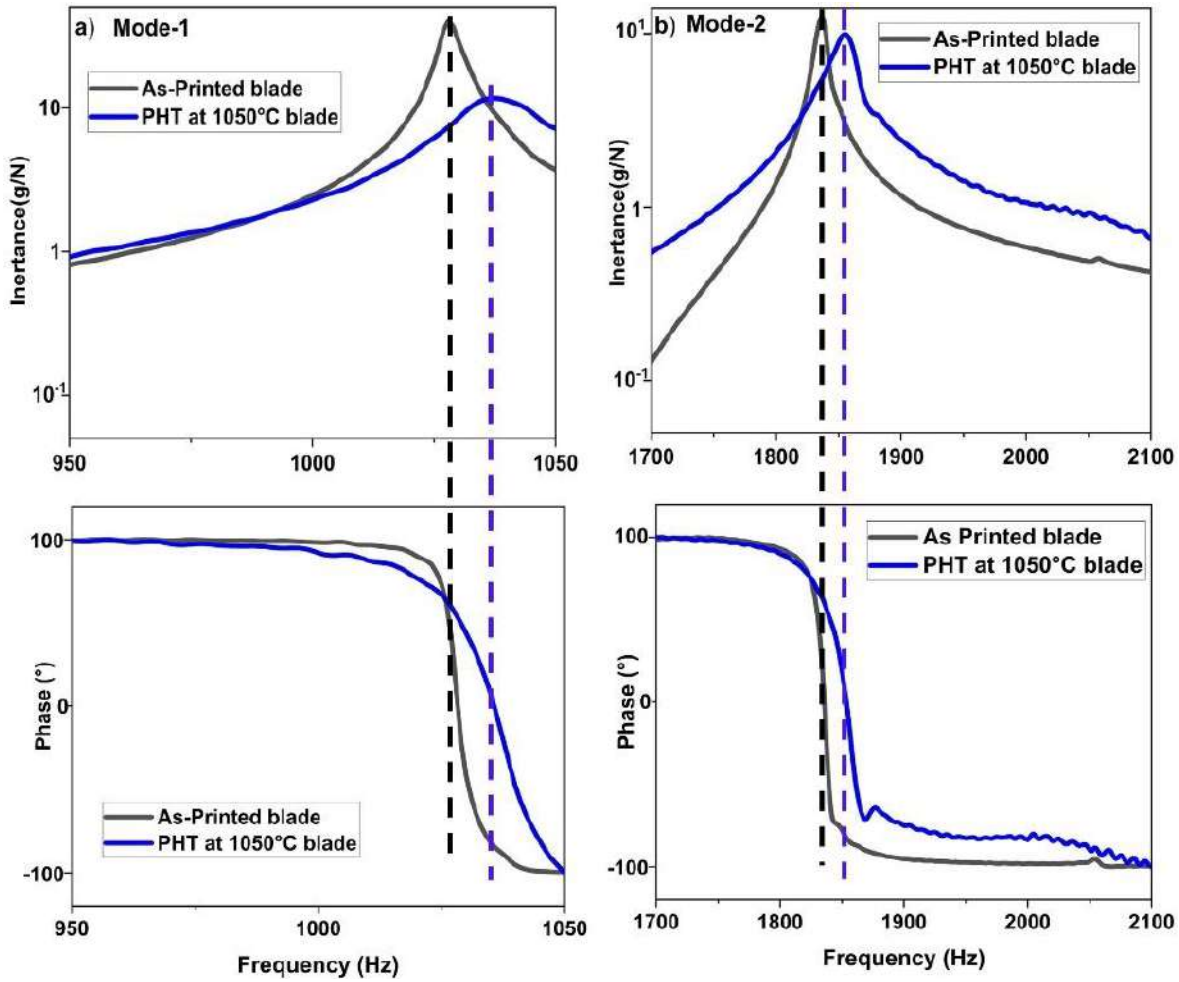

Figure 5. 76: FRF of as-printed and PHT blades: a) Mode 1; b) Mode 2

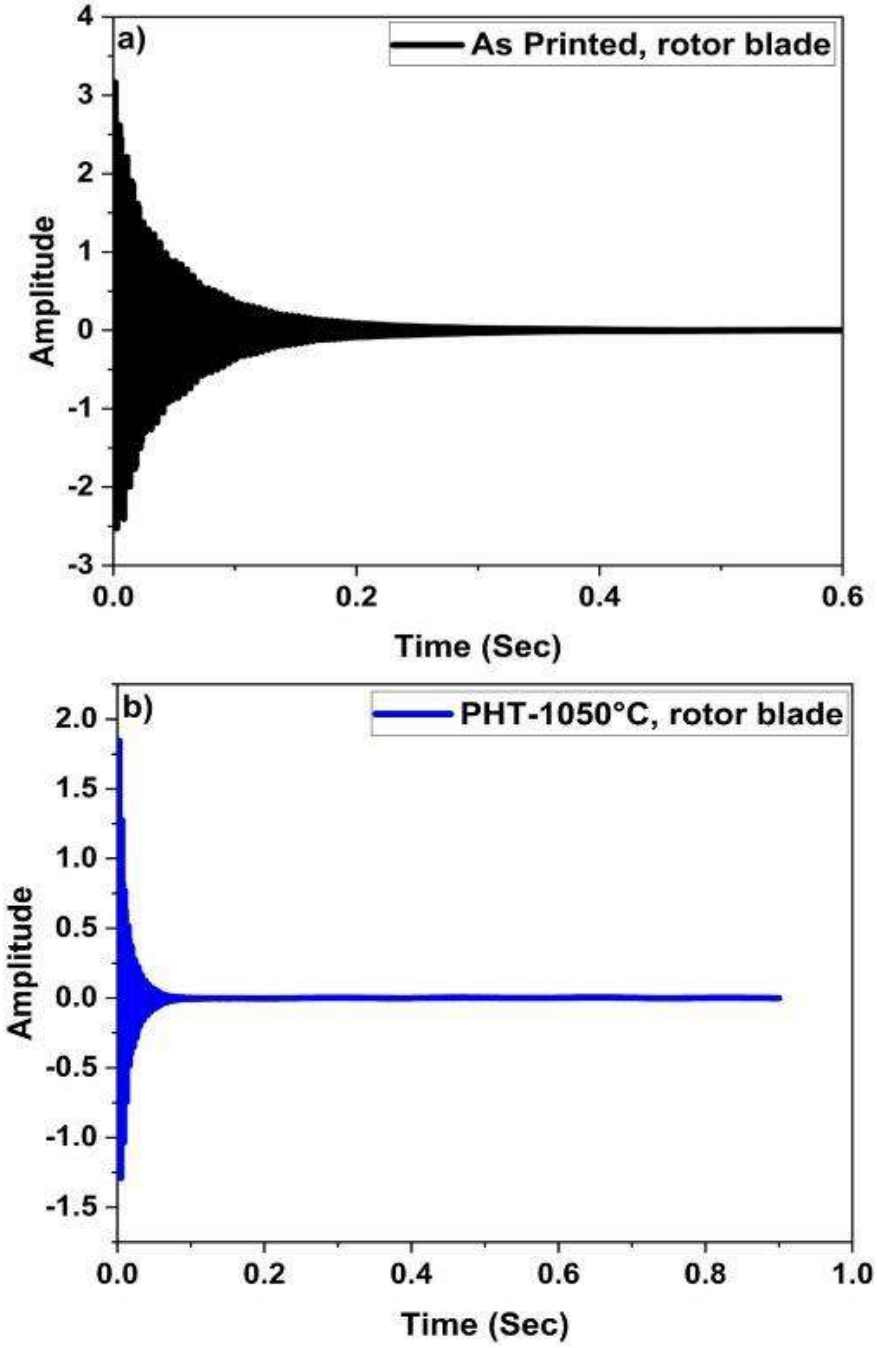

Figure 5. 77: Logarithmic decrement diagram: a) as-printed rotor blade; b) PHT rotor blade

Furthermore, the comparison between sample E, PHT executed rotor blade, and conventionally (wrought) Ti6Al4V having lamellar microstructure [136] is given in Figure 5.78. The damping ratio of sample E is of one order higher owing to the large thickness of (4 mm) compared to the conventional (wrought) Ti6Al4V (2 mm). However, the thickness of the PHT executed rotor blade and conventional manufactured Ti6Al4V with lamellar microstructure is consistent owing to their nearly similar thickness.

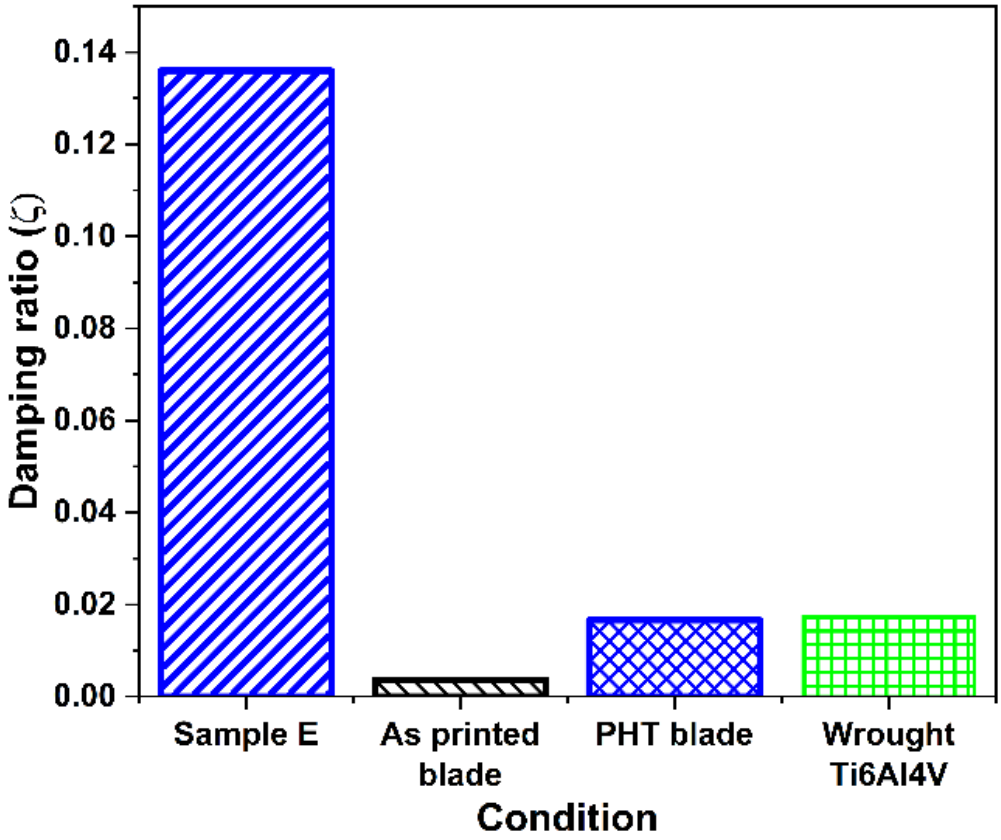

Figure 5. 78: Damping comparison between sample E, PHT subjected, as-printed blade rotor blade, and conventional Ti6Al4V lamellar microstructure sample

5.6.3 FEM modal analysis of LPBF-manufactured Ti6Al4V rotor blades

The FEM modal analysis of the as-printed and heat-treated rotor blade indicated that the maximum deflection occurs at the blade's leading tip, where the hammer was impacted experimentally. The vibrational mode shapes simulation results are shown in Figure 5.79. The natural frequency comparison of experimental and simulation modal analysis is given in Table 5.10. The simulation and experimental results show a slight difference in natural frequencies, possibly due to the factors like porosity in the printed blades. Moreover, the difference could be due to the experimental noise, and the fixed boundary condition is difficult to achieve experimentally[238]. The obtained results in the FEM modal analysis of the rotor blade validate the experimental results.

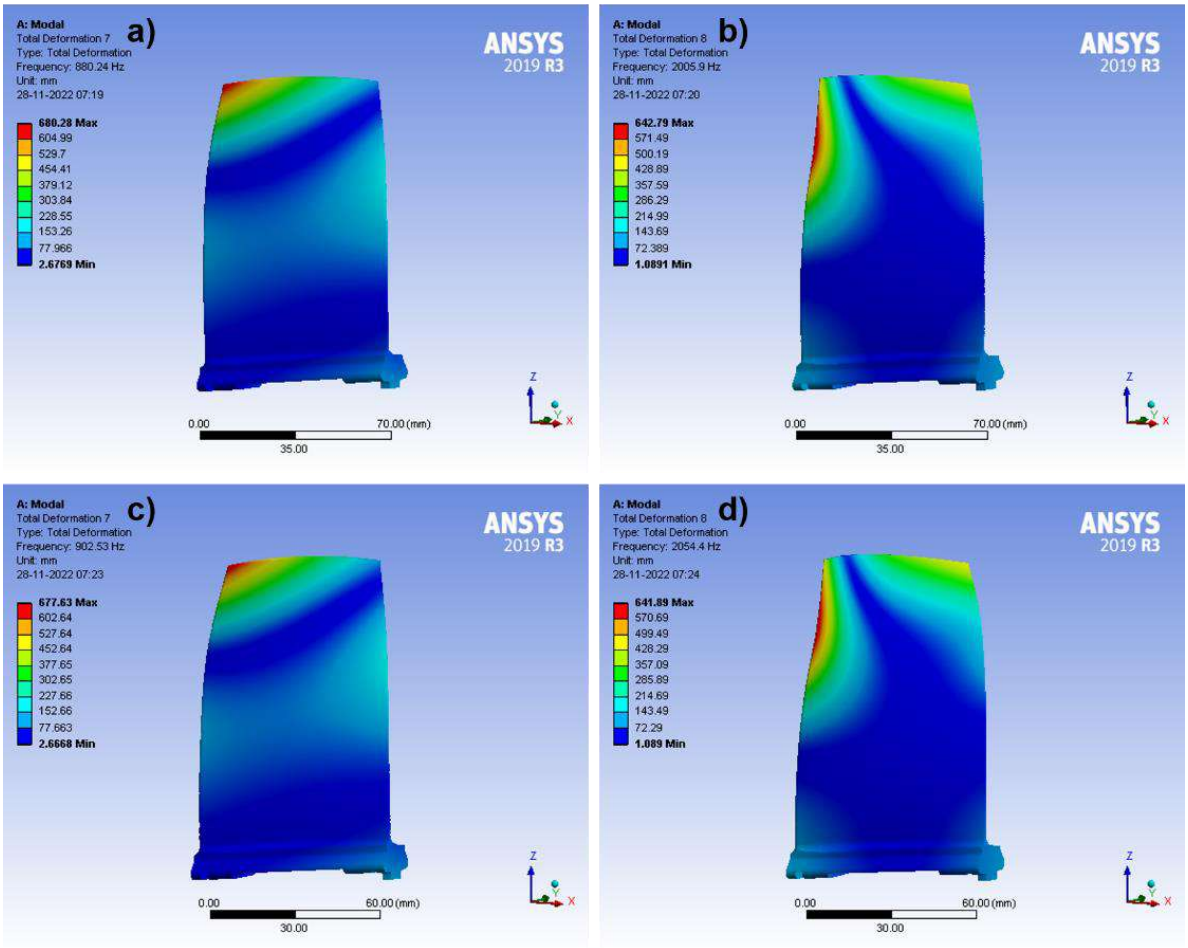

Figure 5. 79: As-printed rotor blade: a) First-order vibration mode; b) second-order vibration mode; PHT rotor blade: c) first-order vibration mode; d) second-order vibration mode

Table 5. 10: Natural frequencies experimental and simulation of Ti6Al4V rotor blades

Mode	As-manufactured blades		PHT blades	
	Experimental (Hz)	Simulation (Hz)	Experimental (Hz)	Simulation (Hz)
Mode 1	1028.55	880.24	1037	902.53
Mode 2	1835.26	2005.10	1855	2054.4

5.6.4 Effect of microstructure on damping behaviour of LPBF-manufactured Ti6Al4V rotor blade parts

It is apparent from Figures 5.72 and 5.73 that sample E predominantly showed a high damping ratio in two mode shapes compared to samples 'A', 'C' and as-printed. Sample 'E', composed of α-Widmanstatten microstructure, consists of elongated β and a small amount of α, as shown in Figures 5.16(a) and 5.17(a). It is well established that the Ti6Al4V heat treated above β transus temperature exhibits a higher amount of β and a low amount of α [140]. The high damping in the Ti6Al4V alloy system can be attributed to the different stiffnesses of different phases. Sample E consists of the α phase and soft β phase, which could have different stiffness of α and β resulting in a difference in energy dissipations which is well corroborated with [136]. Moreover, improvement in damping could be owing to the damping of the interface of matrix and phase. It is important to note that being a soft phase β can attenuate the vibrations, thus enhancing the damping behaviour.

Furthermore, sample 'C' consists of an α+β basketweave microstructure with different colony sizes of α+β. It is observed from the literature that sample 'C' shows a high amount of α compared to the sample heat-treated above β transus temperature (sample E). The α phase consists of an HCP crystal structure which is a hard phase compared to the β phase, resulting in lesser damping. Sample A consists of a higher amount of α, ~ 72%, with a small amount of α' and β. Therefore energy dissipation is restricted due to high dislocation density around α and α', resulting in lower damping than samples C and E [51].

It is noteworthy that as-printed Ti6Al4V consists of α' martensite and α having a reduction in stiffness between α' and α difference owing to the decrease in damping ratio. Also, high damping is a process that occurs when the tension-compression oscillation causes the β phase conditions to change in an anelastic manner. This eliminates the elastic strain energy. The damping tests on conventionally manufactured Ti6Al4V exhibited different damping ratios at other PHT conditions. The evolution of LPBF-manufactured Ti6Al4V microstructure at various PHT conditions is shown in Figure.5.80 (a-d). The elongated β grains were formed when the sample was heat-treated above β transus temperature (1050 ºC).

Moreover, the lamellar α+β grains were also observed, creating a high amount of β. The β phase is responsible for energy dissipation in material damping, which is also observed in the

present study. Moreover, the damping ratio in sample E may also increase due to damping by interface and increased area of α and β phases having different stiffnesses.

The as-printed sample E consists of α' martensite formed due to the rapid cooling in the LPBF process. The developed α' martensite microstructure enhances the microhardness of the Ti6Al4V samples. The increased microhardness of as-printed Ti6Al4V is owing to the high dislocation density around α'. The damping is also achieved by energy dissipation through dislocation motion. However, high dislocation density in as-printed Ti6Al4V obstructs each other resulting in lower damping[239]. The α lath width of samples 'A', 'C' and 'E' are summarized in Figure 5.25. The higher heat treatment temperature enhances the α lath width. The lesser volume fraction of the α phase at high temperature causes the increase in the α lath width due to the higher PHT temperature. The higher the volume fraction of α phases, the more obstruction exists for growth. This is why α laths grow efficiently due to less phase hindrance. Further, the energy dissipates in the soft β phase owing to the high ductility in the β phase. Moreover, the α lath width is enhanced in Sample E, as shown in Figure. 5.24 and 5.25 resulting in a reduction in high dislocation density favouring in enhancing damping behaviour. The reduction in damping with an decrease in hardness is also reported by Kumar et al. [240].

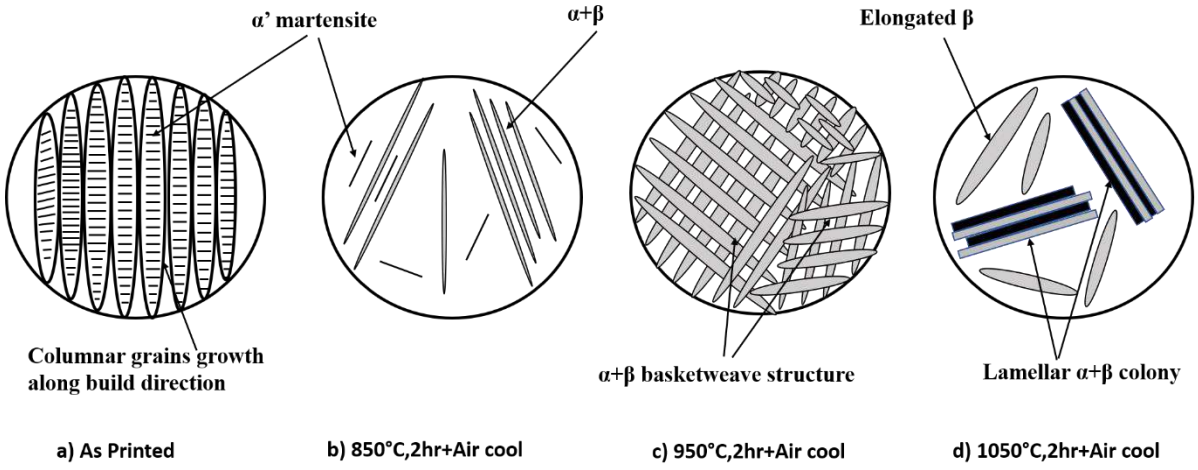

Figure 5. 80: Microstructural evolution of LPBF-manufactured Ti6Al4V in different PHT conditions

Chapter - 6

CONCLUSIONS

Based on the results obtained in the present study, the following conclusions were drawn on the effect of PHT on densification, tensile, HCF and damping behaviour of LPBF-manufactured Ti6Al4V parts:

- A simple in-house developed technique was applied to evaluate the ISS at the interface (between SS and part) during part removal. LPBF manufactured gear-type parts were built with different SS parameters to assess the influence of SS parameters on its ISS. In addition, a dimensional inspection shows that despite altering the LPBF process parameters of SSs, no significant dimensional deviation was observed for the LPBF part. Further optimal parameters for easy part removal were established.
- A skin core scan strategy was adopted to investigate the strength-ductility trade-off aspects in LPBF manufactured part. It was observed that the high scanning speed on skin forms the smaller grains, and the low scanning speed in the core forms the larger grains. The smaller grains on the skin enhances a material's microhardness compared to the core region. These findings are advantageous for tailoring microstructure and thus offer location-specific functional properties enabling the concept of Design for improved functionality. However, the anisotropy was still present in the LPBF manufactured samples.
- The optimized PHT scheme transformed the anisotropic microstructure to homogeneous with (α+β) lamellar microstructure. The lath thickness of α and β phases were smaller under air-cooled conditions than the furnace-cooled conditions. In transverse and longitudinal directions, the volume fraction of β increases by 3% and 12% PHT under furnace-cooled conditions, respectively. XRD revealed that the lower magnitude of closed pack planes and higher content of the β phase in samples subjected to PHT above super-β transus temperature (1050 °C) caused higher hardness than other PHT samples.
- The optimized PHT scheme at high temperature reduces porosities up to nearly two times more than the as-printed samples due to the sintering self-healing phenomenon. The super-micropores were the least affected due to the low surface energy. The

fraction of super micropores of Ti6Al4V samples under horizontal orientation subjected to PHT was reduced to 11.74 %, from 14.5% in the as-printed condition. Similarly, the fraction of super-micropores of Ti6Al4V samples subjected to PHT under vertical orientation was reduced to 14.3% from 19.3% in the as-printed sample.

- The tensile test results showed the isotropic tensile behaviour of the samples subjected to PHT under all the build orientations. The high β content in the sample subjected to PHT showed high ductility, which could be favourable in enhancing the fracture resistance performance. Strain hardening coefficients (n) and strength coefficient (k) were calculated, showing that as-printed samples in all directions are showing high strain hardening owing to the α' present in it.
- The LPBF-manufactured Ti6Al4V samples after PHT showed superior fatigue at higher stress levels despite showing less tensile strength. The improvement in fatigue lives for Ti6Al4V samples after PHT due to enhanced densification and pores closure at high temperatures leading to reduction in pores. Moreover, PHT-processed Ti6Al4V has shown a higher fatigue limit of 50 MPa than as-printed Ti6Al4V parts. The outcome revealed that the combination of enhanced ductility and pore size reduction due to PHT is critical for improving the fatigue resistance of LPBF-processed Ti6Al4V parts.
- The PHT performed at 1050°C enhanced the damping by ~348% and 140% for LPBF-manufactured thin plate parts and rotor blades, respectively. The amplitude decrement is ~ 66% shorter for the 1050°C heat-treated rotor blade than the as-printed rotor blade. The results obtained through FEM modal analysis validate the experimental results.
- Overall optimized PHT scheme employed in the present work has improved the tensile behaviour and functional performance, such as high cycle fatigue and damping of LPBF-manufactured Ti6Al4V products.

Chapter - 7

FUTURE SCOPE

1. A detailed in-depth study may be carried out to understand microstructural evolution (grain size and orientation etc.) and the interplay among the microstructural features on the interface shear strength (between support structure and part).
2. The influence of post-surface treatment on the surface hardness and compressive residual stress improvement may be carried out in view of enhancing the HCF performance of LPBF-manufactured Ti6Al4V parts.
3. The effect of PHTs on erosion and impact behaviour of LPBF-manufactured Ti6Al4V parts may be investigated.

REFERENCES

1. Soares C (2008) 1 - Gas Turbines: An Introduction and Applications. In: Soares C (ed) Gas Turbines. Butterworth-Heinemann, Burlington, pp 1–31

2. Grilli ML, Valerini D, Slobozeanu AE, et al (2021) Critical Raw Materials Saving by Protective Coatings under Extreme Conditions: A Review of Last Trends in Alloys and Coatings for Aerospace Engine Applications. Materials 14:1656. https://doi.org/10.3390/ma14071656

3. Okura T (2015) Materials for Aircraft Engines. ASEN 5063:1–14

4. Zhao K, Lou LH, Ma YH, Hu ZQ (2008) Effect of minor niobium addition on microstructure of a nickel-base directionally solidified superalloy. Materials Science and Engineering: A 476:372–377. https://doi.org/10.1016/j.msea.2007.06.041

5. Gibson I, Rosen DW, Stucker B, Khorasani M (2021) Additive manufacturing technologies. Springer

6. Beaman JJ, Bourell DL, Seepersad CC, Kovar D (2020) Additive Manufacturing Review: Early Past to Current Practice. Journal of Manufacturing Science and Engineering 142:. https://doi.org/10.1115/1.4048193

7. Singamneni S, Yifan LV, Hewitt A, et al (2019) Additive manufacturing for the aircraft industry: A review. J Aeronaut Aerosp Eng 8:

8. Acharya R, Sharon JA, Staroselsky A (2017) Prediction of microstructure in laser powder bed fusion process. Acta Materialia 124:360–371. https://doi.org/10.1016/j.actamat.2016.11.018

9. Frazier WE (2014) Metal Additive Manufacturing: A Review. J of Materi Eng and Perform 23:1917–1928. https://doi.org/10.1007/s11665-014-0958-z

10. Kumar LJ, Krishnadas Nair CG (2017) Current Trends of Additive Manufacturing in the Aerospace Industry. In: Wimpenny DI, Pandey PM, Kumar LJ (eds) Advances in 3D Printing & Additive Manufacturing Technologies. Springer, Singapore, pp 39–54

11. Pinke P, Caplovic L, Kovacs T (2011) The influence of heat treatment on the microstructure of the casted Ti6Al4V titanium alloy. Slovak University of Technology Bratislava Web 11:

12. Arrazola P-J, Garay A, Iriarte L-M, et al (2009) Machinability of titanium alloys (Ti6Al4V and Ti555.3). Journal of Materials Processing Technology 209:2223–2230. https://doi.org/10.1016/j.jmatprotec.2008.06.020

13. Material property charts – Ansys Granta. https://www.grantadesign.com/education/students/charts/. Accessed 21 Mar 2023

14. Hong SY, Ding Y (2001) Cooling approaches and cutting temperatures in cryogenic machining of Ti-6Al-4V. International Journal of Machine Tools and Manufacture 41:1417–1437. https://doi.org/10.1016/S0890-6955(01)00026-8

15. Shen Y, Liu Y, Sun W, et al (2015) High-speed dry compound machining of Ti6Al4V. Journal of Materials Processing Technology 224:200–207. https://doi.org/10.1016/j.jmatprotec.2015.05.012

16. Cao S, Zou Y, Lim CVS, Wu X (2021) Review of laser powder bed fusion (LPBF) fabricated Ti-6Al-4V: process, post-process treatment, microstructure, and property. Light: Advanced Manufacturing 2:313–332

17. Buhairi MA, Foudzi FM, Jamhari FI, et al (2022) Review on volumetric energy density: influence on morphology and mechanical properties of Ti6Al4V manufactured via laser powder bed fusion. Progress in Additive Manufacturing 1–19

18. Deng C, Li R, Yuan T, et al (2021) Microstructure and Mechanical Properties of a Combination Interface between Direct Energy Deposition and Selective Laser Melted Al-Mg-Sc-Zr Alloy. Metals 11:801. https://doi.org/10.3390/met11050801

19. Krol TA, Westhäuser S, Zäh MF, et al (2011) Development of a simulation-based process chain-strategy for different levels of detail for the preprocessing definitions, Symp. Simulationstechnik, Winterthur, Schweiz

20. Muiruri AM, Maringa M, Du PWB, Masu LM (2018) Variation of impact toughness of as-built DMLS Ti6Al4V (ELI) specimens with temperature. South African Journal of Industrial Engineering 29:284–298. https://doi.org/10.7166/29-3-2076

21. Wang D, Yang Y, Yi Z, Su X (2013) Research on the fabricating quality optimization of the overhanging surface in SLM process. The International Journal of Advanced Manufacturing Technology 65:1471–1484

22. Papadakis L, Branner G, Schober A, et al (2012) Numerical modeling of heat effects during thermal manufacturing of aero engine components. In: Proceedings of the World Congress on Engineering

23. Krol TA, Zach F, Seidel C (2012) Optimization of supports in metal-based additive manufacturing by means of finite element models. In: 2012 International Solid Freeform Fabrication Symposium. University of Texas at Austin

24. Subedi SC, Shahba A, Thevamaran M, et al (2022) Towards the optimal design of support structures for laser powder bed fusion-based metal additive manufacturing via thermal equivalent static loads. Additive Manufacturing 57:102956. https://doi.org/10.1016/j.addma.2022.102956

25. Miki T, Nishiwaki S (2022) Topology optimization of the support structure for heat dissipation in additive manufacturing. Finite Elements in Analysis and Design 203:103708. https://doi.org/10.1016/j.finel.2021.103708

26. Dimopoulos A, Zournatzis I, Gan T-H, Chatzakos P (2023) Multi-Response Optimization of Ti6Al4V Support Structures for Laser Powder Bed Fusion Systems. Journal of Manufacturing and Materials Processing 7:22. https://doi.org/10.3390/jmmp7010022

27. Järvinen J-P, Matilainen V, Li X, et al (2014) Characterization of Effect of Support Structures in Laser Additive Manufacturing of Stainless Steel. Physics Procedia 56:72–81. https://doi.org/10.1016/j.phpro.2014.08.099

28. Hussein A, Hao L, Yan C, et al (2013) Advanced lattice support structures for metal additive manufacturing. Journal of Materials Processing Technology 213:1019–1026. https://doi.org/10.1016/j.jmatprotec.2013.01.020

29. Johannes Lindecke PN, Blunk H, Wenzl J-P, et al (2018) Optimization of support structures for the laser additive manufacturing of TiAl6V4 parts. Procedia CIRP 74:53–58. https://doi.org/10.1016/j.procir.2018.08.029

30. Yan C, Hao L, Hussein A, Raymont D (2012) Evaluations of cellular lattice structures manufactured using selective laser melting. International Journal of Machine Tools and Manufacture 62:32–38. https://doi.org/10.1016/j.ijmachtools.2012.06.002

31. Bobbio LD, Qin S, Dunbar A, et al (2017) Characterization of the strength of support structures used in powder bed fusion additive manufacturing of Ti-6Al-4V. Additive Manufacturing 14:60–68. https://doi.org/10.1016/j.addma.2017.01.002

32. Didier P, Le Coz G, Robin G, et al (2021) Consideration of SLM additive manufacturing supports on the stability of flexible structures in finish milling. Journal of Manufacturing Processes 62:213–220. https://doi.org/10.1016/j.jmapro.2020.12.027

33. Manogharan G, Wysk RA, Harrysson OLA (2016) Additive manufacturing–integrated hybrid manufacturing and subtractive processes: economic model and analysis. International Journal of Computer Integrated Manufacturing 29:473–488. https://doi.org/10.1080/0951192X.2015.1067920

34. Pérez-Ruiz JD, Marin F, Martínez S, et al (2022) Stiffening near-net-shape functional parts of Inconel 718 LPBF considering material anisotropy and subsequent machining issues. Mechanical Systems and Signal Processing 168:108675. https://doi.org/10.1016/j.ymssp.2021.108675

35. Calignano F (2014) Design optimization of supports for overhanging structures in aluminum and titanium alloys by selective laser melting. Materials & Design 64:203–213. https://doi.org/10.1016/j.matdes.2014.07.043

36. Zhu L, Feng R, Xi J, et al (2020) A lightweight design of tree-shaped support structures for SLM additive manufacturing. Comput Aided Des Appl 17:716–726

37. Wang C, Qian X (2020) Optimizing Support for Heat Dissipation in Additive Manufacturing. American Society of Mechanical Engineers Digital Collection

38. Paggi U, Ranjan R, Thijs L, et al (2019) New support structures for reduced overheating on downfacing regions of direct metal printed parts. In: 2019 International Solid Freeform Fabrication Symposium. University of Texas at Austin

39. Han Q, Gu H, Soe S, et al (2018) Manufacturability of AlSi10Mg overhang structures fabricated by laser powder bed fusion. Materials & Design 160:1080–1095. https://doi.org/10.1016/j.matdes.2018.10.043

40. Zhang Z-D, Ibhadode O, Ali U, et al (2020) Topology optimization parallel-computing framework based on the inherent strain method for support structure design in laser powder-bed fusion additive manufacturing. Int J Mech Mater Des 16:897–923. https://doi.org/10.1007/s10999-020-09494-x

41. Subedi SC, Thoma DJ, Suresh K (2022) Optimal Truss-Type Supports for Minimal Part Distortion in LPBF. In: 2022 International Solid Freeform Fabrication Symposium

42. Wei C, Chueh Y-H, Zhang X, et al (2019) Easy-To-Remove Composite Support Material and Procedure in Additive Manufacturing of Metallic Components Using Multiple Material Laser-Based Powder Bed Fusion. Journal of Manufacturing Science and Engineering 141:. https://doi.org/10.1115/1.4043536

43. Schmitt M, Kempter B, Schlick G, Reinhart G (2020) Parameter identification approach for support structures in laser powder bed fusion and analysis of influencing factors. Procedia CIRP 94:260–265. https://doi.org/10.1016/j.procir.2020.09.049

44. Bangi JO, Maranga SM, Nganga SP, Mutuli SM (2014) Torque wrench calibration and uncertainty of measurement. Proc IMEKO 22nd TC3, 15th TC5 and 3rd TC 22:

45. ISO - ISO 6789-1:2017 - Assembly tools for screws and nuts — Hand torque tools — Part 1: Requirements and methods for design conformance testing and quality conformance testing: minimum requirements for declaration of conformance. https://www.iso.org/standard/62549.html. Accessed 27 Feb 2023

46. Wadhwani CPK, O'Brien R, Rosen PS, Chung K-H (2020) Testing and calibrating the mechanical-type toggle torque wrenches used in implant dentistry: A dental technique. The Journal of Prosthetic Dentistry 123:403–407. https://doi.org/10.1016/j.prosdent.2019.04.021

47. Wadhwani CPK, O'Brien RT, Rosen PS, Chung K-H (2020) A technique to validate the accuracy of a beam-type mechanical torque limiting device. The Journal of Prosthetic Dentistry 124:647–652. https://doi.org/10.1016/j.prosdent.2019.12.019

48. Yao Z, Jia X, Yu J, et al (2023) Rapid accomplishment of strength/ductility synergy for additively manufactured Ti-6Al-4V facilitated by machine learning. Materials & Design 225:111559. https://doi.org/10.1016/j.matdes.2022.111559

49. Jeong SG, Karthik GM, Kim ES, et al (2022) Architectured heterogeneous alloys with selective laser melting. Scripta Materialia 208:114332. https://doi.org/10.1016/j.scriptamat.2021.114332

50. Dezfoli ARA, Hwang W-S, Huang W-C, Tsai T-W (2017) Determination and controlling of grain structure of metals after laser incidence: Theoretical approach. Sci Rep 7:41527. https://doi.org/10.1038/srep41527

51. Vrancken B, Thijs L, Kruth J-P, Van Humbeeck J (2012) Heat treatment of Ti6Al4V produced by Selective Laser Melting: Microstructure and mechanical properties. Journal of Alloys and Compounds 541:177–185. https://doi.org/10.1016/j.jallcom.2012.07.022

52. Vilaro T, Colin C, Bartout JD (2011) As-Fabricated and Heat-Treated Microstructures of the Ti-6Al-4V Alloy Processed by Selective Laser Melting. Metall and Mat Trans A 42:3190–3199. https://doi.org/10.1007/s11661-011-0731-y

53. Ahmed T, Rack HJ (1998) Phase transformations during cooling in α+β titanium alloys. Materials Science and Engineering: A 243:206–211. https://doi.org/10.1016/S0921-5093(97)00802-2

54. Gorsse S, Hutchinson C, Gouné M, Banerjee R (2017) Additive manufacturing of metals: a brief review of the characteristic microstructures and properties of steels, Ti-6Al-4V and high-entropy alloys. Science and Technology of Advanced Materials 18:584–610. https://doi.org/10.1080/14686996.2017.1361305

55. Chen LY, Huang JC, Lin CH, et al (2017) Anisotropic response of Ti-6Al-4V alloy fabricated by 3D printing selective laser melting. Materials Science and Engineering: A 682:389–395. https://doi.org/10.1016/j.msea.2016.11.061

56. Ni C, Zhu L, Zheng Z, et al (2020) Effect of material anisotropy on ultra-precision machining of Ti-6Al-4V alloy fabricated by selective laser melting. Journal of Alloys and Compounds 848:156457. https://doi.org/10.1016/j.jallcom.2020.156457

57. Wu SQ, Lu YJ, Gan YL, et al (2016) Microstructural evolution and microhardness of a selective-laser-melted Ti–6Al–4V alloy after post heat treatments. Journal of Alloys and Compounds 672:643–652. https://doi.org/10.1016/j.jallcom.2016.02.183

58. Sabban R, Bahl S, Chatterjee K, Suwas S (2019) Globularization using heat treatment in additively manufactured Ti-6Al-4V for high strength and toughness. Acta Materialia 162:239–254. https://doi.org/10.1016/j.actamat.2018.09.064

59. Zhang B, Meng WJ, Shao S, et al (2019) Effect of heat treatments on pore morphology and microstructure of laser additive manufactured parts. Material Design & Processing Communications 1:e29. https://doi.org/10.1002/mdp2.29

60. Yan X, Yin S, Chen C, et al (2018) Effect of heat treatment on the phase transformation and mechanical properties of Ti6Al4V fabricated by selective laser melting. Journal of Alloys and Compounds 764:1056–1071. https://doi.org/10.1016/j.jallcom.2018.06.076

61. Zhang X-Y, Fang G, Leeflang S, et al (2018) Effect of subtransus heat treatment on the microstructure and mechanical properties of additively manufactured Ti-6Al-4V alloy. Journal of Alloys and Compounds 735:1562–1575. https://doi.org/10.1016/j.jallcom.2017.11.263

62. Li H, Jia D, Yang Z, et al (2021) Effect of heat treatment on microstructure evolution and mechanical properties of selective laser melted Ti–6Al–4V and TiB/Ti–6Al–4V composite: A comparative study. Materials Science and Engineering: A 801:140415. https://doi.org/10.1016/j.msea.2020.140415

63. Zhang B, Ham K, Shao S, et al (2017) Effect of heat treatment and hot isostatic pressing on the morphology and size of pores in additive manufactured Ti-6Al-4V parts. In: 2017 International Solid Freeform Fabrication Symposium. University of Texas at Austin

64. Gong H, Rafi K, Gu H, et al (2014) Analysis of defect generation in Ti–6Al–4V parts made using powder bed fusion additive manufacturing processes. Additive Manufacturing 1–4:87–98. https://doi.org/10.1016/j.addma.2014.08.002

65. Thijs L, Verhaeghe F, Craeghs T, et al (2010) A study of the microstructural evolution during selective laser melting of Ti–6Al–4V. Acta Materialia 58:3303–3312. https://doi.org/10.1016/j.actamat.2010.02.004

66. Liu QC, Elambasseril J, Sun SJ, et al (2014) The Effect of Manufacturing Defects on the Fatigue Behaviour of Ti-6Al-4V Specimens Fabricated Using Selective Laser Melting. Advanced

Materials Research 891–892:1519–1524.
https://doi.org/10.4028/www.scientific.net/AMR.891-892.1519

67. Zhang B, Li Y, Bai Q (2017) Defect formation mechanisms in selective laser melting: a review. Chinese Journal of Mechanical Engineering 30:515–527

68. Hu C, Li F, Qu D, et al (2014) 8 - Developments in hot pressing (HP) and hot isostatic pressing (HIP) of ceramic matrix composites. In: Low IM (ed) Advances in Ceramic Matrix Composites (Second Edition). Woodhead Publishing, pp 177–202

69. Ferrucci M, Leach RK, Giusca C, et al (2015) Towards geometrical calibration of x-ray computed tomography systems—a review. Meas Sci Technol 26:092003. https://doi.org/10.1088/0957-0233/26/9/092003

70. Mugwagwa L, Dimitrov D, Matope S, Becker TH (2016) A methodology to evaluate the influence of part geometry on residual stresses in selective laser melting. Faculty of Engineering, Department of Industrial Engineering, Stellenbosch University

71. Kahlin M, Ansell H, Moverare JJ (2017) Fatigue behaviour of notched additive manufactured Ti6Al4V with as-built surfaces. International Journal of Fatigue 101:51–60. https://doi.org/10.1016/j.ijfatigue.2017.04.009

72. du Plessis A, Macdonald E (2020) Hot isostatic pressing in metal additive manufacturing: X-ray tomography reveals details of pore closure. Additive Manufacturing 34:101191. https://doi.org/10.1016/j.addma.2020.101191

73. Karimi J, Suryanarayana C, Okulov I, Prashanth KG (2021) Selective laser melting of Ti6Al4V: Effect of laser re-melting. Materials Science and Engineering: A 805:140558. https://doi.org/10.1016/j.msea.2020.140558

74. Karimi J, Xie MS, Wang Z, Prashanth KG (2021) Influence of substructures on the selective laser melted Ti-6Al-4V alloy as a function of laser re-melting. Journal of Manufacturing Processes 68:1387–1394. https://doi.org/10.1016/j.jmapro.2021.06.059

75. Liu J, Wen P (2022) Metal vaporization and its influence during laser powder bed fusion process. Materials & Design 215:110505. https://doi.org/10.1016/j.matdes.2022.110505

76. Kushwaha A, Subramaniyan AK, Bommanahalli Kenchappa N, Barad S (2022) Microstructure, mechanical, and wear properties of thin-walled Ti6Al4V parts produced using laser powder bed fusion technique. Materials Letters 308:131138. https://doi.org/10.1016/j.matlet.2021.131138

77. Pathania A, Subramaniyan AK, Nagesha BK (2022) Influence of post-heat treatments on microstructural and mechanical properties of LPBF-processed Ti6Al4V alloy. Prog Addit Manuf 7:1323–1343. https://doi.org/10.1007/s40964-022-00306-6

78. Günther J, Krewerth D, Lippmann T, et al (2017) Fatigue life of additively manufactured Ti–6Al–4V in the very high cycle fatigue regime. International Journal of Fatigue 94:236–245. https://doi.org/10.1016/j.ijfatigue.2016.05.018

79. Qiu C, Adkins NJE, Attallah MM (2013) Microstructure and tensile properties of selectively laser-melted and of HIPed laser-melted Ti–6Al–4V. Materials Science and Engineering: A 578:230–239. https://doi.org/10.1016/j.msea.2013.04.099

80. Tammas-Williams S, Withers PJ, Todd I, Prangnell PB (2016) Porosity regrowth during heat treatment of hot isostatically pressed additively manufactured titanium components. Scripta Materialia 122:72–76. https://doi.org/10.1016/j.scriptamat.2016.05.002

81. Kasperovich G, Hausmann J (2015) Improvement of fatigue resistance and ductility of TiAl6V4 processed by selective laser melting. Journal of Materials Processing Technology 220:202–214. https://doi.org/10.1016/j.jmatprotec.2015.01.025

82. Majeed A, Zhang Y, Lv J, et al (2020) Investigation of T4 and T6 heat treatment influences on relative density and porosity of AlSi10Mg alloy components manufactured by SLM. Computers & Industrial Engineering 139:106194. https://doi.org/10.1016/j.cie.2019.106194

83. Liu S, Shin YC (2019) Additive manufacturing of Ti6Al4V alloy: A review. Materials & Design 164:107552. https://doi.org/10.1016/j.matdes.2018.107552

84. Standard Specification for Additive Manufacturing Titanium-6 Aluminum-4 Vanadium with Powder Bed Fusion. https://www.astm.org/f2924-12.html. Accessed 21 Mar 2023

85. Xu W, Brandt M, Sun S, et al (2015) Additive manufacturing of strong and ductile Ti–6Al–4V by selective laser melting via in situ martensite decomposition. Acta Materialia 85:74–84. https://doi.org/10.1016/j.actamat.2014.11.028

86. Ali H, Ma L, Ghadbeigi H, Mumtaz K (2017) In-situ residual stress reduction, martensitic decomposition and mechanical properties enhancement through high temperature powder bed pre-heating of Selective Laser Melted Ti6Al4V. Materials Science and Engineering: A 695:211–220. https://doi.org/10.1016/j.msea.2017.04.033

87. Carroll BE, Palmer TA, Beese AM (2015) Anisotropic tensile behavior of Ti–6Al–4V components fabricated with directed energy deposition additive manufacturing. Acta Materialia 87:309–320. https://doi.org/10.1016/j.actamat.2014.12.054

88. Kok Y, Tan XP, Wang P, et al (2018) Anisotropy and heterogeneity of microstructure and mechanical properties in metal additive manufacturing: A critical review. Materials & Design 139:565–586. https://doi.org/10.1016/j.matdes.2017.11.021

89. Jiao ZH, Xu RD, Yu HC, Wu XR (2017) Evaluation on Tensile and Fatigue Crack Growth Performances of Ti6Al4V Alloy Produced by Selective Laser Melting. Procedia Structural Integrity 7:124–132. https://doi.org/10.1016/j.prostr.2017.11.069

90. Simonelli M, Tse YY, Tuck C (2014) Effect of the build orientation on the mechanical properties and fracture modes of SLM Ti–6Al–4V. Materials Science and Engineering: A 616:1–11. https://doi.org/10.1016/j.msea.2014.07.086

91. Parvez MM, Pan T, Chen Y, et al (2020) High Cycle Fatigue Performance of LPBF 304L Stainless Steel at Nominal and Optimized Parameters. Materials 13:1591. https://doi.org/10.3390/ma13071591

92. Lütjering G (1998) Influence of processing on microstructure and mechanical properties of (α+β) titanium alloys. Materials Science and Engineering: A 243:32–45. https://doi.org/10.1016/S0921-5093(97)00778-8

93. Longhitano GA, Larosa MA, Jardini AL, et al (2018) Correlation between microstructures and mechanical properties under tensile and compression tests of heat-treated Ti-6Al–4V ELI alloy produced by additive manufacturing for biomedical applications. Journal of Materials Processing Technology 252:202–210. https://doi.org/10.1016/j.jmatprotec.2017.09.022

94. Huang Q, Liu X, Yang X, et al (2015) Specific heat treatment of selective laser melted Ti–6Al–4V for biomedical applications. Front Mater Sci 9:373–381. https://doi.org/10.1007/s11706-015-0315-7

95. Ghio E, Cerri E (2022) Additive Manufacturing of AlSi10Mg and Ti6Al4V Lightweight Alloys via Laser Powder Bed Fusion: A Review of Heat Treatments Effects. Materials 15:2047. https://doi.org/10.3390/ma15062047

96. Etesami SA, Fotovvati B, Asadi E (2022) Heat treatment of Ti-6Al-4V alloy manufactured by laser-based powder-bed fusion: Process, microstructures, and mechanical properties correlations. Journal of Alloys and Compounds 895:162618. https://doi.org/10.1016/j.jallcom.2021.162618

97. Akram J, Pal D, Stucker B (2019) Establishing Flow Stress and Elongation Relationships as a Function of Microstructural Features of Ti6Al4V Alloy Processed using SLM. Designs 3:21. https://doi.org/10.3390/designs3020021

98. Yang J, Yu H, Wang Z, Zeng X (2017) Effect of crystallographic orientation on mechanical anisotropy of selective laser melted Ti-6Al-4V alloy. Materials Characterization 127:137–145. https://doi.org/10.1016/j.matchar.2017.01.014

99. Zheng Z, Waheed S, Balint DS, Dunne FPE (2018) Slip transfer across phase boundaries in dual phase titanium alloys and the effect on strain rate sensitivity. International Journal of Plasticity 104:23–38. https://doi.org/10.1016/j.ijplas.2018.01.011

100. Kohn DH, Ducheyne P (1991) Tensile and fatigue strength of hydrogen-treated Ti-6Al-4V alloy. Journal of materials science 26:328–334

101. Mishurova T, Artzt K, Rehmer B, et al (2021) Separation of the impact of residual stress and microstructure on the fatigue performance of LPBF Ti-6Al-4V at elevated temperature. International Journal of Fatigue 148:106239. https://doi.org/10.1016/j.ijfatigue.2021.106239

102. Cepeda-Jiménez CM, Potenza F, Magalini E, et al (2020) Effect of energy density on the microstructure and texture evolution of Ti-6Al-4V manufactured by laser powder bed fusion. Materials Characterization 163:110238. https://doi.org/10.1016/j.matchar.2020.110238

103. Ronneberg T, Davies CM, Hooper PA (2020) Revealing relationships between porosity, microstructure and mechanical properties of laser powder bed fusion 316L stainless steel through heat treatment. Materials & Design 189:108481. https://doi.org/10.1016/j.matdes.2020.108481

104. Ferreri NC, Ghorbanpour S, Bhowmik S, et al (2019) Effects of build orientation and heat treatment on the evolution of microstructure and mechanical properties of alloy Mar-M-509

fabricated via laser powder bed fusion. International Journal of Plasticity 121:116–133. https://doi.org/10.1016/j.ijplas.2019.06.002

105. Marchese G, Parizia S, Rashidi M, et al (2020) The role of texturing and microstructure evolution on the tensile behavior of heat-treated Inconel 625 produced via laser powder bed fusion. Materials Science and Engineering: A 769:138500. https://doi.org/10.1016/j.msea.2019.138500

106. Carlucci G, Patriarca L, Demir AG, et al (2022) Building Orientation and Heat Treatments Effect on the Pseudoelastic Properties of NiTi Produced by LPBF. Shap Mem Superelasticity 8:235–247. https://doi.org/10.1007/s40830-022-00391-0

107. Mandelbrot BB, Passoja DE, Paullay AJ (1984) Fractal character of fracture surfaces of metals. Nature 308:721–722. https://doi.org/10.1038/308721a0

108. Nayak SR, Mishra J, Palai G (2019) Analysing roughness of surface through fractal dimension: A review. Image and Vision Computing 89:21–34. https://doi.org/10.1016/j.imavis.2019.06.015

109. Wu J, Jin X, Mi S, Tang J (2020) An effective method to compute the box-counting dimension based on the mathematical definition and intervals. Results in Engineering 6:100106. https://doi.org/10.1016/j.rineng.2020.100106

110. Hilders OA, Ramos M, Peña ND, Sàenz L (2006) Fractal geometry of fracture surfaces of a duplex stainless steel. J Mater Sci 41:5739–5742. https://doi.org/10.1007/s10853-006-0102-z

111. Sun W, Ma Y, Huang W, et al (2020) Effects of build direction on tensile and fatigue performance of selective laser melting Ti6Al4V titanium alloy. International Journal of Fatigue 130:105260. https://doi.org/10.1016/j.ijfatigue.2019.105260

112. Qian G, Li Y, Paolino DS, et al (2020) Very-high-cycle fatigue behavior of Ti-6Al-4V manufactured by selective laser melting: Effect of build orientation. International Journal of Fatigue 136:105628. https://doi.org/10.1016/j.ijfatigue.2020.105628

113. Gao X, Tao C, Wu S (2023) Anisotropic high cycle fatigue property estimation for laser additive manufactured Ti6Al4V alloy dependence on tomographic imaging of defect population. Journal of Materials Research and Technology 22:1971–1982. https://doi.org/10.1016/j.jmrt.2022.12.069

114. Murakami Y (2012) Material defects as the basis of fatigue design. International Journal of Fatigue 41:2–10. https://doi.org/10.1016/j.ijfatigue.2011.12.001

115. Xu W, Sun S, Elambasseril J, et al (2015) Ti-6Al-4V Additively Manufactured by Selective Laser Melting with Superior Mechanical Properties. JOM 67:668–673. https://doi.org/10.1007/s11837-015-1297-8

116. Leuders S, Vollmer M, Brenne F, et al (2015) Fatigue strength prediction for titanium alloy TiAl6V4 manufactured by selective laser melting. Metallurgical and materials transactions A 46:3816–3823

117. Yang Y, Zhao M, Wang H, et al (2023) Microstructure and Fatigue Performance of Ti6Al4V Produced by Laser Powder Bed Fusion after Post-Heat Treatment. Applied Sciences 13:1828. https://doi.org/10.3390/app13031828

118. Leuders S, Thöne M, Riemer A, et al (2013) On the mechanical behaviour of titanium alloy TiAl6V4 manufactured by selective laser melting: Fatigue resistance and crack growth performance. International Journal of Fatigue 48:300–307. https://doi.org/10.1016/j.ijfatigue.2012.11.011

119. Kumar P, Ramamurty U (2020) High cycle fatigue in selective laser melted Ti-6Al-4V. Acta Materialia 194:305–320. https://doi.org/10.1016/j.actamat.2020.05.041

120. Rafi HK, Karthik NV, Gong H, et al (2013) Microstructures and Mechanical Properties of Ti6Al4V Parts Fabricated by Selective Laser Melting and Electron Beam Melting. J of Materi Eng and Perform 22:3872–3883. https://doi.org/10.1007/s11665-013-0658-0

121. Vilaro T, Colin C, Bartout J-D (2011) As-fabricated and heat-treated microstructures of the Ti-6Al-4V alloy processed by selective laser melting. Metallurgical and materials transactions A 42:3190–3199

122. Nalla RK, Ritchie RO, Boyce BL, et al (2002) Influence of microstructure on high-cycle fatigue of Ti-6Al-4V: Bimodal vs. lamellar structures. Metall Mater Trans A 33:899–918. https://doi.org/10.1007/s11661-002-0160-z

123. Crupi V, Epasto G, Guglielmino E, Squillace A (2017) Influence of microstructure [alpha+beta and beta] on very high cycle fatigue behaviour of Ti-6Al-4V alloy. International Journal of Fatigue 95:64–75. https://doi.org/10.1016/j.ijfatigue.2016.10.002

124. Hilders O, Zambrano N (2014) The effect of aging on impact toughness and fracture surface fractal dimension in SAF 2507 super duplex stainless steel. Journal of Microscopy and Ultrastructure 2:236–244. https://doi.org/10.1016/j.jmau.2014.07.001

125. Macek W (2021) Correlation between Fractal Dimension and Areal Surface Parameters for Fracture Analysis after Bending-Torsion Fatigue. Metals 11:1790. https://doi.org/10.3390/met11111790

126. Macek W (2019) Fractal analysis of the bending-torsion fatigue fracture of aluminium alloy. Engineering Failure Analysis 99:97–107. https://doi.org/10.1016/j.engfailanal.2019.02.007

127. Macek W, Martins RF, Branco R, et al (2022) Fatigue fracture morphology of AISI H13 steel obtained by additive manufacturing. Int J Fract 235:79–98. https://doi.org/10.1007/s10704-022-00615-5

128. Krivonosova EA, Gorchakov AI (2013) Fractal analysis of the fatigue fracture surface of metal of welded joints. Welding International 27:690–693. https://doi.org/10.1080/09507116.2012.753273

129. Yun J-G, Ma C-Q, Yi J-J, Li X-W (2012) Qualitative and quantitative characterizations of fracture surfaces of AL6XN super-austenitic stainless steel fatigued at different stress amplitudes. Progress in Natural Science: Materials International 22:48–52. https://doi.org/10.1016/j.pnsc.2011.12.008

130. Tanaka M, Kato R (2012) Fractal analysis of fracture surfaces and simulation of fracture process using fractal dimension maps in stainless steels fatigued by repeated bending. ISIJ international 52:1683–1692

131. Usov VV, Gopkalo EE, Shkatulyak NM, et al (2015) Texture, microstructure, and fractal features of the low-cycle fatigue failure of the metal in pipeline welded joints. Russian Metallurgy 2015:759–770. https://doi.org/10.1134/S0036029515090128

132. Mir-Haidari S-E, Behdinan K (2022) Nonlinear effects of bolted flange connections in aeroengine casing assemblies. Mechanical Systems and Signal Processing 166:108433. https://doi.org/10.1016/j.ymssp.2021.108433

133. Meng X, Su L (2022) Research on noise reduction of rotary compressor valve components based on damping alloy. Science and Technology for the Built Environment 28:443–450. https://doi.org/10.1080/23744731.2022.2037361

134. Ewins DJ (2010) Control of vibration and resonance in aero engines and rotating machinery – An overview. International Journal of Pressure Vessels and Piping 87:504–510. https://doi.org/10.1016/j.ijpvp.2010.07.001

135. Conrad H (1981) Effect of interstitial solutes on the strength and ductility of titanium. Progress in Materials Science 26:123–403. https://doi.org/10.1016/0079-6425(81)90001-3

136. Lee D-G, Lee S, Lee Y (2008) Effect of precipitates on damping capacity and mechanical properties of Ti–6Al–4V alloy. Materials Science and Engineering: A 486:19–26. https://doi.org/10.1016/j.msea.2007.08.053

137. Amoo LM (2013) On the design and structural analysis of jet engine fan blade structures. Progress in Aerospace Sciences 60:1–11. https://doi.org/10.1016/j.paerosci.2012.08.002

138. Lee YT, Welsch G (1990) Young's modulus and damping of Ti□6Al□4V alloy as a function of heat treatment and oxygen concentration. Materials Science and Engineering: A 128:77–89. https://doi.org/10.1016/0921-5093(90)90097-M

139. Vrancken B, Wauthlé R, Kruth J-P, Van Humbeeck J (2013) Study of the influence of material properties on residual stress in selective laser melting. In: Proceedings of the Solid Freeform Fabrication Symposium. pp 393–407

140. Tsai M-T, Chen Y-W, Chao C-Y, et al (2020) Heat-treatment effects on mechanical properties and microstructure evolution of Ti-6Al-4V alloy fabricated by laser powder bed fusion. Journal of Alloys and Compounds 816:152615. https://doi.org/10.1016/j.jallcom.2019.152615

141. Phani MK, Kumar A, Jayakumar T, et al (2015) Mapping of elasticity and damping in an α + β titanium alloy through atomic force acoustic microscopy. Beilstein J Nanotechnol 6:767–776. https://doi.org/10.3762/bjnano.6.79

142. Fiocchi J, Biffi CA, Scaccabarozzi D, et al (2020) Enhancement of the Damping Behavior of Ti6Al4V Alloy through the Use of Trabecular Structure Produced by Selective Laser Melting. Advanced Engineering Materials 22:1900722. https://doi.org/10.1002/adem.201900722

143. Rosa F, Manzoni S, Casati R (2018) Damping behavior of 316L lattice structures produced by Selective Laser Melting. Materials & Design 160:1010–1018. https://doi.org/10.1016/j.matdes.2018.10.035

144. Scalzo F, Totis G, Vaglio E, Sortino M (2021) Experimental study on the high-damping properties of metallic lattice structures obtained from SLM. Precision Engineering 71:63–77. https://doi.org/10.1016/j.precisioneng.2021.02.010

145. (2020) Additive Calibration Guide

146. Mays TJ (2007) A new classification of pore sizes. Studies in Surface Science and Catalysis 160:57–62

147. García-Moreno A-I, Alvarado-Orozco J-M, Ibarra-Medina J, Martínez-Franco E (2021) Ex-situ porosity classification in metallic components by laser metal deposition: A machine learning-based approach. Journal of Manufacturing Processes 62:523–534. https://doi.org/10.1016/j.jmapro.2020.12.048

148. Torre I. G, Heck RJ, Tarquis AM (2020) MULTIFRAC: An ImageJ plugin for multiscale characterization of 2D and 3D stack images. SoftwareX 12:100574. https://doi.org/10.1016/j.softx.2020.100574

149. Chen C, Chang S, Zhu J, et al (2020) Residual stress of typical parts in laser powder bed fusion. Journal of Manufacturing Processes 59:621–628. https://doi.org/10.1016/j.jmapro.2020.10.009

150. Ghosh A, Biswas S, Turner T, et al (2021) Surface, microstructure, and tensile deformation characterization of LPBF SS316L microstruts micromachined with femtosecond laser. Materials & Design 210:110045. https://doi.org/10.1016/j.matdes.2021.110045

151. Jamshidinia M, Kovacevic R (2015) The influence of heat accumulation on the surface roughness in powder-bed additive manufacturing. Surf Topogr: Metrol Prop 3:014003. https://doi.org/10.1088/2051-672X/3/1/014003

152. Zhang L, Zhu H, Zhang S, et al (2019) Fabricating high dimensional accuracy LPBFed Ti6Al4V part by using bi-parameter method. Optics & Laser Technology 117:79–86. https://doi.org/10.1016/j.optlastec.2019.04.009

153. du Plessis A (2019) Effects of process parameters on porosity in laser powder bed fusion revealed by X-ray tomography. Additive Manufacturing 30:100871. https://doi.org/10.1016/j.addma.2019.100871

154. Budynas RG, Nisbett JK, Shigley JE (2015) Shigley's mechanical engineering design, Tenth edition. McGraw-Hill Education, New York, NY

155. Dieter GE (1976) Mechanical metallurgy, mcgracw-hill. Inc

156. Sames WJ, List FA, Pannala S, et al (2016) The metallurgy and processing science of metal additive manufacturing. International Materials Reviews 61:315–360. https://doi.org/10.1080/09506608.2015.1116649

157. Mulay RP, Moore JA, Florando JN, et al (2016) Microstructure and mechanical properties of Ti–6Al–4V: Mill-annealed versus direct metal laser melted alloys. Materials Science and Engineering: A 666:43–47. https://doi.org/10.1016/j.msea.2016.04.012

158. Qazi JI, Senkov ON, Rahim J, (Sam) Froes FH (2003) Kinetics of martensite decomposition in Ti–6Al–4V–xH alloys. Materials Science and Engineering: A 359:137–149. https://doi.org/10.1016/S0921-5093(03)00350-2

159. Hozoorbakhsh A, Ismail MIS, Aziz NBA (2015) A computational analysis of heat transfer and fluid flow in high-speed scanning of laser micro-welding. International Communications in Heat and Mass Transfer 68:178–187. https://doi.org/10.1016/j.icheatmasstransfer.2015.08.013

160. Tan C, Zhou K, Ma W, et al (2017) Microstructural evolution, nanoprecipitation behavior and mechanical properties of selective laser melted high-performance grade 300 maraging steel. Materials & Design 134:23–34. https://doi.org/10.1016/j.matdes.2017.08.026

161. Acharya R, Sharon JA, Staroselsky A (2017) Prediction of microstructure in laser powder bed fusion process. Acta Materialia 124:360–371. https://doi.org/10.1016/j.actamat.2016.11.018

162. Sercombe T, Jones N, Day R, Kop A (2008) Heat treatment of Ti-6Al-7Nb components produced by selective laser melting. Rapid Prototyping Journal 14:300–304. https://doi.org/10.1108/13552540810907974

163. Raghavan S, Nai MLS, Wang P, et al (2018) Heat treatment of electron beam melted (EBM) Ti-6Al-4V: microstructure to mechanical property correlations. Rapid Prototyping Journal 24:774–783. https://doi.org/10.1108/RPJ-05-2016-0070

164. Agius D, Kourousis KI, Wallbrink C, Song T (2017) Cyclic plasticity and microstructure of as-built SLM Ti-6Al-4V: The effect of build orientation. Materials Science and Engineering: A 701:85–100. https://doi.org/10.1016/j.msea.2017.06.069

165. Syed AK, Ahmad B, Guo H, et al (2019) An experimental study of residual stress and direction-dependence of fatigue crack growth behaviour in as-built and stress-relieved selective-laser-melted Ti6Al4V. Materials Science and Engineering: A 755:246–257. https://doi.org/10.1016/j.msea.2019.04.023

166. Xiu M, Tan YT, Raghavan S, et al (2022) The effect of heat treatment on microstructure, microhardness, and pitting corrosion of Ti6Al4V produced by electron beam melting additive manufacturing process. Int J Adv Manuf Technol. https://doi.org/10.1007/s00170-022-08839-4

167. Kelly SM, Kampe SL (2004) Microstructural evolution in laser-deposited multilayer Ti-6Al-4V builds: Part I. Microstructural characterization. Metallurgical and Materials Transactions A 35:1861–1867

168. Facchini L, Magalini E, Robotti P, et al (2010) Ductility of a Ti-6Al-4V alloy produced by selective laser melting of prealloyed powders. Rapid Prototyping Journal 16:450–459. https://doi.org/10.1108/13552541011083371

169. Thöne M, Leuders S, Riemer A, et al (2012) Influence of Heat-Treatment of Selective Laser Melting Products - e.g. Ti6Al4V. University of Texas at Austin

170. Mengucci P, Santecchia E, Gatto A, et al (2019) Solid-State Phase Transformations in Thermally Treated Ti–6Al–4V Alloy Fabricated via Laser Powder Bed Fusion. Materials 12:2876. https://doi.org/10.3390/ma12182876

171. Callister WD (2000) Fundamentals of materials science and engineering. Wiley London

172. Pederson R, Babushkin O, Skystedt F, Warren R (2003) Use of high temperature X-ray diffractometry to study phase transitions and thermal expansion properties in Ti-6Al-4V. Materials Science and Technology 19:1533–1538. https://doi.org/10.1179/026708303225008013

173. Huang J-Y, Chang C-H, Wang W-C, et al (2020) Systematic evaluation of selective fusion additive manufacturing based on thermal energy source applied in processing of titanium alloy specimens for medical applications. The International Journal of Advanced Manufacturing Technology 109:2421–2429

174. Frkan M, Konecna R, Nicoletto G, Kunz L (2019) Microstructure and fatigue performance of SLM-fabricated Ti6Al4V alloy after different stress-relief heat treatments. Transportation Research Procedia 40:24–29. https://doi.org/10.1016/j.trpro.2019.07.005

175. Oh J, Lee JG, Kim NJ, et al (2004) Effects of thickness on fatigue properties of investment cast Ti-6Al-4V alloy plates. Journal of materials science 39:587–591

176. Khorasani A, Gibson I, Awan US, Ghaderi A (2019) The effect of SLM process parameters on density, hardness, tensile strength and surface quality of Ti-6Al-4V. Additive Manufacturing 25:176–186. https://doi.org/10.1016/j.addma.2018.09.002

177. Chong Y, Bhattacharjee T, Tsuji N (2019) Bi-lamellar microstructure in Ti–6Al–4V: Microstructure evolution and mechanical properties. Materials Science and Engineering: A 762:138077. https://doi.org/10.1016/j.msea.2019.138077

178. Sahoo R, Mantry S, Sahoo TK, et al (2013) Effect of Microstructural Variation on Erosion Wear Behavior of Ti-6Al-4V Alloy. Tribology Transactions 56:555–560. https://doi.org/10.1080/10402004.2013.767400

179. Kumar J, Punnose S, Mukhopadhyay CK, et al (2012) Acoustic Emission During Tensile Deformation of Smooth and Notched Specimens of Near Alpha Titanium Alloy. Research in Nondestructive Evaluation 23:17–31. https://doi.org/10.1080/09349847.2011.622068

180. Promoppatum P, Srinivasan R, Quek SS, et al (2022) Quantification and prediction of lack-of-fusion porosity in the high porosity regime during laser powder bed fusion of Ti-6Al-4V. Journal of Materials Processing Technology 300:117426. https://doi.org/10.1016/j.jmatprotec.2021.117426

181. Wolff SJ, Lin S, Faierson EJ, et al (2017) A framework to link localized cooling and properties of directed energy deposition (DED)-processed Ti-6Al-4V. Acta Materialia 132:106–117. https://doi.org/10.1016/j.actamat.2017.04.027

182. Pathania A, Subramaniyan AK, Nagesha BK (2022) Influence of post-heat treatments on microstructural and mechanical properties of LPBF-processed Ti6Al4V alloy. Prog Addit Manuf. https://doi.org/10.1007/s40964-022-00306-6

183. Tascioglu E, Karabulut Y, Kaynak Y (2020) Influence of heat treatment temperature on the microstructural, mechanical, and wear behavior of 316L stainless steel fabricated by laser powder bed additive manufacturing. The International Journal of Advanced Manufacturing Technology 1–10

184. Ju J, Zhou Y, Wang K, et al (2020) Tribological investigation of additive manufacturing medical Ti6Al4V alloys against Al2O3 ceramic balls in artificial saliva. Journal of the Mechanical Behavior of Biomedical Materials 104:103602. https://doi.org/10.1016/j.jmbbm.2019.103602

185. Sow MC, De Terris T, Castelnau O, et al (2020) Influence of beam diameter on Laser Powder Bed Fusion (L-PBF) process. Additive Manufacturing 36:101532. https://doi.org/10.1016/j.addma.2020.101532

186. King WE, Barth HD, Castillo VM, et al (2014) Observation of keyhole-mode laser melting in laser powder-bed fusion additive manufacturing. Journal of Materials Processing Technology 214:2915–2925. https://doi.org/10.1016/j.jmatprotec.2014.06.005

187. Hann DB, Iammi J, Folkes J (2011) A simple methodology for predicting laser-weld properties from material and laser parameters. J Phys D: Appl Phys 44:445401. https://doi.org/10.1088/0022-3727/44/44/445401

188. Fabbro R (2019) Scaling laws for the laser welding process in keyhole mode. Journal of Materials Processing Technology 264:346–351. https://doi.org/10.1016/j.jmatprotec.2018.09.027

189. Salarian M, Asgari H, Vlasea M (2020) Pore space characteristics and corresponding effect on tensile properties of Inconel 625 fabricated via laser powder bed fusion. Materials Science and Engineering: A 769:138525. https://doi.org/10.1016/j.msea.2019.138525

190. Wang L, Zhang Y, Chia HY, Yan W (2022) Mechanism of keyhole pore formation in metal additive manufacturing. npj Computational Materials 8:1–11

191. Kosonen T, Kakko K, Raitanen N (2021) Evaluation of pore re-opening after HIP in LPBF Ti–6Al–4V. Powder Metallurgy 64:425–433. https://doi.org/10.1080/00325899.2021.1928997

192. Keshavarz MK, Sikan F, Boutet CE, et al (2019) Impact properties of half stress-relieved and hot isostatic pressed Ti–6Al–4V components fabricated by laser powder bed fusion. Materials Science and Engineering: A 760:481–488. https://doi.org/10.1016/j.msea.2019.05.035

193. Chen C, Xie Y, Yan X, et al (2019) Effect of hot isostatic pressing (HIP) on microstructure and mechanical properties of Ti6Al4V alloy fabricated by cold spray additive manufacturing. Additive Manufacturing 27:595–605. https://doi.org/10.1016/j.addma.2019.03.028

194. Majeed A, Muzamil M, Lv J, et al (2019) Heat treatment influences densification and porosity of AlSi10Mg alloy thin-walled parts manufactured by selective laser melting technique. J Braz Soc Mech Sci Eng 41:267. https://doi.org/10.1007/s40430-019-1769-9

195. Tammas-Williams S, Withers PJ, Todd I, Prangnell PB (2016) The effectiveness of hot isostatic pressing for closing porosity in titanium parts manufactured by selective electron beam melting. Metallurgical and materials transactions A 47:1939–1946

196. Uzan NE, Shneck R, Yeheskel O, Frage N (2017) Fatigue of AlSi10Mg specimens fabricated by additive manufacturing selective laser melting (AM-SLM). Materials Science and Engineering: A 704:229–237. https://doi.org/10.1016/j.msea.2017.08.027

197. du Plessis A, Rossouw P (2015) Investigation of Porosity Changes in Cast Ti6Al4V Rods After Hot Isostatic Pressing. J of Materi Eng and Perform 24:3137–3141. https://doi.org/10.1007/s11665-015-1580-4

198. Majeed A, Zhang YF, Lv JX, et al (2018) Study the effect of heat treatment on the relative density of SLM built parts of AlSi10Mg alloy. In: Proceedings of the 48th International Conference on Computers and Industrial Engineering (CIE 2018), Auckland, New Zealand. pp 2–5

199. Ang ASM, Berndt CC (2014) A review of testing methods for thermal spray coatings. International Materials Reviews 59:179–223. https://doi.org/10.1179/1743280414Y.0000000029

200. Raynova S, Imam MA, Yang F, Bolzoni L (2019) Hybrid microwave sintering of blended elemental Ti alloys. Journal of Manufacturing Processes 39:52–57. https://doi.org/10.1016/j.jmapro.2019.02.002

201. Bandar A-M, Vo P, Mongrain R, et al (2014) Effect of heat treatment on the microstructure and mechanical properties of stainless steel 316L coatings produced by cold spray for biomedical applications. Journal of thermal spray technology 23:641–652

202. Crowe T, Guraydin A (2011) The Effects of Heat Treatment on Area Percent Porosity and Corrosion Behavior of High-Nickel Thermal Spray Coatings. Materials Engineering

203. van Dijk N, van der Zwaag S (2018) Self-Healing Phenomena in Metals. Advanced Materials Interfaces 5:1800226. https://doi.org/10.1002/admi.201800226

204. Bhagat RP, Chattoraj US, Sil SK (2006) Porosity of Sinter and Its Relation with the Sintering Indices. ISIJ International 46:1728–1730. https://doi.org/10.2355/isijinternational.46.1728

205. Gómez SY, Hotza D (2018) Predicting powder densification during sintering. Journal of the European Ceramic Society 38:1736–1741. https://doi.org/10.1016/j.jeurceramsoc.2017.10.020

206. He B, Wu W, Zhang L, et al (2018) Microstructural characteristic and mechanical property of Ti6Al4V alloy fabricated by selective laser melting. Vacuum 150:79–83. https://doi.org/10.1016/j.vacuum.2018.01.026

207. Galindo-Fernández MA, Mumtaz K, Rivera-Díaz-del-Castillo PEJ, et al (2018) A microstructure sensitive model for deformation of Ti-6Al-4V describing Cast-and-Wrought and Additive Manufacturing morphologies. Materials & Design 160:350–362. https://doi.org/10.1016/j.matdes.2018.09.028

208. Li KM, Liu YJ, Liu XC, et al (2022) Simultaneous strength-ductility enhancement in as-cast Ti6Al4V alloy by trace Ce. Materials & Design 215:110491. https://doi.org/10.1016/j.matdes.2022.110491

209. Simonelli M, Tse YY, Tuck C (2014) The formation of α + β microstructure in as-fabricated selective laser melting of Ti–6Al–4V. Journal of Materials Research 29:2028–2035. https://doi.org/10.1557/jmr.2014.166

210. Xu X, Nash P (2014) Sintering mechanisms of Armstrong prealloyed Ti–6Al–4V powders. Materials Science and Engineering: A 607:409–416. https://doi.org/10.1016/j.msea.2014.03.045

211. (2017) Investigation of the high-cycle fatigue life of selective laser melted and hot isostatically pressed Ti-6Al-4V. CRC Press

212. Tan X, Kok Y, Toh WQ, et al (2016) Revealing martensitic transformation and α/β interface evolution in electron beam melting three-dimensional-printed Ti-6Al-4V. Scientific reports 6:1–10

213. Park CH, Son YI, Lee CS (2012) Constitutive analysis of compressive deformation behavior of ELI-grade Ti–6Al–4V with different microstructures. J Mater Sci 47:3115–3124. https://doi.org/10.1007/s10853-011-6145-9

214. Chen C, Gu D, Dai D, et al (2019) Laser additive manufacturing of layered TiB2/Ti6Al4V multi-material parts: Understanding thermal behavior evolution. Optics & Laser Technology 119:105666. https://doi.org/10.1016/j.optlastec.2019.105666

215. Alipour S, Moridi A, Liou F, Emdadi A (2022) The Trajectory of Additively Manufactured Titanium Alloys with Superior Mechanical Properties and Engineered Microstructures. Additive Manufacturing 60:103245. https://doi.org/10.1016/j.addma.2022.103245

216. Bermingham MJ, Nicastro L, Kent D, et al (2018) Optimising the mechanical properties of Ti-6Al-4V components produced by wire + arc additive manufacturing with post-process heat treatments. Journal of Alloys and Compounds 753:247–255. https://doi.org/10.1016/j.jallcom.2018.04.158

217. Shui X, Yamanaka K, Mori M, et al (2017) Effects of post-processing on cyclic fatigue response of a titanium alloy additively manufactured by electron beam melting. Materials Science and Engineering: A 680:239–248. https://doi.org/10.1016/j.msea.2016.10.059

218. Edwards P, Ramulu M (2014) Fatigue performance evaluation of selective laser melted Ti–6Al–4V. Materials Science and Engineering: A 598:327–337. https://doi.org/10.1016/j.msea.2014.01.041

219. Dareh Baghi A, Nafisi S, Hashemi R, et al (2021) Experimental realisation of build orientation effects on the mechanical properties of truly as-built Ti-6Al-4V SLM parts. Journal of Manufacturing Processes 64:140–152. https://doi.org/10.1016/j.jmapro.2021.01.027

220. Rafi HK, Starr TL, Stucker BE (2013) A comparison of the tensile, fatigue, and fracture behavior of Ti–6Al–4V and 15-5 PH stainless steel parts made by selective laser melting. Int J Adv Manuf Technol 69:1299–1309. https://doi.org/10.1007/s00170-013-5106-7

221. Mertens A, Reginster S, Paydas H, et al (2014) Mechanical properties of alloy Ti–6Al–4V and of stainless steel 316L processed by selective laser melting: influence of out-of-equilibrium microstructures. Powder Metallurgy 57:184–189. https://doi.org/10.1179/1743290114Y.0000000092

222. Murr LE, Quinones SA, Gaytan SM, et al (2009) Microstructure and mechanical behavior of Ti–6Al–4V produced by rapid-layer manufacturing, for biomedical applications. Journal of the Mechanical Behavior of Biomedical Materials 2:20–32. https://doi.org/10.1016/j.jmbbm.2008.05.004

223. Das J, Linke B (2017) Evaluation and systematic selection of significant multi-scale surface roughness parameters (SRPs) as process monitoring index. Journal of Materials Processing Technology 244:157–165. https://doi.org/10.1016/j.jmatprotec.2017.01.017

224. Kumar SA, Sundar R, Raman SGS, et al (2014) Influence of laser peening on microstructure and fatigue lives of Ti–6Al–4V. Transactions of Nonferrous Metals Society of China 24:3111–3117. https://doi.org/10.1016/S1003-6326(14)63449-X

225. Lutjering G, Williams JC, Gysler A MICROSTRUCTURE AND MECHANICAL PROPERTIES OF TITANIUM ALLOYS

226. Ackelid U, Svensson M (2009) Additive Manufacturing of Dense Metal Parts by Electron Beam Melting

227. Shamir M, Syed AK, Janik V, et al (2020) The role of microstructure and local crystallographic orientation near porosity defects on the high cycle fatigue life of an additive manufactured Ti-6Al-4V. Materials Characterization 169:110576. https://doi.org/10.1016/j.matchar.2020.110576

228. Tammas-Williams S, Withers PJ, Todd I, Prangnell PB (2017) The influence of porosity on fatigue crack initiation in additively manufactured titanium components. Scientific reports 7:1–13

229. Afroz L, Das R, Qian M, et al (2022) Fatigue behaviour of laser powder bed fusion (L-PBF) Ti–6Al–4V, Al–Si–Mg and stainless steels: a brief overview. Int J Fract 235:3–46. https://doi.org/10.1007/s10704-022-00641-3

230. Sterling AJ, Torries B, Shamsaei N, et al (2016) Fatigue behavior and failure mechanisms of direct laser deposited Ti–6Al–4V. Materials Science and Engineering: A 655:100–112. https://doi.org/10.1016/j.msea.2015.12.026

231. Chastand V, Tezenas A, Cadoret Y, et al (2016) Fatigue characterization of Titanium Ti-6Al-4V samples produced by Additive Manufacturing. Procedia Structural Integrity 2:3168–3176. https://doi.org/10.1016/j.prostr.2016.06.395

232. Pegues JW, Shao S, Shamsaei N, et al (2020) Fatigue of additive manufactured Ti-6Al-4V, Part I: The effects of powder feedstock, manufacturing, and post-process conditions on the resulting microstructure and defects. International Journal of Fatigue 132:105358. https://doi.org/10.1016/j.ijfatigue.2019.105358

233. Sen I, Gopinath K, Datta R, Ramamurty U (2010) Fatigue in Ti–6Al–4V–B alloys. Acta Materialia 58:6799–6809. https://doi.org/10.1016/j.actamat.2010.09.008

234. Ma Y, Xue Q, Wang H, et al (2017) Deformation twinning in fatigue crack tip plastic zone of Ti-6Al-4V alloy with Widmanstatten microstructure. Materials Characterization 132:338–347. https://doi.org/10.1016/j.matchar.2017.08.029

235. Cai C, Zheng H, Khan MS, Hung KC (2002) Modeling of material damping properties in ANSYS. In: CADFEM users' meeting & ANSYS conference. pp 9–11

236. Yarar E, Ertürk AT, Açıkgöz Ç, Karabay S (2022) Experimental and numerical vibration analysis of surface mechanical attrition treatment. Journal of Vibration and Control 10775463221139600. https://doi.org/10.1177/10775463221139600

237. Eslaminejad A, Ziejewski M, Karami G (2019) An experimental–numerical modal analysis for the study of shell-fluid interactions in a clamped hemispherical shell. Applied Acoustics 152:110–117. https://doi.org/10.1016/j.apacoust.2019.03.029

238. Dahak M, Touat N, Benseddiq N (2017) On the classification of normalized natural frequencies for damage detection in cantilever beam. Journal of Sound and Vibration 402:70–84. https://doi.org/10.1016/j.jsv.2017.05.007

239. Liu J, Zhang K, Gao X, et al (2022) Effects of the morphology of grain boundary α-phase on the anisotropic deformation behaviors of additive manufactured Ti–6Al–4V. Materials & Design 223:111150. https://doi.org/10.1016/j.matdes.2022.111150

240. Kumar A, Meenashisundaram GK, Manakari V, et al (2017) Lanthanum effect on improving CTE, damping, hardness and tensile response of Mg-3Al alloy. Journal of Alloys and Compounds 695:3612–3620. https://doi.org/10.1016/j.jallcom.2016.11.400

LIST OF PUBLICATIONS BASED ON THIS THESIS

International Peer-Reviewed Journals

1. **P, Akshay**; S, Anand Kumar; BK, Nagesh, Influence of post-heat treatments on microstructural and mechanical properties of LPBF-processed Ti6Al4V alloy, Progress in Additive Manufacturing 7 (6), 1323-1343.
2. **P, Akshay**; S, Anand Kumar; BK, Nagesh, Influence of Post-Heat Treatment with Super β transus temperature on the Tensile behaviour of LPBF processed Ti6Al4V, Journal of Process Mechanical Engineering, (***revised manuscript*** – under review).
3. **P, Akshay**; S, Anand Kumar; BK, Nagesh, Effect of Shear Strength on the Support Removal of LPBF Manufactured Gear-type Ti6Al4V Parts, Journal of Process Mechanical Engineering, (***revised manuscript***-under review)
4. **P, Akshay**; S, Anand Kumar; BK, Nagesh, Fractal Dimension Analysis of Post-Heat Treated LPBF Processed Ti6Al4V under Fatigue Loading, Metals, (***revised manuscript*** – under review)
5. **P, Akshay**; S, Anand Kumar; BK, Nagesh, Densification behaviour of laser powder bed fusion processed Ti6Al4V: Effects of customized heat treatment (CHT) and build direction, Journal of Process Mechanical Engineering, (***revised manuscript*** – under review).
6. **P, Akshay**; S, Anand Kumar; BK, Nagesh, Influence of Post-Heat Treatment with Super β transus temperature on the Fatigue behaviour of LPBF processed Ti6Al4V, International Journal of Fracture, (Under review).
7. **P, Akshay**; S, Anand Kumar; BK, Nagesh, Sanjay, BG, Effect of Post-Heat Treatment with Super β transus temperature on the Damping Behaviour of LPBF processed Ti6Al4V Thin Rotor Blade, Journal of Materials: Design and Applications, (Under review).
8. **P, Akshay**; S, Anand Kumar; BK, Nagesh, Skin-core scanning strategy in LPBF processed Ti6Al4V: Effects on Microstructure and Microhardness, Materials Performance and Characterization, (Under review).

Conference proceeding paper:

1. **P, Akshay**; S, Anand Kumar; BK, Nagesh, Post-processing of the support structure of LPBF-processed Ti6Al4V part: Effect of process parameters, Structural Integrity Procedia (Under review).

International Conference paper:

2. **P, Akshay**; S, Anand Kumar; BK, Nagesh, Post-processing of the support structure of LPBF-processed Ti6Al4V part: Effect of process parameters, Oral Presentation, International Conference, Structural Integrity and Reliability of Advanced Materials obtained through Additive Manufacturing SIRAMM-23, held on March 8-11, 2023, Romania